UNIVERSITY OF SOUTHAMPTON

A COMPUTATIONAL FLUID DYNAMICS INVESTIGATION INTO THE PARTICULATE EROSION OF OILFIELD CONTROL VALVES

VOLUME 1

BY

ALISTER FRANK FORDER

A dissertation submitted in the partial fulfillment of the requirements for the degree of Doctor of Philosophy at the University of Southampton

Faculty of Engineering and Applied Science

January 2001

UNIVERSITY OF SOUTHAMPTON

ABSTRACT

FACULTY OF ENGINEERING AND APPLIED SCIENCE
DEPARTMENT OF MECHANICAL ENGINEERING

Doctor of Philosophy

A COMPUTATIONAL FLUID DYNAMICS INVESTIGATION INTO THE PARTICULATE EROSION OF OILFIELD CONTROL VALVES

by Alister Frank Forder

In fulfilment of the requirements of a Doctorate of Philosophy, this research programme details the development of a numerical technique, whereby the solid particle erosion phenomena experienced within petroleum control valves can be investigated. The study has been facilitated by the collaboration of the University of Southampton and BP Exploration Operating Co. Ltd, under the Engineering & Physical Science Research Council CASE scheme.

Sand particles, produced in addition to petroleum fluids, present a major erosional hazard to transport and process control equipment within the oil industry. The control valve, or choke, is most susceptible to erosion, experiencing failures in a matter of days for the most extreme cases. Figures obtained by BP suggest that 35% of choke failures can be attributed to erosion for one major oilfield; such a failure rate presents a major economic handicap with regards to both lost production and change-out costs.

The primary objective of the research programme was the extension of a commercial Computational Fluid Dynamic *(CFD)* code, CFX-F3D, such that the intensity and distribution of solid particle erosion rates within complex geometric configurations, such as chokes, could be predicted. Particle trajectories were computed through the momentum argument with the turbulent flow field; the flow field being predicted through the standard turbulence closure model of the *CFD* code. The erosion rates were computed as a function of individual particle impact characteristics, given target material type. Three dimensional surface plots of the choke internals displayed the particle impact velocities, angle of impact and erosion rates. Erosion hotspots are identified, allowing design evolution to be easily incorporated and analysed. Such a process improves our understanding of the erosion mechanisms induced.

The validity of the software developments were proven against a number of experimental data sets, including the erosion of full scale control chokes. Such were the successes of the modifications work undertaken, and the applicability of the erosion model incorporated into the code of CFX-F3D, that very accurate erosion prediction, in terms of both location and intensity, were facilitated. Prediction errors of less than 8% were achieved, being a marked success given consideration to the complexities involved.

Table of Contents

List of Figures and Tables

Acknowledgements

I would like to take this opportunity to acknowledge the financial assistance provided by the Engineering and Physical Science Research Council and British Petroleum Exploration Operating Company Ltd. I would also like to express my appreciation of the support and generosity provided by Copper Cameron Ltd. of Longford Ireland and ABB. Kent Introl Ltd. of Brighouse UK.

Those persons I would like to thank individually include, my academic supervisor Prof. Martin Thew, for his encouragement and belief in my abilities; my industrial supervisor at BP, Dr Dave Harrison, for his technical/financial input and his genuine interest in the project. Mark Brooke of Copper Cameron Ltd. for his honesty and technical direction, and Dr Robert Wood for a sympathetic ear and his experience in the research area. I also extend my gratitude to Dr Wood for taking up the chalice of my continued supervision and guidance upon the retirement of Prof. Thew.

Finally, I would like to thank my wife, Marie, and my children, Liam, Ella and Reis, for their unending support and ability to put up with me, my moods and my workloads.

Nomenclature

A	characteristic material constant.	---
A_p	projected area of particle.	m^2
c	speed of sound in material.	m/s
C_d	speed of sound in liquid droplet.	m/s
C_f	valve pressure recovery factor.	---
C_k	characteristic velocity of cutting erosion.	m/s
C_p	specific molar heat capacity.	kJ/kmol
C_v	valve flow coefficient.	---
C_1	empirical constant.	---
D_k	characteristic velocity of deformation erosion.	m/s
D_L	dynamic load applied by liquid droplet at impact.	N/m^2
d_o	threshold erodent particle size below which erosion does not occur.	m
d_p	diameter of particle.	m
E	particle coefficient of restitution.	---
E_{par}	parallel component of the coefficient of restitution.	---
E_{perp}	perpendicular component of the coefficient of restitution.	---
E_c	cutting erosion factor (energy required to remove a unit volume of material by cutting erosion).	J/m^3
E_f	deformation erosion factor (energy required to remove a unit volume of material by deformation erosion).	J/m^3
E_p	Young's modulus for particle.	N/m^2
E_t	Young's modulus for target.	N/m^2
F_{du}	particle fragmentation factor (0-1).	---
f_p	fraction of particle cutting in an idealised manner.	---
h_{el}	elastic deformation depth of impact crater.	m
H	depth of crater concavity.	m
H_{pe}	plastic-elastic deformation depth of impact crater.	m
H_t	static hardness of target material (Hv).	---
H_p	particle hardness (Hv).	---
I_p	moment of inertia of particle.	J/m^3
k	thermal conductivity of target material.	kW/mK
K	ratio of vertical force to horizontal force acting on the particle ≈ 2.	---
K'	threshold normal velocity component below which erosion does not occur.	m/s
k_1, k_2	empirical constants determined by experimental data fitting.	---

K_E	expansion correction factor.	---
K_t	kinetic energy transferred to target per unit mass of impacting particles.	J
m	molecular mass of target material.	kg/kmol
m_p	mass of particle.	kg
m_w	molecular weight.	kg/kmol
n	characteristic velocity exponent (value 2-3).	---
N_{ER}	normalised liquid droplet erosion rate.	---
N_p	total cycles to failure at strain amplitude.	---
P	horizontal component of flow pressure.	N/m^2
P_{av}	average pressure with elastic impact.	N/m^2
P_{max}	maximum pressure with elastic impact.	N/m^2
P_1	inlet pressure of fluid.	N/m^2
P_p	circular perimeter projection of particle.	m^2
q_p	Poisson's ratio for particle.	---
q_t	Poisson's ratio for target.	---
Q	volumetric flow rate.	m^3/hr
Q_{el}	elastic deformation energy.	J
Q_{pe}	plastic-elastic deformation energy.	J
Q_{pl}	plastic deformation energy.	J
Q_T	total energy transferred at impact.	J
r_c	total contact radius of particle.	m
r_{el}	elastic contact radius of particle.	m
r_p	radius of particle.	m
r_{pl}	plastic contact radius of particle.	m
R_{epc}	critical particle Reynolds number.	---
R_f	roundness factor of particle (value 0.1-1).	---
R_{vf}	squeeze film retardation factor at impact.	---
S	proportionality constant in dimensional analysis.	---
S_g	specific gravity.	---
T_m	melting temperature of target material.	°C
T_1	inlet temperature of fluid.	°C
U	particle impact velocity.	m/s
U_d	droplet impact velocity	m/s
U_h	horizontal component of particle impact velocity.	m/s
U_o	threshold velocity below which deformation is entirely elastic and no erosion damage occurs.	m/s

U_r	reference velocity at which $\varepsilon 1$ and $\varepsilon 2$ are evaluated.	m/s
u_{rf}	reflected velocity of particle at impact.	m/s
U_{sg}	superficial gas velocity.	m/s
U_t	horizontal component of particle impact velocity.	m/s
v_1	inlet specific volume.	m^3/hr
V_H	multi-stage correction factor.	---
W	eroded volume.	m^3
W_c	eroded volume due to cutting.	m^3
W_d	eroded volume due to deformation.	m^3
W_e	Weber number.	---
W_t	solid particle erosion induced at impact.	m^3
W_{td}	liquid droplet erosion induced at impact.	mm
Y	yield stress of target.	N/m^2
y	elastic load limit.	N/m^2
Z	compressibility factor.	---
α	angle of particle impact.	deg.
α_c	critical angle of embedment.	deg.
ε	eroded volume.	m^3
ε_1	maximum primary erosion for reference velocity.	m^3
ε_2	maximum secondary erosion for reference velocity.	m^3
ε_p	plastic strain range.	μm/m
ρ_d	density of liquid droplet.	kg/m^3
ρ_g	fluid density.	kg/m^3
ρ_p	density of particle.	kg/ m^3
ρ_t	density of target.	kg/ m^3
σ	plastic flow stress of target.	N/m^2
σ_k	Prandtl number for turbulent kinetic energy.	---
σ_ε	Prandtl number for viscous dissipation.	---
σ_{st}	surface tension of liquid droplet.	N/m
Ψ	ratio of depth of contact to depth of cut ≈ 2.	---
Δ_p	sizing pressure drop.	bar
ΔHm	enthalpy of melting of the target material.	kJ/kmol
τ	a function of the latent heat of melting and the melting temperature of the target material.	---
θ_d	droplet diameter.	mm
θ_{max}	maximum droplet diameter.	mm

θp	particle diameter.	m
θ_1	upstream droplet diameter.	mm
θ_2	downstream droplet diameter.	mm
ϕ	empirical load index.	---
ϑ	velocity scale of turbulence.	---
l	length scale of turbulence.	---

1. Introduction To The Project

1.1 The Stimulus

It is essential that a flow control system be utilised to control hydrocarbon production from the reservoir; where liquids, gases, suspended solids or any combination flow under a differential pressure from the well. The differential pressure required to lift the product being supplied through either the hydrostatic pressure of the well or by an artificial lifting technique such as downhole pumps or water flood. If no control were to be imposed upon the rate of hydrocarbon extraction, irreversible damage to the structure of the reservoir would result. Such damage gives rise to lost revenue through the loss of otherwise recoverable hydrocarbon deposits.

The control system prevents such a happening by restricting the rate of hydrocarbon extraction through the installation of control valves; being fitted to individual risers from the reservoir. Such an installation pattern provides pressure balancing within the reservoir, allowing the combined flow rates to be optimised through time specified drainage; thus maximising production and hence income generated. An additional advantage of the control valve, known as the control choke, is that it enables a reduction in the pressure rating of the subsequent processing facility through early pressure let down.

To provide flow control, the control choke acts as a throttling device, utilising energy dissipation as its means of operation. A differential pressure across the control choke is converted into a flow velocity via a flow restriction, such as a port. This high velocity flow is then dissipated by a combination of friction, turbulence and diffusion; generating the desired pressure drop and flow control characteristics. The cross sectional area of the ports presented to the flow, or the area ratio of the port to the inlet, controls the magnitude of the pressure drop and the resulting volumetric flow rate.

As hydrocarbons are extracted from the reservoir, the porous rock structure that holds the petroleum fluids can fragment with localised collapses. That reservoir rock which is most troublesome, regarding the erosion problem, is sandstone; however, petroleum fluids may also be held in differing porous structures. Rock fragmentation within the reservoir results in solids, normally sand, being produced in addition to the water, oil and gas. It is noteworthy that the stage of reservoir development influences the rate of sand production, in addition to the manner in which the reservoir is operated. When the reservoir is first brought on-line, sand production rates are normally high in this initial commission period. This problem is further exacerbated by higher than normal operating pressure within the reservoir during this time. A similar situation arises when the well has been shut-in for an extended period.

Due to the operating principle of the control choke (i.e. the generation of high velocity flows), rapid erosion occurs when solids are entrained within the process stream. In the most aggressive fields, where the sand concentrations and operating pressures are high, the time to valve failure can be as low as weeks. As an indication to the severity of the erosion problem, BP Exploration have experienced choke failures due to loss of flow control every 8-14 days, for a 900 psi (6.2 MN/m^2) pressure drop well. Figure 1-1 and Figure 1-2 detail the damage to the control choke in question. The well attributed to such failures produced 2000 bbls of oil per day; as such the economic penalties for choke failure are high. Over a year, given a crude price of $15 per bbl, the projected loss of production alone is of the order of $80,000; assuming a valve overhaul time of two hours.

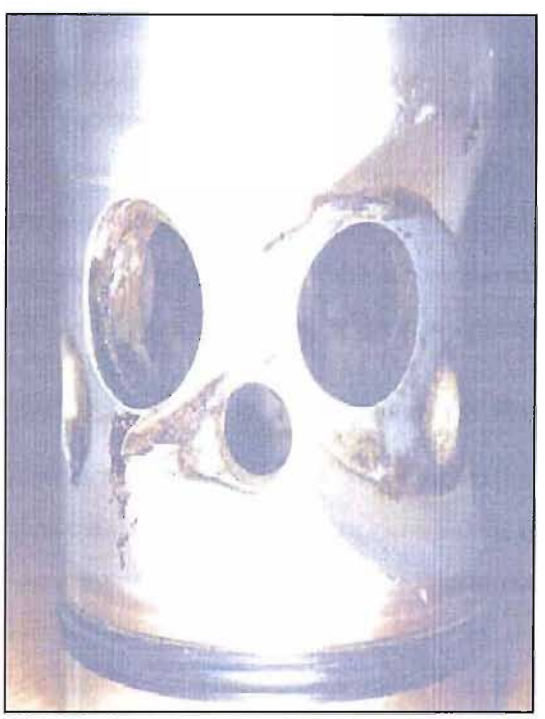

Figure 1-1 Sand Erosion of the Cage of a 3" Control Choke

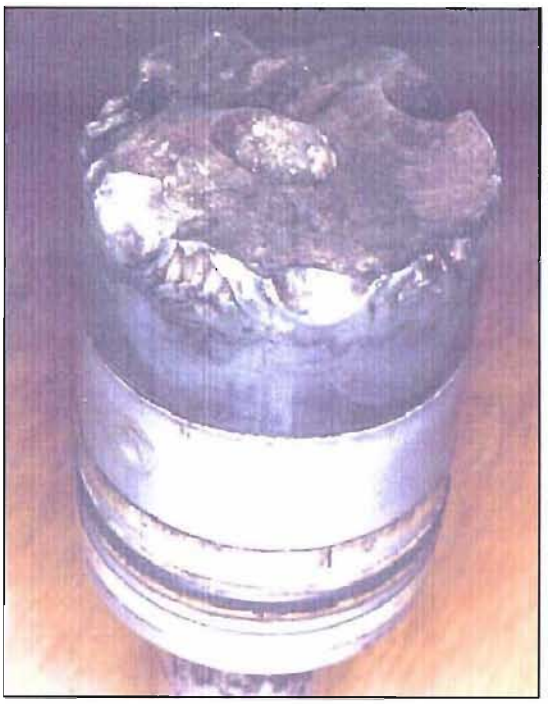

Figure 1-2 Sand Erosion of the Plug of a 3" Control Choke

A survey at BP Exploration **[Ref. 69],** which became the main impetus to this project, revealed a failure rate due to erosion of 35%, or 105 failures of a total 258 valves logged during a two year period. See Figure 1-3. It is important to note that some of the failures attributed to 'broken trim' and 'flow control' may have also been contributed to by erosion mechanisms; as such the failure rates due to erosion may be higher.

Despite the decades of operating experience, there seems to be little factual data on erosion limitation in chokes. Traditionally, with topside well control, such an erosion problem was simply accepted as a consequence of production from a sandy well. However, with the emergence of improved subsea technology, deep water or small marginal fields that were previously uneconomical are being exploited;

such as the Scheihallion, Foinaven and ETAP fields. Here control chokes are being installed subsea, however the failure and subsequent intervention to change out the control choke has major cost implications.

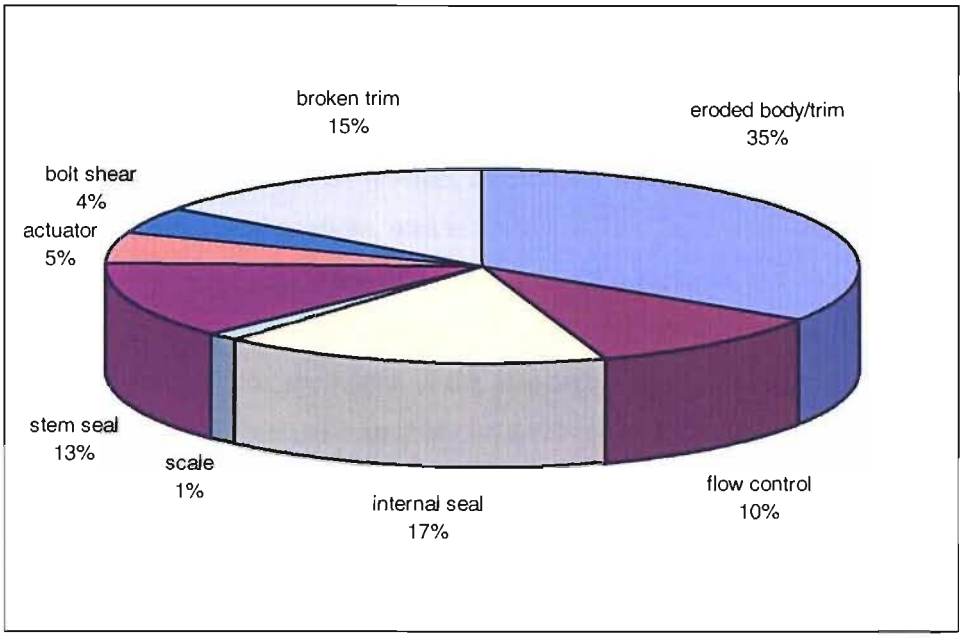

Figure 1-3 Choke Valve Failures at BP Prudhoe Bay (87-89) [Ref. 69].

The present cost of subsea choke failure is in the region of $500,000, given loss of revenue and the hire of a support vessel. The costs involved in a failure rate due to erosion, if at 35%, are not acceptable. Thus, the service life of subsea chokes is at a premium, meaning the main cause of failure, erosion, must be addressed; the reader is referred to Section 3.1.1.

Such a situation is further exemplified by recent drives towards down-hole flow control. Here, the control choke will be installed within the well tubing, below the Christmas tree and internal to the reservoir. The reasoning for such an application of flow control is the improved extraction capabilities that can be achieved. The control choke will not be 'pulled' if failure occurs; due to the economics. As such, it is imperative that a fit for purpose choke, which is sufficiently robust, be developed for such applications.

The Objectives of the Research Project

Although sand erosion cannot be eliminated completely, steps may be taken to minimise its effects. Two techniques are available to the engineer. Firstly, one may employ ever more exotic materials, such as diamond and ceramic. Such materials display good erosion resistance characteristics; however, they are both expensive to manufacture and difficult to engineer. Secondly, the basic design can be investigated, specifically the interactions of the flow field and the entrained solids, thus promoting an improved understanding of the erosion process. This understanding can then be utilised for recommendations as to

erosion limitation. The latter approach is the concern of this research programme. Through the support of BP Exploration Operating Co. Ltd, under the Engineering and Physical Science Research Council CASE award scheme, Computational Fluid Dynamics investigations of the erosion of oilfield control valves were undertaken.

Computational Fluid Dynamics (*CFD*) provides an excellent vehicle for the prediction of erosion rates within complex geometric configurations, such as control chokes. The commercial *CFD* package used in this study is CFX-F3D. CFX-F3D is one of the four main *CFD* packages available to-date, others being FLUENT, PHONICS and STAR-CD. The compressible or incompressible turbulent flow field through the choke is computed through the application of the time-averaged Navier-Stokes equations, solved on a finite volume grid. The grid contains a number of control cells, proving localised information regarding the flow structure of the geometry. Given the resolved flow field, individual particles may be tracked through the flow domain, allowing each discrete particle impact to be noted. In its basic form CFX-F3D has no ability to produce erosion or particle impact data. To overcome such limitations, the author has developed and embedded extensive FORTRAN routines within CFX-F3D. These FORTRAN routines, being extensions of the particle tracking source code of CFX-F3D, allow the relevant particle impact and erosion data to be computed and manipulated.

The particle impact information is localised in nature, providing such details as the particle impact velocities and localised angle of impact. This impact information, in addition to constants describing target material properties and particle types, is fed to an erosion model included within the embedded FORTRAN of CFX-F3D. The erosion model then predicts localised erosion rates across the internals of the choke. The data produced by the erosion model is then presented in terms of localised surface plots for the choke internals, allowing penetration rates to be calculated and erosion 'hotspots' to be located. These surface plots provide an invaluable insight into the behaviour of particles within the flow domain. The main stages to erosion modelling through *CFD*, include;

1. Predict the turbulent flow field within the choke.
2. Predict the trajectories of sand particles within the flow field, including particle impacts.
3. Predict erosion characteristics as a function of the particle impacts and material types.
4. Display particle impact information and erosion data as three dimensional shaded contour plots.

The shaded contour plots provide an excellent vehicle for display large quantities of information, allowing rapid feed back to the user as to the predicted erosion intensity. Actions based upon these surface plots can then be taken, allowing a design evolution process to be undertaken quickly due to the ease of results interpretation. Graphical information provided includes; the location of the impacts, the localised particle impact velocities, the localised particle impact angles, the localised particle

[1] Total Number of Valves in Service 258. Total Number of Valve Failures 298

kinetic energy at impact and the localised erosion rates. An experienced user can then utilise this information to better his understanding of the various interaction processes occurring, enabling erosion limitation to be achieved through an improved design methodology and evolution process.

1.3 Structure of Thesis

The thesis is constructed of eleven chapters, including an introduction to the project and its objectives. Chapter two presents a critique of past works, where conclusions have been drawn as to the merits and the importance of the works presented. Chapter three extends upon Chapter two, providing the reader with a review of current control choke technology; identifying popular designs and the failings of these designs in terms of their erosive tendencies. The physical process of generating and utilising an erosion model is the subject of Chapter four. Here an erosion model is presented, which is applicable for use, given the process conditions experienced within control chokes. The erosive response of tungsten carbide, a principal material within chokes, is also provided.

Chapters five and six review current CFD techniques, detailing the fundamental theories used to compute the properties of the turbulent flow field within the flow domain and the resulting trajectories of entrained solids within that flow field. Furthermore, Chapter six presents a statistical analysis of sands commonly produced by oilfields; essential to accurate erosion predictions. To allow confident erosion predictions to be made, substantial development work to the base *CFD* code was required. The extent and techniques employed within these developments have been described in Chapter seven. One vital development was that of surface plotting techniques, allowing the computed erosion data to be presented graphically in a user-friendly fashion.

Chapter eight presents a number of numerical studies of erosion undertaken, utilising the techniques described in the previous Chapters. The benefits of the CFD erosion model, both in terms of its ability to capture observed erosion trends within the field and as a design evolution tool are displayed. Sensitivity studies are presented, detailing the influence of the principal modelling parameters. Chapter nine provides a summary of the extensive test work undertaken to provide a validation benchmark for the CFD erosion model. This test work included full valve erosion testing, at the BP Sunbury high pressure flow loop facility, and flat sample testing to validate empirical correlations.

Chapter ten gives details of an extensive comparative study undertaken. Based upon the experimental erosion testing of full valves, as detailed in Chapter nine, a numerical simulation was undertaken. The findings of the simulation are presented, with discussion of the influencing factors and possible improvements to the design given. Chapter eleven concludes the study and makes recommendations regarding further work, outside the scope of the present project. An Appendix structure has been included to support the various Chapters.

2. A Literature Review and Critique to Erosion Theories

2.1 Introduction

The erosion phenomena generated by the impact of solid particles on a surface has been a problem to the process industry for many years. During this time various workers have considered the phenomena, generating a large quantity of information. However, the majority of the literature is aimed at assessing the erosive reaction of flat samples of material and the development of empirical models to describe that behaviour. Much emphasis has been placed on empirical relationships due to the complicity of the erosive system. Table 2-5, provides a summary of those variables that need consideration in the erosion modelling process. This list, by no means exhausted, shows one key feature of erosion modelling evident from the literature, much work is still required in the field of erosion study to obtain a full understanding of the underlying mechanisms. At present numerous assumptions are required to produce an erosion model of acceptable numerical size.

Erosion related literature is extensive, however, the contents of the literature has limited use in the specific area of oilfield component erosion. This primarily stems from the use of specialist materials within these components, the aggressive flow medium that are commonly conveyed and the dynamic erosion systems experienced. The limitation of usable literature is further complicated due to commercial sensitivity issues. To aid the reader of this review, the information generated has been presented in three categories;

1. Flat sample experimental studies aimed at improving our understanding of the erosion phenomena.
2. The development of erosion models as predictive tools.
3. Numerical studies undertaken to develop complex modelling scenarios and the comparison of measured and predicted erosion data.

2.2 Experimental Erosion Studies, an Understanding of Material Behaviour

2.2.1 The Influence of Particle Impact Velocities

Appendix A, provides a summary of selected erosion studies undertaken by past and present workers. Here a wide variety of material types and erodent types have been presented, giving details as to the erodent impact angles and velocities. Furthermore, the velocity exponents utilised within various erosion models have been summarised, see section 2.3. Each worker has either developed his own or used another model to investigate the erosion noted experimentally. The velocity exponent is then used as an indication of the surface erosivity. Erosion in its base form is recognised as being a linear relationship of the impact velocity, proportional to the velocity exponent; $\varepsilon \propto u^n$. Additional terms are then applied to refine the accuracy of this assumption, including the angle of impact. The velocity exponents of Appendix A ranged from 0.3 to 6.5, as a function of the system considered.

From the summary provided by Appendix A, and discussion here within, the enormity of the literature available in the field becomes transparent. Additional complications arise through the 'combination' of erosive effects, where such influences as target material type, impact velocities, angle of impacts and erodent type all contribute towards the results. As a result of such combination effects, comparisons between differing workers is difficult. However, general erosion trends are highlighted, allowing conclusions to be drawn regarding the erosive system and the resulting material behaviour.

An observation, related to the kinetic energy of the particle at impact, is that the greater the erodent velocity at impact, the greater the induced erosion. This is a universal observation which is independent of the target material and the erodent type utilised within the erosion system. This observation is reflected in the velocity exponents given in Appendix A. Figure 2-1 [**Ref. 38**] presents the typical velocity dependence of a material, in this case a stainless steel. Note the gradient, which represents the velocity exponent given in appendix A.

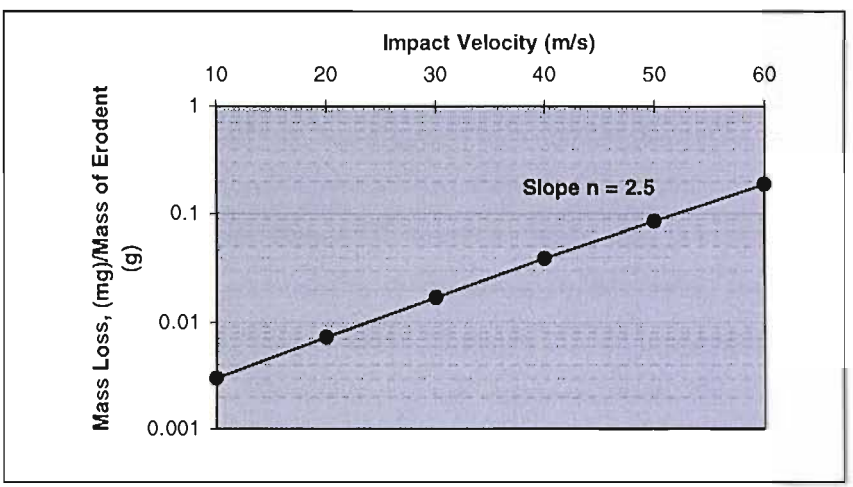

Figure 2-1 Velocity Dependence of Slurry Jet Erosion of 310 Stainless Steel (100 Mesh SiC at 90° Erodent Angle)

2.2.2 The Influence of particle Impact Angles

Appendix B expands on appendix A, summarising the angle dependency of erosion, including the relationship of erodent impact angle on the resulting erosion rates. The relationship between impact velocity and erosion can be related directly to the velocity exponent. However, the angle dependency presents a more complex relationship which is neither material or erodent independent. Details are provided regarding the critical erodent angle and the general relationship of erosion against angle. The critical erodent angle represents that angle at which maximum erosion occurs for a material type, given constant conditions.

Research into the problem of solid particle erosion originated in the 1930's. Siebel and Brockstedt **[Ref. 82]** investigated the erosion of plates, where the sand erodent was driven by a perpendicular jet of air. They investigated the erosion of ductile and brittle materials, in the form of alloyed and unalloyed steels, finding the results to be very much the same for both cases. These findings were contrary to observations they had made regarding erosion of pipes carrying a particulate suspension. Here, the greater the material hardness the lower the erosion rates experienced. The limitation of the study was its failure to recognise the angle dependency of the erosion process. Any two materials may experience similar erosion rates for an erodent impact angle, as was observed in this case for normal incidence investigated by Siebel and Brockstedt. Figure 2-2, presents the erosional behaviour of two differing materials. In this instance, the corresponding erosion rate angle is 48 degrees.

Wellinger and Brockstedt **[Ref. 94]** improved the Siebel and Brockstedt work, conducting air driven erosion tests at various angles of impingement to demonstrate the merits of differing materials. A ductile steel of HV 125 kg/mm^2, experienced maximum erosion at an erodent angle of 30°, whilst a brittle steel, HV 840 kg/mm^2, experienced maximum erosion at 90°. This supports the now well known erosion characteristics of ideal brittle and ductile materials **[Ref. 9]**, as presented in Figure 2-2. Here, two principal erosion mechanisms were identified; being the well known *deformation*[2] and *cutting* erosion mechanisms respectively. See chapter 4 for a detailed discussion of these mechanisms.

Appendix B supports these findings. Generically brittle materials, such as tungsten carbide, glass and ceramics all experience critical erodent angles at 90°. Erosion to this critical angle of 90° is relatively uniform, generally following the idealised curve of Figure 2-2. At low angles of impact, typically below 15°, these material types suffer very low or zero erosional attack. This occurs as the materials have a hardness which is greater than that of the erodent, hence the tendency of the erodent to 'cut' at the target surface is minimised at these low angles of impact. These material types suffer from fatigue affects, where upon repeated impact, mainly driven by the perpendicular velocity component at impact, surface fracture occurs. These fatigue effects are most predominant at high angles, hence the critical erodent angle of 90°.

For ductile or soft materials, aluminium, copper or annealed steel, the critical erodent angle occurs at relatively low angles of impact. Typically, the critical erodent angle occurs at approximately 10 to 40°. This peak in erosion corresponds to the materials tendency to suffer from cutting damage. Here,

[2] To avoid confusion, it must be brought to the readers' attention that the name deformation is used to describe a number of erosion mechanisms, not solely the plastic deforming of the targets surface. This broad name includes such mechanisms as crack growth and fatigue effects. The present author does not wholly agree with the use of such a misleading name. However, as it is a standard term that appears frequently in the literature, the convention will be held to avoid confusion with fellow workers.

the hardness of the target material is less than that of the erodent. As such, the erodent can cut at the surface of the target material. This cutting mechanism is most efficient at low angles of impact, where the parallel component of the impact velocity dominates. Furthermore, due to the ability of these material types to absorb energy as elastic deformation, the tendency towards the fatigue effects experienced with brittle materials is minimised. Thus, for this material group, erosion increases rapidly from 0° to the critical angle, subsequently falling slowly as the erodent angle of impact increases beyond the critical erodent angle.

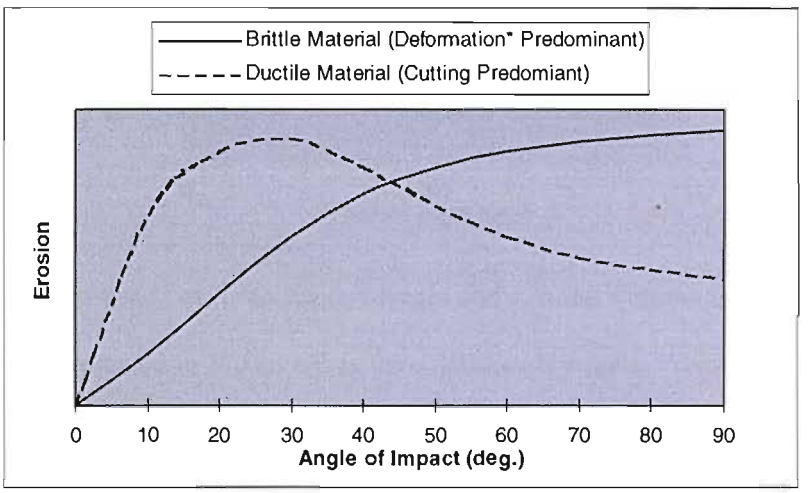

Figure 2-2 General Erosion Trends for Broadly Ductile and Brittle Material Types.

Such observations are valid for ideal homogenous materials, those that clearly fall into the specific regimes. However, many materials, such as alloy steels, cannot be so easily defined. This failure gives rise to difficulties in modelling of the erosion event, where one is limited by a number of assumptions. The reader is referred to section 2.3 on the development of erosion models.

As a precautionary note, the erodent angles presented in the literature describe that angle between the surface of the flat specimen and the centre line of the nozzle directing the flow onto the sample. The various authors presented in Appendix B, have assumed that the erodent angle at impact equals the nozzle angle. Numerical studies undertaken by the present author, see Chapter nine, have shown that this assumption is clearly inaccurate for slurry flows; where water or a similar fluid is the transport medium. Here due to the stochastic behaviour of the particles within the highly energetic eddy regions of the flow, prior to impact, the deviation of the impact angle from the nozzle angle can be high.

Figure 2-3 [**Ref. 76**] summarises the average particle impact angle of a slurry erosion system against the nozzle angle. One may observe that the difference is marked. Furthermore, the linear correlation of the CFD erosion model is excellent. It is noteworthy, that the coupling between the nozzle angle

and average impact angle is strongly dependent upon the carrier fluid and the particle size. The lower the fluid density/viscosity and the greater the particle size, the smaller the deviation.

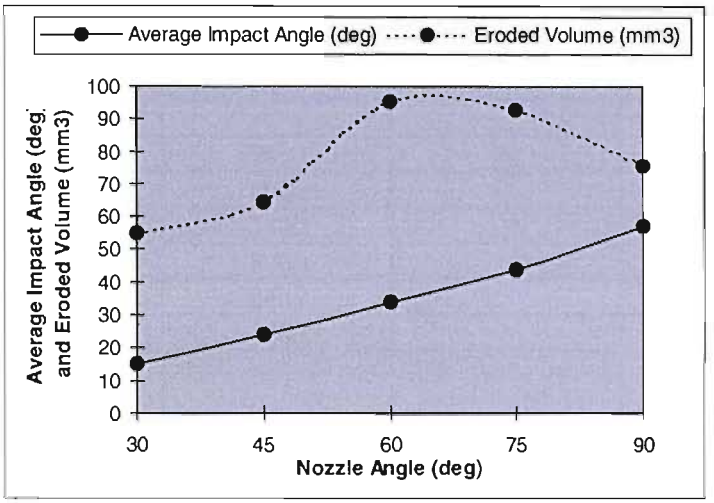

Figure 2-3 Dependency of Aver. Impact Angle and Eroded Volume on Nozzle Angle.

The eroded volume presented in Figure 2-3 is for a 1020 carbon steel. From Figure 2-2 one would assume a critical impact angle of approximately 30-40 degrees for such a ductile material. The peak in the eroded volume for a nozzle angle of 60-75 degrees, is misleading. Here, due to the variation in the underlying impact angle, the actual critical angles of erosion do correspond. The curve of average impact angles details an average impact angle of 30-40 degrees, for a nozzle angle of 60-75 degrees. As such the importance of correct comprehension of the erosive system is imperative.

2.2.3 The Influence of the Particle and Material Types

Complications arise through the erodent type experienced. The properties of erodent materials, such as hardness, can vary dramatically and determines the erosion mechanism, which partly dictates the volume loss experienced. In general the greater the hardness of the erodent, the greater the cutting tendency. However, fracture toughness is usually obtain in preference to hardness, as such the erodent has a greater tendency to fracture at impact. Thus, it is possible for the overall erosion rate to be reduced for an increased erodent hardness. Tilly [**Ref. 88-Ref. 90**] investigated this phenomenon, using a diverse range of erodents; including diamond, SiC and sand. Given constant operating conditions and material type, the velocity exponent can be seen to vary; Appendix A. See Figure 2-4.

Table 2-1 shows the typical hardness of common materials. The variations in hardness occur due to the compositional and microscopic state, such as local variations in grain size, cold working and heat treatment. Quartz is that erodent most common to oil production, here the hardness is approximately 750-1250 kg/mm^2. This is greater than even martensitic steel, hence its erosive potential is great, as has been demonstrated through field experience.

MATERIAL	DENSITY (kg/m^3)	FRACTURE TOUGHNESS ($MN/m^{3/2}$)	VICKERS HARDNESS (kg/mm^2)
Erodents			
Diamond			6000-10000
Silicon carbide	3100	5.2	2100
Quartz	2650		750-1200
Target (steel type)			
Carbon Steel	7800	70	240
316 Stainless Steel	8000		300
Duplex Stainless Steel	7850		350
SMO	8000		330
Stellite 6	8400		400
Boronized Stellite 6	8400		1500
Target (cermets & ceramics)			
DC-05 WC	15250	9	1800
CS-10 WC	14800	10	1750
CR-37 WC	14600	12	1350
Boart S6 WC	14970	10.4	1550
Boart S11 WC	14420	13.4	1300
PSZ	5700	12-15	1120
Si_3N_4	3200	6.3	2000
B_4C	2500	3.5	2600
ZrO_2-Y_3	6070	5-10	1330

Table 2-1 Typical Mechanical Properties for Common Erodents and Targets

Further to the erodent properties, the size of the erodent influences the resulting erosion and the corresponding critical erodent angle. Typical particle sizes which have been studied were between 5 and 500 microns. Sheldon **[Ref. 78]** showed that the larger the erodent, the greater the induced erosion. For a SiC grit erodent the velocity exponent given in appendix A increases with mesh or particle size. Sheldon did not find a particle threshold size, beyond which no further increase in erosion was experienced for a corresponding increase in particle size. The erodent size has also been shown to influence the critical erodent angle. Sheldon found that the erosion of tool steel by SiC grit, the critical erodent angle occurred at 20° for a small particle size, whilst the critical angle occurred at 50° for larger particle sizes. This observation may be explained through the effective flow stress that also influence the erosional attack as a function of particle size.

In contrast to Sheldon, numerous workers have noted a threshold size of particles. This phenomenon is presented in Figure 2-4 **[Ref. 45]**. The relationship is not linear, implying that the rate of kinetic energy transfer, which is linear, is not the principle mechanism. Addition effects have an influence the erosion rate; such effects may be best explained by considerations of the strain rate at impact and the true size effect of the impact event on the strength of the material.

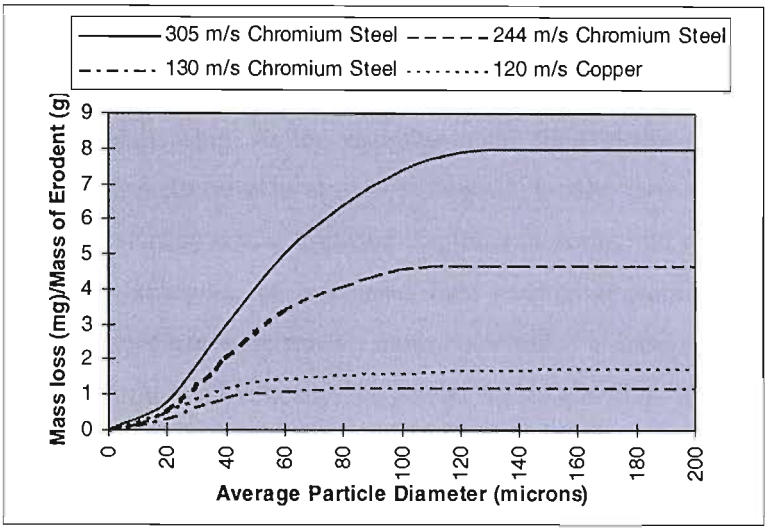

Figure 2-4 Erosional Influence of Particle Size on 11% Chromium Steel and Copper (Sand at 90° Erodent Angle)

The flow stress of a very small volume of material, as effected by the tip diameter of the erodent, is very much higher than that of the bulk material. This rapid increase in flow stress for decreasing material volume lies in the difficulty of nucleating and moving dislocations in small volumes. Such an effect implies that diminished plastic deformation occurs with the reducing scales of the impact event or particle size; hence the observed particle size effect. One may further hypothesis that such size effects may be partly contributed to by inherent flaws within the erodent. As the size of the erodent increases, the number of flaws or fissures that the particle carries will increase. Hence, the tendency for the particle to fracture at impact increases. As such, a greater proportion of the kinetic energy at impact will be dissipated as particle destruction, not target surface destruction. Tilly [**Ref. 90**] supported this hypothesis with his proposed two stage erosion mechanism. Here he recognised explicitly that impacting particles at near-normal incidence may fragment. He further investigated the secondary erosion effects of these fragments. See equation C.6 of appendix C.

As such, one may conclude that significant advantages regarding erosion limitation can be obtained by minimising the mean size of the erodent particles through filtration; with marked reductions in erosion for particles below 100 microns. Flow effects also contribute significantly at such a size, see Table 2-2.

Furthermore, particle size is important in the erosion of cermets, such as tungsten carbide. Here small particles have a tendency to undermine the binder phase, resulting in erosion through the loss of entire carbide particles. See Section 4.2.1 for further details.

2.2.4 The Influence of the Fluid Type

The fluid viscosity directly influences the induced erosion. Numerous workers, presented in Table 2-2, have investigated the relationship. As the viscosity of the fluid increases, the resulting erosion decreases proportionally. This decrease in erosion is twofold. Firstly, flow effects of a heavy fluid imply that the overall flow velocity is low, implying that the trajectories and particle impact velocities will also be low. Secondly, at impact the suspension fluid must be displaced before particle impact can occur. The fluid viscosity dictates the particle momentum which is dissipated within this near wall boundary layer. The greater the fluid viscosity, the greater the deceleration of the particle in this near wall region, thus the lower the energy transmitted to the target surface.

Clark [**Ref. 21**] has presented a relationship which relates fluid viscosity and particle mass to particle deceleration within this near wall region. This function describes surface tension effects, which are lacking within a *CFD* model. Hence this relation has been incorporated within the particle tracking routines of CFX-F3D, allowing an improved representation of the particle impact velocity to be passed to the erosion model. See section 6.3.2.

ERODENT	TEST FLUID	EROSION-VISCOSITY RELATION	REFERENCE
SiC 220 mesh	Water, 10W oil, 20W oil, 30W oil.	ε decreased as μ increased	Bridwell [**Ref. 16**]
Sand	Water, Diesel fuel, Spindle oil No. 2, Diesel oil DC-11, Automotive oil AK-15	$\varepsilon \propto 1/\mu$	Kozirev [**Ref. 51**]
Glass and Steel	Water, Water-glycerine, Diesel oil.	ε decreased as μ increased. Order of magnitude decrease in impact velocity for two orders of magnitude increase in viscosity. 50-500 μm particle.	Clark [**Ref. 21**]
Sand	Water, Ethyl alcohol, Bromobenzene, Carbon tetrachloride, Mercury, Paraffin.	$\varepsilon \propto -\log(\mu)$	Rochester & Brunton [**Ref. 74**]

Table 2-2 The Effect of Fluid Viscosity on Erosion.

Thus, one may conclude that erosion is complex. Parts of the erosion data presented in the literature are plainly in error through either poor experimental procedure or inadequate comprehension of the erosion system. Further, many of the erosion systems under consideration present scant relation to the erosion system experienced within the petroleum industry. One study that stands in good stead is that performed by Haugen et al. [**Ref. 38**].

2.2.5 Erosion of Candidate Materials for Erosion Resistance in Choke Valve

Twenty-four materials were tested by Haugen [**Ref. 38**] in a dry air test rig, consisting of a 6 mm diameter bore of 1 m length and a 10 mm diameter bore of 2 m length. The stand-off distance from the specimen to the end of the barrel was set to 20 mm. The materials tested consisted of a combination of standard materials, surface coatings, several solid tungsten carbides and ceramics. See Table 2-3 [**Ref. 38**] for the full listing. The sand used was of typical North Sea distribution, see section 6.4.1, being passed only once across the specimen due to the high rate of attrition. Each test was repeated until linear results were obtained. Due to surface and macroscopic effects, an incubation period to steady state erosion is normal. This incubation, although short, may significantly effect the results if not accommodated correctly.

The particle impact velocities were predicted using the particle tracking module of the commercial *CFD* code, FLUENT. For fluid velocities of 22, 55 and 320 m/s, the corresponding particle impact velocities were predicted to be 18-20, 40-45 and 200-220 m/s. The reported errors of such techniques were estimated to be 15-20%. However, such error estimates may be conservative. Due to the low bore diameters used, severe interaction of the particles with the large boundary layer will result. As *CFD* codes commonly employ wall functions to resolve the near wall flow field, this important boundary layer region will not be correctly resolved, inducing errors to the particle trajectory calculation. Further, the use of a standard drag correlation for the particle trajectory calculation is only suitable for the low flow velocities; the assumption fails for the high flow velocities. For compressible flow, the standard correlation used is only valid up to a Mach number of approximately 0.3 [**Ref. 19**]. Beyond this region, the drag coefficient becomes a function of the Mach number as well as the particle Reynolds number.

The erodent angle was set by adjusting the angle of the specimen, the angles utilised were principally 22.5° and 90°. A small number of tests being conducted at 7.5°. The reasoning for these erodent angles was that the maxima of cutting and deformation erosion, for ductile and brittle materials respectively, occur at these angles. See Figure 2-2. This assumption may be correct for ideal materials, however, for the more complex coatings and ceramic materials investigated this assumption fails. From appendix B, the critical erodent angle is seen to vary for differing ductile materials, as such the angle of 22.5° cannot be relied upon to represent the erosion maxima for ductile materials. Additional tests for each material are necessary to establish the true value of the critical erodent angle. Table 2-3 presents the results of this study, showing the mass loss from the target per kilogram of erodent. The material ranking was based simply on the arithmetic sum of results, as such cannot be relied upon due to the limitation of experimental data.

TARGET MATERIAL	45-50 m/s 90° (mg/kg)	45-50 m/s 22.5° (mg/kg)	200-220 m/s 90° (mg/kg)	200-220 m/s 22.5° (mg/kg)	NUMERICAL RANKING
Carbon Steel	14	23	1085	1700	14
316 Stainless Steel	16	20	1770	1845	20
Duplex Steel	13	23	1400	1825	18
Cast Stellite 6	17	13	1870	1030	15
Boronized Stellite	1.7	1.7	860	265	11
Electrochemical Nickel Ni-250	15	27	1070	1930	17
Electrochemical Nickel Ni-500	17	22	1460	1460	16
Thermal Sprayed WC-60% Nickel	27	13	4670	1145	23
Thermal Sprayed WC-40% Nickel	32	17	4070	1470	22
D-Gun WC, thin	108	33	13000	2700	24
D-Gun WC, thick	16	4	860	265	12
WC, DC 05	0.7	0.58	22	11	3
WC, CS 10	1.6	1.0	45	17	4
WC, CR 37	1.2	0.83	50	17	5
95% Al_2O_3	130	20	2500	700	19
99.5% Al_2O_3	100	25	620	360	10
PSZ (Partly stabilised zircona)	48	6	1880	360	13
ZrO_2-Y_3 (Yttria stabilised zircona)	1.2	0.8	68	30	6
SiC (Silicon carbide)	8.9	1.5	150	22	8
Si_3N_4 (Silicon nitride)	0.37	0.17	7	1.1	2
TiB_2 (Titanium boride)	15	2.4	270	48	9
B_4C (Boron carbide)	0.97	0.37	3.7	2.0	1
SiSiC (Silicon infiltrated carbide)	2.5	0.5	150	27	7

Table 2-3 Measured Mass Loss given Angle, Velocity and Material Type

Of the materials tested, the most erosion resistant were found to be the ceramics B_4C and Si_3N_4, whilst the tungsten carbides also performed very well. It is noteworthy that only one coating, D-Gun WC provided an improved erosion resistance over carbon steel. Much work is still required in the area of coatings to ensure good adhesion with the substrate.

Carbon steel was the material most investigated. It was found to behave in a ductile manner with a critical erodent angle of between 15 and 30°. It was reported that this critical angle varies with the

impact velocity, which contradicts the findings of Figure 2-1. Figure 2-1 shows that the erosion rate is a linear function of the impact velocity. However, the variance in material loss for each critical erodent angle is only slight, with a reported general angle insensitivity to erosion between 15 and 45°, thus allowing the assumption of linear velocity dependence to be held. For the location of the critical erodent angle, a strong linear impact velocity dependency was reported, with a velocity exponent of 2.6. This corresponds well with the findings of the present and other authors. The erosion at an impact angle of 90° was found to be 50 to 60% of that at the critical erodent angle.

The erosion rates of steel type materials being normalised against that of carbon steel, providing an insight into the merits of each; Figure 2-5 [**Ref. 38**]. The 316 and duplex materials displayed a ductile response, whilst the Stellites showed brittle behaviour. However, the exact behaviour regarding the critical erodent angle could not be described due to the lack of tests at intermediate angles.

The erosion resistance of the steel grades is relatively constant, whilst the Stellite materials show greater variation. Such a variation is attributed to the hardness of Stellite; see Table 2-1. Thus, one may conclude that steel grade materials suffer primarily from cutting erosion, whilst the Stellite materials erode through a process of surface fragmentation predominate at high angles.

Due to the hardness of Stellite 6, the cutting tendency at the low angle tested (22.5°) was reduced. Boronised Stellite provides a factor of 10 improvement over carbon steel at these angles, whilst Stellite provides a factor of 2 improvement. However, at 90° the erosion rate is high, this effect is promoted when coupled with the high impact velocity. This phenomenon is attributed to the hard surface layer of Boronised Stellite, which has a hardness of 1500 HV. This hard surface layer fractures at such high impact angles due to the large stress concentration effects generated, resulting in rapid mass loss. This effect can also be seen for standard Stellite, where erosion rates for 90° impacts are considerable higher that those of the 22.5° impacts. The brittle nature of the material leads to rapid mass loss. An important observation is that each of the materials tested in the 'steel' group, displayed a poor erosion resistance, when compared with carbon steel; at normal impact angles and high impact velocity (200 m/s). A hypothesis as to such a phenomenon is carbon steels' ability to absorb energy as non-damaging elastic deformation, the greater the violence of the impact event, the more influential this phenomena becomes.

It is noteworthy that the erosive system utilised here is exceptionally aggressive. Studies undertaken by the present author have shown that the maximum particle impact velocity for typical North Sea sand is unlikely to exceed 100 m/s, with peak angles of impact not in excess of 85°, given stochastic particle behaviour, chapter 6. Therefore, an unjust portrait of Stellite may be given by such an aggressive erosive system that tends to over-emphasize brittle fracture at perpendicular impact angles;

which in reality are rarely reached. However, this observation is valid for all materials tested. Improvements in erosion resistance can be obtained though the use of Stellite, provided the average erodent angles are low. The advantage of a *CFD* code is that data regarding the impact angle distribution is known, allowing conclusion to be drawn as to the merits of Stellite for each application. Furthermore, design evolution can be implemented to ensure the merits of Stellite can be exploited. This is beneficial if there is a potential for cavitation, in addition to erosion. Stellite has good cavitation resistance, allowing both erosion and cavitation limitation to be achieved through correct design, grounded by *CFD*.

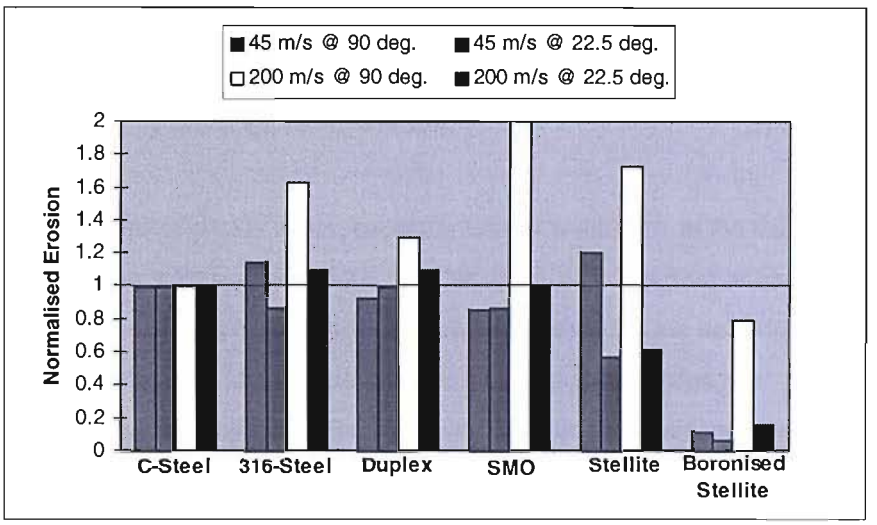

Figure 2-5 Erosion Rates of Various Materials Normalised against Carbon Steel

The coatings all performed poorly, as such no further discussion will be given to them here. However, the interested reader is referred to the work of Dr Robert Wood and others at the University of Southampton. The main failing of the coatings was that adequate adhesion with the substrate could not be achieved. As a result the coatings rapidly flaked away from the substrate, giving high erosion rates.

The cermets and ceramics provided the best erosion resistance, with each displaying the classical brittle material behaviour; see Figure 2-2. Figure 2-6 [**Ref. 38**] shows the erosion behaviour of such materials normalised against that of 11% cobalt binder tungsten carbide with a fine grain size (2 to 4 microns diameter). DC05 is a 5% nickel and cobalt binder tungsten carbide with an extra fine grain size (sub 2 microns). CR37 is a 37% nickel binder tungsten carbide with a medium grain size. The general trends in the erosion resistance of tungsten carbide is that the lower the binder content and the finer the grain size, the superior the resistance through an increased hardness. Improvements in erosion resistance, over a standard carbon steel, of the order of 50 to 300 times, can be achieved with tungsten carbide.

However, from Table 2-1 it can be seen that the fracture toughness decreases with decreasing binder content. It is the binder that provides the materials ductility and toughness. Thus, the tungsten carbide has an increased tendency towards brittle fracture, which is an important consideration within choke technology. In addition to erosion performance, one must consider the toughness of the carbide grade and its corrosion resistance when selecting a suitable tungsten carbide grade.

This observation is also valid for the ceramic materials. Silicon nitride (Si_3N_4) and boron carbide (B_4C) provide the best erosion resistance of all the materials tested. However, the fracture toughness of such materials is very low due to their highly brittle nature. Such materials would not be specified within a choke due to the risk of trim shatter. A foreseeable use of these very hard ceramic forms would be inserts within a tungsten carbide trim. Allowing a design evolution to localise the damage to one principal area, being protected by such inserts.

In general, ceramics perform poorly at perpendicular impact angles due to the their brittle nature. The impact energy cannot be partly absorbed as non-damaging elastic deformation, as with the steels, implying cracks are readily propagated to form surface fragments. This behaviour was observed by the workers **[Ref. 38]** via SEM investigation, where cracking and 'erosion pits' were reported. SEM investigations of the tungsten carbide cermets revealed that the predominant erosion mechanism was carbide grain loss. Samples taken before and after erosion testing revealed that the surface layers contained 'fewer' carbide particles post test.

This carbide loss occurs either by the undercutting of the binder phase, resulting in whole carbide loss, or the direct impact of the erodent on the carbide particle. These direct impacts result in the fracture of the carbide particles, which are then partly torn from the matrix. The authors **[Ref. 38]** reported that those cermets with the best erosion resistance, experienced low levels of binder disruption. Due to the low binder content of such tungsten carbide grades as DC05, only small areas of binder are exposed, minimising the undercutting of the binder phase and hence carbide loss. However, the lower the binder content, the poorer the carbide adhesion to the binder, promoting the tendency to entire carbide knock out from the matrix.

It is important to note that the erosion of tungsten carbide is a complex process, which is not fully understood. The exact relationship between the binder content and the overall erosion rate needs further work to classify the angle dependency. See chapter 4 for the discussion on tungsten carbide erosion.

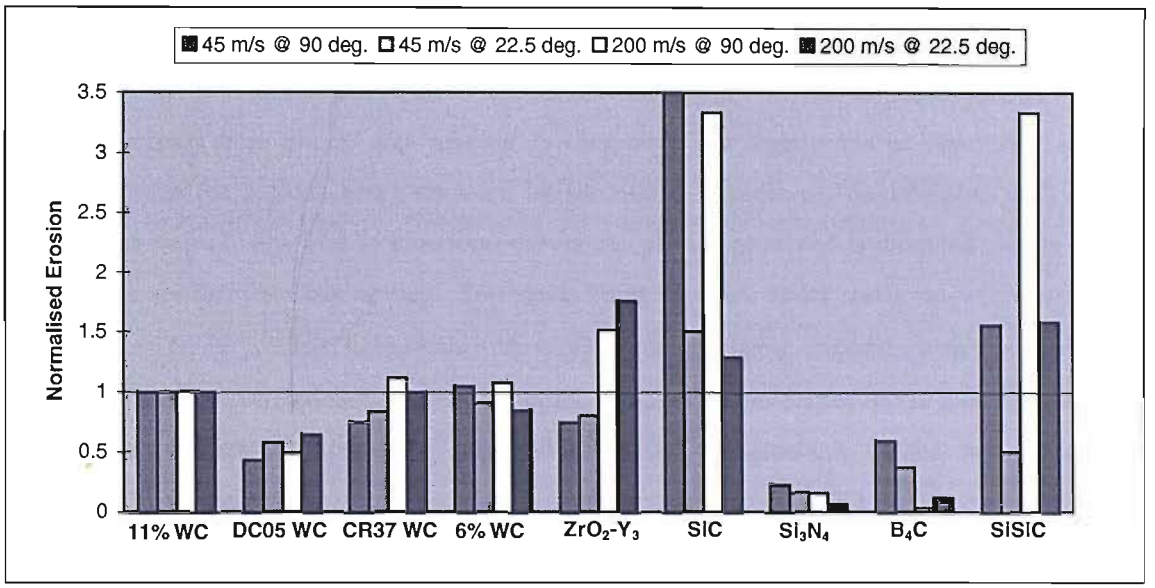

Figure 2-6 Erosion Rates of Various Materials Normalised against 11% Cobolt Binder Tungsten Carbide

Lars Nϕkleberg [**Ref. 67**] of Norske Hydro was involved in the development of a Polycrystalline Diamond (PCD) choke, providing a highly erosion resistant choke whilst avoiding the trim shatter failings associated with the super hard ceramics. Stainless steel, 6% cobalt binder tungsten carbide and PCD materials were erosion tested to determine their relative erosion resistance. The erosive system utilised was similar to that of Haugen [**Ref. 38**]; the erodent angle was constant at 90°, the impact velocity was 250±30 m/s and the erodent size was 140 to 300 microns in diameter. The finding of Nϕkleberg are consistent with that of Haugen, with the superior merits of the PCD material being shown; providing two orders of magnitude improvement in erosion resistance over tungsten carbide.

MATERIAL	EROSION RATE (mg/kg erodent)
Stainless Steel	1700 ± 100
WC 6% Cobalt binder	14 ± 2
PCD	0.088 ± 0.003

Table 2-4 Measured Erosion Rates for Various Material Types.

The major failing of PCD is the difficulties associated with engineering the material. Product shapes are very limited, enforcing severe restrictions as to possible choke designs. The only choke style that can be partly constructed from PCD at present is the needle and seat design. See Section 3.4.1. However, such a design has distinct erosion problems within the outlet spool, which cannot be readily solved by PCD due to the cost and difficulties associated with it manufacture. Hence, the advantages of such a material are limited.

2.3 The Development of Predictive Erosion Models

Hotley [**Ref. 43**] gave discussion to the fundamental mechanisms of erosion, identifying two distinct regions; he named these 'shock' and 'rubbing' erosive wear. The regions that he highlighted still hold true today, with the regions being renamed by successive workers as 'deformation' and 'cutting' erosive wear respectively. The erosive wear curves that Hotley produced highlighted clearly the two erosive wear mechanisms that operate. Soft steels being superior under shock or deformation wear condition (α = 60-90°), whilst hard steels were superior under rubbing or cutting wear conditions (α = 60-90°). No further correlation was given regarding the physical properties of the materials involved, nor was any theoretical explanation provided as to the fundamentals of the two mechanisms highlighted by the study.

The first predictive erosion models appeared in the early 1960's. Finnie [**Ref. 26**], following the work of Hotley, postulated that erosion took place by cutting and deformation mechanisms. Finnie's work was successful in theoretically identifying the fundamental mechanisms at work for both the deformation and cutting regimes of erosive wear; see Chapter 4. This early work by Finnie is still valid today, providing a foundation stone upon which many co-workers have extended or developed additional erosion models. As a result of Finnie's success, a detail discussion of his work will be provided, followed by a summary of the models proposed by co-workers.

Finnie developed a robust *cutting* erosion model; however, his efforts to construct a robust *deformation* model were not productive due to his inability to accurately describe the fundamental mechanism. The approach taken was to describe the volume loss per impact, for both deformation and cutting wear, through the application of the equations of motion for a rigid particle interacting with the surface. The volume of material removed was then estimated by equating the swept area of the particles trajectory. This approach worked extremely well for ductile materials, where the cutting model described the cutting action of the erodent particles as a function of the impact craters swept volume. However, for brittle materials this simple approach was not valid, as surface cutting was not the predominant mechanism. Finnie concluded this failing to be attributed to the manner of brittle material erosion. Brittle materials eroded through a process of surface fragmentation, where stress concentrations upon the impact site lead to crack propagation.

For brittle materials, writing the equations of motion lead to an expression for the stresses between the rigid particle and the surface. The stresses computed were then applied to predict the initial fracture of the material due to the formation of surface and sub-surface cracks. However, once fracture has occurred, the material removal rate depended on the propagation of the cracks in the material and their interaction with other fracture features. Thus, Finnie's approach for brittle materials failed as the predominant erosion mechanism was crack propagation, not crack initiation. Finnie proposed that all

that appeared possible, at that time, in the way of understanding the erosion of brittle materials was to examine the conditions leading to crack generation. Experimental studies being required to examine the influence of particle impact velocity and erodent angle on the rate of crack production and hence material loss. As a result, studies of deformation wear were confined to curve fitting exercises, tailoring the empirical correlations used within the erosion models to describe crack behaviour.

In generating the equations of motion for the erosion of ductile materials, Finnie made certain assumptions regarding the forces acting on a particle in the absence of an exact solution. The assumptions included that the particle was rigid and did not fracture at impact. The cutting face of the particle was uniform, with a constant width that was large compared to the depth of cut; allowing plane strain to be assumed. Plane strain inferred that a constant plastic flow stress could be employed, which was reached immediately upon impact. However, no provision was made regarding the shape, size and density of the particle; such features were incorporated through a somewhat ambiguous relative mass constant for the particle. Furthermore, the width of the crater was assumed to be constant, as opposed to varying with time. The reader is referred to Appendix C and Section 2.3.1 for the form the Finnie's cutting equation.

2.3.1 Analytical Summary of Predictive Erosion Models

Appendix C provides a selection of some of the analytical erosion models published in the literature. The fundamental erosion mechanism or basis upon which each of the models has been constructed is included; showing the diversity of approaches taken to solve the problem of predicting erosion.

Finnie [**Ref. 27**] was the first to develop a cutting model for erosion, proposing Equation C.0. Here the volume loss due to the cutting action of a single rigid particle was assumed to be directly proportional to the kinetic energy at impact, being inversely proportional to the plastic flow stress of the target and directly proportional to the angle of incidence. K is the ratio of vertical forces to horizontal forces acting on the particle, used to denote if the particle is cutting in an ideal fashion, that is the cutting efficiency of the particle. This is normally assigned a value of 2. The model was based on a number of simplifying assumptions that allowed him to derive an equation of motion for a single particle as it strikes a surface; see Section 2.3, paragraph 5. After several modifications Finnie [**Ref. 26**] proposed that the volumetric erosion rate (volume of material removed per unit mass of erodent impact) was given by equation C.1. The equation was a modification of C.0, including additional terms for the moment of inertia of the particle and the particle size. The equation was found to perform well for estimates of material removal with angles of impacts between approximately 0° and 40° from the surface; i.e. the cutting erosion mechanism. However, it was noted that predictions were consistently lower then experimental observations for angles of impact above 40°, due to the model's inability to describe crack propagation.

Hashish [**Ref. 37**] extended the work undertaken by Finnie, proposing Equation C.2. His aim was not to alter the fundamentals of Finnie's approach, but to limit the number of simplifying assumptions made. For example, Finnie assumed that the width of the crater left by cutting erosion was constant. Hashish, correctly, proposed that the width of the crater varies with time, whilst the particle was assumed to be non-deformable and did not fracture or become embedded within the target material. Hashish found that particle type strongly influenced the erosion rate. The sharper or larger the particle, the greater the induced cutting erosion. Thus, the Hashish model includes a detailed description of the particle type; including the particle size, density and sharpness. Further to defining the particle, a characteristic velocity was derived to describe the cutting efficiency. The characteristic velocity defines the proportion of impact energy dissipated as non-damaging elastic deformation. Through the inclusion of these details, good prediction results could be obtained, however, they were once again limited to the cutting regime of erosion; below 40°.

Bitter [**Ref. 9**] accounted for both the cutting and deformation mechanisms of erosion, using an energy approach he derived equations C.3 and C.4 respectively. Bitter found that an energy approach worked well when considering deformation erosion due to the fundamental mechanisms involved; where energy, per unit volume, required to propagate cracks in a specific material could be noted experimentally. Such an approach, overcame the difficulties experienced by Finnie in attempting to account for deformation erosion by an equation of motion approach. Finnie's technique could only determine the loading stress experienced at the surface, it could not capture crack propagated and flake formation which is the basis of deformation erosion. Conversely, Bitter found that the energy approach could not be utilised to predict cutting erosion. Bitter concluded that due to the differing fundamentals of each erosion mechanisms, differing solution techniques must be sought for each erosion regime. This conclusion has been noted by the present author, underlining the necessity of a dual equation approach to accurately describe the full range of erosion; i.e. 0 to 90°.

Neilson and Gilchrist [**Ref. 65**] extended the energy approach derived by Bitter through the inclusion of a parallel component to the impacting force imposed by the particle, giving equation C.5. Furthermore, they sought to combine distinct models for the cutting and deformation regimes of erosion. Both Bitter and Neilson highlighted weaknesses in the model due to the empirical nature of some parameters included within it. Typically the necessity of including *Ef,* the deformation erosion factor which denotes the energy required to remove a unit volume of material by deformation erosion. This parameter must normally be measured experimentally, however, once a suitable value has been obtained, subsequent numerical predictions have good accuracy. The deformation model of Bitter also experiences such a dependency upon empirical correlation.

Tilly [**Ref. 90**] proposed a two stage mechanism for the prediction of cutting erosion. He developed equation C.6 for the total erosion as the sum of primary and secondary erosion effects. The primary erosion is due to the contribution by cutting, whilst the secondary erosion is due to particle fragmentation. The model gives consideration to both particle size and fracture characteristics. The model developed by Tilly is somewhat impractical to use due to the need to experimentally determine the threshold conditions, degree of particle fragmentation, and maximum erosion at a reference velocity. Upon these experimentally derived parameters, Tilly unwisely proposed that erosion behaviour could be extrapolated for differing particle sizes and impact velocities. From Section 2.2, it is apparent that erosion is an extremely complex process, where the influence of such parameters as the particle size is non-linear.

Head and Harr [**Ref. 40**] developed a statistical model for erosion, giving equation C.7. In addition to the normal operating variables of an erosion model, such as the impact velocity and angle of impingement, consideration was given to particle and target characteristics. Characteristics accounted for included the shape of the particle and its hardness; the hardness of the target, its tensile yield strength, its ultimate strength and the strain to fracture. Dimensional analysis of these variables was then performed which included a multiple linear weighted regression analysis program, with the model being modified to account for the effects presented by an erosion test facility. It was shown that the model had acceptable accuracy when applied to particle velocities of up to 300 m/s, with a maximum angle of impingement of 70°. This limit on the angle of impingement denotes that the model is only truly valid in the cutting regime, due to poor numerical predictions for the deformation regime. An extensive sample size was employed in the construction of the model, allowing it to provide good insight into which variables are of importance to the erosion process. However, due to the nature of the model's construction, the field of application is limited with the model itself being excessively complex and impractical in use.

Grant and Tabakoff [**Ref. 35**] developed an empirical equation C.8 based on particle dynamics and rebound characteristics. As the model is totally empirically based, no consideration is given to mechanisms of erosion. The equation can reportedly account for erosion damage in both the cutting and deformation regimes, i.e. low and high angles of impact respectfully. They showed that the erosion rate curve predicted was a good fit to experimental data. However, the angle of maximum erosion was not well resolved, being higher then that determined experimentally. Once again, a limitation of this model style is that the collision parameters used in the erosion model must be determined experimentally.

Jennings [**Ref. 48**] presented a novel approach to the process of erosion modelling. He proposed that at certain particle loading rates and target material properties localised melting of the target could

occur. He derived equation C.9 on this basis using dimensional analysis. Variables that were considered included the density, thermal conductivity, melting temperature, enthalpy of melting and molecular weight of the target material. The strain rate of the particle at impact was assumed to be proportional to the particle shape. The model itself must be assessed experimentally, with the evaluation of the erosion rate correlated by a measurement of the impact and rebound velocities. A dimensionless scaling factor, as determined experimentally, can then be applied to give an erosion prediction. Although the model has theoretically a wide range of applicability, it is limited by the necessity of the dimensionless parameter which must be derived empirically for all possible applications.

Sheldon and Kanhere [**Ref. 79**] derived an erosion model (equation C.10) based upon the indentation hardness of the target material. The relationship is not completely fundamental in nature, only being valid for spherical particles impacting at a normal incidence with a low velocity. The Manson-Coffin law of plastic reversal was utilised to account for the erosion as a function of fatigue in the deformation regime, see Equation 2-1 [**Ref. 62**]. The erosion rate was assumed to be inversely proportional to the fatigue life of the target and directly proportional to the volume of material undergoing plastic strain reversal; as a function of particle size. The model is very limited in application, being only applicable to normal incidence. However, it is of worth as it directly tackles the fundamentals of deformation erosion, i.e. surface/sub-surface plastic deformation and localised fatigue failure, providing good insight into the weighting of various parameters in deformation erosion process.

Equation 2-1 $$c = \sqrt{N_p}\,\varepsilon_p$$

Extending the low cycle fatigue approach to the erosion modelling process, Hutchings [**Ref. 44**] argued that the dynamic hardness and ductility of the target should govern the materials response to erosion. Once again, Hutchings model was confined to erosion at normal incidence by spherical particles at low velocities. Since the erosion process involves the accumulation of plastic strain in the surface/sub-surface of the target, Hutchings proposed that the removal of surface fragments from the target occurs when the plastic strain within the material reaches a critical value, that is material dependent. From the criterion of critical strain, a value for the mean number of plastic strain cycles needed to remove a surface fragment was deduced, once again using the Manson-Coffin law, Equation 2-1 [**Ref. 62**]. Equating the kinetic energy of the impinging spherical particle with the work done in forming the indentation crater, equation C.11 was derived. The model predicts a velocity exponent of 3, with the incorporation of target properties including density, dynamic hardness and ductility. The numerical study concluded that it may be necessary to combine high hardness and ductility within the one material to provide good erosion resistance characteristics.

Beckmann and Gotzmann [**Ref. 7**] derived equation C.12 upon the hypothesis that the volume of material removed by the erosion process is proportional to the shear forces in the surface region affected by the particle impact. The model was originally formulated on the basis of the deformation caused by the impact of a single spherical particle on a ductile target. The model needs empirical evaluation of, τ, which is dependent upon the latent heat of melting and the melting temperature of the target material. Furthermore, the erosion resistance of the target material is given by loading index, ϕ, which is directly proportional to the impact velocity of the particle, and inversely proportional to the square of the target's hardness. Experimentally derived empirical corrections were proposed for non-spherical particles.

Finally, Shewmon and Sundararajan [**Ref. 80**] proposed erosion by a shear localisation model in the form of equation C.13. The model proposed that deformation erosion occurs under adiabatic conditions, with target material being lost through the formation and subsequent fracture of lips around the impact crater. They hypothesised that the increment in flow stress due to strain hardening is balanced by the decrement in flow stress due to thermal softening. The model is isolated to high angles of impacts, with the inclusion of experimentally derived empirical parameters.

2.3.2 Assessment of Predictive Erosion Models

The development of an accurate predictive erosion model is extremely difficult due to the number of variables which must be considered or through the selection of valid simplifying assumptions. Table 2-5 lists a selection of the variable which must be considered, each of these variables influences the global erosion process to a greater or lesser extent. Due to the complexity of the modelling situation, none of the models developed, thus far, is wholly adequate, as no one model is able to consider all of the pertinent variables of the erosion process. Thus the user and/or the developer of the erosion model must select those variables appropriate to the specific modelling situations. Furthermore a variety of erosive systems exist, each having a differing combination of pertinent variables. The user must also make this distinction in selection of a suitable erosion model. Table 2-6 presents a summary of the variables considered in each of the erosion models presented in Section 2.3.1. This summary highlights the failings of present models to take into account all aspects of the erosion process.

Most authors of the models developed choose to ignore the characteristics of individual particles. Bahadur [**Ref. 4**] established that the size and angularity of particles significantly affect the measured erosion rate, with size and angularity being directly proportional to erosion. Hutchings [**Ref. 44**] quotes an order of magnitude difference in the erosion rate induced by spherical and highly angular particles. Hutchings also demonstrated the sensitivity of erosion to the particle hardness, in general erosion is proportional to particle hardness. Only the computationally expensive model of Head and Harr (equation C.7) considered particle hardness. Similarly, the friability of a particle raises the

question of particle fracture at impact. In general one can reasonably assume that degradation will occur to the particle at impact, however it is only Tilly (equation C.6) who includes fragmentation characteristics to his model. Furthermore, all models assume that the particle is non-deformable at impact.

The characteristics of the target material are also extensively simplified, with the material being assumed to be homogeneous, and devoid of microscopic features which come into play at the scale of particle erosion. Target material properties which control erosion rates are normally denoted in the predictive model by a number of common material constants, such as hardness, and several empirical constants determined experimentally.

OPERATING PARAMETERS	ERODENT CHARACTERISTICS	TARGET CHARACTERISTICS
Impact velocity	Particle size	Target ductility
Angle of impact	Particle shape	Target hardness
Turbulent characteristics	Particle density	Fatigue strength
Temperature/viscosity effects	Particle hardness	Residual stress
Carrier fluid properties	Fracture toughness	Heat treatment
Erodent concentrations (ppm)	Poisson's ratio	Fracture toughness
Critical Angle	Young's modules	Flow Stress
Rebound Velocity	Temperature	Thermal properties
		Work Hardening
		Poisson's ratio
		Young's modules
		Plastic Strain Rate
		Melting Temperature
		Weibull Flaw Parameter
		Grain Size
		Depth of Deformation
		Transverse Rupture Stress
		Erosion resilience

Table 2-5 Variables under Consideration in Erosion Modelling

It is normal for target hardness to be used as the only quantifying factor, being utilised in a quasi-static fashion, i.e. devoid of strain-rate sensitivity etc. The limitations of using hardness alone can be demonstrated by erosion testing of AISI 4140 steel in various state of heat treatment. Badahur [**Ref. 6**] showed that there appeared to be no correlation between the erosion rate and target hardness, or ultimate strength. However, there did appear to be a relationship between erosion rate and target ductility.

Such an observation may not be applicable to all material types, however, it emphasises the weaknesses in some of the simplifying assumptions made. Hutchings (equation C.11) included the

concept of material ductility, however, the model he derived is only suitable for spherical particles at normal angles of incidence.

As mentioned, the models discussed assume that the material being eroded is homogeneous and isotropic. However, some important materials which are utilised for there erosion resilience are heterogeneous on the scale of erosion damage caused by impacting particles; such as ceramics and tungsten carbide materials. Such materials contain a significant number of micro-cracks, pores/inclusions, and weak grain boundaries. So far, no satisfactory erosion model for this style of material has been developed, with even the mechanism of material removal being unclear in many cases. As a result predictive studies aimed at classification of erosion in heterogeneous materials are heavily empirically based.

All of the models derived classify erosion through the concept of the impact characteristics, i.e. the impact velocity and angle of impingement. The models showed that there is a direct proportionally between the erosion rate and the velocity exponent, n, varying between approximately 2 and 6. This factor is in good agreement with much of the erosional data reported in the literature.

The models do not include correlation for the particle-particle interactions which may occur at the impact site, due to high particle flux rates. Such a situation arises as the models are generally constructed upon the dynamics of a single particle interacting with the target's surface. The failure to include particle-particle interactions is satisfactory as this aspect of erosion modelling is not normally the concern of the erosion model, but in the realm of particle trajectory computations. See Section 6.2.5.

The major failing of the erosion models developed is that most are dependent upon a number of factors which must be derived experimentally, before predictive studies can be undertaken. Of the models presented in appendix C, all are empirically dependent apart from that of Shewmon [**Ref. 80**]. This model is limited in its application due to the nature of it construction. Such a dependence upon empirical constants is limiting in the general applicability of the erosion models. However, once a sufficiently broad database of empirical constants has been established for common erosional conditions, good applicability can be achieved. Such a dependence upon empirical constants cannot be avoided, at present, due to the complexity of the modelling situation and the number of assumptions that are required. Each assumption must be supported, hence the need for empirical constants remains due to a general lack of knowledge regarding the fundamental mechanisms of erosion.

EROSION MODEL	C0	C1	C2	C3	C4	C5	C6	C7	C8	C9	C10	C11	C12	C13
Particle														
Density			✓		✓						✓		✓	✓
Hardness								✓						
Moment of Inertia		✓												
Sharpness			✓		✓			✓		✓				
Mass	✓	✓		✓	✓	✓								
Size		✓	✓				✓				✓			
Impact Velocity	✓	✓	✓	✓	✓	✓	✓	✓	✓		✓	✓	✓	✓
Rebound Velocity						✓			✓	✓				
Kinetic Energy														
Angle of Impact	✓	✓	✓	✓	✓	✓		✓	✓	✓		✓	✓	✓
Particle Fracture							✓							
Critical Angle									✓					
Ideal Cutting Fraction	✓	✓												
Temperature														
Poisson's Ratio					✓									
Young's Modules					✓									
Target														
Density	✓	✓		✓		✓		✓		✓	✓	✓	✓	✓
Hardness								✓			✓	✓	✓	✓
Flow Stress	✓	✓	✓		✓							✓		
Young's Modules					✓									
Poisson's Ratio					✓									
Fracture Toughness														
Transverse Rupture Stress			✓		✓									
Critical Strain												✓		
Depth of Deformation														
Plastic Strain Rate														
Thermal Conductivity										✓				✓
Melting Temp.										✓				✓
Melting Enthalpy										✓				
Cutting Energy				✓		✓								
Deformation Energy					✓	✓								
Erosion Resilience								✓						
Weibull Flaw Parameter														
Grain Size														
No. of Variables in Model	6	8	7	5	12	7	3	7	4	7	5	6	5	7
No. of Constants in Model	2	2	3	3	3	1	6	10	4	1	1	1	1	8

Table 2-6 Variables Considered in the Various Erosion Models

The inadequacy of the models developed for erosion prediction, as detailed, are reasonable if one considers the complexity of the modelling situation, including the multiplicity of variables involved and the dynamic interaction between the particle and target material. In terms of the complexity of multiple particle erosion, the examination of the eroded surface shows the evidence of dynamic indentation, microcutting, flake formation, lip fragmentation and plowing. We can hypothesize that the horizontal component of the momentum of the impacting particle produces plowing and microcutting, with the repetitive nature of the impacts contributing to the flattening of lips produced by indentation, microcutting and plowing, thereby generating a multi-layer flaky structure. The successive deformation of the surface presumably produces cracking in the plastically deformed material and the fragmentation of the edges.

As such a multiplicity of mechanisms occur simultaneously in the erosional situation, with any single model being expected to capture this detail. Clearly, this is somewhat of a 'tall order', and several workers, including the present author, have adapted a dual equation erosion model which attempts to predict the erosional contribution by more then one mechanisms, i.e. cutting and deformation erosion. This is not an ideal solution, however, it provides a best solution technique, which predicts erosion with acceptable accuracy. Further complications not normally considered within erosion modelling include;

1. High strain rate deformation as a function of impact velocity, particle geometry and target material characteristics.
2. Localised temperature rise as a function of particle mass, velocity and concentration in the carrier fluid, coefficient of restitution, indentation and thermal characteristics of the target material.
3. Distribution of particle impacts (time dependent), impact velocities, size and shape of particles.
4. Interaction between incoming and rebounding particles.
5. Particle fragmentation and hardness.
6. Embedment of particles on the target surface.
7. Development of plastic deformation within surface layers and the incubation period.
8. Work-hardening and annealing effects.
9. Cyclic softening and hardening.
10. Variations in impingement angle due to crater formation and surface roughness.

2.4 Numerical Studies of Erosion

A useful numerical study was that performed by Sato et al [**Ref. 76**]. A *CFD* simulation of the erosion within a turbulent duct was reported; the duct being constructed of copper. The erodent was spherical glass particles of mean diameter 60 microns, standard deviation 14.5 microns. The erosion models incorporated within the code were those of Finnie and Bitter; given by equations C.0 and C.4 of

Appendix C. The authors recognised the now well known erosion regimes of cutting and deformation wear. The erosion models require empirical constants to describe the erosive system, allowing subtleties of the system to be absorbed; see Table 2-6 and supporting text. These empirical constants, three in all, were found through comparison of experimental and numerical work; similar to that undertaken by the present author, see Chapter 9. The empirical constants were found to have the values; C_1 = 0.015, K = 6.0 and Ef = 7E+11 J/m^3. The value of Ef is similar to that found for the various materials investigated by the present author for Equation 4-78. However, no comment can be given as to the validity of cutting empirical constants, due to the differing cutting model employed by the present author.

The suspension fluid was air, solved through the application of the low-Reynolds number k-Epsilon turbulence closure model. This form of the model was used as it is able to resolve the near wall turbulence characteristics well. The model integrates the flow solution up to the wall, avoiding the need for wall functions. Particle trajectories were solved through the momentum argument, in a Lagrangian frame of reference; where consideration was given to the normal forces acting on a particle. Particle-particle collisions were neglected due to the low particle flux rates. Furthermore, the two-way couplings between the continuos and suspended phases were ignored.

The principal aim of the study was the development of a valid modelling procedure. Further, to the selection of appropriate erosion constant, much attention was given to turbulent dispersion of the particles and rebound characterisation. Studies were completed with both stochastic and deterministic particle tracking and uniform/non-uniform rebound characterisation. Stochastic tracking was conducted in a similar fashion as that described by Section 6.2.3, where turbulent eddies were considered to operate over a given length or time scale. The contribution to the mean velocity to represent the instantaneous fluid velocity was assumed to be a random sample from a Gaussian distribution function. The standard deviation corresponded to the localised isotropic turbulence structure, via $\sigma = (2/3k)^{0.5}$, allowing the local probability density function to be specified.

Rebound characterisation was undertaken through the exchange of linear and angular momentum within the particle. Sato stated that the perpendicular velocity component of the particle at impact 'is normally retained' due to a contribution from the angular momentum of the particle. The rotational velocity of the particle occurring due to surface irregularities at impact, expressed as;

Equation 2-2
$$\frac{d\omega}{dt} = -\frac{15\rho}{16\pi\rho_p}\left|\omega - \frac{1}{2}rotU\right|C_{TR}\left(\omega - \frac{1}{2}rotU\right)$$

Thus, the perpendicular velocity component was assumed to be retained, implying a perpendicular coefficient of restitution of one, due to the interaction of angular and linear momentum. This

assumption is clearly invalid, see Section 6.3.1. A more appropriate value for the coefficient, as verified within the literature, is approximately 0.6-0.8 [**Ref. 35** & **Ref. 3**], implying that particle trajectory calculations could have had an error of upto 40%. A small portion of the impacting particles may have sufficient angular momentum to satisfy this assumption, provided they are sufficiently irregular. However, the particles employed in the study are spherical, inferring that angular momentum will have a tendency to convert itself in parallel not perpendicular velocity. Naturally, upon attrition of the glass particles, an irregular profile will be promoted; however, such attrition cannot account for 100% of particle impacts. No details were provided as to the treatment of the parallel velocity component.

Bar this failing of a principal assumption, the results obtained are good; displaying the merits of stochastic tracking and non-uniform rebound characterisation. It was found that the uniform rebound characterisation consistently underestimated the erosion, due to fewer particle impacts. As such only non-uniform rebound characterisation was used, allowing the merits of stochastic and deterministic tracking to be investigated. Figure 2-7 [**Ref. 76**] presents this relationship.

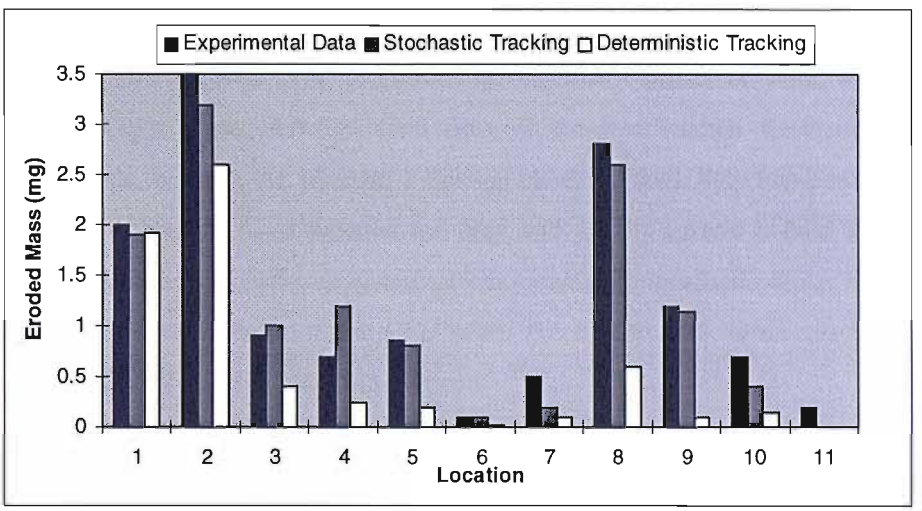

Figure 2-7 Comparison of Stochastic and Deterministic Particle Tracking

It can be seen that although the data is by no means a perfect fit, the stochastic approach to erosion modelling presents the best correlation. This is due to the interaction of the flow field and particles along a straight duct. Without turbulent dispersion, the particles do not readily strike the walling due to the uniform mean vector field calculated by the turbulence closure models. As such erosion will be underestimated and the merits of stochastic tracking are seen. A further observation of stochastic tracking is that the 'spread' of erosion is greater, promoting a more general erosion pattern that is consistent with field observations. The deterministic approach tends to produce peaks of erosion due to the idealised trajectory strategy employed; this can be seen by locations 1 and 2, denoting a bend. Here, the erosion predicted by the deterministic approach is acceptable in these locations. However,

this approach has distinct failings in remaining locations. On the conclusions of this study, and additional work undertaken by the present author, turbulent dispersion to allow stochastic tracking is the default method for erosion modelling within this study.

Die Norske Vertias Industry (DNV) and Norsk Hydro have been co-operating in the field of choke erosion, under a JIP project. Two papers have been subsequently published [**Ref. 38**, **Ref. 67**]. The JIP produced a PCD choke, being an evolution of the conventional needle and seat choke; see Section 3.2.3.1. The choke is presently undergoing trails on a North Sea field. Cameron (Ireland) Ltd, fabricated the choke, as a result of Cameron's involvement in the project, commercially sensitive information regarding this project was made available to myself. Naturally, such sensitive information cannot be reported here. However, from the information made available, I have reservations as to the accuracy of the numerical modelling undertaken. Furthermore, as is the case with all needle and seat chokes, erosion is experienced in the outlet spool; see section 3.6.1. The trim area may be protected with PCD, however, the outlet spool will need an extensive wear sleeve. Here a WC wear sleeve of ten inlet diameters is normally recommended, rendering the choke oversized and difficult to install.

Haugen [**Ref. 38**], detailed briefly the numerical erosion modelling process which produced the design evolution reported above. The procedure is one that consists of three steps; firstly the modelling of the single phase turbulent field flow of the hydrocarbon fluid, undertaken by a commercial *CFD* code, utilising the standard *k*-Epsilon closure model. Step two predicts the particle trajectories, simply through a force balance for drag and gravity effects solved in a Lagrangian reference frame. Step three solves the erosional intensity given the localised particle impact data, this final action was undertaken external to the *CFD* code. The model used within this final step is that first developed by Tilly [**Ref. 89**], holding the form;

Equation 2-3

$$\varepsilon = M_P k_1 F(\alpha) U^n$$

$$\text{where} \quad F(\alpha) = \sum_{i=1}^{8} (-1)^{i+1} A_i \left(\frac{\alpha\pi}{180}\right)^i$$

$F(\alpha)$ details the angle dependency of erosion, providing the well known correlation of Figure 2-2. The constants within the power series for $F(\alpha)$ are defined as;

A_1	A_2	A_3	A_4	A_5	A_6	A_7	A_8
9.370	42.295	110.864	175.804	170.137	98.298	31.211	4.170

Two empirical constants are needed within the model, these constants have been classified through experimentation for a wide range of material types. The recommended values for these constants are

given in Table 2-7. However, as a note of caution, these constants were established on the merits of a very limited test programme. The majority of materials were tested at two impact velocities, 45 and 200 m/s, and two angles of impact, 22.5° and 90°. It is reason to assume that a good correlation can be obtained from such limited experimental data. Erosion rates vary considerable with erodent angle, see Section 4.1. Haugen, assumed the erosive behaviour of brittle materials was a linear relationship of the angle of impact, which is a wholly inadequate assumption, see Figure 2-2. Additional tests, at varying angles of impacts are required to increase the statistical confidence of the correlation developed. However, the authors recognise this fact, stating that the empirical constants should only be used as guidance. The exception to this limitation is carbon steel, this material was used as the reference, hence a detailed assessment was completed.

MATERIAL	k_1 (E+09)	n
Carbon Steel	2.0	2.6
Hot Sprayed WC-60% Ni	5.2 E-02	3.4
Hot Sprayed WC-40% Ni	1.2 E-02	3.2
D-Gun WC, 0.25 mm	6.1 E-01	2.7
WC, DC 05	1.1 E-01	2.3
WC, CS 10	3.2 E-01	2.2
WC, CR 37	8.8 E-02	2.5
95% Al_2O_3	6.8 E+01	2.0
99.5% Al_2O_3	9.5 E+02	1.2
PSZ	4.1	2.5
ZrO_2-Y_3	4.0 E-02	2.7
SiC	6.5	1.9
Si_3N_4	2.0 E-01	2.0
TiB_2	9.3	1.9
B_4C	3.0 E+01	0.9
SiSiC	7.2 E-02	2.7

Table 2-7 Recommended Values for the Empirical Constants of Haugen Model

Further to establishing the empirical constants of Table 2-7 [**Ref. 38**], a brief résumé was provided regarding the design optimisation work undertaken on the evolution needle and seat. Extensive laboratory testing and numerical simulations were reported, however only the main results were given. Different steel designs of the choke were developed and tested, being tested under a moderate pressure drop of 10 bar.

The factorial improvement in erosion resistance for the evolution choke over the traditional design was quoted as being of the order of 10^2-10^3 times. Such an improvement is relatively easy to achieve. The traditional choke design is one that contains rapid variations in flow area and little profiling, being principally design for simplicity and benign duties. Erosion limitation can be easily obtained by minimising the particle impact angles, through careful profiling and consideration to particle

trajectories. The advantage of profiling is that the erosional attack is more generalised, with erosion initiation sites and 'hotspots' being reduced.

The authors state that the numerical procedure reproduces the experimental data with 'good accuracy', with respect to both the location and intensity of the erosional attack. However, I would bring this statement to question given the further insights into this research programme obtained through Cameron (Ireland) Ltd.

Lars Nϕkleberg of Norske Hydro has worked extensively in the field of choke erosion. A recent paper [**Ref. 67**] presented a numerical investigation of both solid particle erosion and that due to liquid droplet erosion. The *CFD* code employed was Fluent 4.2, using the three stage approach to erosion modelling as described for Haugen above. Wear models for solid particle erosion and liquid droplet erosion were embedded within the code. No further discussion to the flashing wear phenomenon will be given; the interested reader is referred to the paper. The solid particle erosion model utilised was that of Haugen, Equation 2-3, using the constants given by Table 2-7. As with Haugen, the angle dependency of erosion for brittle materials was assumed to be linear. As stated previously, this assumption is clearly incorrect.

Numerical modelling of the turbulent flow field using the standard *k*-Epsilon closure model was reported to have been completed for a number of chokes and openings. Particle trajectories were determined through the Lagrangian integration approach, incorporating stochastic particle behaviour and the normal drag correlation. The example presented was of a needle and seat choke at 50% open. No details were provided as to the dimensions of the choke; i.e. flange diameters. All trim parts were specified as tungsten carbide. The fluid under-investigation was a non-specified hydrocarbon gas, experiencing a pressure drop from 560 to 300 bar. No details were provided as to the particle size distribution. The version of Fluent employed was only able to consider spherical particles, no provision for non-spherical particles was made through the application of shape factors. The observations of the study were;

1. Sonic gas flow in the throat section.
2. Supersonic gas flow in the 'bean[3]', or vena contracta.
3. Maximum particle impact velocities ≈ 120 m/s at the location of maximum erosion.
4. Low particle impact angles, 46° at location of maximum erosion.
5. Predicted penetration rate of 1.7 mm per year for 15 kg of sand per day.

[3] Oil industry term used to describe an one inch square opening, or a part there of i.e. a 64th. Thus, to 'bean' the choke up, means to open the chokes to increase the flow area.

The simulations shown erosion patterns similar to that observed through field experience and from trial choke tests undertaken at Det Norske Veritas. This work is coupled with that of Haugen. I disputed that work and I will once again uphold that statement. My concerns stem from what appears to be a clear lack of comprehension as to how best apply *CFD* techniques. Principal observations to support this statement lay in the coarse grid employed, the inlet and outlet conditions, and the unrealistic coefficient of restitution utilised. Boundary conditions within commercial *CFD* codes assume that in flow and out flow from the domain is classified as fully developed pipe flow. The inlet patch is set to the body cavity of the choke, ignoring any upstream pipe convergence that is common to the inlet spool of chokes. Furthermore, a divergence in the outlet is specified just prior to the outlet patch. This divergence is shown to induce a backflow region across the outlet patch. The backflow region disrupts the continuity equation, leading to flow inaccuracies further upstream. Such solution inaccuracies are easily rectified by extending the flow domain to enable fully developed pipe flow to be achieved. However, their presence highlights a lack of understanding by the author.

A further indication as to flow errors appeared in the unrealistic value set for the coefficient of restitution. The unrealistic value was required to force the predicted erosion patterns to partly resemble that observed experimentally. The values assigned were as high as 0.95. Further, no angle dependency to the coefficient of restitution was reported, see Section 6.3.1. Such values clearly highlight flow field and trajectory calculation errors, implying that the author should have re-visited the solution for the flow field to correct the errors detailed above.

Nϕkleberg [**Ref. 67**] concluded that erosion limitation could be achieved through *CFD* techniques, allowing the erodent angle to be minimised through carefully implemented design developments. An additional advantage of a *CFD* erosion model is that areas where specialist materials are required can be identified, minimising the danger of over engineering the choke and the high costs associated.

Further, it is noteworthy that in certain sour applications or where CO_2 is present, corrosion of the tungsten carbide binder, in addition to erosion, may become significant. This erosion-corrosion synergy of a tungsten carbide promotes a rapid undermining of the binder phase, promoting whole carbide loss upon direct particle impacts, hence accelerated material loss. To combat such a situation a corrosion resistant nickel based binder phase is utilised. The erosion resistance of such a binder is less than that of a cobalt binder under pure erosion; however, improved wear resistance can be achieved under an erosion-corrosion synergy. SINTEF of Norway state such an observation in their experimental work; however, data regarding the magnitude of any improvement is limited, due to the highly complex wear environment.

3. Choke Valves, Flow and Erosion Characteristics

3.1 An Introduction to Choke Valves

The choke is a hydrodynamic device that provides pressure and flow control via energy dissipation. The energy, dissipated into the fluid as heat and noise, is a function of the differential pressure across the valve and the mass flow through it. The greater the pressure drop or flowrate, the greater the energy dissipated. Typical energy levels associated with a choke can be of the order of 1 to 3 MW [**Ref. 70**], duty dependent. Fluid pressure is converted into velocity via a flow restriction, this velocity is then dissipated by a combination of friction, turbulence and diffusion. Each style of choke has the ability to vary the cross sectional area of the flow restriction presented to the flow, thus providing variable control via the open position. Figure 3-1 shows the typical pressure and velocity history of a fluid as it passes through the choke, where the trim is that part which undertakes the flow control duty.

The energy dissipation methods can be exploited in a number of ways to provide hydrodynamic control. The first, and that most commonly used, is to manipulate/change momentum to provide kinetic energy losses. The high velocity jets generated via the flow restriction are forced to impinge upon one another, dissipating energy through turbulence and diffusion losses due to sudden expansions and changes of direction. Small frictional losses also occur across the flow restriction, however these are negligible. A less common approach is to use kinetic energy to overcome principally frictional losses. The flow restriction in this case is a series of tight passageways, with the fluid being forced through the restriction via a high differential pressure. The wall-fluid interactions generate large frictional losses and hence energy dissipation. This type of choke is not normally utilised due to the problems associated with blockage of the passageways.

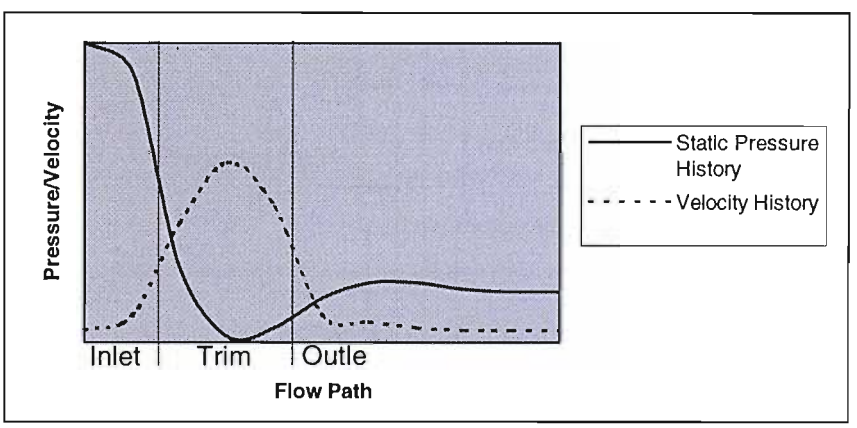

Figure 3-1 Pressure and Velocity History of a Typical Choke

The position of the control choke within the well head assembly is shown by Figure 3-2. Here, a well bore is drilled, being lined with a casing which is cemented into position. The casing supports the well

bore, whilst preventing cross-flow of the hydrocarbon product between the differing layers of the reservoir. A production tubing is run, being fixed via the production packer and the tubing hanger. The production packer prevents the annulus area between the tubing and the casing from 'seeing' any pressure. The casing is perforated to allow the flow of hydrocarbons into the production tubing. The Christmas tree tops the well, supporting the necessary well head equipment. The Christmas tree may be position on the seabed, within a template, or situated on the platform.

3.1.1 The Implications of Subsea Requirements

Before discussion is made of the technological nature of the control choke; the implications of the recent emergence of subsea technology is noteworthy. The North Sea has reached maturity, as such the easily exploited fields have been developed. A situation has arisen, where it is only the marginal fields which remain. Marginal in this instances implies those fields which have scattered reservoirs, having no single large accumulation, and those fields which lay in deep water. Examples of these field types are the ETAP field of the Central North Sea, and the Scheihallion and Foinaven fields which are situated in deep water West of Shetland. Such fields call for the application of subsea technology, where cost reductions are realised if the field is situated in deep water, or where the reservoirs of the field are not situated in an exploitable geographic area.

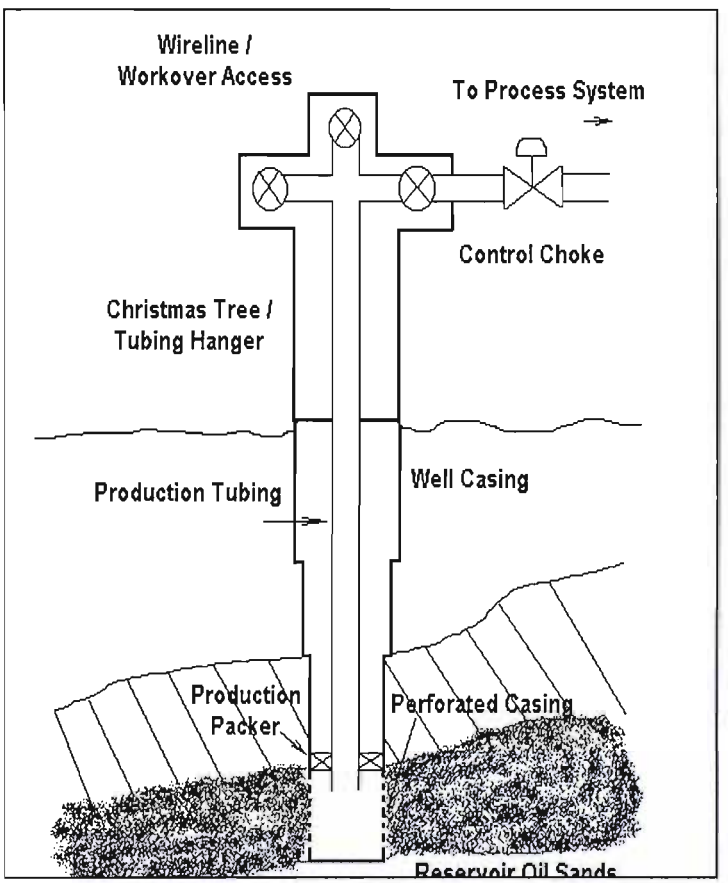

Figure 3-2 Simplified Well and Well Head Completion

Figure 3-3 details the distribution of fields in the Central North Sea. The ETAP field is denoted by the blue shading. Here nine fields are serviced by two platform installations, situated over the Mungo and Marnock reservoirs.

The remaining reservoirs utilise subsea technology to exploit the reserves, each being tied back to the Central Processing Facility situated over the Marnock reservoir, see Figure 3-4. Such a development would not have been possible for the application of subsea technology, of which the control choke is an important component.

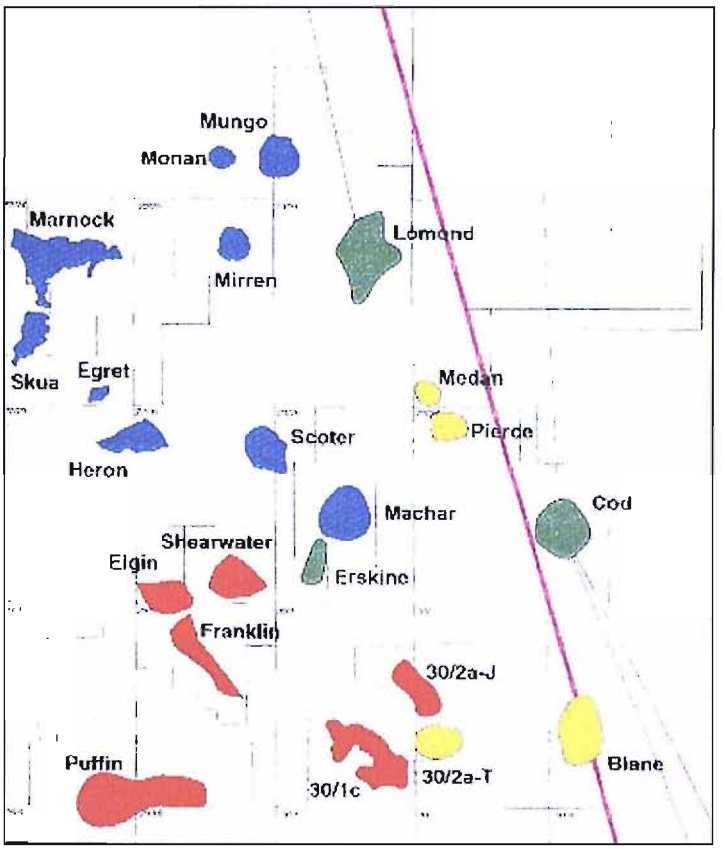

Figure 3-3 Distribution and Size of Fields within the Central North Sea

Figure 3-5 details the typical layout of a deep water subsea development. Here a Floating Production Storage and Offloading (FPSO) facility has been utilised. The benefit of such facilities is that they may be utilised within deep water developments that would not normally support the costs of a fixed platform. Note the arrangement of subsea wells within Figure 3-5, here flexible risers are employed to connect the well to the production facility. The hydrocarbon product is stored upon the production facility, being transported to shore through an export tanker. Such an arrangement avoids the need for pipelines, thus lending this exploration arrangement to application in remote locations.

The economic exploitation of subsea oil and gas reserves is heavily dependent on the availability of choke valves and other flowline components which offer a long and reliable service life. Such a situation is exemplified under erosive service conditions where its is essential that the service life of any subsea component be maximised.

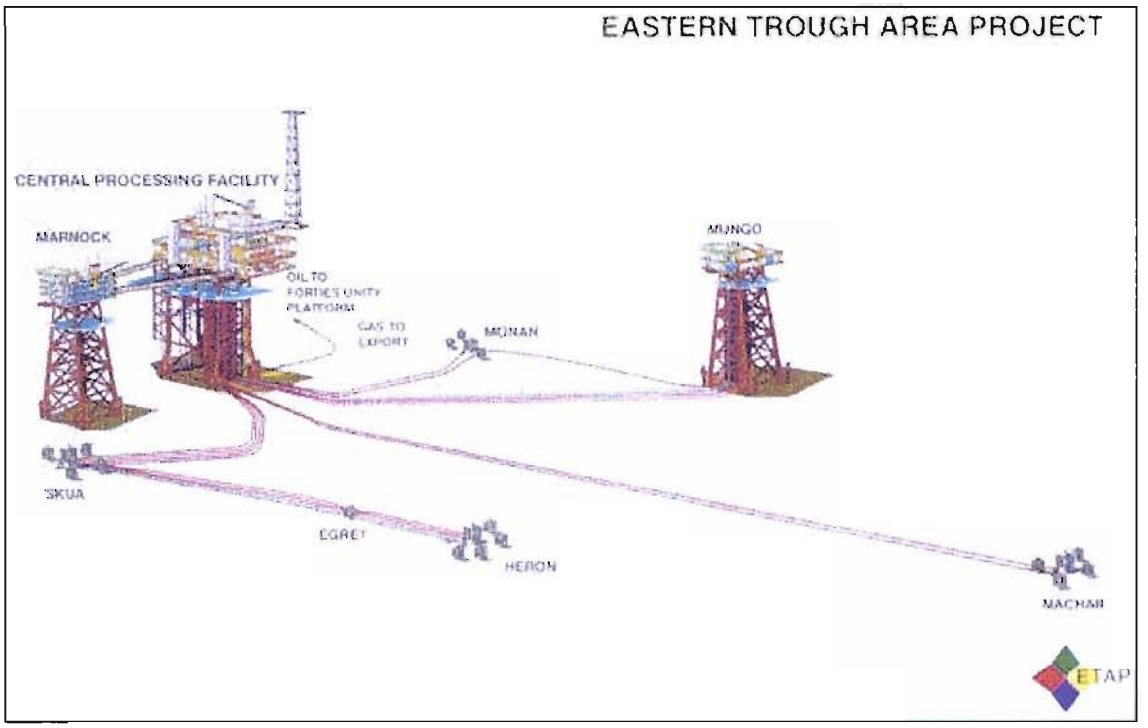

Figure 3-4 Layout Schematic of the ETAP Field Infrastructure

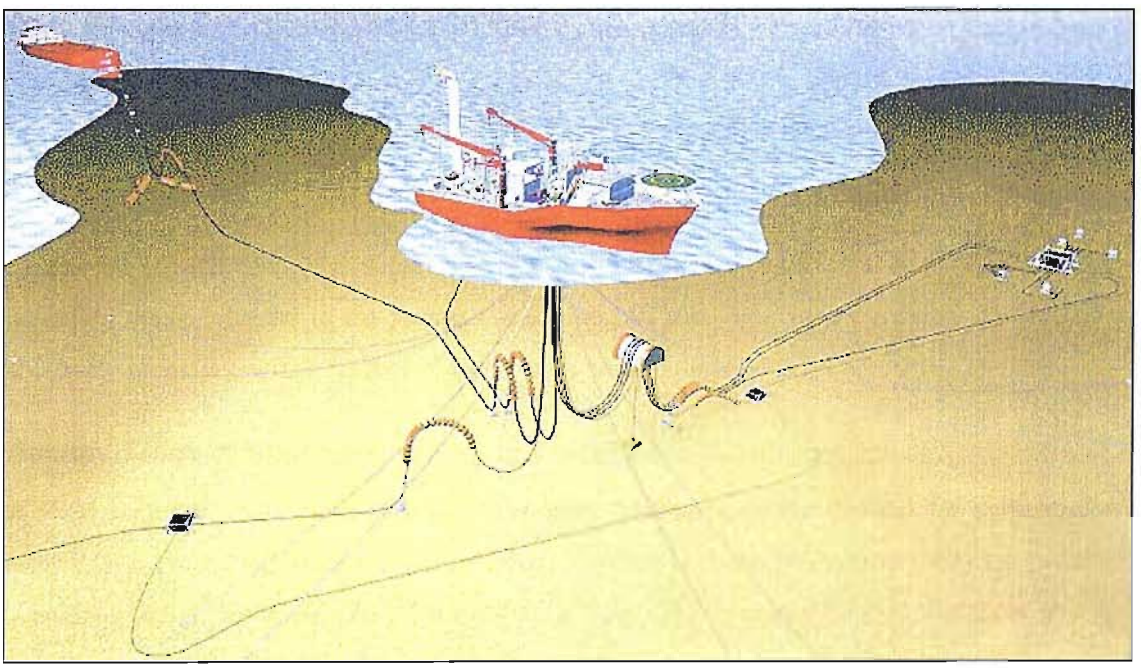

Figure 3-5 Subsea Layout of the Banff Field (North Sea)

An example of a subsea retrievable choke is presented in Figure 3-6. Here the choke is undergoing retrievability trials to confirm the change-out operation for the trim. The trim (of a cage type design) is seen in the centre of the picture, being landed in the body (below) by the Remotely Operated Vehicle - ROV - (partly obscured top). The large yellow object sitting atop of the trim is the actuator, which is also retrieved.

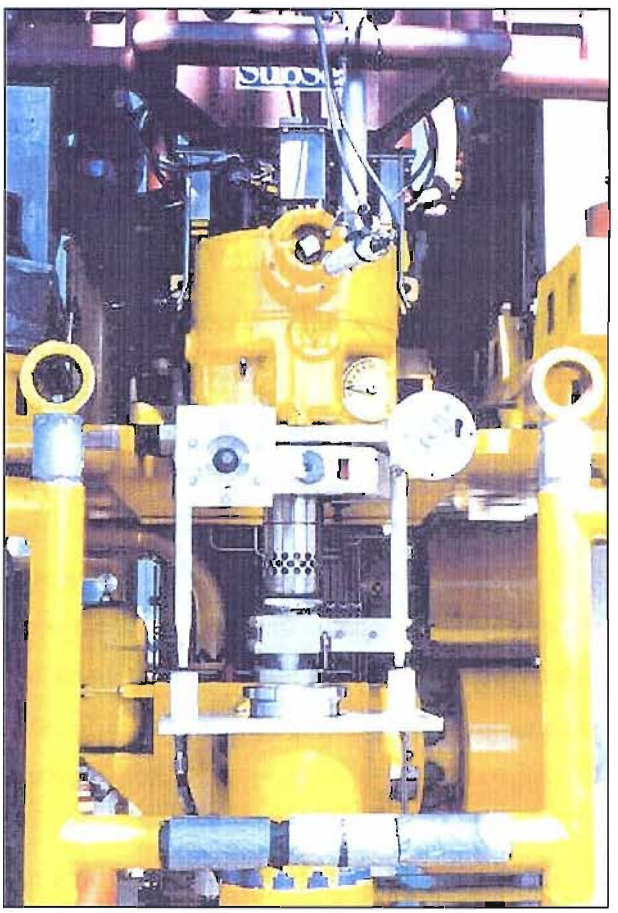

Figure 3-6 ROV Retrieval Trials on a Subsea Choke

The operator can make significant gains in the CAPEX, Capital Expenditure, of a project through the application of such subsea technology. However, difficulties can arise in managing the OPEX, Operating Expenditure, of the project if one is heavily dependent upon subsea technology. The cause of this difficulty is the inaccessibility of such subsea installation. If a component should fail to operate correctly, then the cost of component work-over can be very high. A support-vessel, in the form of a semi-submersible or DSV (Diving Support Vessel), is normally required to undertake such work. The costs of the daily hire of such vessels varies; however, a typical range is of the order of $100,000 to $500,000; depending upon the rig location.

As a result of such costs, it is common for a degree of component failure to be accepted, with design flexibility being essential to the subsea installation. As such work-overs are only undertaken when absolutely necessary, with a number of repair tasks being completed at once.

Generic Types of Choke Valves

A wide range of choke valve designs have been developed as the demand for performance and reliability has increased; furthermore, the market for control choke products is a very competitive one, simulating design variations. As a result of such influences, it cannot be said that there is a typical choke valve design. However, there are key features that are common to the generic design.

1. The geometry of the choke valve body.
2. The method of choke valve adjustment.

3. Trim style, or that part of the choke that is performs flow control.
4. Choke valve control techniques.

3.2.1 Body of the Choke Valve

End fittings are standardised by the nominal diameter of the interconnecting piping; the flange sizes typically varies between 2 and 9 inches (50 to 225 mm). Pressure rating ranges from 200 to 1000 bar, with various seal technologies employed to accommodate the pressure ratings and pressure loading type. Body shapes are normally with the inlet and outlet opposed by 90°, this aids installation and access to the internal flow control components. However, such a radial inlet configuration is not ideal from an erosive view point, as the flow field is severely disrupted.

3.2.2 Choke Valve Adjustment

To achieve variations in the area of restriction as seen by the flow medium, simple linear or rotary motion is employed to adjust the relative position of the trim. It is important that the adjustment mechanism can achieve a reliable change of position that is repeatable, providing consistent operation over various flow and pressure drop regimes.

The amount of adjustment required to obtain the desired flow characteristic is primarily dependent upon the shape, size and number of orifices used in the trim. As the configuration of the trim within the standard body varies, the resulting flow characteristics of the choke alter. To obtain the required level of control it is an advantage to have an adjustment system that is readily adaptable to the trim configuration.

An external actuation system is required, in its simplest form this may be a hand-wheel, whilst for remote or subsea application a hydraulic stepping actuator is commonly utilised. Through the control umbilical, a hydraulic pressure is supplied, which is utilised to drive the choke adjustment mechanism. A simple rotary stepping motion is converted into a linear motion, allowing the trim components to be positioned correctly. The number of steps or rotary motion required to fully stroke the choke depends upon the differential pressure across the choke and its end dimensions. Further, the operator may have specific requirements regarding the maximum closing time of the choke. In an emergency situation, the choke may be closed as quickly as possible, thus rapidly reducing line pressure.

3.2.3 Choke Valve Trim Style

The trim is the heart of the choke, performs the flow control requirement. The trim consists of two parts, one that is fixed and one that is adjustable. The relative movement between the two parts of the trim provides variations in the cross sectional area of the flow path, thus providing variable control. Trim types available include the following styles, see Appendix D-1 to D-4 for design details.

1. needle and seat
2. cage with internal plug
3. cage with external sleeve
4. cage with internal sleeve
5. Multiple variable orifice (MOV)

Multi-stages technology may be utilised, allowing the pressure drop to be achieved over a number of stages. Such an approach is primarily used where cavitation is a concern. For water injection duties, seven stage pressure drops are common. Water injection being the injection of water into the reservoir to maintain pressure and hence boost oil recovery.

Tightening legislation both on and offshore has meant that noise levels must be controlled. Due to the energy dissipation levels experienced within chokes, this component can be extremely noisy, producing noise levels in excess of 95 dBA. Such a noise level can damage hearing and is unacceptable in terms of HSE. The noise produced across a multi-stage pressure drop is lower than that of a single-stage choke; due to the reduced flow velocities. Multi-stage chokes have large wetted areas, as such surface effects tend to dominate, promoting energy dissipation through friction or viscous shear at the wall. Such a dissipation method is quieter then mid stream dissipation methods, where a higher proportion of the dissipated energy is converted into noise.

3.2.3.1 Needle and Seat Choke

Two trim parts are incorporated, one that is capable of linear adjustments, being shaped as a tapered needle that is fixed to the valve stem. The other is shaped as a tapered seat, fixed in the exit bore of the body. See Appendix D-1. The tapered shape of the needle is such that an annular orifice is created with the seat. This variable annular clearing, is utilised to provide the required throttling action for flow control.

A benefit of such a design can be obtained by incorporating additional stem travel. The needle can be withdrawn entirely from the seat, allowing large solids to be passed. Further, the needle and stem assembly can be omitted to provide a positive or fixed 'bean[2]' choke, having a fixed pressure drop. Positive shut-off by this type of trim configuration cannot be relied upon once erosion has occurred.

3.2.3.2 Cage Choke with Internal Plug

A two part design for the trim is utilised. A circular cage containing multiple orifices being fixed in the outlet spool of the body, positioned so that the flow direction is radially inwards. An internal plug positioned inside the flow cage, capable of linear adjustments, is employed to vary the cross sectional area of the orifices configuration seen by the flow, providing variable flow control; see Appendix D-2. The flow cage can be tailored to obtain the desired pressure drop characteristics by altering the arrangement, shape and number of ports. Since the flow path of this trim style is through the orifices,

its ability to pass large solids is poor in comparison to the needle and seat style. See Chapter 6 for details of typical solid sizes.

3.2.3.3 Cage Choke with External Sleeve

This valve style is similar to that of the cage and internal plug. Again the design utilises a flow cage, containing a specific arrangements of port, being fixed in the outlet spool. Flow control is imposed by altering the ratio of the inlet cross sectional area to that of the exposed ports within the flow cage, achieved by the linear movement of an external sleeve fitted around the flow cage; see Appendix D-3. The flow direction is once again is radially inwards, with the passing of large solids being poor. The flow characteristics of the trim are altered once again by the hole arrangement within the cage.

3.2.3.4 Cage Choke with Internal Sleeve

The trim consists once again of a flow cage fitted to the outlet spool, whilst flow control is provided by the adjustment of an internal sleeve. Variations in the hole arrangements provide differing flow characteristics. The number of holes or orifices utilised within each style of cage choke can vary considerably, ranging from four upwards. The holes are normally broken down into zones, with approximately four holes in each zone. The Cameron CC30 style chokes utilise twelve ports or holes in total, set into three zones of four. Zones are normally identified by ports of differing sizes. Typically zone one contains holes of 3 mm diameter, whilst zone two contains holes of 6 mm diameter.

With all of the cage style chokes, positive shut-off cannot be relied upon. Shut-off is normally achieved by closing the sleeve or plug down onto a taper seat region. This seating region can become rapidly damaged, resulting in leakage across the choke. However, a choke is primarily design for pressure control, not shut-off. As with all choke styles, they should never be used as an isolation valve; valves for this purpose include globe and gate valves.

3.2.3.5 Multiple Orifice Valve (MOV)

Two similar discs are employed as the trim components, each containing orifices located about identical datum's. The bottom disc is fixed to the valve body over the outlet spool. The top disc is pressed against the fixed disc, being rotated via the valve stem. Rotation of the top disc provides flow control by the alignment of the orifices, thus generating the throttling effect required; see Appendix D-4. Variations in the orifice arrangement and shape generate limited variations in the flow characteristics of the choke.

Surface finish and flatness between the discs must be high or else there is a tendency for inter-disc leakage. The pressure differential at shut-off acts to energise the seal; however positive shut-off

cannot normally be relied upon. The passing of solids is limited to the size of the orifice and the degree of throttling.

3.3 Choke Valve Flow Control Characteristics

As the flow requirements of a valve change, possibly due to the stage of reservoir development, it is desirable to have various types of flow control characteristics available. As detailed previously, variations in the flow characteristics of the trim can be achieve through alterations to the arrangement, geometry and number of orifices utilised within the trim assembly. There are three basic types of flow control characteristics available; Quick Opening, Linear and Equal Percentage. See Figure 3-7

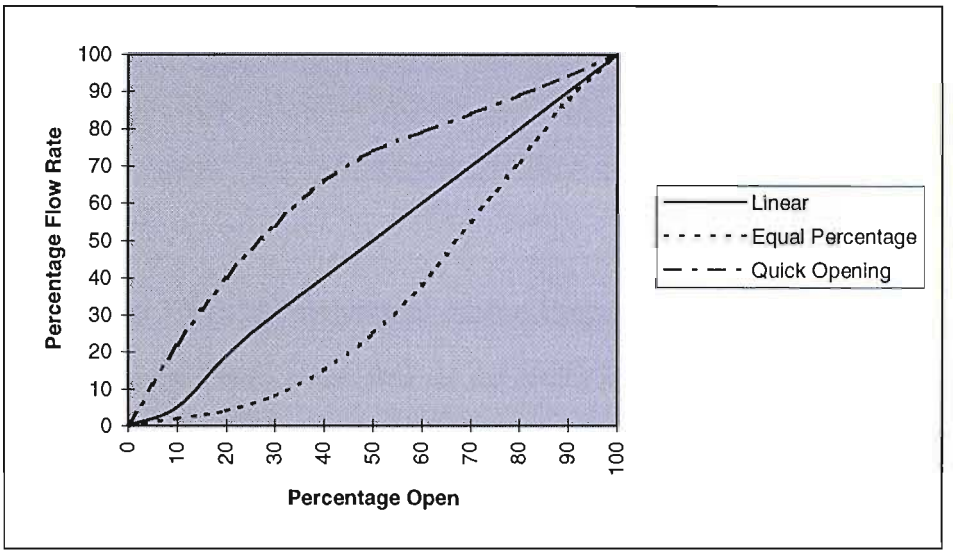

Figure 3-7 Choke Valve Control Characteristics

A linear characteristic is the common control form, offering proportional control over almost the entire operating range of the choke valve; bar an initial dead band area. Quick opening and equal percentage characteristics are employed where finer control is required over only a specific part of the choke opening. Quick opening provides good control when large valve openings are utilised. Equal percentage provides good control when small valve openings are utilised.

Figure 3-8 show the projected flow rates against the stage of well development, the field here is the Scheihallion development. The proportions of each phase varies significantly over the life of the field. Such a variance in the requirements placed upon the choke imposes difficulties in terms of correctly sizing the valve.

Table 3-1 details the limitation of use for each choke type. One may observe that there is a minimum choke opening, given in terms of the pressure drop, below which operation should be avoided. These values denote a rapid increase in the erosion rate experienced, as the choke nears the closed position. As such one must either supply a facility to replace the choke trim, as flow conditions vary, or provide an initial design which is capable of providing flow control over the entire range of operation. The initial

approach may be accommodated easily with platform based installations, however, such a technique is limited for subsea applications due to the costs involved.

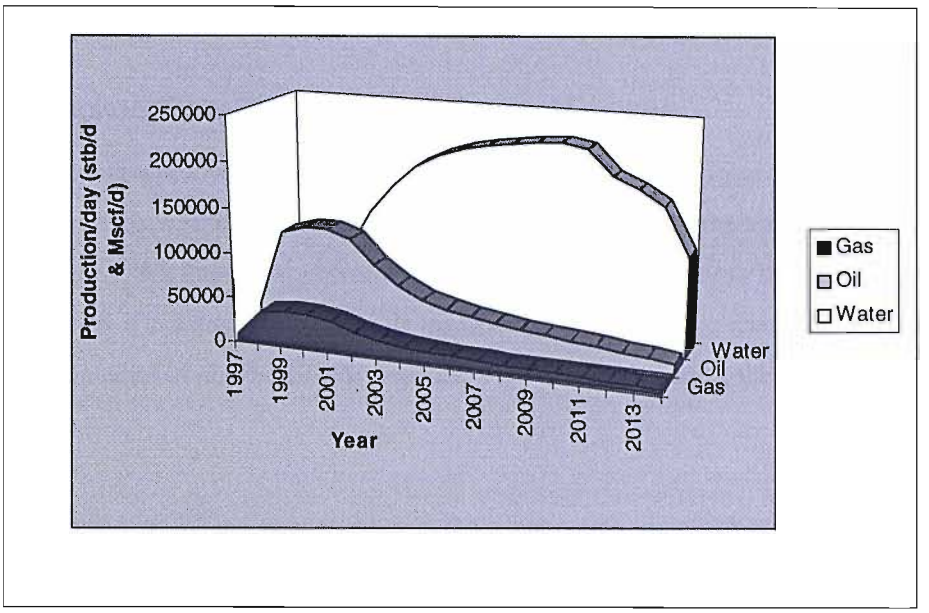

Figure 3-8 Field Development Against Projected Production Rates

Certain valve designs are limited in that they are not readily adapted to all three control techniques. Typically, needle and seat style chokes suffer this problem due to the controlling portion of the trim being an annular clearance. The most adaptable designs are those which incorporate cage style trims, were banks of holes can be arranged and sized to provide the desired flow characteristics.

3.3.1 Measurement of Flow Restriction within the Choke

The measure of flow restriction, or valve opening, can take a number of forms, including, *Cv* or valve flow coefficient, percentage, 64ths and hand-wheel turns. That must commonly used in terms of choke design and sizing is *Cv*. Appendix H provides a full definition of *Cv*. The flow control characteristic of a number of 3" (75 mm) choke designs have the curves detailed in Figure 3-9.

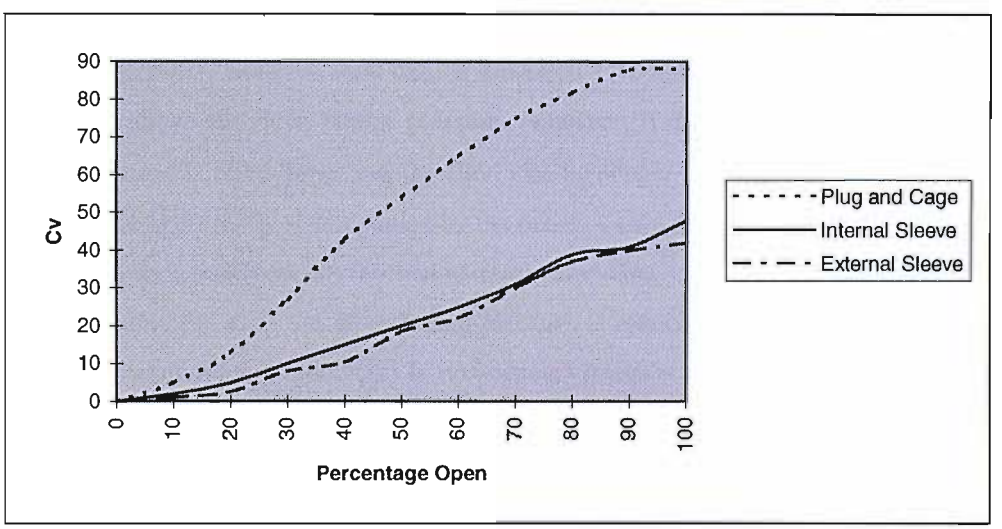

Figure 3-9 Flow Curves for the 'Cameron' CC30 Range of Chokes

Primarily the diameter of the cage utilised and the relative space constraints of each design. The plug and cage style has the greatest cage diameter, hence the highest *Cv* through the provision for a large flow area.

3.3.2 The Choked Flow Phenomena in Control Chokes

An interesting phenomenon occurs when the fluid is severely throttled. Here *choked* flow can occur. Choked flow describes a situation where upon any further closing of the valve no further pressure drop can be obtained. We know that pressure drop is directly proportional to the opening of the valve, however, a situation is reached where there is insufficient hydrodynamic energy to provide a further pressure drop. The point of choked flow is dependent upon the valve style, the fluid type and the fluid pressure at inlet.

The physical explanation of the phenomenon is the propagation of information. The information of any reduction of pressure downstream of the throat has to be propagated upstream through a rare refraction wave. However, the fastest portion of such a wave has a velocity that equals the local sonic velocity. Once the velocity at the throat reaches sonic velocity, no information can be transmitted upstream, hence the inlet fluid is unaware of any further reduction of pressure downstream of the throat, resulting in no further increase in the flow rate.

In a choke, the minimum flow area is located immediately after the flow restriction, or orifice, at the vena contracta. Choking of the flow starts to occur when the velocity of the fluid at the vena contracta reaches the local sonic velocity. Once the maximum velocity has been achieved, further reduction of the downstream pressure will lead to an increase in the size of the vena contracta. However, the flow does not become fully choked until the vena contracta has moved back towards the orifice and reached its maximum size, as constrained by the physical dimensions of the orifices.

A similar situation occurs with incompressible flows; however, one has the additional complication of the fluid vapour pressure. Here the fluid can be treated as incompressible if the static pressure at the vena contracta is above the fluid vapour pressure. However, if the static pressure drops below the fluid vapour pressure, bubbles form and the fluid can no longer be assumed to be incompressible. Such an occurrence is normally accompanied by the onset of choked flow and cavitation. At this stage the pressure at the vena contracta has reached its minimum value, known as the 'super-cooled' vapour pressure. Beyond this point, as the downstream pressure is reduced, no further increase in the flow rate can occur. Any subsequent reductions in downstream pressure will only result in greater levels of cavitation. Due to the onset of cavitation, it is essential that choked flow is avoided for incompressible fluid.

3.4 The Flow Characteristics and Erosion Tendency of Choke Valves

The severity of the erosion experienced is dependent upon, amongst others, the size of the erodent particles, the concentrations of those particles and the target material properties. However, the factors of most importance are the location and velocity of the particles at impact; as imposed by the flow field. Severe interaction occur between entrained solids and the internal surfaces of the choke; producing both localised and general erosion areas. Erosional trends of differing choke style can be identified, giving a basic relationship between the flow field and the erosion induced. Naturally, a good understanding of the fundamental erosion characteristics that each choke design displays is essential in fully understanding choke erosion and it's *CFD* analysis.

Erosion normally occurs within the trim area and downstream assembly, resulting in loss of flow control and the potential for failure to atmosphere. Erosion is particularly severe in gas duties due to the high associated velocities; further, boundary layer effects are negligible for gas flow. The fluid type has not been discussed in the following section; however, the general erosion patterns induced by either liquid or gas as the transport fluid, are normally similar. The reader is referred to Chapter 8 for further details regarding the influence of the suspension fluid.

For even the most conservative calculations of the Reynolds Number, clearly the flow field in and around the trim will be highly turbulent. This turbulence is common to all valve types, with design styles attempting to limit its effect by manipulation of the flow field. Control of erosion is achieved by limiting the number and intensity of particle impacts or through the use of specialist materials.

To aid in the description of flow induced erosion, primary and secondary erosion areas have been identified. Primary erosion can be identified as erosion induced due to the introduction of a disturbance in the flow field; the trim assembly. Secondary erosion is induced solely through downstream effects of the restriction. The wording of primary and secondary erosion is not meant to imply that one type of erosion is predominant over the other.

3.4.1 Erosion of the Needle and Seat Choke

The tapered shape of the plug is such that an annular orifice is created between itself and the seat. This annular orifice is so tapered as to direct the annular jet into the centre of the exit bore, away from the wall. However, the directed jet impinges upon itself at the centre of the exit bore, causing the flow to be reflected into the outlet wall, causing secondary erosion at this site. This style of choke is known for generating excessive downstream erosion. This secondary erosion can be very high, cutting through the body of the choke. Primary erosion occurs at the throttling faces of the seat and plug.

An interesting phenomenon experienced within the needle and seat style of chokes is flow biasing due to the presence of the radial inlet, not shown in this instance. Here the majority of the fluid flows to the back of the body annulus, resulting in slightly higher flow velocities past the needle on that side furthest from the inlet. The fluid jet in this region does not readily detach itself from the wall, resulting in an area of high erosional intensity. If the inlet were at the bottom of Figure 3-10, the area of highest erosional attack would be experienced at the top of the outlet spool, as denoted by Biased Erosion.

Erosion in the primary areas normally results in grooving of the needle. Here erosion starts at any one location, possibly coinciding with the flow biasing effect described in the proceeding passage. This area then acts as a focus for the erosional attack, resulting in deep channels being cut into the needle.

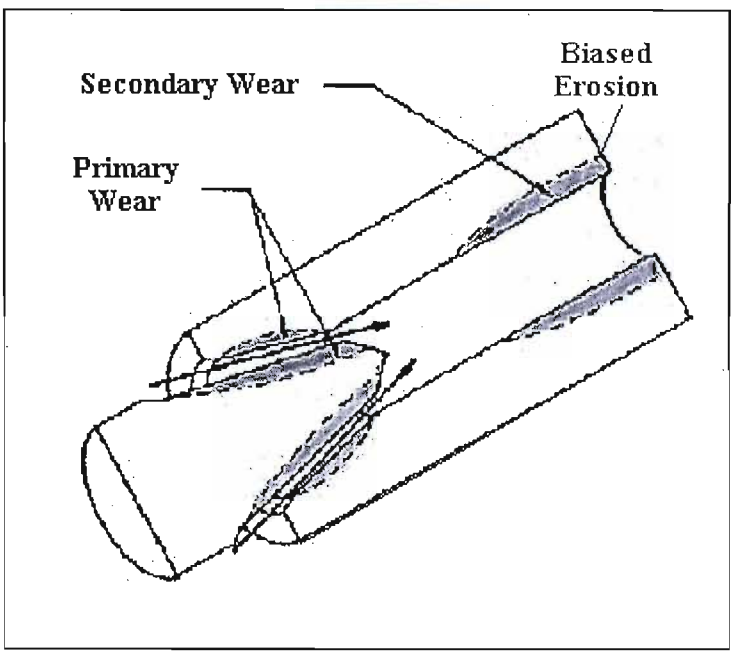

Figure 3-10 Erosion Areas within a Needle and Seat Choke

The greater the pressure drop, the higher the induced flow field velocity and the greater the reflection of the impinging jets into the walling. Intensive erosion at both the primary and secondary sites can occur, it is normal to use tungsten carbide wear sleeves in the outlet spool. Pressure drops across this style of trim are generally restricted to not more than 70-75% of the inlet pressure or severe erosion will result. For particularly aggressive flows, this pressure drop may be limited to 50%. Shut-off by this choke style is poor due to the rapid deterioration of the seating surfaces. The benefits of such chokes are that they are simple and cheap.

3.4.2 Erosion of the Cage Choke with Internal Plug

This choke design is the most common control choke design utilised within the petroleum industry, with its design being robust and well understood. Although the design has its limitations, it has

sufficient strength and flexibility to be applied to most choke applications. The design consists of mutually opposite ports located in a circular flow cage. Such an arrangement is employed to force the emerging jets to positively impinge upon themselves in the centre of the flow cage. Thus, causing a reaction that will, theoretically, decrease the overall flow velocity and hence the associated energy of the flow field. A reduced erosion is achieved as the turbulent flow is concentrated within the centre of the outlet, providing a flow that is coherent and does not readily impinge upon the walling. However, the jetting from the flow cage can be unstable, resulting in direct impingement upon the opposite wall.

The stability of the jetting is dependent upon the size and number of the ports in the flow cage. Many small jets have a tendency to 'miss' one another, being further exacerbated by poor machining tolerances upon the port dimensions and directionality. If the ports are large, one jet may become dominant, thus generating direct impingement. Further, large jets can promote the creation of vortices in the trim and outlet spool area. As such, one must carefully specify the port sizes and arrangement. Tests by manufacturers on 2, 4, 6, 8, 10 and 12 ports per zone of the flow cage have found that 4[4] ports in each zone provides the optimal configurations. The jets are of sufficient size to positively impinge upon themselves, whilst not being oversized such that one may become dominant.

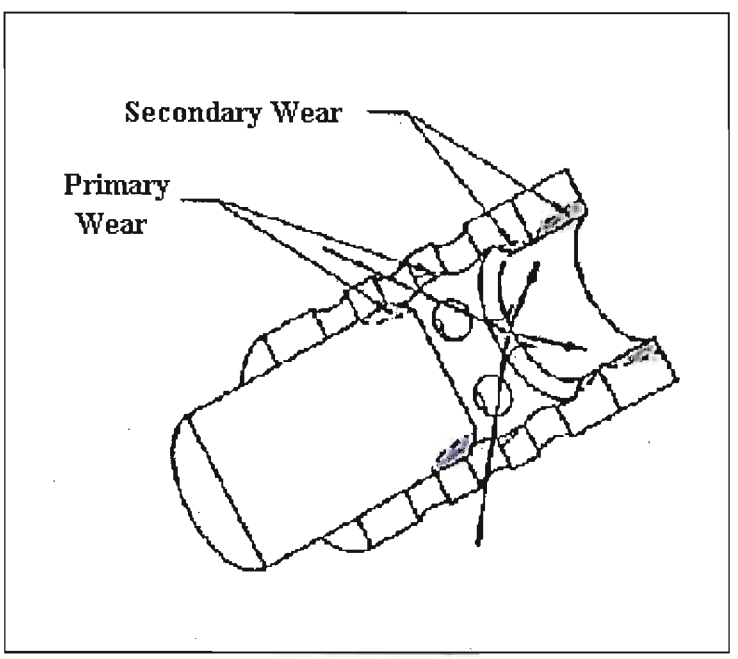

Figure 3-11 Erosion Areas within a Plug and Cage Choke

Due to the requirement of variable pressure drop characteristics, the plug will normally partially overlap a number of ports within the flow cage, resulting in the generation of a deflection angle. The deflection angle cause the flow to be directed into the outlet spool; see Figure 3-11. The angle of deflection generally increases with the degree of throttling. The deflected jets impinge upon

[4] Courtesy of Copper Cameron.

themselves before being reflected back into the valve walling, generating secondary wear areas in the outlet spool of the choke.

Primary erosion occurs in the throttling region of the trim, where the plug and the ports of the flow cage overlap erosion is most aggressive. Further erosion is experienced across the bottom face of the plug where the jets may either recirculate upon themselves or deflected jets impinge into the bottom of the plug. It is normally essential to specify a tungsten carbide material for the plug, otherwise loss of flow control can rapidly occur. An example of the erosion damage induced to the plug can be observed in Figure 1-2. The loss of flow control occurs due to the critical area at the end of the plug being eroded. This area undertakes all throttling actions, hence its loss prevents the choke from obtaining the desired pressure drop characteristics, even when the choke is fully closed. The rate of erosion is not normally as severe as those experienced in plug and seat style valve trims, with pressure drops in the region of 80% of the inlet pressure being maintainable. The secondary erosion may be minimised by the fitting of wear sleeves in the exit bore.

The trim of this type of choke is normally a tungsten carbide material. Tungsten carbide has a relatively low fracture toughness, hence the trim has a tendency to scatter. Mechanisms that may induce trim scatter are the production of large solids, i.e. approximately 1-3 cm in diameter, or the impact of a high velocity liquid slug. The risk of trim scatter may be minimised in the plug and cage choke design through the application of a stainless steel outer sleeve. The sacrificial sleeve is fitted around the flow cage; see Figure 1-1.

3.4.3 Erosion of the Cage Choke with External Sleeve

The cage design is very similar to that of the internal plug, with the cage having mutually opposite ports that provide flow control through the relative movement of an external sleeve. This generates a flow that must, theoretically, positively impinge upon itself, thus reducing the net energy and erosion tendency. Similar to the plug and cage design, a deflection angle is generated where the sleeve overlaps the ports of the flow cage.

The deflection angle generated between the overlap of the sleeve and the ports, has a reduced tendency, over the plug and cage design, to force the jets into the outlet spool. The exact angle of deflection is dependent upon the choke opening, and flow conditions. Impingement of the deflected flow upon itself occurs at the centre of the trim, causing the flow to be reflected back into the trim walling and the bottom of the sleeve; see Figure 3-12. However, due to the cavity above the flow cage, the ratio of volumetric area to energy dissipation is good, thus reducing the tendency for the jets to strike at either the walling or to propagate into the outlet spool.

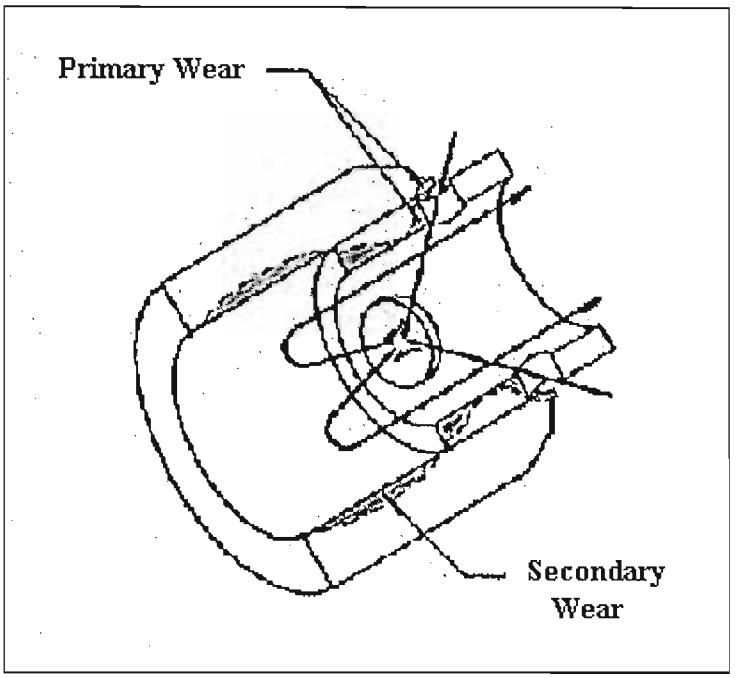

Figure 3-12 Erosion Areas within an External Sleeve Choke

The majority of the turbulence generated through choking and the resultant erosion is contained within the flow cage area, with the outlet spool being almost entirely isolated from such severe turbulence. The overall effect is to create a flow field that does not readily impinge upon the outlet wall. As such, primary erosion occurs at the throttling surfaces, the bottom edge of the sleeve and the ports, whilst secondary erosion occurs within the flow cage and sleeve.

However, as with the internal plug, the throttling surfaces are exposed to erosion, which can result in loss of flow control. In the instance of the external sleeve, the velocity of the flow at the throttling surfaces is lower than that of the internal plug. The throttling surfaces of the internal plug are situated at the vena-contracta, just after the ports of the cage, whilst those of the external sleeve are positioned before the vena-contracta of the port. As such flow control can normally be maintained for a longer period with the external sleeve design than that of the internal plug due to the lower velocities at the throttling surfaces.

Secondary erosion within the trim can be a problem for this choke style. Here, as the majority of the high intensity turbulence is contained within the trim, high erosion rates can occur. This erosion may be sufficient to erode holes through the trim and the top of the sleeve, resulting in loss of flow control. An additional problem is leakage between the sleeve and the flow cage. At high pressure differentials, if the tolerance between the sleeve and flow cage is poor, an additional flow path may be created. Due to the confined nature of these flow paths, the induced velocities may be very high, resulting in rapid erosion and loss of flow control.

Large pressure drops are maintainable with this style of trim, being in the order of 90% of the inlet pressure. Erosion rates in the exit bore are low and maintainable. However, if an incorrect material is selected for the trim components rapid erosion, both primary and secondary, can occur. Such styles of choke valve trims are well suited to gas duty, however the cost of an external sleeve choke is normally greater than that of the internal plug.

A weakness of this design style is that the tungsten carbide flow cage is exposed. Unlike the plug and cage design, a stainless steel outer sleeve cannot be fitted around the flow cage; as the throttling action, in this instance, occurs on the external surfaces of the cage. Upon the production of large solids or high velocity liquid slugs, the cage may shatter due to the poor fracture toughness of tungsten carbide. An additional limitation is that it is only possible to secure the flow cage at one end, tending to promote fatigue and harmonic frequency effects within the cage.

The external sleeve design offers, in general, an improved erosion resistance over that of the plug and cage design. However, due to the weaknesses of the external sleeve design regarding trim scatter, their usage can be limited, being somewhat eclipsed by the robustness and general practicality offered by the plug and cage design.

3.4.4 Erosion of the Multiple Orifice Valve (MOV)

The twin disc configuration of the multiple orifice variable trim produces a flow field downstream of the orifices that is most turbulent. Once more, across the restriction of the ports, when they are partly open, a deflection angle is formed. This deflection angle, depending on the size of the opening, drives the emerging jets away from the centre line of the exit bore, directly into the walling of the outlet spool; see Figure 3-13.

At full or 100% opening of the orifices, the orifices are in alignment with the deflected flow being parallel to the centre line of the exit bore. Hence it is desirable to operate this style of choke valve with small pressure drops, achievable by large openings of the orifices. Otherwise erosion at high pressure differentials can be very severe with the potential for catastrophic valve body failure to atmosphere. Pressure drops of approximately 70% of the inlet pressure can only be maintainable for light duty.

Primary erosion occurs at the ports, whilst secondary erosion occurs in the exit bore of the valve body. This secondary erosion is normally more severe than that experienced in other trim styles as partial flow energy dissipation cannot occur through the impingement of the jets upon themselves. The fitting of wear sleeves in the outlet spool is normally essential. The benefit of the MOV is that they are simple and cheap.

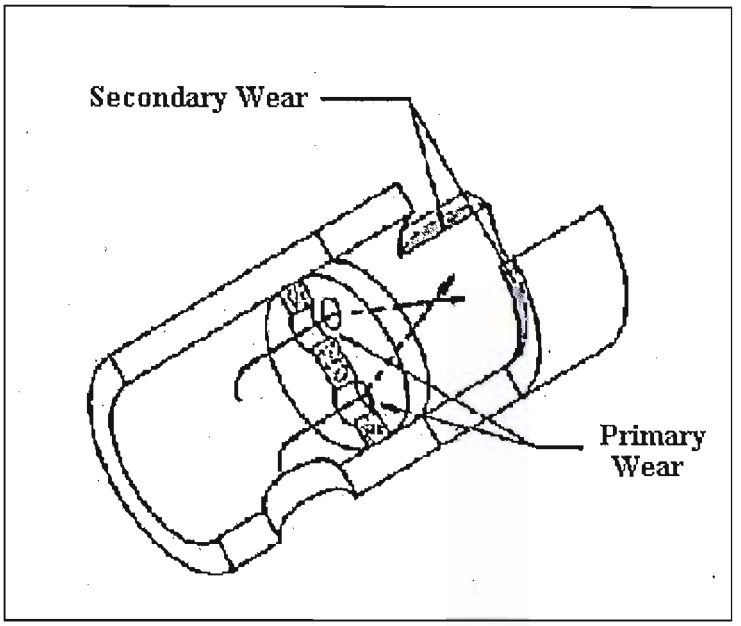

Figure 3-13 Erosion Areas within an MOV

3.4.5 Summary of Choke Design Erosion Performance.

Table 3-1 presents a general summary of the general behaviour of each generic choke type. It is possible that slight variation may be experienced for differing choke design types and manufactures; however, the general conclusions are valid.

3.5 Materials used in the Construction of Choke Valves

3.5.1 Control Choke Body Materials

The material or materials used in the construction of choke valves are selected primarily according to the medium it is to convey and the wear mechanisms that are expected to occur. Erosion, although predominant as a failure cause for chokes, see Figure 1-3, is only one of the many wear mechanisms that can damage valves. Other wear mechanisms that may act, depending upon valve design and duty, include cavitation, corrosion, abrasion and adhesion. However, the body of a choke should normally only be exposed to a dynamic pressure; as such materials used within the body are relatively standard. Figure 3-14 shows the results of a survey of 916 valves undertaken at BP Exploration [**Ref. 69**].

Specialist materials such as duplex steels may be used where there is a specific corrosion problem. All materials for components such as the choke valve body are, as a minimum, normally in accordance with the American standard (API 6A). Body areas expected to experience severe wear, typically secondary wear due to erosion of the exit bore or cavitation, can be fitted with removable inserts or wear sleeves. Such materials are similar to those used for the trim components due to their superior wear resistance.

	NEEDLE AND SEAT	CAGE AND INTERNAL PLUG	CAGE AND EXTERNAL SLEEVE	MOV
TRIM CONFIGURATION	Quick opening and linear.	Quick opening, linear and equal percentage.	Quick opening, linear and equal percentage.	Linear.
SEATING ACTION	Needle - throttling face. Seat - throttling face.	Plug - leading edge. Cage - downstream taper.	Sleeve- inside & outside leading edges. Cage - upstream taper.	Throttling faces of discs.
RESULT OF WEAR ON SEATING	Seating in primary wear area. Seating deteriorates rapidly with use.	Seating in primary wear area. Seating deteriorates rapidly with use.	Seating removed from primary wear area. Seating maintained with use.	Seating in primary wear area. Seating deteriorates rapidly with use.
WEAR CONTAINED WITHIN THE TRIM	No.	No.	Yes.	No.
WEAR OCCURS IN OUTLET SPOOL	Yes.	Yes.	No.	Yes.
EROSIVE ACTION	Jet impinges in centre of outlet, before being deflected downstream into the outlet wall.	Jet impinges in centre of outlet, before being deflected downstream into the outlet wall.	Jet impinges in centre of outlet, before being deflected upwards into the trim and top of sleeve.	Jetting action occurs directly towards the wall of the outlet.
RESULTS OF EROSIVE ACTION	High erosion rates of both the needle & seat and the outlet spool.	Erosion of the bottom of plug, the outlet spool. Radiusing of the cage ports.	Erosion of the trim and sleeve, at the throttling surfaces and top. Radiusing of the cage ports.	High erosion rates around the orifices and in the outlet spool.
OVERALL EROSION PERFORMANCE	Poor.	Good.	Good/Excellent.	Poor.
GENERAL ROBUSTNESS	Good.	Good.	Average.	Average.
CONTROLLABILITY	Poor.	Excellent.	Excellent.	Average.
LIMITATION ON PRESSURE DROP (% OF P1)	70	80	90	70
SIMPLICITY OF DESIGN AND ENGINEERING	Good.	Average.	Poor.	Good.
COST	Low.	Moderate.	High.	Low.

Table 3-1 Summary of Choke Design Erosion Performance

Alternatively, weld cladding can be utilised to improve the wear resistance of a material, such weld claddings include 625 Nickel alloy weld overlay.

3.5.2 Control Choke Trim Materials

The trim is that part of the choke that is exposed to the most aggressive service conditions. As such the wear characteristics of any material used within the trim assembly must be good or excellent. Four

main material types are normally used within the trim assembly, being suited to the excessive demands made of these primary components; see Figure 3-15 **[Ref. 69].**

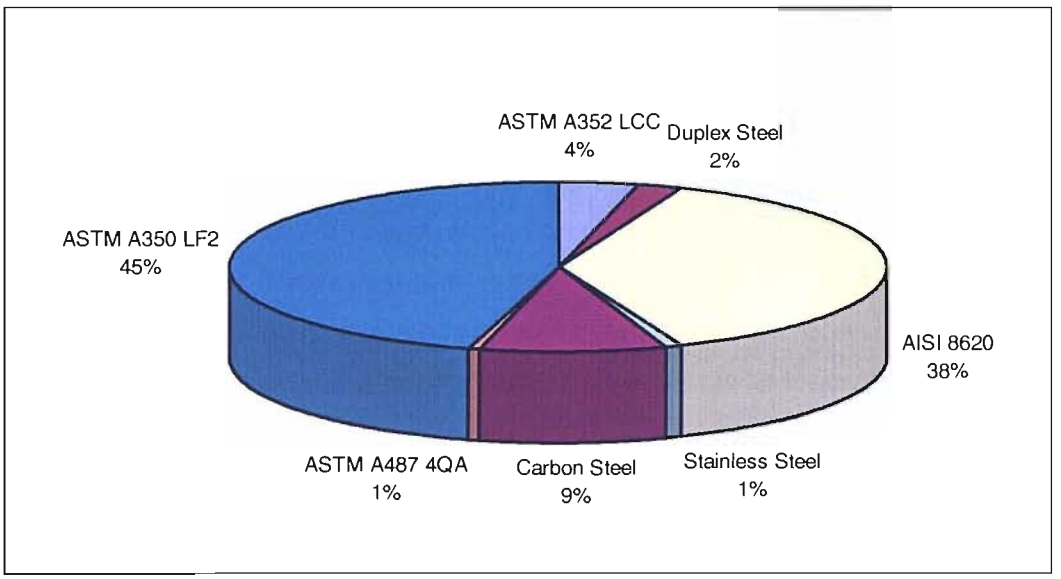

Figure 3-14 Materials used in the Construction of Control Choke Bodies

In addition to the main material groups shown, each material group can be further divided into the grades of material utilised. An example of the grade to be used can be shown if consideration is given to predominant material group, tungsten carbide. Here a very wide spectrum of material grades are available, as determined by the binder content and the grain size. Each of the grades displays slight variations in the bulk characteristics and wear resistance. If the service is aggressive, then a 6% cobalt binder tungsten carbide, with a grain size of approximately 2 micron, would be suitable. However, if it is known that the field produces large solids, the 6% material would be unsuitable due to its brittle nature. The impact of such a large solid would result in the trim shattering. Here, an 11% cobalt binder would be employed due to the increased fracture toughness of this grade.

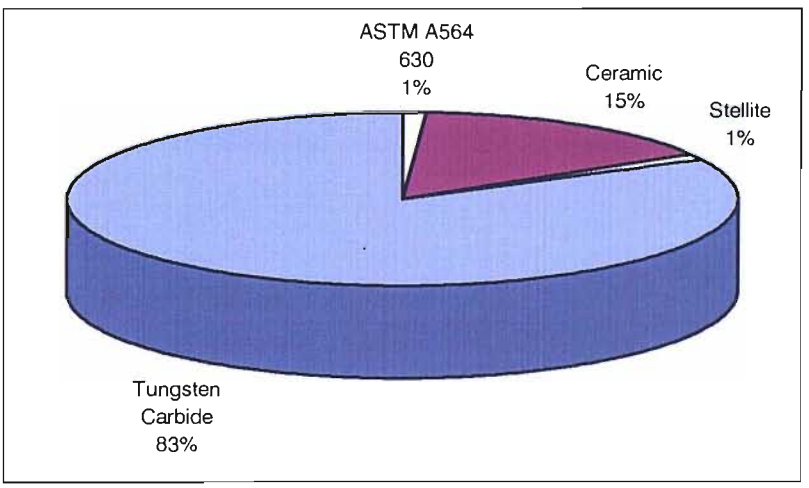

Figure 3-15 Materials used in the Construction of Control Choke Trims

Similarly, if the process stream contains a corrosive element, the cobalt binder would not be suitable. In this instance, a nickel-chromium binder is required as the cobalt binder tends to corrode at an excessive rate.

A further complication for materials that are to undergo erosive duties is the type of erosion to be experienced. Previously, erosion was expressed as a volume loss phenomenon that occurred due to particle impact with the material surface. However, erosion may be divided into two distinct groupings, being cutting and deformation erosion see Chapter 4. These erosion mechanisms are angle dependent, with material behaviour at particle impact depending on the angle of impact. The degree of variation in material behaviour can be marked for certain materials, as such, one must know the average impact angle before comprehensive material selection can be undertaken. A *CFD* code can provide such information, see Chapter 8.

In the situation of choke valves, due to the turbulent motion experienced, a complex combination of both erosion types occur simultaneously. Thus, the selection of a material that is resistant to both erosion types is difficult to achieve. It is common practice for valve manufacturers to employ ever harder materials in an attempt to minimise erosion. However, it is likely that these materials will display some erosive wear in service.

In an attempt to improve the wear resistance of a material, coating technologies are now being investigated. Here, in one approach, chemical vapour deposition is being utilised to coat tungsten carbide with diamond; the thickness of the coating being of the order of few to hundreds of microns. Provided good adhesion can be achieved between the substrate and the coating, wear resistance can be improved dramatically. The advantage of a *CFD* code is that areas of high erosional intensity can be identified and coating technology utilised in these locations; thus, minimising the costs of this expensive wear limitation technique.

4. Solid Particle Erosion and its Modelling

4.1 An Introduction to Solid Particle Erosion

This Chapter draws from and builds upon the observations made in Chapter 2; from Chapter 2 it is readily understood that the solid particle erosion process is an extremely complex phenomenon. The process is dependent upon many inputs, being summarised in Table 2-5. Those inputs of principal influence include the velocity and angle of the particle at impact, the physical characteristics of the particle and the target material, and finally the properties of the suspension fluid. To enable a numerical analysis to be undertaken regarding the likely magnitude of the erosion induced, these influences must be addressed. This is achieved by either inclusion of the influences within an erosion model, or through the prediction of the particles trajectory as it arrives at the surface of the target. The latter element is dealt with by Chapter 6, whilst the development of a suitable erosion model is considered here.

Numerous workers have tackled the problem of erosion modelling, utilising a range of mechanisms to describe the influences acting within the erosion process. Section 2.3 and the supporting Appendix give a summary of the models developed to describe erosion and the underlying mechanisms assumed to be dominant. The models proposed can be re-iterated as;

1. cutting
2. deformation
3. cutting with particle fragmentation
4. dimensional analysis of empirical data
5. empirical particle dynamics
6. indentation hardness
7. low cycle fatigue
8. work of shear force
9. shear localisation

The aim of this project was to develop a procedure whereby the solid particle erosion rates in complex shapes such as control chokes could be predicted. As such it was necessary to embed an erosion model within the numerical procedure developed. Due to time constraints and the relatively wide focus of the research project, it was impossible for the author to develop his own erosion model. The author was forced to draw an appropriate erosion model from the literature, with slight modifications being made to that model to ensure its form was applicable.

The selection of an appropriate erosion model, required that the underlying erosion mechanism experienced within the erosive system of interest be identified. Solid particle erosion within control choke can be broadly summarised by Table 4-1.

The variation range of inputs to the erosion modelling process is seen to be wide, adding further to its complexity. As such, it is essential that the underlying mechanisms selected display wide

applicability. To this end, two principal erosion mechanisms have been highlighted, although sub-mechanisms do exist. These erosion mechanisms are those most widely published in the literature, further adding to the wide applicability of the selected models. The two mechanisms identified are the *cutting* and *deformation*[5] erosion processes. The conclusion that cutting and deformation erosion are the most prominent mechanisms operating may be in dispute with some workers. However, applicability is maximised through the selection of these well established mechanisms, being the key consideration in this instance.

ELEMENT	PROPERTY / OBSERVATION
Particles. Commonly sand.	Density: 2650 kg/m^3 Hardness: 1200 Hv Poisson's ratio: 0.227 Young's modulus: 59.2E+09 N/m^2 Mean Size: 100-350 μm Shape: angular to sub-round
Particle impact characteristics.	Impact velocities: 2-100 m/s Angle of impact: 3-88° Assumed to be non-deformable and non-fragmentary.
Target materials. Commonly steels or cermets such as sintered tungsten carbide.	Density range: 7800-15,000 kg/m^3 Hardness range: 240-1800 Hv Fracture toughness range: 9-70 MN/m$^{3/2}$ Yield stress/Transverse rupture stress 0.3-3.4E+09 N/m^2 Poisson's ratio range: 0.21-0.293 Young's modulus range: 0.19-2.235E+11 N/m^2
Suspension fluid. Hydrocarbons	Any combination of Gas/Oil/Water

Table 4-1 Broad summary of the Erosive System with Control Chokes

4.1.1 The Cutting Erosion Mechanism

At low impact angles, typically 0 to 40° from the surface, the impacting solid particle has a tendency to cut at the target material. The sharper the particle, the greater this tendency. If a particle strikes a horizontal surface at an acute angle, the target material is subjected to shear. The shear being over an

[5] To avoid confusion, it must be brought to the readers attention that the name deformation is used to describe a number of erosion mechanisms, not solely the plastic deforming of the targets surface. This broad name includes such mechanisms as crack growth and fatigue effects. The present author does not wholly agree with the use of such a misleading name. However, as it is a standard term that appears frequently in the literature, the convention will be held to avoid confusion with fellow workers.

area equal to the vertical cross section of that part of the particle that has penetrated into the surface. If the shearing strength of the target material is exceeded, surface destruction will occur. The target material strength is normally exceeded relatively easily due to the local proximity of the applied load. The hardness of the target material influences the severity of the cutting mechanism, until the target material hardness equals that of the erodent, at which point cutting erosion should theoretically cease.

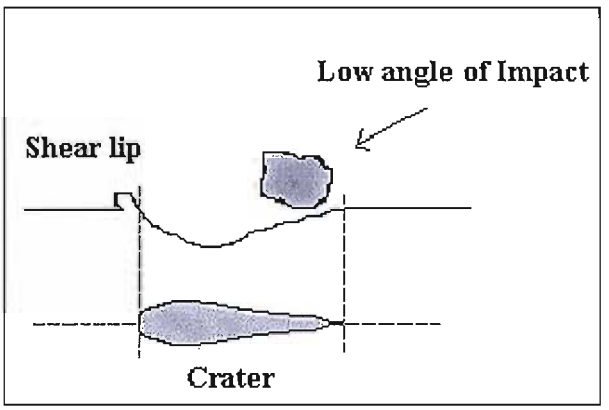

Figure 4-1 Low Angle Cutting Erosion

Figure 4-1, gives a simple representation of the cutting erosion process, showing the shape of the crater in terms of both depth and width. Chippings are produced by the cutting erosion process, with part of the crater material being extruded to the rear of the crater. These shear lips are particularly vulnerable to subsequent impacts. Such vulnerability occurs as the erosion process tends to seek out and exploit weaknesses within the target material; including such flaws as surface irregularities and phase boundaries. The scale of erosion defined is very small, being of the order of microns or less.

4.1.2 The Deformation Erosion Mechanism

At high impact angles, typically 30 to 90°, a pressure spike is generated under the impact site. Such a pressure spike generates what is known as deformation erosion. Consider the impact of a spherical particle that is only elastically deformable. At impact, stress concentrations are set up within the target material as a result of elastic deformation. The maximum stress concentration occurs in the centre of the contact area, at a depth of approximately half the radius of the projected contact area [**Ref. 9**]. Provided this maximum stress does not exceed the yield stress of the material, only elastic deformation will occur. Figure 4-2 [**Ref. 9**] details the typical stress concentration field generated below the impact site; where P_{av} is the average load pressure and d_a is the diameter of the contact area. Bar the possibility of fatigue damage due to the repetition of elastic deformation; surface disruption should be avoided if the elastic load limit is not exceeded.

However, due to the local proximity of the stress concentration and the increase of the effective stress when one works at such small scales, it is possible for the yield stress of the target material to be

exceeded. Plastic deformation occurs at the point of maximum stress, as detailed in Figure 4-2 [**Ref. 9**]. In general, the repeated collision of a large number of particles on the target induces a plastically deformed surface and sub-surface layer, driven by the work hardening mechanism. Such plastic deformation increases the elastic limit until it equals that of the strength of the material. Upon subsequent impacts, the elastic limit and hence the strength of the material may be exceeded. The application of an applied stress results in surface destruction due to delamination, the generation of surface and sub-surface micro-cracks and the coalescence of voids to produce surface fragmentation. See Figure 4-3.

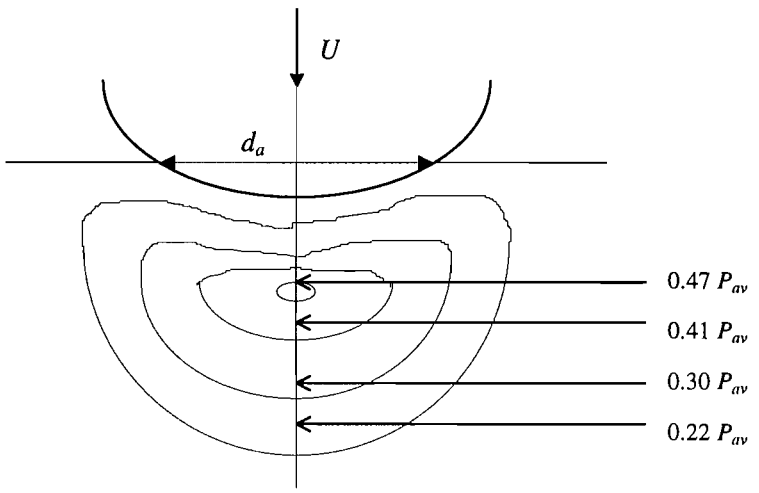

Figure 4-2 Stress Concentrations under the Contact Site

Both cutting and deformation erosion mechanisms can reasonably be assumed to coexist simultaneously, with an impact event generating surface destruction through a combination of surface cutting of the target and sub-surface cracking by the action of the deformation erosion stress concentration effect. To enable accurate erosion predictions to be achieved, a dual erosion model approach is taken. Here, discrete models are generated for each of the mechanisms described above. The generation and structure of the cutting and deformation erosion models are described in Sections 4.3.1 and 4.3.2 respectfully.

4.2 The Erosive Behaviour of Engineering Materials

The concluding statement of the previous section is supported experimentally. Given a characteristic wear curve of an engineering material, differing portions of that curve are attributed to one of the above mechanisms. Figure 4-4[6] and Figure 4-5 [**Ref. 9**], detail the erosion response of steel and tungsten carbide materials commonly found in control chokes. Shown are the individual contributions due to cutting and deformation erosion. The total erosion experienced is simply the sum of the two

[6] Figure 4-4 was generated by the author through the application of Equation 4-81.

contributions. The tungsten carbide material, which has a high hardness, experiences relatively little cutting erosion. Deformation wear is predominate in this material due to the low fracture toughness.

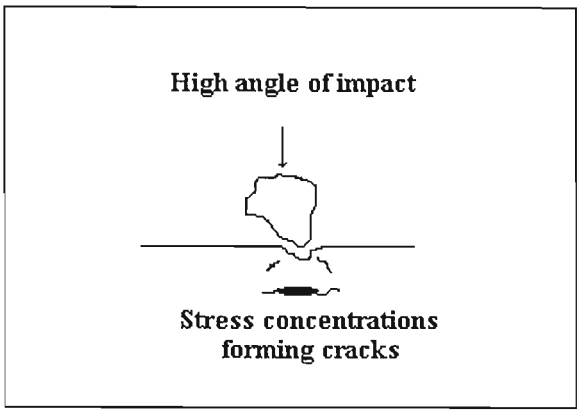

Figure 4-3 High Angle Deformation Erosion

The reverse occurs for the carbon steels, such steels are able to deform elastically, allowing a portion of the impact energy at high angles to be dissipated as elastic work. This limits the high angle deformation wear to fatigue effects and work hardening. However, carbon steels are relatively soft materials, showing little resilience to cutting erosion. The peak of cutting erosion occurs at approximately 30° from the surface as a result of this action.

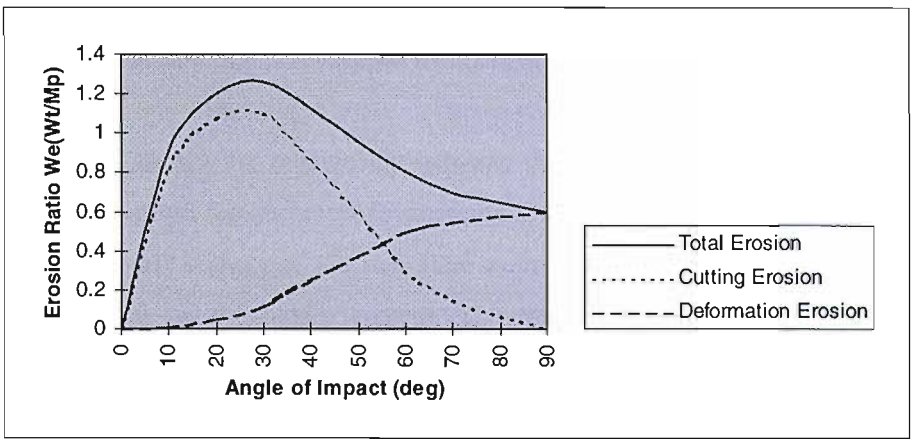

Figure 4-4 Angle Dependency of Erosion for an AISI 1020 Steel

Steel is a relatively simply material to understand due to its near homogenous structure, which readily lends itself to the simply definitions of cutting and deformation. However, heterogeneous materials, such as tungsten carbide, do not so readily lend themselves to such theory. Tungsten carbide is that material most commonly used for the choke trim, as such a good understanding of its erosive tendencies is essential for accurate erosion predictions. However, due to its heterogeneous nature, an accurate tungsten carbide model cannot be derived from first principles. The engineer must rely heavily on empirical data to ensure the model is accurately tailored. Furthermore, a good understanding of the underlying material construction and behaviour is essential.

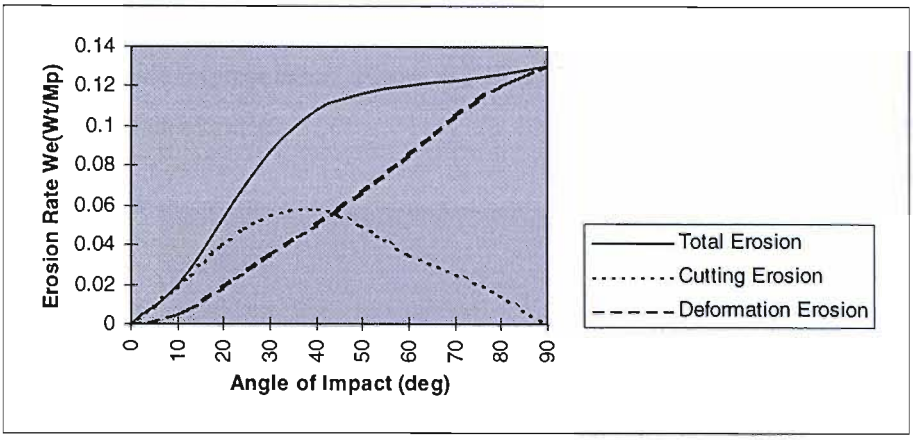

Figure 4-5 Angle Dependency of Erosion for a 6% Cobalt Binder Tungsten Carbide

4.2.1 The Erosive Behaviour of Sintered Tungsten Carbide

Cemented carbides or cermets are basically constructed of a hard phase, held by a softer binder material, typically cobalt or nickel. The dominant erosion mechanism is dependent principally upon the scale of individual particle impacts. Figure 4-6 presents a simplistic cross section of a tungsten carbide specimen, where a proportion of the surface binder is exposed. If the particle impact area is sufficiently small, preferential erosion of the binder phase can occur. This binder erosion results in the undercutting and eventual loss of whole carbide grains. As the particle size increases, the exposed binder area is smaller than that of the impact particles, erosion of both the carbide grains and binder occurs. Here the carbides are physically ripped from the binder or fracture at impact.

Figure 4-7 [**Ref. 45**] shows the relationship between the volume fraction of the surface and the resulting erosion rate, given the impact of 10 μm particles at 90° from the surface. The suspension is air, with a particle impact velocity of 133 m/s. Here we may see that there is a strong and monotonic dependence of erosion on the binder content. The greater the binder content, the greater the undercutting of the carbide particles and the resulting erosion.

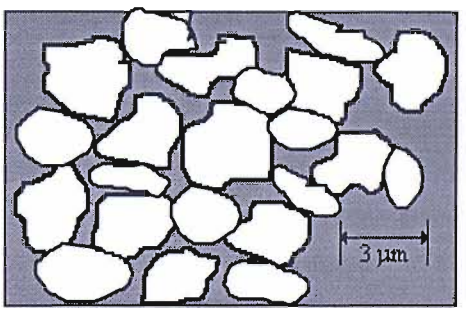

NB. Typical binder contents are 5 to 12% by wt.

Figure 4-6 Simplistic Cross Sectional of a Tungsten Carbide Specimen.

Further to binder content, the angles of particle impact influence the erosion rate and type. As with all brittle type materials, erosion is greatest at an impact angle of 90° from the surface. It is at this angle

that carbide fracture is most prominent. The larger the impacting particles size, the greater the tendency towards carbide fragmentation. Figure 4-8 [**Ref. 45**] presents erosion as a function of both angles of impact and binder content.

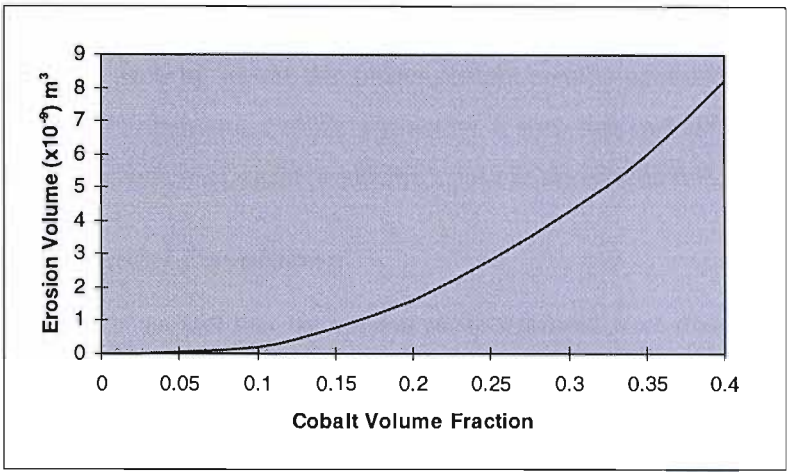

Figure 4-7 Erosion Dependence on Cobalt Binder Volume Fraction for Tungsten Carbide Materials

(Sand in Air: Particle size 10 μm, Impact angle 30°, Impact velocity 133 m/s)

The 30° erodent angle curve represents that erosion principally due to undercutting of the carbides. Due to the low impact angles the particle momentum at impact is less than that of higher impact angles. As such undercutting of the binder is prominent, being reflected in the increasing erosion rate with increased binder content. In this case the increase in erosion rate is not as marked as that of Figure 4-7. The reason for this lies in the increased particle size, the particle size in this instant is 100 μm as opposed to 10 μm.

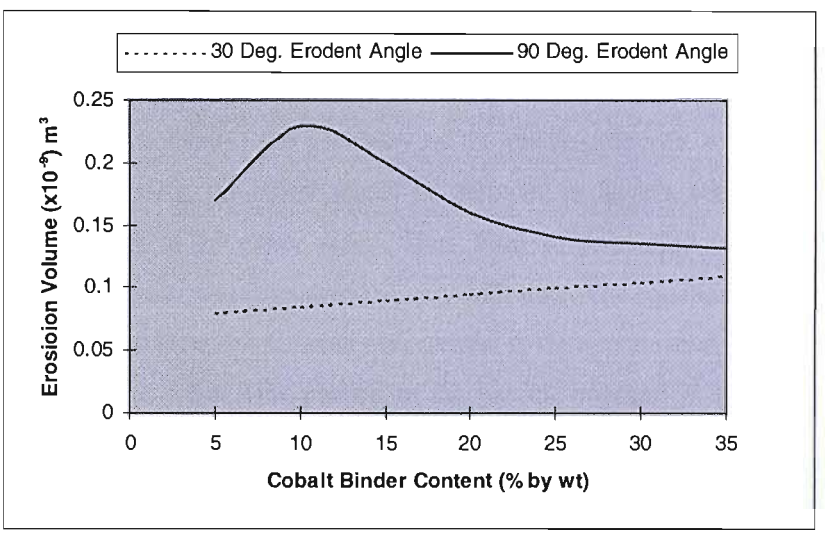

Figure 4-8 Erosion Dependence on Binder Content for Tungsten Carbide

(Sand in Air: Particle size 100 μm, Impact angle 30 & 90°, Impact velocity 40 m/s)

An interesting phenomenon occurs at an erodent angle of 90°. As mentioned, the dominant erosion mechanism is carbide fracture and knock-out due to the increased rates of energy transfer at impact.

The tendency for particle knock-out is related to the adhesion supplied by the binder. The greater the binder content, the greater the carbide adhesion to the substrate, resulting in an improved fracture toughness of the bulk material. This can be seen above a binder content of approximately 12% by wt, where the erosion rate decreases. However, a sharp peak in the erosion rate is seen for a binder content of approximately 10% by wt. At this binder content carbide adhesion is poor, promoting a peak in the erosion rate. Furthermore, carbide orientation is such that carbide fragmentation is most prevalent at this binder content, once again producing a peak in the erosion rate.

4.3 The Erosion Model Developed

It is important to reinforce the fact that the erosion models utilised were drawn from the literature; with minor modifications being made by the author to both the Hashish and Bitter correlations to ensure their applicability to this work. This approach was assumed due to the complexity of the erosion modelling process, with the development of a unique model being a time consuming folly due to the wealth of robust models available in the literature.

4.3.1 The Cutting Erosion Model Utilised

Figure 4-1 shows the trajectory of an abrasive particle as it plows or cuts into the target material due to the inertia it possesses. Ductile cutting models, as developed by Finnie [**Ref. 25** & **Ref. 26**] and Hashish [**Ref. 37**], seek to predict the volume of material removed at each particle impact. As such the goal of each author was to solve the equation of motion of a particle as it cuts through the target material. Knowledge of the path, as dictated by material and impact characteristics, allows erosion predictions to be made. Such an approach has been very successful, allowing accurate predictions to be made.

Traditionally in erosion mechanics, the geometry of the crater produced was considered to be 2-dimensional; Finnie. Typically, the crater would be assumed to have a constant width. However, clearly with time the width of the crater varies. Thus, Hashish postulated a 3-dimensional analysis whereby the width of the crater was considered to vary with time. The equations of motion derived by Hashish will be summarised here; this summary is essential to the appreciation of how modern erosion mechanics treats an impact event. That portion of the particle engaged in the cutting process was assumed to be the particle tip diameter, d. We assume that the particle is non-deformable and does not fragmentate on impact.

4.3.1.1 The Particle Trajectory Calculation within the Cutting Erosion Model

From Figure 4-9, we may understand that the motion of the particle tip, O, can be described through consideration of the x_t and y_t co-ordinates, being related to the particle's centre of gravity through

Equation 4-1 and Equation 4-2. The centre of gravity, *C.G*, translates by x and y, whilst rotating through θ after a time t.

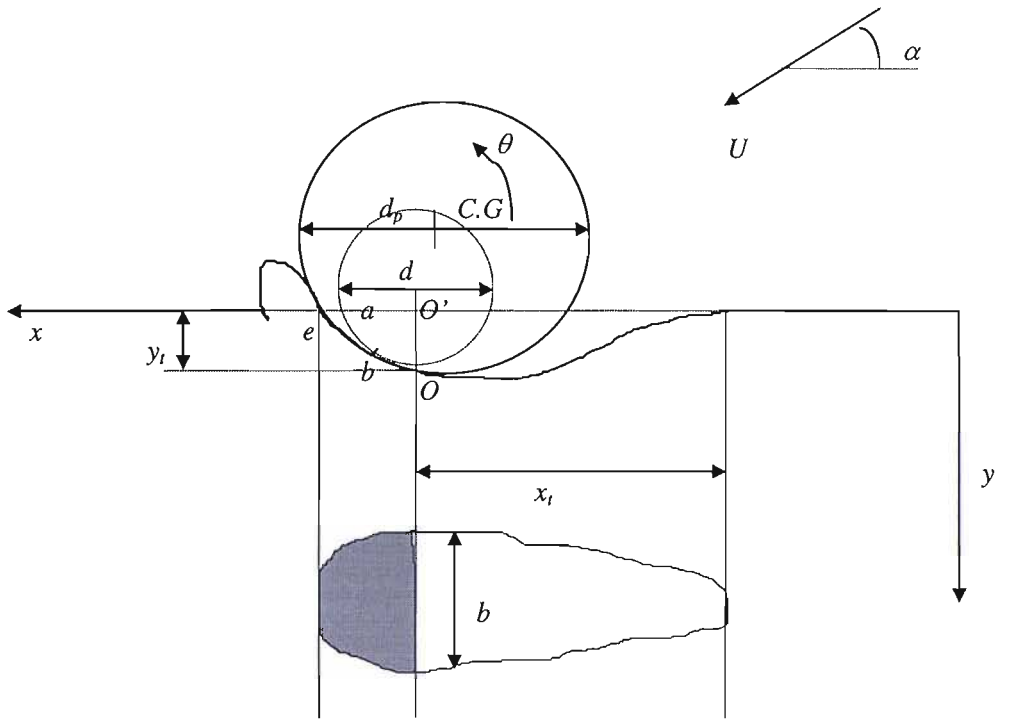

Figure 4-9 Parameters Under Consideration in Cutting Erosion

Equation 4-1 $$x_t = x - \frac{d_p}{2}\theta$$

Equation 4-2 $$y_t \approx y$$

The contact distance of the particle is assumed to be the surface length *O* to *e*. The target material presents a resistance which is assumed to be normal to the surface length, *O-e*; being analysed through the two components R_x and R_y. A frictional force would be experienced, being tangential to the surface *O-e*; however, for reasons of simplicity the frictional force is neglected from the analysis.

The projected contact area of the surface normal to the y direction, A_y, may be expressed as follows;

Equation 4-3 $$A_y = \frac{\pi}{2}a^2$$

a is taken to be the surface length *O-e*. However, when the depth of the crater y is small when compared to the effective tip diameter, d, we can assume Equation 4-1 to be true.

Equation 4-4 $$a = \sqrt{yd}$$

This assumption then renders Equation 4-3 to hold the form of Equation 4-5.

Equation 4-5 $$A_y = \frac{\pi}{2} yd$$

A similar analysis may be utilised to determine the projected contact area of the particle normal to the x direction, holding the form of

Equation 4-6 $$A_x = \frac{4}{3} y\sqrt{yd}$$

To determine the resistance forces acting on the particle, the yield stress of the material must be utilised. Here, the assumption is made that the yield stress is constant over both the contact area and the range of strain rates experienced. However, this assumption is invalid, as the yield stress alters with both of the above conditions. As such, this assumption requires further work.

In addition to the resistance force exerted on the particle by the target material, a rotational force acts on the particle at impact due to the low angle of incidence. As such the entirety of the particle energy is not consumed in overcoming the resistance force presented by the target material; a proportion of the particle energy is translated into rotational inertia at impact. The material resistance forces and the torque component at impact may be expressed as Equation 4-7 to Equation 4-9, given the averaged yield stress, σ.

Equation 4-7 $$R_x = A_x \sigma = \frac{4}{3} \sigma y\sqrt{yd}$$

Equation 4-8 $$R_y = A_y \sigma = \frac{\pi}{2} \sigma yd$$

Equation 4-9 $$T_R = R_x \frac{d_p}{2}$$

The equations of motion for the particle may now be written as Equation 4-10 to Equation 4-12.

Equation 4-10 $$m\ddot{x} = -\frac{4}{3} \sigma y\sqrt{yd}$$

Equation 4-11 $$m\ddot{y} = -\frac{\pi}{2} \sigma yd$$

Equation 4-12 $$I\ddot{\theta} = \frac{2}{3} \sigma d_p y\sqrt{yd}$$

To determine the volume of material removed due to the trajectory of the particle into the target material, we must solve the equations of motion to yield the x component of the particle tip velocity at

any time t, i.e. x_t. To solve both Equation 4-10 and Equation 4-12, we must first determine the y component of the particle tip velocity, from Equation 4-11. Equation 4-11 may be re-arranged to yield Equation 4-13 given Equation 4-14.

Equation 4-13 $$\ddot{y} = -\beta_1^2 y$$

Equation 4-14 $$\beta_1 = \sqrt{\frac{\pi\sigma d}{2m}}$$

The general solution to Equation 4-13 can be shown to be Equation 4-15. With the following boundary conditions applied, y = 0 at t = 0, the constant C will be zero. As such Equation 4-15 now holds the form of Equation 4-16.

Equation 4-15 $$y = C\cos\beta_1 t + D\sin\beta_1 t$$

Equation 4-16 $$\dot{y} = D\beta_1 \cos\beta_1 t$$

The constant D of Equation 4-16 is solved by applying the condition that the y component of the particle tip velocity, at $t = 0.0$, is given by $V\sin\alpha$. Given that C equals zero whilst the solution of D is known, the general solution for y, Equation 4-15, can be shown to hold the form of Equation 4-17.

Equation 4-17 $$y = \frac{U\sin\alpha}{\beta_1}\sin\beta_1 t$$

Equation 4-17 may now be substituted, to allow the solution of Equation 4-10 and Equation 4-12. It is our requirement to solve for x_t, rather than the separate forms of x and θ, this is achieved through the application of Equation 4-1, which yields Equation 4-18.

Equation 4-18 $$\ddot{x}_t = \ddot{x} - \frac{d_p}{2}\ddot{r}$$

Equation 4-10 and Equation 4-12 may be re-written to hold the forms of Equation 4-19 and Equation 4-20, given Equation 4-14.

Equation 4-19 $$\ddot{x} = -\frac{8\beta_1^2}{3\pi\sqrt{d}} y\sqrt{y}$$

Equation 4-20 $$\frac{d_p}{2}\ddot{\theta} = \frac{2\beta_1^2}{3\pi\sqrt{d}}\frac{md_p^2}{I} y\sqrt{y}$$

Substituting Equation 4-19 and Equation 4-20 into Equation 4-18 yields Equation 4-21.

Equation 4-21 $$\ddot{x}_t = -\Omega y\sqrt{y}$$ where

Equation 4-22 $$\Omega = \frac{8\beta_1^2\gamma}{3\pi\sqrt{d}}$$ and

Equation 4-23 $$\gamma = 1 + \frac{mr_p^2}{I}$$

The advantage of the above function is that the sphericity of the particle can be included. Equation 4-21 may now be expressed as Equation 4-24.

Equation 4-24 $$\ddot{x}_t = -\Omega\left(\frac{U\sin\alpha}{\beta_1}\right)^{1.5}\left(\sin\beta_1 t\right)^{1.5}$$

Formal integration of Equation 4-24 yield the solution for the x component of the particle tip velocity at any time t, Equation 4-26.

Equation 4-25 $$\int_{U\cos\alpha}^{\dot{x}} d\dot{x}_t = -\Omega\left(\frac{U\sin\alpha}{\beta_1}\right)^{1.5}\int_0^t\left(\sin\beta_1 t\right)^{1.5}\,dt$$

i.e.

Equation 4-26 $$\dot{x}_t = U\cos\alpha - \Omega\left(\frac{U\sin\alpha}{\beta_1}\right)^{1.5}\int_0^t\left(\sin\beta_1 t\right)^{1.5}dt$$

4.3.1.2 The Prediction of Volume Displacement within the Cutting Erosion Model

Now that the equations of motion have been derived, we may predicts the eroded volume at each impact event. However, before this can be undertaken, one must classify the impact type and the resulting swept volume δv. Here we consider three impact types, as represented by Figure 4-10.

1. Non-embedment. The particle exits the target material and the eroded volume is taken to be the swept volume behind the particle. The eroded volume may be simply expressed as Equation 4-27.

   Equation 4-27 $$\delta v = \int_o^t A_x\dot{x}_t\,dt$$

2. Embedment. The particle's component of velocity x, becomes zero whilst the y component is negative, i.e. moving upwards.
3. Embedment. The particle's component of velocity x, becomes zero whilst the y component is still positive, i.e. moving downwards.

The latter two impact types will not be treated here. These embedment events cannot be resolved through the use of equation of motion type analysis. In such cases, we cannot assume that the energy

transferred to the target material is solely dissipated as localised shear to produce volume loss. Energy is also dissipated through a number of complementary mechanisms that cannot be captured through the equations of motion approach. These complementary mechanisms influence the erosion induced, generating the failings experienced with the equations of motion approach [**Ref. 26**].

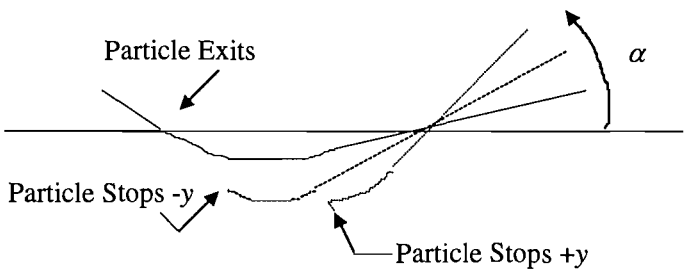

Figure 4-10 Cutting Erosion Impact Type

To enable these impact events to be included within the erosion prediction, an alternative analysis method must be developed. The deformation approach to erosion modelling enables these impact events to be considered. Here, one must resort to an energy approach, whereby, the energy required to remove a unit volume of material is determined experimentally. The reader is referred to Section 4.3.2, for further details regarding this approach.

Thus, Hashish derived a model to determine the volume of material removed by non-embedment cutting erosion. Before the derivation to this model is presented, the underlying assumption will be re-iterated to ensure their clarity. The particle is assumed to be non-deformable and non-fragmentary at impact. The co-ordinates of the crater are 3-dimensional. The cutting face of the particle is uniform and that a constant yield flow stress, σ, is reached immediately upon impact.

The solution for y is known through Equation 4-17. As such, Equation 4-6 can be re-arranged to yield the time dependent projected contact area A_x, Equation 4-28.

Equation 4-28
$$A_x = \frac{4}{3}\sqrt{d}\left(\frac{U\sin\alpha}{\beta_1}\right)^{1.5}\left(\sin\beta_1 t\right)^{1.5}$$

Before we proceed further with the derivation of δv, the following definitions will be made for simplicity.

Equation 4-29
$$\Omega_1 = \frac{4}{3}\sqrt{d}\left(\frac{U\sin\alpha}{\beta_1}\right)^{1.5}$$

Equation 4-30
$$\Omega_2 = U\cos\alpha$$

Equation 4-31

$$\Omega_3 = \left(\frac{U\sin\alpha}{\beta_1}\right)^{1.5}\Omega$$

Furthermore, we may define the integral I_n as follows.

Equation 4-32

$$I_n = \int_0^z (\sin z)^{1.5}\,dz$$

where $z = \beta_1 t$

Through the application of these definitions, Equation 4-29 to Equation 4-32, Equation 4-28 may be combined with Equation 4-25 to yield Equation 4-33.

Equation 4-33

$$\delta v = I_n\left(\frac{\Omega_1\Omega_2}{\beta_1}\right)\left(1-\frac{1}{2}\frac{I_n\Omega_3}{\beta_1\Omega_2}\right)$$

To solve δv we must first determine the numerical value of I_n. This is simply achieved by integration with the limits shown in Equation 4-34.

Equation 4-34

$$I_n = \int_0^{\pi} (\sin z)^{1.5}\,dz = 1.748 \approx \frac{7}{4}$$

Using this result, Equation 4-33, may be re-arranged to hold the form of Equation 4-35.

Equation 4-35

$$\delta v = \frac{7}{4}\left(\frac{\Omega_1\Omega_2}{\beta_1}\right)\left(1-\frac{1}{2}\frac{7\Omega_3}{4\beta_1\Omega_2}\right)$$

We may non-dimensionalise Equation 4-35, presented by Equation 4-36 , being written in its full form.

Equation 4-36

$$\frac{\delta v}{d^3} = \frac{7}{6}\left(\frac{U}{U_k}\right)^{2.5}\sin 2\alpha\sqrt{\sin\alpha}\left(1-\frac{7}{3}\frac{\gamma}{\pi}\frac{U}{U_k}\frac{\sin\alpha^{1.5}}{\cos\alpha}\right)$$

U_k is the characteristic velocity, which holds the form of Equation 4-37. The advantage of knowledge regarding the characteristic velocity, is that the physical properties of the particle may be incorporated into the erosion prediction through this term.

Equation 4-37

$$U_k = \beta_1 d$$

Given Equation 4-14, the characteristic velocity, can be presented as Equation 4-38.

Equation 4-38

$$U_k = \sqrt{\frac{\pi\sigma d^3}{2m_p}}$$

The mass and shape of the particle may be defined as Equation 4-39 and Equation 4-40 respectively.

Equation 4-39 $$m_p = \frac{\pi}{6}\rho_p d_p^3$$

Equation 4-40 $$R_f = \frac{d}{d_p}$$

The particle roundness factor, R_f, has a typical range of 0.1-1; where 1 indicates a spherical particle, whilst 0.1 denotes an angular particle. Equation 4-38 may now be expressed as Equation 4-41, given consideration of the particle mass and shape.

Equation 4-41 $$U_k = \sqrt{\frac{3\sigma R_f^3}{\rho_p}}$$

Equation 4-36 will only be valid if the particle's angle of impact is sufficiently shallow to allow the particle to exit the material. The time at which the particle exits the material is determined by substituting $y = 0$ into Equation 4-17, thus yielding Equation 4-42.

Equation 4-42 $$t_{cl} = \frac{\pi}{\beta_1}$$

The limiting or critical angle which allow the particle to exit the material may be determined, given the following conditions;

1. $y = 0$ when $t = t_{cl}$
2. $\dot{x}_t = 0$ when $t = t_{cl}$

The first condition is satisfied through Equation 4-42 and the definition of I_n = 7/4. The second condition is satisfied by Equation 4-25. Equation 4-25 may be re-arranged to hold the form of Equation 4-43, given the definitions of Equation 4-29 to Equation 4-31.

Equation 4-43 $$\dot{x}_t = \Omega_2 - \frac{l_n \Omega_3}{\beta_1}$$

Given the boundary condition $\dot{x}_t = 0$, we can solve Equation 4-43.

Equation 4-44 $$\frac{I_n \Omega_3}{\beta_1 \Omega_2} = 1$$

By substituting Equation 4-30, Equation 4-31 and the solution for Equation 4-34 into the Equation 4-44, we may reach a definition for the critical angle, α_c; above which the particle will become embedded within the target material due to the high angle of impact.

Equation 4-45 $$\tan\alpha_c \sqrt{\sin\alpha_c} = \frac{3\pi}{14\gamma}\sqrt{\frac{V_k}{U}}$$

For angles below α_c, Equation 4-36 may be simplified provided the criterion laid down in Equation 4-46 is satisfied.

Equation 4-46

$$\frac{7}{3}\frac{\gamma}{\pi}\sqrt{\frac{U}{V_k}\frac{\sin\alpha^{1.5}}{\cos\alpha}} << 1$$

Now, Equation 4-36 may be expressed as Equation 4-47.

Equation 4-47

$$\frac{\delta v}{d^3} = \frac{7}{6}\left(\frac{U}{V_k}\right)^{2.5}\sin 2\alpha\sqrt{\sin\alpha}$$

From Equation 4-39 and Equation 4-40 we hold knowledge of the physical properties of the particle. These terms may be substituted into Equation 4-47, yielding Equation 4-48.

Equation 4-48

$$\delta v = \frac{7}{\pi}\frac{R_f^3 m_p}{\rho_p}\left(\frac{U}{V_k}\right)^{2.5}\sin 2\alpha\sqrt{\sin\alpha}$$

To appreciate the weighting or influence of each of the parameters involved in the cutting model presented by Hashish, we may present Equation 4-49, noting the dominance of certain terms.

Equation 4-49

$$\delta v = 0.564\left(\frac{m_p\rho_p^{0.25}U^{2.5}}{\sigma^{1.25}R_f^{0.75}}\right)\sin 2\alpha\sqrt{\sin\alpha}$$

Hashish presented his erosion model in terms of erosion ratios. The erosion factor, E, defined as the weight of material removed per unit weight of erodent, can be expressed as; given that the angle of impact is below the critical angle of impact, presented in Equation 4-45.

Equation 4-50

$$E = \frac{7}{\pi}R_f^3\frac{\rho_t}{\rho_p}\left(\frac{U}{V_k}\right)^{2.5}\sin 2\alpha\sqrt{\sin\alpha}$$

It is normally convenient to express the erosion predicted in terms of the volume loss. Equation 4-51 presents the volume loss erosion factor, E_v, being the ratio of target material volume removed to the volume of the erodent particle.

Equation 4-51

$$E_v = \frac{7}{\pi}R_f^3\left(\frac{U}{V_k}\right)^{2.5}\sin 2\alpha\sqrt{\sin\alpha}$$

Equation 4-51 may be further simplified through the application of the modified characteristic velocity, presented by Equation 4-52.

Equation 4-52

$$C_k = \frac{V_k}{R_f^{1.2}} = \sqrt{\frac{3\sigma R_f^{0.6}}{\rho_p}}$$

The form of Equation 4-53 is that presented by Hashish to describe cutting erosion below the critical angle of embedment, being the volume ratio of erosion. This form is that upheld and extended by the present author in Section 4.3.1.3.

Equation 4-53

$$E_v = \frac{7}{\pi}\left(\frac{U}{C_k}\right)^{2.5} \sin 2\alpha \sqrt{\sin \alpha}$$

4.3.1.3 Discussion and Developments to the Hashish Cutting Erosion Model

Equation 4-53 presents the ratio of volumes within the erosion process; being the target material volume removed over the volume of the erodent particle. We are interested in the volume of material removed at each impact event; as such Equation 4-53 must be re-written, given consideration to the volume of each particle. For simplicity, we assume that the particle is spherical, with the particle volume being simply defined by Equation 4-54.

Equation 4-54

$$Vol_p = \frac{4}{3}\pi r^3$$

Thus, the eroded volume at each impact event is by Equation 4-55.

Equation 4-55

$$Wc = \frac{100}{2\sqrt{29}} r_p^3 \left(\frac{U}{C_k}\right)^n \sin 2\alpha \sqrt{\sin \alpha}$$

Here, the velocity at impact, U, and the angle at impact, α, are given by FORTRAN routines developed to run in conjunction with CFX-F3D, see Chapter 7. The velocity exponent, n, can be altered to reflect subtle variations in the erosion process not addressed elsewhere. The typical range for the velocity exponent is between 2 and 3, that value recommended by Hashish was 2.5. C_k, the characteristic velocity of cutting erosion is a constant that combines particle and target material characteristics regarding the type of impact experienced. This characteristic velocity distinguishes between elastic and/or plastic collisions, hence the erosive potential of each impact. The distinction is made by modifying the impact velocity to represent the proportions of elastic/plastic deformation experienced at impact. The characteristic velocity of cutting erosion is given by Equation 4-52. This definition is presented for a steel type material, where the yield stress is easily obtained.

The present author has re-arranged C_k to yield a correlation for tungsten carbide. Tungsten carbide does not have an accurately measurable yield stress, due to its physical composition; see section 4.2.1. Technical literature quotes the Transverse Rupture Stress (*TRS*) as an alternative. The *TRS* is simply a three point bending test to destruction. This is the constant used within Equation 4-56, which is for use with tungsten carbide alone. It is recognised that *TRS* is not an ideal alternative to the yield stress, however it is a readily available constant which allows Equation 4-55 to be applied and tuned through the function n. The reader is reminded that the erosion models applied within this work are empirically based.

Equation 4-56

$$C_k = \sqrt{\frac{10.TRS.R_f^{0.6}}{\rho_p}}$$

The characteristic velocity combines the physical properties of the particle and target material. The terms attempts to distinguish the cutting efficiency of the particle, denoting the degree of plastic/elastic deformation induced at impact. This has distinct advantages over the more empirically based erosion models discussed in Chapter 2, due to the increased flexibility and adaptability of this approach. The smaller the characteristic velocity, the greater the volume of material removed, through an increased tendency towards plastic deformation. A large characteristic velocity indicates a tendency towards non-damaging elastic deformation. The characteristic velocity will be small when the shape factor, R_f, is small, i.e. the particle is sharp, the materials yield stress or Transverse Rupture Stress is low and the particle is dense.

4.3.2 The Deformation Erosion Model Utilised

Finnie [**Ref. 25**] initially attempted to apply the equations of motion in a trajectory approach, described previously in Section 4.3.1, to the high angle erosion phenomena; now known as deformation erosion. His attempts failed through his inability to accurately capture the crack propagation and flake formation mechanisms which underpin the deformation erosion process. The trajectory approach only lead to an expression for the loading at the targets surface, not the rate of crack growth.

Bitter, recognising these failures, utilised an energy approach, allowing accountability for the energy absorbed by the target in propagating cracks and the associated deformation processes. However, this in itself was an admission of his inability to also capture the deformation mechanisms. The energy approach simply allows one to undertake a curve fitting exercise to best describe the erosive response of a material, reducing any erosion correlation to an empirical one.

4.3.2.1 The Energy Balance of the Deformation Erosion Model

To assess the particle impact conditions under which erosion or size reduction just begins, the St Venants' theory of elastic wave propagation, in two colliding bodies, may be applied. The following relationship was reported by Bitter, Equation 4-57.

Equation 4-57

$$\frac{\sigma_{max}}{E_t} = A\left[\frac{U}{c}\right]^{2n}$$

The limitation of Equation 4-57 is that whilst the onset point of size reduction is denoted, the extent of any damage cannot be quantified. To enable a quantitative approach regarding size reduction, one must first consider one of the colliding bodies to be infinitely large when compared with the other body. This assumption allows us to apply the Hertizan formula for a purely elastic collision, Equation 4-58, which presents the maximum force exerted at the contact area of the colliding bodies.

Equation 4-58

$$P_{\max} = \left[\frac{20\pi}{3} d_p\right] r_p^2 \left[\frac{1}{6\left(\frac{1-q_p^2}{E_p} + \frac{1-q_t^2}{E_t}\right)}\right]^{0.4} U^{1.2}$$

One may further derive an expression for the projected contact area of the elastic load acting on the target surface, detailed in Equation 4-59.

Equation 4-59

$$r_c = \left[0.75 P_{\max} r_p \left(\frac{1-q_p^2}{E_p} + \frac{1-q_t^2}{E_t}\right)\right]^{0.33}$$

With knowledge regarding the applied load and the overall contact area, the average surface force may be expressed as Equation 4-60.

Equation 4-60

$$P_{av} = \frac{P_{\max}}{\pi r_c^2} = \frac{2}{3}\left[\frac{40}{\pi^4} d_p \left(\frac{1}{\frac{1-q_p^2}{E_p} + \frac{1-q_t^2}{E_t}}\right)^4\right]^{0.2} U^{0.4} = cU^{0.4}$$

Accordingly, the average surface force is approximately equal to two thirds of the applied maximum surface force, occurring in the centre of the contact area. This relationship is shown in Figure 4-11 for the purely elastic impact described. As such, the largest load that can be supported by the target without inducing size reduction, through plastic deformation, is the elastic load limit *y*. The highest average surface force achievable during a purely elastic impact is then two thirds of the elastic load limit.

This relationship, of two thirds *y*, may be substituted into Equation 4-60, thus yielding the impact velocity at which the elastic load limit is just reached; Equation 4-61.

Equation 4-61

$$U_{el} = \left(\frac{2Y}{3c}\right)^{2.5} = \frac{\pi^2}{2\sqrt{10}} y^{2.5} \left(\frac{1}{d_p}\right)^{0.5} \left[\frac{1-q_p^2}{E_p} + \frac{1-q_t^2}{E_t}\right]^2$$

Once we have established the onset point of plastic deformation, we may now consider the occurrence of a plastic-elastic impact. This requires further assumptions, namely that the impacting particle is non-deformable, whilst the target material undergoes both plastic and elastic deformation. Secondly, no deformation hardening of the target material occurs, enabling the elastic load limit, and hence the impact velocity at which the elastic limit is just reached, to be constant.

The final assumption may initially appear invalid, however, through consideration it may be justified. The erosion modelling reported here is considered to be steady state, that is any incubation period has

long been exceeded. As such, the surface layers will already be compressed and work hardened. The subsequent removal of the top layer will expose the underlying layers which will have been previously work hardened. We know from Figure 4-2 that the maximum force at impact occurs at a depth of approximately half the radius of the projected contact area. Resultantly, the elastic load limit and the related impact velocity at which the elastic load limit is just reached, are relatively constant.

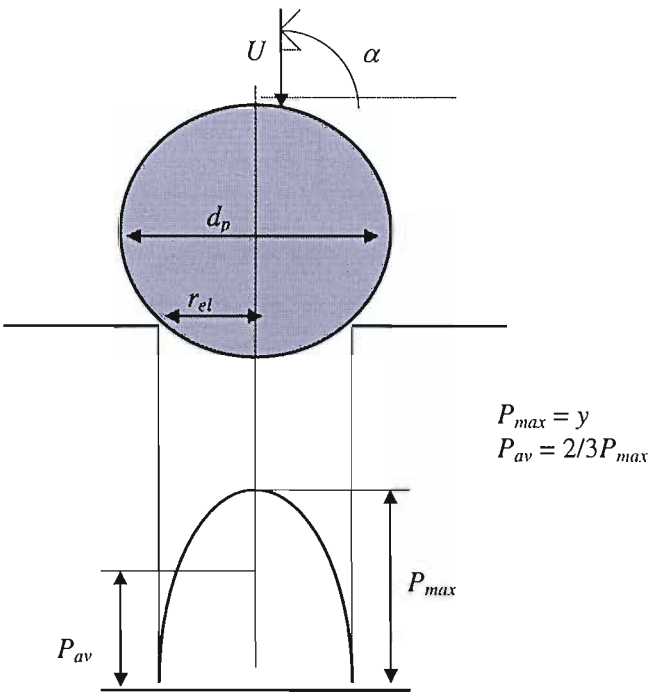

Figure 4-11 Pressure distribution at contact area; elastic impact.

When a particle strikes the target, elastic deformation occurs until the elastic load limit is reached in the centre of the contact area. The resulting decrease in distance between the centres of gravity of the two bodies due to this elastic deformation may be expressed as Equation 4-62. Here, one may once again employ the Hertizan equation, as the deformation under consideration is purely elastic.

Equation 4-62

$$h_{el} = \frac{\pi^2}{4} y^2 r_p \left[\frac{1 - q_p^2}{E_p} + \frac{1 - q_t^2}{E_t} \right]^2$$

From Equation 4-61 and Equation 4-62 it follows that;

Equation 4-63

$$r_p h_{el}^2 = \frac{15}{8} \frac{m_p}{\pi y} U_{el}^2$$

Once the elastic load limit has been reached, plastic deformation sets in at the centre of the contact area. Upon further penetration of the particle into the target, the dimensions of the area experiencing plastic deformation will increase. The assumption made at this instance is that the area of plastic deformation is small when compared with the cross sectional area of the impacting particle.

As the particle is assumed to be non-deformable, it is supposed that the area loaded to the elastic load limit has a radius of curvature which equals that of the particle. Similarly, the concavity remaining in the target post impact is supposed to be equal to that of the particle. Now, the total decrease in distance between the centres of gravity of the impacting bodies, undergoing plastic-elastic deformation, is given by Equation 4-64.

Equation 4-64 $$H_{pe} = H + h_{el}$$

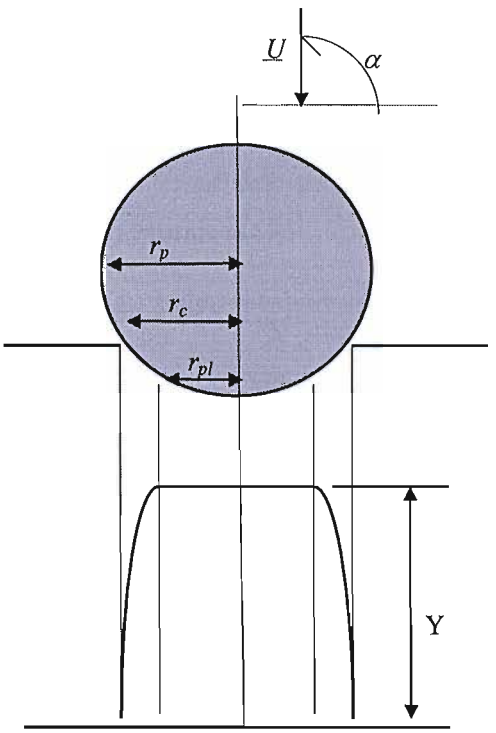

Figure 4-12 Pressure distribution at contact area; plastic-elastic impact

Just prior to the particle's retreat from the target, the edge of the concavity is just loaded to a force equal to the elastic load limit. Whilst outside the concavity, the particle touches the target, with the specified load decreasing from the elastic load limit at the edge of the concavity, to zero at the edge of the overall contact area; see Figure 4-12.

If we consider the projection of the total contact area to have a radius of r_c, Equation 4-65, then we must assume that H and h_{el} are small when compared to the diameter of the particle.

Equation 4-65 $$\pi r_c^2 = 2\pi r_p (H + h_{el})$$

Further, if the radius of the plastically deformed area is r_{pl}, then;

Equation 4-66 $$\pi r_{pl}^2 = 2\pi r_p H$$

Through Equation 4-65 and Equation 4-66 we may determine that area loaded plastically to equal Equation 4-67.

Equation 4-67 $$\pi t_c^2 - \pi t_{pl}^2 = 2\pi r_p (H + h_{el}) - 2\pi r_p H = 2\pi r_p h_{el} = \pi r_{el}^2$$

It follows that in the case of a plastic-elastic impact, that part of the contact area subjected to elastic deformation alone is independent of the size of the impact crater formed. Furthermore, this area is equal to the Hertizan contact area for a purely elastic impact when the elastic load limit is just reached. If we hold the assumption that the maximum area surface load is two thirds y, then the energy absorbed by the elastic deformation, Equation 4-68, may be determined, given Equation 4-61.

Equation 4-68 $$Q_{el} = \tfrac{1}{2} m_p U_{el}^2$$

Similarly, the potential energy of the elastic deformation in the area subjected to both plastic and elastic loading may be expressed by Equation 4-69.

Equation 4-69 $$Q_{pe} = \tfrac{1}{2} h_{el} y \pi r_{pl}^2$$

The total elastic deformation energy held within the target may then be shown to hold the form;

Equation 4-70 $$Q_{el} + Q_{pe} = \tfrac{1}{2} h_{el} y \pi r_{pl}^2 + \tfrac{1}{2} m_p U_{el}^2$$

Just prior to the particle retreat from the target, the maximum value of r_{pl} will have been reached, in addition to the elastic deformation energy stored in the target. Due to the accumulation of elastic reaction forces, the particle is rejected from the target, where we assume that the amount of energy supplied to the particle equals that stored. This elastic reaction results in the reflected particle velocity calculated by Equation 4-71.

Equation 4-71 $$\tfrac{1}{2} m_p u_{rf}^{\ 2} = \tfrac{1}{2} h_{el} y \pi r_{pl}^2 \max + \tfrac{1}{2} m_p U_{el}^2$$

For a permanent indentation to be formed at impact, the energy supplied must equal that given by Equation 4-72.

Equation 4-72 $$Q_{pl} = \int_0^{H_{\max}} \pi r_p^2 y dH \approx \pi r_p H_{\max}^2 y$$

Now that we posses knowledge regarding all three impact regimes; elastic, plastic-elastic and plastic, we may perform an energy balance on the particle impact.

Equation 4-73 $$\tfrac{1}{2} m_p U^2 = Q_{el} + Q_{pe} + Q_{pl} = Q_T$$

However, from Equation 4-63 and the knowledge that $r_p^2{}_{max}$ equals $2r_p H_{\max}$, we may express the plastic-elastic energy as Equation 4-74.

Equation 4-74

$$Q_{pe} = \tfrac{1}{2} h_{el} y \pi r_{pl\max}^2 = h_{el} y \pi r_p H_{\max} = \sqrt{\pi y r_p h_{el}^2} \sqrt{\pi y r_p H_{\max}^2} = \sqrt{\tfrac{15}{4} Q_{el} Q_{pl}}$$

As such the energy balance may now be expressed as;

Equation 4-75

$$Q_T = Q_{el} + \sqrt{\tfrac{15}{4} Q_{el} Q_{pl}} + Q_{pl} = \left[\sqrt{Q_{el}} + \sqrt{Q_{pl}}\right]^2 - 0.061\sqrt{Q_{el} Q_{pl}}$$

4.3.2.2 The Prediction of Volume Displacement within the Deformation Erosion Model

Now that an energy balance for the forces acting has been derived, we may proceed to predict the eroded volume at each particle impact event. Since Q_{el} is considered small in relation to Q_{pl}, we may re-arrange Q_T to yield the following relationship;

Equation 4-76

$$Q_{pl} \approx \left[\sqrt{Q_T} - \sqrt{Q_{el}}\right]^2 = \tfrac{1}{2} m_p \left[U - D_k\right]^2$$

Here, the velocity at which the elastic load limit is just reached, and the resulting elastic energy absorbed at impact, have been substituted for D_k. D_k is the deformation erosion factor, being an expression which characterises the physical properties of the target material and particle. Refer to Section 4.3.2.3 for discourse regarding D_k.

From Equation 4-76 we may observe that the energy transferred at impact is directly proportional to the mass of the particle and its velocity. The energy absorbed by the target may then be acted upon to quantify the degree of size reduction induced by the deformation erosion mechanisms.

To allow us to relate the energy absorption of the target material to the degree of erosion experienced, the deformation erosion factor E_f is introduced. This is simply a constant which forces the predicted erosion data to fit the desired curve through a semi-empirical correlation. The deformation erosion factor is a measure of the quantity of energy required to remove a unit volume of the target material by deformation erosion, thus yielding the relationship given by Equation 4-77.

Equation 4-77

$$W_d = \frac{m_p \left(U - D_k\right)^2}{2 E_f}$$

The impact angle influences the rate at which energy is absorbed by the target, hence the degree of erosion experienced. To account for this, we assume that the relationship regarding angle and erosion may be accurately described by *sin*. This is a valid assumption given the evidence presented in Chapter 2 and previously in this Chapter. The final form of the deformation erosion model, as presented by Bitter, is given by Equation 4-78.

Equation 4-78

$$W_d = \frac{m_p\left(U\sin\alpha - D_k\right)^2}{2E_f}$$

4.3.2.3 Discussion and Developments to the Bitter Deformation Erosion Model

The energy, as dictated by the deformation erosion factor, is partly expended in plastic deformation of the target and partly by actual material removal. In the instance of a metal, the majority of the impact energy is consumed in plastic deformation, with actual metal removal by deformation mechanisms being negligible. Clearly not all the energy attributed to plastic deformation is consumed in this manner, in addition to lattice distortion, energy is liberated as heat as a result of re-crystallisation. The degree of energy dissipated as heat is determined by the re-crystallisation temperature of the material, the heat conduction and the degree of deformation. These properties are assumed to be constant, hence the degree of energy supplied as heat is constant. Thus, the deformation erosion factor, E_f, will be constant at constant temperatures.

A brittle material cannot readily absorb impact energy through plastic deformation. This type of material may be considered as being either heterogeneous or homogenous. With a heterogeneous material, the cemented particles may be dislodged in their entirety from the substrate, due to the impact. See section 4.2. The erosion resistance of such a material is mainly determined by the strength of the substrate, not the cemented particles. Thus, the deformation erosion factor is dependent upon the modulus of elasticity and the bond strength of the conglomerate of cemented particles, approximately proportional to; y^2/E_t.

A similar analogy can be applied for pseudo-homogenous materials such as the carbon steel group (where the scale of erosion does not directly influence the individual phases), where once again $E_f \propto y^2/E_t$. Whilst cemented particles are not removed in this instance, the response of the material can be captured by the mean material properties.

The comparisons drawn above regarding proportionality's are only approximations. Due to localised material differences, such as grain size, it is beneficial if not essential to support the deformation erosion factor by experimentation.

The characteristic velocity, D_k, (Equation 4-79 and Equation 4-80) for deformation erosion denotes the erosion resistance of the target. Here, D_k, is simply the velocity at which the elastic load limit of the target material is just reached, being a reformulation of Equation 4-61. This allows the assumption to be made that the remaining impact energy is directly consumed by material destruction. The greater the tendency towards plastic deformation that an impacting particle induces, through poor erosion

resistance of the target, the greater the predicted erosion. A similar analogy to the characteristic velocity of cutting erosion can be drawn, the smaller the characteristic velocity, the quicker the target yield stress is exceeded, and hence the greater the erosive potential due to a tendency towards plastic deformation of the target.

Equation 4-79

$$D_k = \frac{\pi^2}{2\sqrt{10}}(1.59Y)^{2.5}\left(\frac{R_f}{\rho_t}\right)^{0.5}\left[\frac{1-q_p{}^2}{E_p}+\frac{1-q_t{}^2}{E_t}\right]^2$$

Equation 4-80

$$D_k = \sqrt{2\pi}(TRS)^{2.4}\left(\frac{R_f}{\rho_t}\right)^{0.5}\left[\frac{1-q_p{}^2}{E_p}+\frac{1-q_t{}^2}{E_t}\right]^2$$

As with the cutting erosion characteristic velocity, D_k has been adapted such that the Transverse Rupture Stress of tungsten carbide can be used as an alternative to the yield stress. Hence, Equation 4-80 is that form used for erosion predictions using tungsten carbide.

Equation 4-78 is valid if, $U\sin\alpha \geq D_k$. If, $U\sin\alpha \leq D_k$, then no deformation erosion will occur as the collision is purely elastic.

Bitter suggested that the sharpness of a particle could be included by the use of an apparent density in the characteristic velocity, D_k. The addition of an apparent density results in a reduced value for D_k, increasing the tendency towards plastic deformation. Further to the work of Bitter, which is somewhat ambiguous, the present author modified D_k, to include a roundness factor, R_f, for the particle, Equation 4-79 and Equation 4-80. This does away with the need for empirically derived apparent densities, where the roundness factor directly manipulates the target density. The value of the roundness factor is the same as that found in the cutting erosion model; $R_f = 1$, denotes a spherical particle, whist $R_f \sim 0.3$, denotes an angular particle.

4.3.3 The General Form of the Erosion Model Utilised

In Figure 4-4 and Figure 4-5, W_t denotes the total erosion as measured experimentally. W_c represents the predicted erosion contribution provided by the cutting model, whilst W_d denotes the predicted erosion contribution due to a deformation model.

The total erosion is then predicted from the summation of the two contributions, simply;

Equation 4-81

$$W_t = W_c + W_d$$

Thus, the parallel erosion model technique can be used to investigate a wide range of applications, given that well-known material constants, such as yield stress and the transverse rupture stress, are known for individual target materials.

4.4 Concluding Comments on the Erosion Model

The cutting erosion model utilises the particle trajectory approach of solving the equations of motion, whilst the deformation erosion model is forced to employ an energy balance approach. Whilst such a combination of approaches enables a solution to be achieved, assumptions are required to facilitate such a solution. These assumptions encompass themselves in the form of empirical erosion constants that force the solution to hold the correct numerical size and form; these empirical constant are n and E_f of the cutting and deformation model respectfully. This observation simply reinforces that made previous in the literature review; section 2.3.2.

The limitation of the need for empirical constants is two-fold. Firstly, the selection of an appropriate value is at best tentative, requiring support through experimentation. Secondly, the constants must be universal, having applicability over a wide range of impact regimes. The diversity in impact regimes experienced may be broadly summarised as impact angles of 0 to 90° and impact velocities of 1 to 100 m/s. The associated energy levels of such a wide impact range is clearly very extensive, placing much demand on the value of the constants selected.

However, at present such model dependency upon empirical constants represents best practice, thus highlighting the need for further work in this area of study. Unfortunately, such an intensive study is beyond the scope of the present study. Whilst the accuracy of the erosion models have not been tackled, this topic has been covered in detail by Chapter 8, along with the key influences on the erosion process.

5. Computational Fluid Dynamics (CFD)

5.1 Introduction

Computational Fluid Dynamics (CFD) is the analysis of process systems that involve fluid flow, heat transfer and other associated phenomena such as particle trajectory calculation, chemical reaction, combustion and spray drying. Solutions regarding the above process are made by computer based simulation, involving many millions of calculations. The technique is very powerful and spans a wide range of industrial applications.

The technique offers substantial time and cost savings over conventional experimental techniques, allowing an insight into a process system which would have previously been experimentally impossible or difficult. The initial cost of an operating system can be high, however, the system is extremely versatile, having the capacity to investigate a multitude of applications if implemented correctly.

The following Chapter is broadly broken down into two distinct areas. The first area, spanning Sections 5.1.1 to 5.2, gives a general overview of the CFD modelling process. The overview provides details regarding the principal elements common to all commercial CFD codes and a discussion of how CFX-F3D, the CFD code utilised in this study, is operated. A discussion is also held on the usage of CFD, including the difficulties experienced with any code. This theme of difficulties experienced and assumption required within the modelling process is upheld throughout the entire Chapter.

The second area has a higher level of technical content. The second area focuses on developing an understanding of turbulence and the subsequent modelling of that turbulence process. Much emphasis is placed upon the importance of the turbulence closure system which is required to close the necessary transport equations, thus providing the time-averaged mean flow features of the turbulent flow field. That flow experienced within the complex and energetic system of the control choke is highly turbulent. As such, the turbulence closure model plays a vital role in the entire modelling process, hence the importance placed upon this subject area. An explanation of the incorporated turbulence closure models of CFX-F3D is given, discussing in detail the structure and assumptions of each of the closure models. The Chapter closes with comments on the relative performance of each of the closure models, with recommendations being drawn as to which model is most appropriate to the task of modelling the highly turbulent flow field of the control choke system.

5.1.1 The use of a *CFD* Code

The heart of a *CFD* code is the numerical algorithm that provides solutions regarding fluid flow problems. To provide access to this complex numerical algorithm, user interfaces are included in all

commercial packages. These interfaces allow the problem to be initially defined, then allow the numerical results to be displayed in a readily understood graphical manner. As such there are three key stages to all *CFD* codes, being the pre-processor, the solver and the post-processor.

5.1.2 The Pre-Processor

The pre-processor allows the user to specify the extent of the computational domain and then perform the subsequent transformation of this information into a form usable by the solver. The activities undertaken at the pre-processing stage include;

- definition of the dimensions of the computational domain.
- grid generation by the division of the domain into a number of sub-domains.
- selection and definition of physical and chemical processes to be investigated.
- definition of physical properties.
- specification of conditions at the boundaries of the computational domain.

Substantial time and effort is consumed in the specification of the problem, with figures quoted in the region of 50% of the total time spent on *CFD*. In order to partially alleviate this situation, interfaces with CAD packages are now available.

The solution to the flow problem is defined at the central node within each cell or control volume. It follows that the larger the number of control volumes, hence nodes, the greater the accuracy of the resulting prediction. However, computational expense is also coupled to the number of control volumes, as such one must arrive at a compromise between the accuracy of results and the time to produce them. The optimal grid is normally non-uniform, as such there are facilities within most *CFD* packages to define such non-uniform grids. This allows finer grid spacing to be set to areas which experience large variations from point to point.

Effort is currently underway to incorporate into the commercial *CFD* codes a self-adaptive meshing capacity, allowing a coupling between the pre-processor and the solver. Here, grid refinements in areas of rapid variation became automatic, reducing the skill requirements of the user to specify a suitable grid. However, such techniques are very demanding computationally, with substantial work still required in the area to produce a form which is sufficiently robust for inclusion in a commercial code. Thus, at present the optimisation of the grid still remains a user skill which can only be acquired through experience, being a suitable compromise between refinement, computational accuracy and expense.

5.1.2.1 Grid Generation within CFX-F3D: CFX-MESHBUILD

A number of grid generation facilities are available to the user of CFX-F3D. However, the more advanced grid generation facilities have a cost which is not acceptable to a academic institution. Such

is an unfortunate circumstance, as it is these advanced packages that are most applicable to the complex geometries experienced within this study. The default grid generation facility of CFX-F3D is a package known as CFX-MESHBUILD. Whilst this package is adequate for simple to moderate complexity geometries, its usage is limited for the generation of complex control choke geometries.

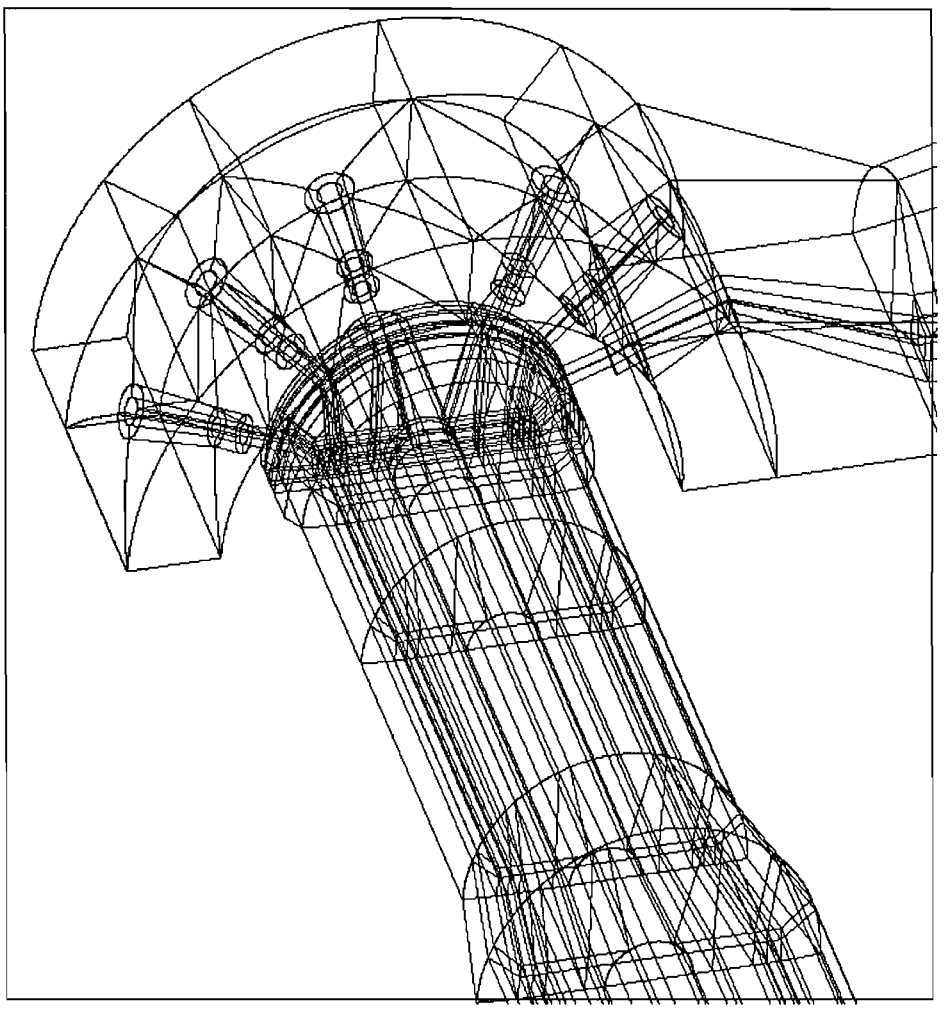

Figure 5-1 Blocking Strategy utilised for Complex Geometry - Plug and Cage Control Choke

The limitation stems from the manner in which the physical co-ordinates of the flow domain are specified, where a hierarchy of geometry features must be utilised. A minimum two 'points' specify the position of 'curves', a curve is then employed to specify an 'edge'. Four edges specify the co-ordinates of a 'face'. Six faces are then required to declare a 'block'. It is within a block that the body fitted finite volume grid can be generated. The block shapes do not have to be uniform, being distorted through a number of techniques, thus providing the best fit for the desired geometric shape.

CFX-MESHBUILD is a multi-block grid generator. This implies that a number of blocks may be joined together to form the overall shape of the flow domain. Herein lies a further complication. The

faces of each block must be consistent with the faces of all the surrounding blocks. That is, neighbouring faces must be of exact dimensions; else the grid cannot be correctly propagated between blocks. As such, careful consideration must be given to the 'blocking strategy' employed for each individual flow domain. Consideration must be given to all blocks in the geometry, and the implications of that block on the surrounding blocks.

The difficulty of this approach lies in areas where extremes of dimensions are experienced; simply, where a small block must be joined to a large block. Under such a circumstance, virtual internal blocks must be set within the larger block, increasing both the number of blocks required and the complexity of the problem. Figure 5-1 details this effect, where the complexity of the geometry may be observed. In the instance of the Plug and Cage control choke shown, the key elements within the geometry were the six ports that penetrate through the cage; the reader is referred to Chapter 3 for greater detail regarding this design type. The six port blocks were built first, with the remainder of the geometry being 'hang' from these blocks. One may observe that these blocks extend from the centre line of the geometry to the outer radius, with inter-connecting blocks form the flow domain. The statistics for the geometry shown are detailed in table 5-1.

Geometric Feature	Total Number
Points	2408
Curves	512
Edges	2272
Faces	1936
Blocks	547
Inter-Block Boundaries	1348
Patches	588
Boundary Nodes	116946
Grid Cells	274056

Table 5-1 Numerical Summary of Geometric Features within a Complex Problem

An appreciation of the difficulty in developing a suitable blocking strategy may be gained from the summary of geometric features, Table 5-1. A total of 547 blocks were defined, which involved the consideration of 1348 inter-block boundaries or joins between blocks. The time to generate such a complex geometry was considerable, running into weeks. A further difficulty of such a complex geometry was the possibility of errors; such errors would include the failure to correctly define an inter-block boundary. Such a failure would cause a 'wall' to appear in mid-flow. These errors would not normally manifest themselves until the flow field has been solved; the solution time for the geometry shown was approximately 150 hours, or 7 days. As such, the time to 'de-bug' such a complex geometry was of the order of 4 weeks, requiring several iterations of the solve/correct cycle. These facts, combined with the initial time to generate the flow domain, underlines the need to improve the front end or pre-processing facility.

Once the blocking strategy has been implemented, the boundary constraints of the flow domain must also be set. These constraints are set through the application of patches. Such patches provide information regarding the surface type, inlet & mass flow boundaries, pressure boundaries and symmetry planes. This combination of patches allows the user to fully define all of the necessary boundary constraints of the problem. For the example shown in figure 5-1, a total of 588 patches were set manually; including inlets/outlets, symmetry planes and the specification of wall patches to dictate the material type of the surface. See Chapter 7.

Once this patch information has been declared, the computational grid may then be generated, see Figure 7-2 for an example of a computational grid. From figure 5-1 and the supporting figure 7-2, one may appreciate the effort required in generating a suitable computational grid. The difficulty lies in creating a grid which is sufficiently accurate to resolve the key features of the flow field, whilst remaining numerically acceptable in terms of solution time. This balance can be achieved by specifying the sub-division of individual edges within the flow domain and the grid type along those edges. A further complication is the degree of distortion induced into the blocks to achieve the overall shape of the flow domain. If this distortion is excessive, it is possible for the volume of control cells fitted to the block to be zero, or in extreme cases negative. A solution cannot be reached under such circumstances, and the blocking strategy must be revised. Such a revision would be the inclusion of additional blocks to minimise the degree of distortion within individual blocks. Figure 5-3 provides a summary of the grid generation process. No further discussion of this generation process will be given here, the interested reader is referred to the CFX user guide.

CFX-MESHBUILD writes a log file and a geometry file once the geometry and grid have been generated. The log file contains information regarding physical co-ordinates of the problem, such as the points location and the subsequent blocking arrangement. The geometry file holds the details of the computational grid generated and the boundary constraints. The geometry file is that read by the solver of CFX, providing the relevant information to construct a solution.

5.1.2.2 Specifying the Fluid System within CFX-F3D: CFX-SETUP

Once the computational grid has been generated, the user must also define the fluid system to be solved. Through the application of CFX-SETUP, a command file is created, instructing the solver of CFX-F3D the solution procedure to follow. Figure 5-3 details the basic structure of the command file, whilst Appendix F provides an example of the command file employed by CFX-F3D. It is noteworthy that many combinations of the command file exist. That example present here is just one variation, which is most applicable to this study. Refer to the CFX user manual for further details.

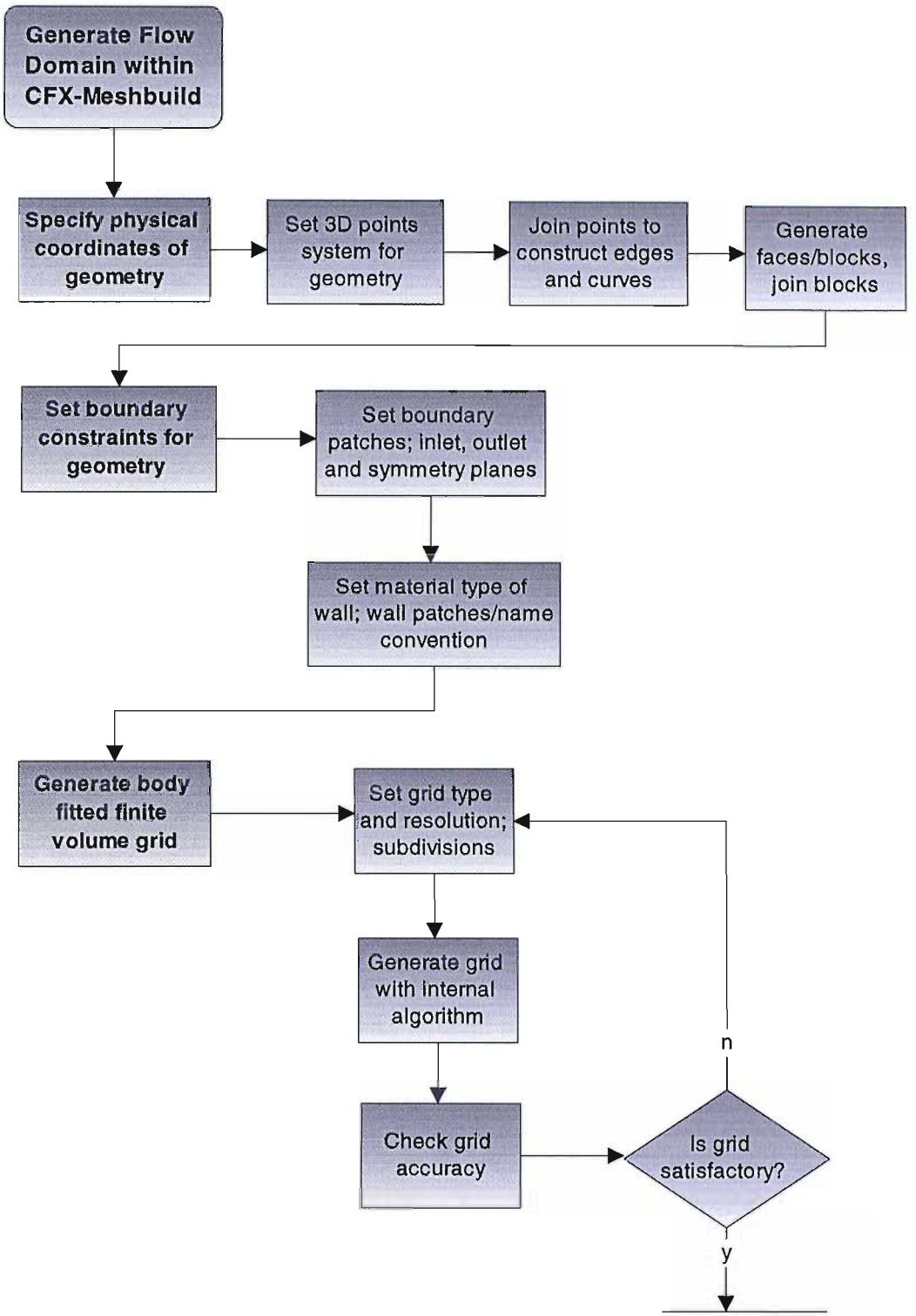

Figure 5-2 Generation Summary of Computational Grids within CFX-MESHBUILD

The left column of the flow chart displays those principal functions which are common to all variations of the command file; whilst the remaining two columns detail various option available under each of these principal functions.

The physical size of the problem is set under the SET LIMITS menu. Here, one must declare the computational requirements of the calculation; including such details as the maximum number of blocks and patches. The OPTION menu allows the user to detail the fluid system to be solved, including whether the flow should be treated as laminar or turbulent, the compressibility of the fluid and whether one is solving for suspended particles. Refer to Chapter 7 for greater details regarding particle trajectories.

The VARIABLE NAMES provides facility to specify additional variables to be solved. This is of great importance with regards to generating computational space within which data manipulation and surface plotting of erosion data can be undertaken; see Section 7.6. MODEL TOPOLOGY sets information regarding the blocking arrangement utilised, including the dependency of each block on the surrounding blocks. By default this is read from the geometry file created with CFX-MESHBUILD. MODEL DATA allows the restart facility to be utilised. This is of importance with regards to erosion modelling, allowing the accumulation of several computational runs to be achieved. The physical properties of the fluid are set by either selecting a standard fluid held within CFX, or one may discretely defined the physical properties of the fluid; including such details as the density, viscosity and molar weight.

The turbulence parameters are also set under the MODEL DATA menu. The facility allows the turbulence closure model to be specified. Furthermore, complex turbulence interactions may be detailed, such as manipulation of the log constant for the wall function. The particle transport model is defined under this option menu, allowing the solution strategy, including the integration parameters, to be detailed. Facility is also provided to detail additional forces acting on the particle momentum balance. The physical properties of the particle, such as density, are also set in this menu.

The SOLVER DATA menu dictates how the transport equations of the flow field are tackled. The menu includes such features as convergence testing criterion, the equation solver to be utilised and solution aids to overcome divergence difficulties in highly turbulence and complex flow fields. Such solution aids include deferred correction, under relaxation and false timesteps.

The CREATE GRID command specifies the source of the computational grid. The default setting is to read the geometry file created within CFX-MESHBUILD. MODEL BOUNDARY CONDITIONS is the final principal command.

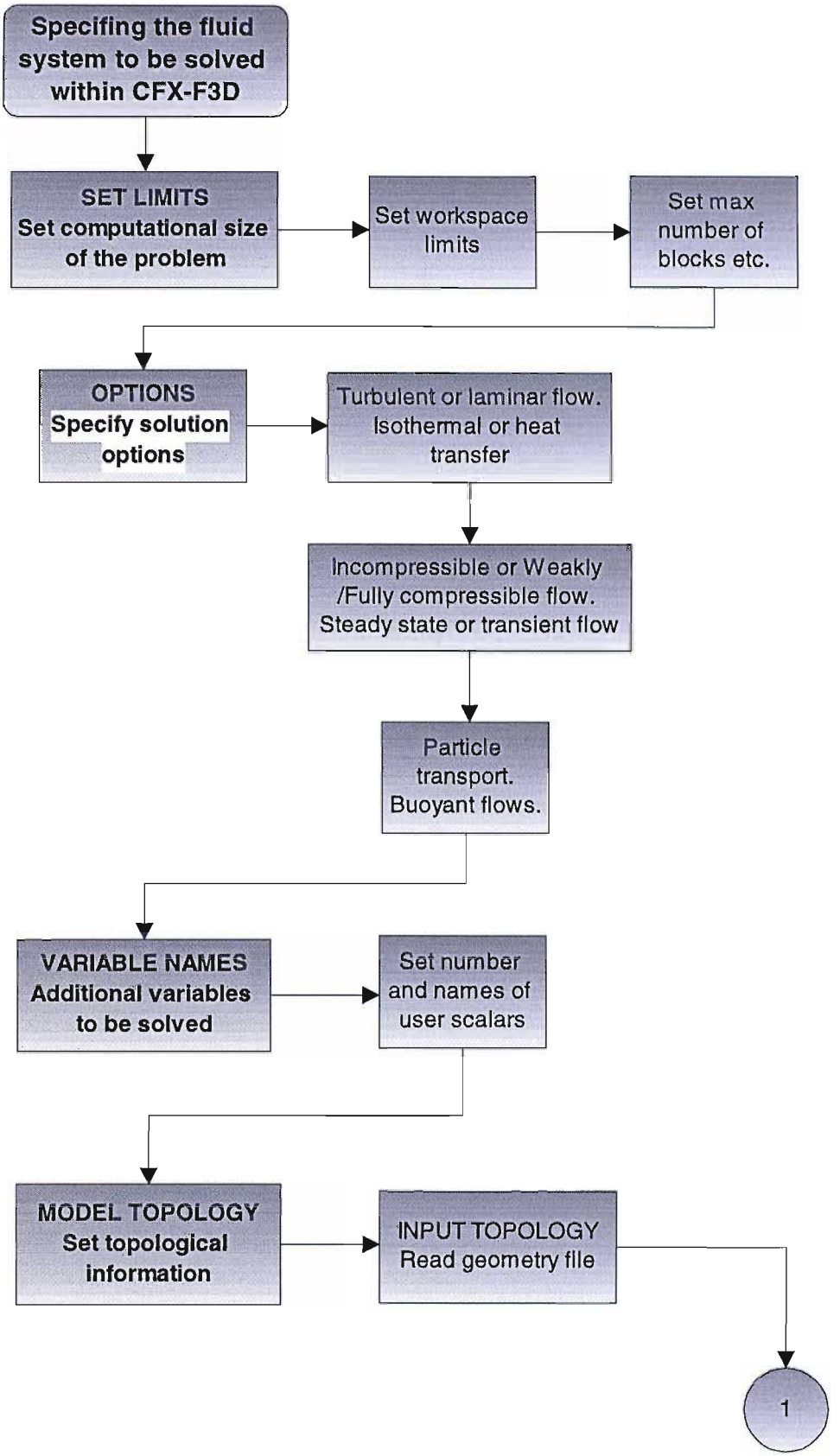
Specifing the fluid system to be solved within CFX-F3D
SET LIMITS Set computational size of the problem
Set workspace limits
Set max number of blocks etc.
OPTIONS Specify solution options
Turbulent or laminar flow. Isothermal or heat transfer
Incompressible or Weakly /Fully compressible flow. Steady state or transient flow
Particle transport. Buoyant flows.
VARIABLE NAMES Additional variables to be solved
Set number and names of user scalars
MODEL TOPOLOGY Set topological information
INPUT TOPOLOGY Read geometry file
1

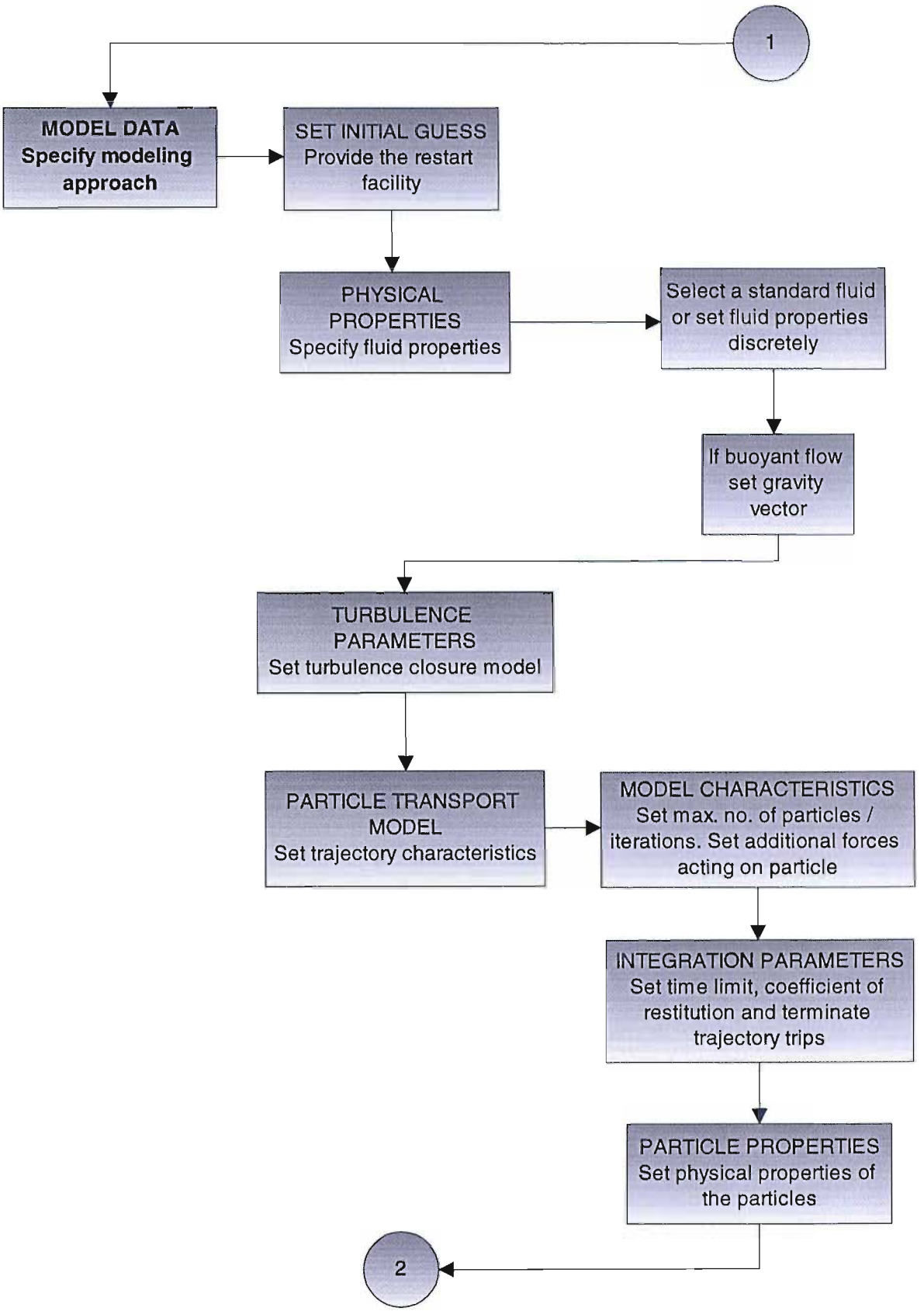
1
MODEL DATA
Specify modeling approach
SET INITIAL GUESS
Provide the restart facility
PHYSICAL PROPERTIES
Specify fluid properties
Select a standard fluid or set fluid properties discretely
If buoyant flow set gravity vector
TURBULENCE PARAMETERS
Set turbulence closure model
PARTICLE TRANSPORT MODEL
Set trajectory characteristics
MODEL CHARACTERISTICS
Set max. no. of particles / iterations. Set additional forces acting on particle
INTEGRATION PARAMETERS
Set time limit, coefficient of restitution and terminate trajectory trips
PARTICLE PROPERTIES
Set physical properties of the particles
2

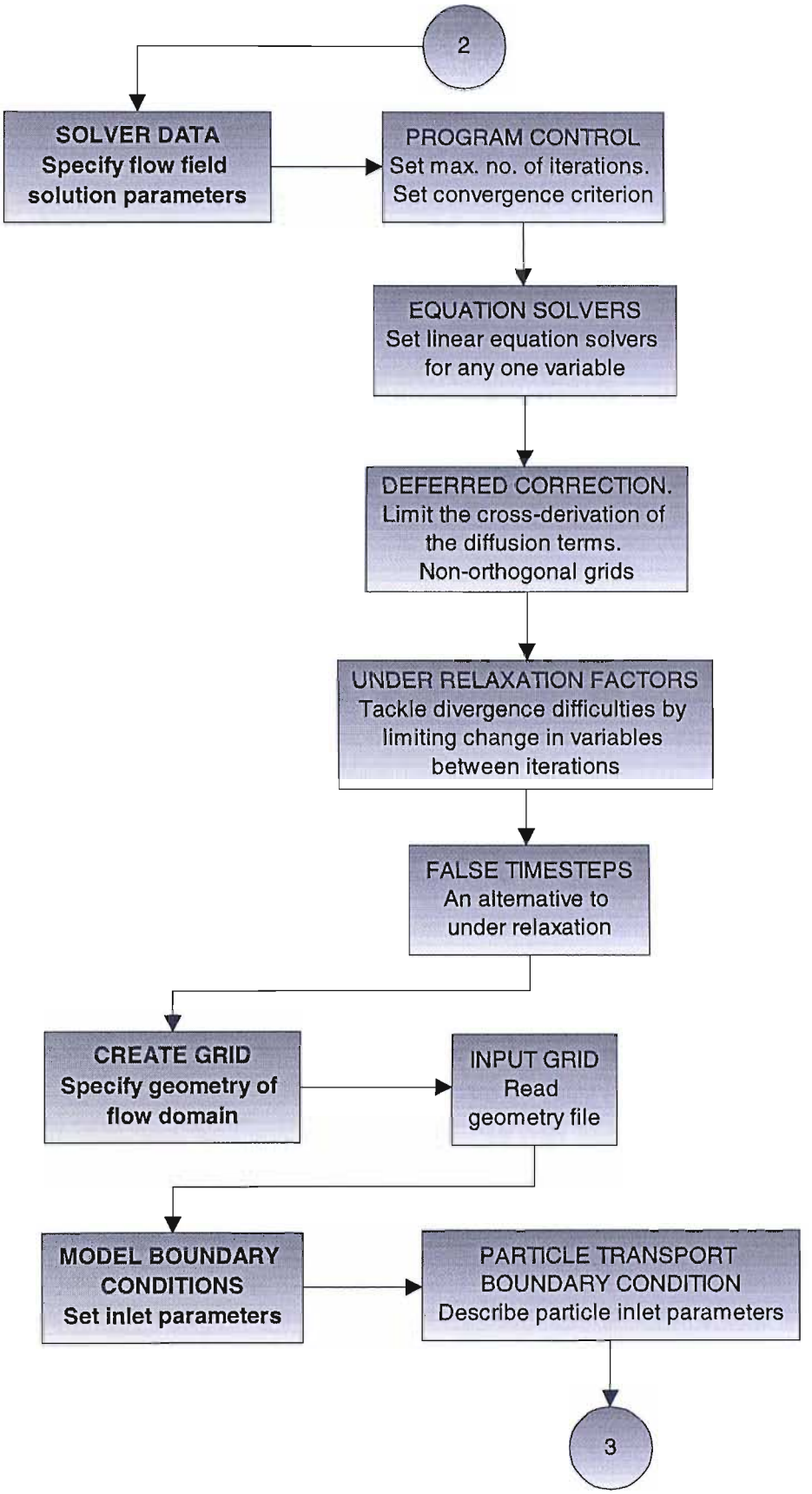
2
SOLVER DATA
Specify flow field solution parameters
PROGRAM CONTROL
Set max. no. of iterations.
Set convergence criterion
EQUATION SOLVERS
Set linear equation solvers for any one variable
DEFERRED CORRECTION.
Limit the cross-derivation of the diffusion terms.
Non-orthogonal grids
UNDER RELAXATION FACTORS
Tackle divergence difficulties by limiting change in variables between iterations
FALSE TIMESTEPS
An alternative to under relaxation
CREATE GRID
Specify geometry of flow domain
INPUT GRID
Read geometry file
MODEL BOUNDARY CONDITIONS
Set inlet parameters
PARTICLE TRANSPORT BOUNDARY CONDITION
Describe particle inlet parameters
3

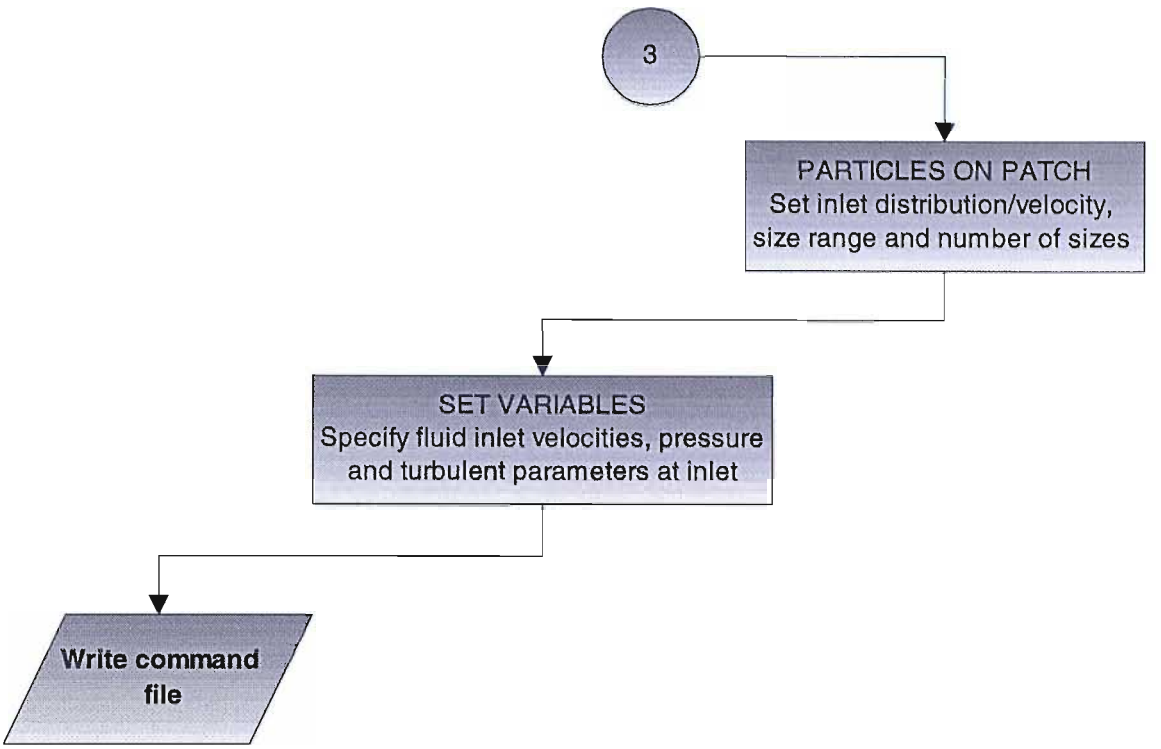

Figure 5-3 A Summary of the Generation of the Command File within CFX-SETUP

The menu allows the physical boundary set within CFX-MESHBUILD to be set numerically, including the fluid pressure and velocity at inlet. Further, the particle properties at inlet are declared, including the particle size distribution and number of particle sizes, and the particle velocity and mass flux at inlet. The particle distribution profile at inlet is also defined, commonly one sets a particle trajectory calculation to be initiated at each cell centre on the inlet patch.

5.1.3 The Post-Processor of CFX-F3D

Within CFX, the post-processor utilised is CFX-VIEW, being essentially a data visualisation tool. The post-processor reads the output files produced by CFX-F3D, including the particle trajectory file and the dump file. The dump file contains all the point solutions for the computational grid, allowing both graphical portrays of the data produced and the ability to re-start the solution.

CFX-VIEW allows the contents of both the dump file and the particle trajectory file to be manipulated, providing a number of graphical representations of the solution data produced by the solver. Possible representations of the data include;

- computational domain and grid display.
- vector plots for all fluid variables.
- contour and shaded contour plots for all fluid variables.
- surface plots of all fluid variables and particle impact/erosion variables.

- particle trajectories, including particle size and speed.
- particle volume fractions.
- view manipulation and screen dump facilities to produce hard copies.
- production of line graph data.

5.1.4 The Solver of Commercial CFD Codes

The solver, as the name suggests, does the work of a CFD code. It's task is to provide solutions to the numerous transport equations, resolving the flow field given the flow domain and boundary conditions specified within the pre-processing stage. The numerical methods undertaken to achieve this task include;

1. make approximations as to the values of the unknown flow variables.
2. substitution of the approximate values for the unknowns into the governing equations, followed by mathematical manipulation to produce algebraic equations. This process is known as discretisation.
3. the solution, by an iterative method such as Gauss-Seidel, of the algebraic equations.

Three main solution methods have been developed for the solver. The main differences between the methods is how the flow variables are initially approximated and the techniques utilised in generating the algebraic equations, i.e. discretisation. The methods fall under three headings; finite difference or volume, finite element and spectral methods. Here we shall not concern ourselves with the finite element and spectral methods as these are not common. The main stay of all commercial *CFD* codes is the finite volume method. This solution method is utilised by CFX-F3D, FLUENT, PHOENICS and STAR-CD. It is through step one that the finite volume method differs. Here the governing equation of the fluid flow are formally integrated over all of the finite control volumes within the domain. This formal integration allows conservation of the relevant properties for each of the finite control volumes. This conservation of a general flow variable ϕ can be expressed in words as a balance between the various processes tending to increase or decrease the variable.

Rate of change of ϕ in the control volume w.r.t time	=	Net flux of ϕ due to convection into the control volume	+	Net flux of ϕ due to diffusion into the control volume	+	Net rate of creation or destruction of ϕ inside the control volume

It is this clear relationship regarding conservation that forms the major attraction of the finite volume method, making it readily understood by the user.

Discretisation techniques with *CFD* codes treat the key transport phenomena; including, convection (transport due to fluid flow), diffusion (transport due to point to point variables), source terms (associated with the creation or destruction of a variable) and the rate of change of that variable with respect to time. The underlying physical phenomena are non-linear and complex, as such an iterative solution method is required.

5.2 Comments on Problem Solving with a Commercial CFD Code

As we know, CFD provides a huge potential in terms of product design, development and a detailed understanding of the flow characteristics that the device displays; allowing substantial cost and time savings to be realised. However, the techniques developed are complex, requiring a good understanding of the underlying physical assumptions made within the code. At best the code is only as good as the physical assumptions embedded within it, as such the assumptions must be correctly utilised to their full potential. If this is not the case, then the numerical accuracy of the package reduces to the skill of the operator and not the embedded physics. Thus, the user must be skilled in all areas of CFD modelling, including the operation of the pre-processing, solution generation and post-processing. Each area requires a differing set of skills, which, if not implemented correctly, can generate inaccuracies within the final solution.

Firstly, the problem must be identified, formulated and set up correctly with a grid which is sufficiently refined to capture the main flow details. Unfortunately, even the simplest of flow problems needs simplification to produce a problem of 'manageable' size. Thus, it is essential that the key features of the flow be identified and implemented carefully. The loss of salient flow features due to poor problem identification has to be avoided to ensure the problem is not reduced, hence the user needs a good understanding of the basis flow phenomena.

Secondly, a good understanding of the numerical solution algorithms is also crucial. Three basic mathematical techniques are available to aid us, these include; convergence, consistency and stability. Convergence is the property of a numerical method which allows the solution to approach the exact solution as the grid spacing, or size of the control volumes, reduces towards zero. A good indication of the grid's efficiency is whether the residuals of the mean flow properties are reduced upon successive numerical iterations. If no convergence or residual reduction is observed, then one may assume that the numerical algorithm and grid combination are inadequate and computational errors will be present.

Consistency is the numerical scheme's ability to produce a set of algebraic equations which can be shown to be equivalent to the original governing equations, ensuring repeatability to the solution. Finally, stability is the numerical robustness of the numerical scheme and its ability to damp out errors as the numerical method proceeds. If the solution scheme is inherently unstable, even round-off errors in

the initial data will cause wild oscillations or divergence. Thus, through the application of such techniques the numerical progress of the solution can be monitored and conclusions drawn as to the accuracy of any solutions reached. Modifications to the solution scheme can be made if errors are suspected.

As mentioned, there are two aspects which are normally used to characterise whether a successful simulation has been reached, being the convergence of the iterative process and the grid independence. The solution algorithm is iterative, and in a converged solution the residuals, or a measure of the overall conservation of the flow properties, are very small. This progress towards a converged solution can be greatly assisted by providing a suitably refined grid and by careful selection of the settings of various under-relaxation factors and solution acceleration devices. There are no straightforward guidelines for the selection of such settings as they are problem dependent. Optimisation of the solution speed can only be achieved through extensive use of the code itself, hence the experience of the operator.

There is no formal way of estimating the errors induced by an inadequately resolved grid. Good initial grid design relies largely on an insight into the expected flow field. A background in the fluid dynamics of the problem is invaluable and experience with the griding of similar problems helps. The only way to eliminate grid errors is to perform a grid dependence study. Here a coarse grid is successively refined until certain key results undergo no further change. The grid is then said to be independent. However, such an independency study is normally extremely costly in terms of computational effort, being exasperated by the increasing complexity of the problem. As such, the user is normally limited to specifying a grid resolution which is as refined as the available hardware will permit.

Finally, every numerical algorithm has its own characteristic error pattern, euphemisms for such errors include, numerical diffusion, false diffusion and numerical flow. The likely error pattern and its effect on the simulation can only be guessed at through a thorough understanding of the individual algorithm.

At the end of a simulation the user must judge whether the results are 'good enough' for his or her requirements. Such a judgement can only be gained through a good interpretation of the numerical results produced by the solver. Thus, it is essential that a structured approach is used in the assessment of the solution reached. A CFD code is an extremely complex piece of software, as such a methodical approach must be utilised, else the exercise is belittled through user deficiencies. It is impossible to assess the validity of the physical models embedded with the CFD code or even the accuracy of final results by any other means than comparison with experimental work. However, this validation in itself requires highly detailed flow information regarding the turbulent effects within the flow field. This can only be achieved through techniques such as laser Doppler anemometry and is not undertaken lightly.

The normal approach utilised by users if a comparison of bulk flow feature, such as the extension of a backflow region within the flow domain.

5.3 Turbulence and its Modelling; The Closure Model

All flows of engineering interest become unstable above a certain Reynolds number. At low Reynolds numbers flows are laminar and uniform, at higher Reynolds numbers the flow regime becomes turbulent, developing a chaotic and random state of motion where the local velocities and associated variables fluctuate continuously with time.

Flows in the laminar region are completely described by the instantaneous continuity and Navier-Stokes equations. However, due to the appearance of fluctuations associated with turbulence the continuity and Navier-Stokes equations need to be time-averaged. With turbulent flows at high Reynolds numbers, a wide range of length scales are observed for the turbulent eddies. The turbulent flow may contain eddies of sizes down to 10-100 microns in length, appearing at frequencies of up to 10 kHz [**Ref. 53**]. One can appreciate the number of eddies operating within any one computational domain and the computing power required to directly simulate each of these eddies. Speziale [**Ref. 84**] hypothesised that if direct simulation of turbulent pipe flow, Reynolds number 500,000, were to be undertaken in an acceptable time scale, the current generation of CRAY computers would need to be 10 million times faster.

Thus one can see that the computational requirements for the direct simulation of the instantaneous Navier-Stokes equations for fully turbulent flow are truly phenomenal. At present computer hardware is totally inadequate, thus we are forced to solve the time-averaged Navier-Stokes equations. Such an approach avoids the need to predict the effect of each and every eddy within the flow. Fortunately, the requirements of the 'everyday' user are normally satisfied by the time averaged properties of the flow; i.e. mean velocity.

5.3.1 Developing the Reynolds Equations and their Solution

We can now develop the Reynolds equation for predicting the mean flow properties and examine the effects of turbulence on the mean flow and its solution. If we consider a flow property, 'Φ', we can describe its mean-time average through Equation 5-1 [**Ref. 19**].

Equation 5-1

$$\Phi = \frac{1}{\Delta t}\int_{0}^{\Delta t} \varphi(t)\,dt$$

Ideally, the limit on the time interval should tend towards infinity, however, satisfactory results for the steady mean flow can normally be achieved if the time interval is greater then the frequency of the largest eddies of common turbulent flow field, i.e. 1-10 Hz [**Ref. 53**].

The flow property is time dependent, thus we can utilise Reynolds decomposition to introduce the mean properties in the flow equations; Equation 5-2 [**Ref. 19**]. Here the property equals the sum of the steady mean component and a time-varying fluctuating component with a zero mean value, i.e.

Equation 5-2 $$\Phi = \overline{\Phi} + \Phi'$$

The kinetic energy, k, per unit mass associated with the turbulence is defined by the Equation 5-3 [**Ref. 77**], where the velocity components are the means;

Equation 5-3 $$k = \frac{1}{2}(\overline{u'^2} + \overline{v'^2} + \overline{w'^2})$$

The turbulence intensity, T_i, is a function of the kinetic energy of turbulence and a reference mean velocity;

Equation 5-4 $$Ti = \frac{(\frac{2}{3}k)^{0.5}}{Uref}$$

As an aid to the understanding of the influence of the turbulent fluctuations on the mean flow we must first consider the instantaneous Navier-Stokes and Continuity equations. Refer to Appendix G for a description of the Navier-Stokes and Continuity equations in terms of an incompressible viscous flow [**Ref. 77**].

5.3.2 The Closure Problem of Turbulence

The instantaneous continuity, Equation G-1 and Navier-Stokes equations, Equation G-2 to Equation G-4, form a set of equations which is closed, as such the four unknowns, u, v, w and p can be solved directly. However, the computational requirements to undertake such a procedure for turbulent flows are truly phenomenal, being completely beyond any computer hardware at present and the foreseeable future.

To overcome such excessive computational requirements, time-averaging is undertaken to provide the mean flow properties. The time-averaging process on the momentum equations effectively removes all details concerning the state of the flow contained in the instantaneous fluctuations. However, as a result of the time-averaging process we introduce six additional unknowns in the time-averaged momentum equations, known as the Reynolds stresses. Similarly, additional terms also appear in the time-averaged scalar transport equations. As such the time-averaged momentum transport equations and scalar transport equations cannot now be solved directly, even though the computational demands are now manageable.

Thus, there is a need to develop a turbulence closure model which will close the set of equations as with the instantaneous case. It is the task of the turbulence closure model to provide a computational procedures of sufficient accuracy and generality to predict the Reynolds stress and the scalar transport terms, thus providing a closed equation set.

A variety of closure models have been proposed in the literature, however, only a limited number are implemented in commercial codes due to queries regarding generality and robustness. Section 5.4 details the closure models commonly used.

5.4 The Turbulence Closure Models

A turbulence closure model is a computational procedure devised to close the system of equations developed to describe the mean flow; Equation J-18 to Equation J-22. In particular, we always need expressions for the Reynolds stresses (Equation J-19 to Equation J-21) and the turbulent scalar transport terms; Equation J-22. Of the closure models developed, each must have wide applicability, be accurate, simple and economical to operate. Those commonly used include;

1. Classical models based on the time-averaged Reynolds equations.
    a. zero equation model - mixing length model.
    b. two equation model - *k*-Epsilon model.
    c. Reynolds stress model.
    d. algebraic stress model.
2. Large eddy simulation based on space filtered equations.

The classical models are based on the time-averaged Reynolds equations as presented in Section 5.3.1. Large Eddy Simulations (*LES*) are models where the time-dependent equations are solved for the mean flow and the largest eddies. The smallest eddies are not directly simulated, being time-averaged to provide the mean as with the classical approach. The argument for this approach is that it is only the largest eddies that strongly interact with the mean flow, containing the majority of the turbulent energy. Furthermore, the computational requirements to directly simulate all of the turbulent eddies is excessive. However, the computational requirements to simulate only the largest eddies in addition to the mean flow is still very high. *LES* is confined to research laboratories, being too costly to merit inclusion in commercial *CFD* codes. Substantial improvements in computer hardware may reverse this situation, however this will not be consideration further. The interest reader, is referred to Abbott and Basco [**Ref. 2**], where an introduction to *LES* and other advanced turbulent closure techniques may be found

Referring solely to the classical models, the mixing length and *k*-Epsilon models are presently the most widely used and validated closure techniques. However, the mixing length model has now been largely superseded by the *k*-Epsilon model due to the increase in performance of computer hardware. As such the mixing length model will be given no further consideration here.

The *k*-Epsilon is based on the assumption that there is a relationship between the action of the viscous stresses and the turbulent Reynolds stresses. Newton's law of viscosity proposed that the viscous stresses

could be taken to be proportional to the rate of deformation of a fluid element. For an incompressible fluid this gives Equation 5-5 [**Ref. 77**].

Equation 5-5

$$\tau_{ij} = \mu e_{ij} = \mu\left(\frac{\partial u_i}{\partial x_j} + \frac{\partial u_j}{\partial x_i}\right)$$

A similar analogy was developed to describe the Reynolds stresses, it was observed that the turbulent stresses increased as the mean rate of deformation of a fluid element increased. Thus, it was proposed by Boussinesq that the Reynolds stresses could be linked to the mean rate of deformation using Equation 5-6 [**Ref. 77**].

Equation 5-6

$$\tau_{ij} = -\rho\overline{u_i' u_j'} = \mu_t\left(\frac{\partial U_i}{\partial x_j} + \frac{\partial U_j}{\partial x_i}\right)$$

The only variation to arise from Equation 5-5, is the addition of the turbulent or eddy viscosity. This dynamic eddy viscosity can be related to the kinematic eddy viscosity through the fluid density;

Equation 5-7

$$\nu_t = \frac{\mu}{\rho}_t$$

The turbulent transport of other flow properties are modelled in a similar fashion. By analogy, the turbulent transport of a scalar is taken to be proportional to the mean gradient of the property being transported;

Equation 5-8

$$-\overline{\rho u_i' \varphi'} = \Gamma_t \frac{\partial \Phi}{\partial x_i}$$

Here the turbulent diffusivity is Γ_t. Since the turbulent transport of all flow properties occurs under the same mechanism, eddy mixing, it is reasonable to assume that Γ_t equals μ_t. To assess the validity of this assumption we introduce the Prandtl/Schmidt number;

Equation 5-9

$$\sigma_t = \frac{\mu_t}{\Gamma_t}$$

Experimental observations of this ratio have established that it is constant for a wide variety of flows, being very close to unity. The majority of *CFD* codes assume that the ratio equals one.

The *k*-Epsilon closure model considers the transport of turbulent properties by the mean flow and diffusion, solving for the production and destruction of turbulence. Two partial differential equations simulate the generation of turbulent kinetic energy, *k*, and the dissipation of turbulent kinetic energy, Epsilon, thus giving rise to the name of this style of closure model.

The underlying assumption of this model is that the turbulence predicted is isotropic. That is the eddy viscosity, or the ratio between the Reynolds stresses and the mean rate of deformation, is the same in all directions. There is no biasing of the turbulence in the flow direction. Such a far ranging assumption can

lead to the closure model failing in certain situations due to prediction inaccuracies. A more detailed definitions of the closure models benefits and failings in given in Section 5.3.1.

To overcome such a limitation it is necessary to derive and solve transport equations for each of the six Reynolds stresses, which fully describe the time averaged turbulent flow field. Initially it may appear that the thinking behind solving transport equations for a stress is somewhat unconventional. However, the Reynolds stresses first appear on the left of the momentum equations, being physically generated by convective momentum transport due to velocity fluctuations. Fluid momentum, both mean and fluctuating, can be transported by fluid particles, thus the Reynolds stresses also appear to be transported. The Reynolds stresses are the product of the momentum transport through a point.

Each of the transport equations for the six Reynolds stresses, contain terms whose individual effects are unknown. The unknowns terms within the partial differential equations include diffusion, pressure-strain and dissipation effects, which cannot be measured experimentally. The Reynolds stress closure model utilises the six Reynolds stresses to describe anisotropic turbulence, hence must make assumptions regarding the unknowns in the transport equations for the Reynolds stress. The design of these transport equations has been an area of intense research within *CFD* studies. As a result of the assumptions surrounding the transport equations this style of closure model has not been as well tested as the more established *k*-Epsilon model.

The partial differential equations that describe the Reynolds stresses are solved in conjunction with a transport equation for the dissipation of turbulent kinetic energy, Epsilon. As such the solver must now solve seven additional transport equations as opposed to the two additional transport equations for the *k*-Epsilon model. Such an addition results in the Reynolds stress model being computationally expensive.

In an attempt to reduce the cost of a model which utilises the Reynolds stresses, the Algebraic stress model was developed. Through the application of far-reaching assumptions, the partial differential equations for the Reynolds stresses are reduced into algebraic form. These algebraic transport equations are then solved in addition to the production and destruction transport equations of turbulence, i.e. *k* and Epsilon respectfully. Thus, anisotropic turbulence can be simulated, coupled with an efficient solution system. However, the assumptions used within the algebraic stress model are very extensive and care must be taken in the use of this model.

A detailed description of the *k*-Epsilon, Reynolds or Differential Stress and Algebraic Stress closure models are provided within the Appendices. The merits of each model is discussed below. All three closure models are available within CFX-F3D. Further to the above models, CFX-F3D has three additional closure models; including, Low Reynolds Number *k*-Epsilon, RNG *k*-Epsilon and Reynolds

or Differential Flux. However, such models are merely extensions or adaptations of the *k*-Epsilon and Reynolds Stress models described within the Appendices. As such no further information regarding this additional models will be provided.

5.5 Relative Performance of the Various Closure Model of Turbulence

5.5.1 The *k*-Epsilon Turbulence Closure Model

The *k*-Epsilon model is the most common and widely validated of the turbulence closure models. The model is well suited to confined flows where high Reynolds shear stresses are of most importance. Notable successes have been achieved in calculations involving thin shear layers and re-circulating flows.

The *k*-Epsilon model shows poor correlation for unconfined flows and those containing secondary flow effects due to turbulence, i.e. flows driven by the anisotropic normal Reynolds stresses. Examples of such flows are weak shear layers and non-circular ducts. Difficulties also arise in the prediction of spread rates in axisymmetrical jets, with the spread rate being severely overpredicted. Such errors arise due to the model's tendency to predict a rate of turbulence kinetic energy production which is much less than the rate of dissipation. Finally, the model has difficulties predicting swirling flows and flows which have large extra strain, such as those experienced in rapidly diverging passages. These effects arise as the model contains no description for the effects of curvature on turbulence.

Thus, the *k*-Epsilon model is only capable of predicting flow field trends within control chokes, due to the deficiencies described above; i.e. secondary flow effects and rapidly diverging passages. However, the model is economical, numerically robust and provides a good staging post to the second-order turbulence closure models. A broad summary of the points noted include;

1. well established and most widely tested of the turbulence closure models.
2. wide applicability.
3. good performance for most confined flows of industrial interest.
4. turbulent stresses are expressed as directly proportional to the mean rate of strain.
5. the proportionality coefficient in the stress-strain relationship, the eddy viscosity, is expressed solely by two parameters; i.e. the time and length scales.
6. the k and ε assume a linear relationship between the turbulent stresses and the mean rate of strain.
7. most economical of the turbulence closure models.
8. numerically robust.
9. requires boundary conditions to be specified.
10. anisotropic turbulence not considered.
11. poor performance for a number of important flow classes

i. rotating flows
ii. unconfined flows
iii. flow in non-circular ducts
iv. flows with large extra strains.

5.5.2 The Reynolds Stress Turbulence Closure Model

The Reynolds stress model is the most complex and computationally expensive of the turbulence closure models, due to the addition of the partial differential equations to describe the transport of Reynolds stresses. However, it is the simplest of the present turbulence models which has the ability to fully describe all of the mean flow properties and Reynolds stresses in a fully anisotropic fashion.

This model type is not as well validated as the *k*-Epsilon model, as such one cannot be as confident of the results; right or wrong. However, the extension and improvement of this model is a very active area of research. With forthcoming increases in computational power of industrial work stations, the usage of this model will become more widespread due to its excellent potential.

With regards to flow modelling within control chokes, the Reynolds stress model will offer, without doubt, the most accurate calculation of the mean flow properties and Reynolds stresses within the choke. However, such accuracy must be justified in terms of the computational expense that the model demands. Thus a broad summary of the models characteristics is:

1. accurate calculation of the mean flow properties and the Reynolds stresses.
2. potentially the most general of all the turbulence closure models.
3. anisotropic flow considered in full.
4. extra strain, buoyant flows and rotational effects correlated well.
5. requires boundary conditions.
6. not widely validated at present.
7. not as computationally robust as the *k*-Epsilon model.
8. very computationally expensive.
9. performs just as poorly as the *k*-Epsilon model for certain flows due to identical problems with the ε equation.

5.5.3 The Algebraic Stress Turbulence Closure Model

The algebraic stress model provides the potential to bridge the gap between the isotropic *k*-Epsilon model and the computationally hungry Reynolds stress model; through the use of algebraic equations to compute the Reynolds stresses as opposed to partial differential equations.

However, the model is constructed on assumptions which need to be considered carefully before detailed modelling can proceed. In situations where it is known that the k-Epsilon model performs poorly, the algebraic stress model can be used where the transport assumptions made do not compromise the computational accuracy, i.e. where the convective and diffusive terms are negligible or where the Reynolds stress over turbulent kinetic energy ratio does not vary rapidly across the flow field.

The resolution of the turbulent flow field within control choke provides a good potential for this adaptive model, allowing anisotropic turbulence effects to be included, whilst avoiding excessive computational effort. Good accuracy of results for both the mean flow properties and the Reynolds stresses should be obtained within an acceptable time frame. However, as this model has shown a tendency to be numerically unsuitable, its application must be undertaken with care. Thus, a broad summary of the models characteristics is:

1. economical method in which the anisotropic Reynolds stresses can be considered.
2. only marginally more expensive than the k-Epsilon model.
3. wide applicability.
4. extra strain, buoyant flows and rotational effects correlated well.
5. questionable numerical robustness
6. requires boundary conditions.
7. not widely validated.
8. performs just as poorly as the k-Epsilon model for certain flows due to identical problems with the ε equation.
9. model is restricted by the assumption regarding convective and diffusive effects, limit testing required.

5.5.4 Conclusions on Turbulence Closure Models

An increased interest in the application of turbulence models to the calculation of complex three-dimensional flows over the past years has revealed many shortcomings within the models described above. None of the models in their present form can fully capture the significant changes of a turbulence flow field imposed by even mild three-dimensional effects. Indeed, the physical understanding of the effects of strong skew-induced vorticity, embedded vortices and even stress induced vortices upon the turbulent structure of the flow field is still insufficient. Thus, plausible extensions to the models to capture such details are difficult to arrive at.

Recent predictions published in the literature, using the standard models detailed above, have drawn very good comparisons with experimental data for simple three-dimensional flows. However, such cases are more of an exception then a rule, with the solution of complex three-dimensional flows still presenting a

major challenge. Major weaknesses within the closure models may still be discovered, although some are already more than obvious; i.e. the *k*-Epsilon model with its isotropic eddy viscosity is generally inadequate for complex three-dimensional flows.

Computationally, the *k*-Epsilon model has advantages over the Reynolds stress model in terms of robustness and economy. The same can be claimed for the Algebraic stress model, provided simple geometries are considered. However, the Algebraic stress models have shown that they are prone to numerical instabilities and convergence problems, hence the question arises whether it would be a sounder approach to utilise the full Reynolds stress model, provided that computing facilities are adequate. Further, for complex and irregular flow domains, where the use of non-orthogonal co-ordinates for the control volumes is required, the Algebraic stress model becomes ever more cumbersome and its advantages over the Reynolds stress model diminishes.

The above comments may be in disagreement with some *CFD* users, since at best the evidence upon which the statements are constructed is circumstantial. For instance, the unsatisfactory prediction of the rate of spread of a axi-symmetric jet can sometimes be adequately resolved by even the *k*-Epsilon model. Controversies such as this arise from uncertainties and inconsistencies in the definition of inflow turbulence quantities, the treatment of boundary conditions such as wall treatments, and insufficient accuracy within the applied numerical solution scheme. Thus, such insufficiencies can obscure the real performances of the turbulence closure models and hence lead to misjudgements.

Computational fluid dynamics is an extremely powerful tool, however, due to its limitation, it must be applied carefully by a user with a sufficient background knowledge.

6. Particle Trajectory Calculations and Oilfield Sand Classification

6.1 Introduction

The capability to predict the velocity history of a dilute suspension of particles suspended in a fluid is of importance to many process industries. In this study the primary objective is to compute the solid particle erosion rates on the internals of control chokes. However, before one can reach such a goal, accurate computation of the trajectories of the entrained particles is required.

The primary problem in computing the trajectories of the particulate suspension lies in the treatment given to the coupling of mass, momentum and energy between the two phases. This two-way coupling is simply illustrated below.

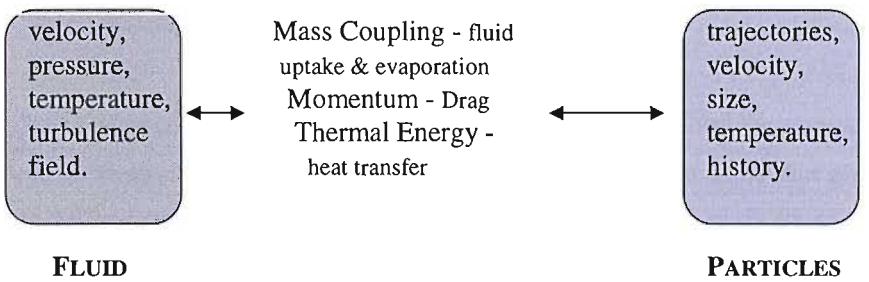

It is assumed that mass and heat coupling between the phases are negligible. i.e. the sand particles are non-porous and behave in an isothermal fashion. This then reduces the coupling phenomena to the exchange of momentum between phases; although this in itself is a non-trivial problem. Thus, we are concerned solely with the phenomena whereby a particle traversing the fluid flow field, induces;

- acceleration or deceleration resulting in a momentum argument between the two phases.

6.2 The Computation of Particle Trajectories; The Lagrangian Approach

From Chapter 5, we know the solution for the mean properties of the flow field, in the form of time averaged algebraic and partial-differential equations. Furthermore, the solution is in the form of a finite volume grid, with each of the control cells containing information regarding the localised flow properties, in addition to co-ordinate information.

We can utilise this information to compute the particle trajectory and velocity history, given the integrated forms of the equation of motion for a particle suspended in a fluid. Solving for particle velocities and trajectories is achieved through a Lagrangian frame of reference; which is most suitable for the dilute particulate phase. A limitation of this approach is that we are forced to ignore particle-particle interactions. One has the option to compute the particle trajectories in an Eulerian frame of

reference. However, this is a continuum approach, which is unjustified for the low particle concentrations experienced in oil field applications.

Information regarding the trajectory characteristics of the particles is recorded at each cell boundary in the form of; time, x, y and z co-ordinates and u, v and w velocities. As with the resolution of the turbulent flow field it is necessary to set boundary conditions. These boundary conditions include;

1. the location and number of starting points
2. the particle velocity at inlet
3. the size distribution and number of particle sizes
4. the density of the particle
5. the shape of the particle
6. the coefficient of restitution of the particle
7. total mass flow rate of the particles
8. consideration for local turbulence effects

The particle trajectories are computed as a function of the above and the computed flow field. Each trajectory can represent a number of particles, with each having the same start position and trajectory. The number of particles that each trajectory calculation represents is dependent upon the total mass flow rate or mass flux and particle size distribution specified within the command file. Given the density and diameter of each particle, its mass is known. The number of particles that each trajectory calculation represents is given by dividing the mass flux by the specified number of starting positions. This provides the individual mass flow rates at each starting position. The number of particles each start position or trajectory calculation represents being given by that mass flow rate divided by the particle mass. The total number of particles flowing is then the summation of the number of particles each trajectory calculation represents.

Furthermore, the number of sizes determines the total number of trajectories computed. Each particle size starts from each of the specified start positions. Hence, if one has ten sizes, i.e. 60 to 300 microns, and thirty start position, the total number of trajectories is simply three hundred. These three hundred trajectories calculations may represent a total of three thousand particles, if each trajectory calculation represents ten particles.

6.2.1 Particle Momentum Source in Cell - The Two-Way Coupling

The solution technique, which couples the two phases can be executed in one of two methods. First, one can ignore the effects of the particles on the mean flow field, thus assuming a one-way momentum coupling from the fluid to the particulate phase. Such an approach is adequate for very low particle concentrations, where one is only analysing small particles that have insufficient

momentum to affect the flow field. Alternatively, a two-way coupling of the momentum between phases can be incorporated into the solution, allowing more concentrated solutions to be solved. Here, as with the above, the flow field is solved initially assuming that no particles are present. Using this flow field, the particle trajectories can be computed. These particle trajectories then provide an additional momentum source term for the turbulent flow field equations, i.e. Equations 5-37 and 5-38. The flow field is solved once again incorporating these additional momentum source terms within the appropriate cells, thus giving rise to the momentum source in cell method. The new turbulent flow field computed is then used to determine new particle trajectories.

Calculating new source terms and incorporating them into the fluid flow field equations constitutes the effect of the particulate suspension on the fluid phase, thereby completing the cycle of mutual interaction or two-way coupling between phases. After several iterations of this process, as defined by the user, the flow field equations are satisfied and a solution which accounts for the mutual interaction between the two phases is obtained. However, it is important to note that the particle source terms for the flow field have only been fully established for the momentum equations. As such the effect of the particles on the turbulence quantities, k and Epsilon, needs further work to fully understand the two-way coupling **[Ref. 23].**

Given the complications of the two-way coupling and the subsequent difficulties associated with utilising an iterative approach to erosion predictions, the preferred solution method is the one-way coupling, whereby it is assumed that the particulate loading is sufficiently low not to contravene this solution method. This is a valid assumption if Table 6-2 is considered, here typical sand production rates and concentrations are given. A typical sand concentration would be 20 ppm by volume, or in percentile terms 0.002 % by volume, a very low number.

6.2.2 Particulate Equations of Motion - The Momentum Equation

To evaluate the particle trajectories and velocity history it is necessary to develop equations of motion for that particle. A moving fluid exerts a force F on the immersed body. Typically, $F = D + L$, where D is the drag force that acts in the opposite direction to the fluid motion, due to the differences in linear velocity between the continuous and suspended phases. Consideration is also given to pressure gradient forces of the surrounding fluid and gravitational effects. L is the lift force normal to the fluid motion. CFX-F3D ignores the lift forces, such as Staffman and Magunus forces due to viscous shear stress and particle rotation respectfully. No further consideration is given to such forces here, however these forces may be included through the use of sub-routines within CFX-F3D. Virtual mass forces, Basset forces and other cohesion forces are normally neglected in view of the large differential density between phases. However, if a heavy crude is the continuos phase, slight improvements in the numerical accuracy may be achieved by their inclusion. The author did not consider such effects.

The equations for the rate of change of particle velocity are obtained directly from Newton's second law. The velocities are obtained by simply integrating the equation of motion. In their simplest form the equation of motion can be presented by Equation 6-1 **[Ref. 23].**

Equation 6-1

$$m\frac{\partial u}{\partial t} = C_D \rho (U - u)|U - u|\frac{A_p}{2} + F$$

The drag force exerted on the immersed body arises through two mechanisms. The first is due to the viscous surface shear stresses, known as skin friction. Whilst, the second is due to the pressure distribution around the body, known as form drag. The total drag force is most conveniently expressed by the non-dimensional drag coefficient C_D. This can be defined by Equation 6-2 **[Ref. 19]**

Equation 6-2

$$C_D = \frac{D}{0.5\rho u^2 A_p}$$

We may non-dimensionalise Equation 6-2 through the use of the particle Reynolds number. For a particle of given shape, undergoing motion in an incompressible Newtonian fluid;

Equation 6-3

$$\mathrm{Re}_p = \frac{\rho u d}{\mu}$$

Through the application of the particle Reynolds number, the drag coefficient can be broken down into four distinct regions whereby one or both of the drag types dominate **[Ref. 19]**

(1) - Stokes regime $0 < \mathrm{Re}_p < 0.2$

Here the drag is due entirely to skin friction and can be computed analytically, giving Stokes law;

$$C_D = \frac{24}{\mathrm{Re}_p}$$

(2) - Allen regime $0 < \mathrm{Re}_p < 500\text{-}1000$

This regime is also known as the viscous or transitional region. Both skin and form drag are equally important with the drag coefficient decreasing monotonically with the particle Reynolds number.

$$C_D = \frac{24}{\mathrm{Re}_p}\left(1 + 0.15\mathrm{Re}_p^{\,0.687}\right)$$

(3) - Newton's regime $500\text{-}1000 < \mathrm{Re}_p < 1\text{-}2 \times 10^5$

This is known as the turbulent region where form drag dominates. Here the drag coefficient becomes constant and independent of the particle Reynolds number.

$$C_D = 0.44$$

(4) - Super-Critical regime $Re_p > 1\text{-}2 \times 10^5$

At very large particle Reynolds numbers, the drag coefficient drops suddenly. This occurs due to the flow in the particle boundary layer changing from laminar to turbulent. As a result separation occurs nearer the rear of the particle, significantly reducing the form drag. Form drag still dominates, and the drag coefficient is once again independent of the particle Reynolds number.

$$C_D = 0.1$$

The Allen regime is most common, being that normally implemented within commercial *CFD* codes. However, there is scope with CFX-F3D to allow the drag coefficient to be set explicitly by the user through the application of sub-routines.

A standard drag curve facility is normally available with the codes **[Ref. 19],** that is applicable to all the regimes, having the form;

Equation 6-4

$$C_D = \frac{24}{Re_p} + \frac{5.48}{Re_p^{0.573}} + 0.36$$

The standard drag coefficient is the default used within CFX-F3D.

A limitation is that the correlations are only truly valid for incompressible flows. For compressible flows, the correlations given above are only valid up to a Mach number of approximately 0.3 **[Ref. 19]**. Beyond this region, the drag coefficient becomes a function of the Mach number as well as the particle Reynolds number. In the case of control chokes flowing gas, one can normally expect the flow velocity just after the controlling ports, or vena-contracta, to approach sonic or be sonic for choked conditions. Thus the drag correlations are invalid. However, this high velocity is very localised, with the flow velocity rapidly decreasing to below the Mach 0.3 upon further expansion of the flow. As this high velocity region is confined, with the remainder of the flow being within the Mach 0.3 limit, we can use the drag correlations with a good degree of confidence.

Considerable economy in the computing time for the particle trajectories can be realised by integrating the trajectory equation once analytically. Thus, rewriting Equation 6-1 for the particle motion yields [Ref. 23];

Equation 6-5

$$\frac{\partial u}{\partial t} = \left(\frac{18 \mu f}{\rho d^2} \right) (U - u) + F$$

$$\text{where } f = \frac{C_D Re_p}{24}$$

We now integrate Equation 6-5, assuming that the fluid velocity is constant over the time of integration. Thus, providing the particulate velocity, given the steady state turbulent flow field [Ref. 23]. The process is repeated for the remaining dimensions.

Equation 6-6

$$u = U - (u - V_o)\exp\left(\frac{-\Delta t}{\tau}\right) + F\tau\left[1 - \exp\left(\frac{-\Delta t}{\tau}\right)\right]$$

Here V_o is the initial particle velocity as defined in the boundary conditions or at the particles entry into the cell, Δt is the integration time interval and τ is the characteristic time scale given by;

Equation 6-7

$$\tau = \frac{\rho d^2}{18\mu f}$$

6.2.2.1 Additional Forces Acting on the Particle

As mentioned the main momentum contribution from the fluid phase is that due to the momentum coupling or drag. However, additional forces are acting which need to be accounted for; including the following [Ref. 19].

(1) - The pressure gradient force, acting around the particle due to the pressure of the continuous phase.

Equation 6-8

$$F_P = \frac{1}{4}\pi d^3 \Delta P$$

(2) - The buoyancy force acting between the two phases due to gravity.

Equation 6-9

$$F_B = \frac{1}{6}\pi d^3 (\rho_P - \rho) g$$

(3) - The added or virtual mass force due to the particle velocity, not normally applicable.

Equation 6-10

$$F_A = \frac{1}{6}\pi d^3 \rho \frac{\partial u}{\partial t}$$

(4) - The rotating co-ordinates force term.

Equation 6-11

$$F_R = \frac{1}{6}\pi d^3 \rho_P \left(-2\omega u - \omega\omega x\right)$$

6.2.3 The turbulent dispersion of particles.

The flow field solved by the turbulence closure models is time average, i.e. only the mean velocity flow field is resolved due to the computational limitations, Chapter 5. However, during a particle's motion, it interacts strongly with many discrete turbulent eddies. The effects of these turbulent eddies on the particle trajectories can be included through the application of the turbulent dispersion force term. Here the continuum velocity in the momentum equations above is taken to be the mean velocity calculated by the closure models plus a contribution due to effects of localised turbulence. The

contribution to the continuum velocity due to eddy effects, thus providing a representation of the instantaneous velocity, is taken to be twice the local turbulent kinetic energy [**Ref. 19**].

Equation 6-12 $$u_{TD} = u + 2k$$

The turbulence that is imposed is assumed to be made up of a collection of randomly directed eddies, where the interaction time of any one eddy is assumed to be the lower of either the lifetime of the eddy or the transit time required for the particle to pass through the eddy. The eddy time scale or lifetime t_E and the characteristic length scale l_E of a numerical eddy are assumed to equal those of the energy containing eddies of the flow; t_E and l_E are given by the following [**Ref. 19**].

Equation 6-13 $$t_E = 1.5^{0.5} C_\mu^{0.75} \frac{k}{\varepsilon}$$

Equation 6-14 $$l_E = C_\mu^{0.75} \frac{k^{1.5}}{\varepsilon}$$

A limitation of the turbulent dispersion treatment described is that the turbulent eddies are considered to be isotropic. Here consideration is only given to the rate of creation and destruction of turbulence, the directional influences of the Reynolds stresses is not included. The result of neglecting the Reynolds stresses is that whilst the particles are randomly excited in all directions equally, the tendency towards stream-wise excitation cannot be captured.

6.2.4 Drag Exerted by the Particulate Phase on the Continuum Phase

For completeness we consider the drag exerted upon the continuous phase by the particulate phase, whilst this is not the preferred solution technique, applications do exist which warrant it's consideration. The discussion given for the momentum equation was confined to the exchange of momentum from the continuum to the particle phase. To complete the cycle of mutual interaction or two-way coupling between phases one must propose an equation for the drag exerted by the presence of particles on the continuous phase, allowing the turbulent flow field to consider source terms generated by particles. Once again we are interested in the momentum exchange, hence we must consider drag [Ref. 19]. Please note that α denotes the continuous phase, whilst β denotes the dispersed or particulate phase. First we must consider the number of particles per unit volume, n_P given by;

Equation 6-15 $$n_p = \frac{r_\beta}{V_p} = \frac{6 r_\beta}{\pi d^3}$$

The drag exerted by a single particle on the continuous phase is given by;

Equation 6-16 $$D_p = \frac{1}{2} C_D \rho_\alpha A_P \left| U_\beta - U_\alpha \right| \left(U_\beta - U_\alpha \right)$$

Hence the total drag per unit volume on the continuous phase is given by;

Equation 6-17

$$D_{\alpha\beta} = n_p D_p = \frac{3}{4}\frac{C_D}{d}\rho_\alpha r_\beta \left|U_\beta - U_\alpha\right|\left(U_\beta - U_\alpha\right)$$

6.2.5 The Particle Volume Fraction

A useful feature of CFX-F3D is the ability to compute the particle volume fraction, being calculated across all nodal locations. Surface plots of the volume fraction may be produced, providing useful information regarding possible erosion sites given particle concentration levels.

A benefit of knowledge regarding the volume fraction is an insight into near wall particle-particle interactions and the resultant effects on the predicted erosion. An item of further work would be the development of a correlation to consider particle-particle interactions. At present, through computational limitations, it is assumed that no particle-particle interactions occur. Through the volume fraction one has the opportunity to implement such a correlation, albeit somewhat crude. In addition to the erosion model possessing information regarding the particle impact parameters; the volume fraction would also be passed to the model. Once the volume fraction had exceeded a known threshold, a previously specified set of actions could then be initiated. For example, the predicted erosion would be decreased as a function of increasing volume fraction, due to the impacting particle's reduced ability to strike at the wall. The exact structure of this correlation would require further attention.

Within CFX-F3D, the volume fraction is computed by consideration of the particle size and the time that particle occupies anyone cell. It is noteworthy, that there is nothing in the code to stop the fraction becoming greater than 1.0. This is physically impossible, but numerically convenient.

6.3 Modifications to the Trajectory Calculation; The Particle Impact Parameters

The capability, to not only predict the erosion intensity, but distribution of erosion is of great importance. Previously, discussion was given to the prediction of particle trajectories within the bulk flow through the momentum argument. Here, we are concerned with the interactions of the particle and the wall. If one has inadequate treatment of these particle-wall interactions, referred to here within as the particle impact parameters, then the subsequent prediction of the erosion distribution will be incorrect.

CFX-F3D, in its base form, has very poor treatment of these particle impact parameters. The sole consideration given is a crude correlation to determine the reflected velocity, in the form of the coefficient of restitution, see below for definitions. To rectify this situation, a number of

modifications have been written into the particle tracking routines of CFX-F3D which enable improved treatment of the particle impact parameters. These modifications may be summarised as follows;

1. improved treatment of the coefficient of restitution; inclusion of parallel and perpendicular consideration.
2. squeeze film retardation effects at impact.
3. critical particle Reynolds number at impact.

6.3.1 The Coefficient of Restitution

At a particle impact, the velocity of the rebounding particle will be lower than the incoming velocity due to energy transfer; kinetic energy at impact being dissipated as heat, noise and target material deformation. We assume that the particle does not deform at impact. The magnitude of energy dissipation at impact is numerically detailed by the momentum based coefficient of restitution; *E*. The coefficient being the ratio of the outgoing perpendicular velocity component over the incoming perpendicular velocity component. One denotes a purely elastic impact. Traditionally, it was assumed that the impact will have negligible effect on the particles parallel velocity component. Further, the coefficient holds a single value, defining energy dissipation over the entire range of angles; 0-90 degrees. This is the form embedded within the base code of CFX-F3D. Figure 6-1 shows the particle velocity components at impact. The traditional treatment of the coefficient of restitution and reflected velocity is depicted by Equation 6-18 and Equation 6-19.

Equation 6-18

$$E_{perp} = \frac{U2_{(perp)}}{U1_{(perp)}}$$

Equation 6-19

$$U2 = U1_{(par)} - E_{perp}\left\{U1_{(perp)}\right\}$$

However, Grant et al. **[Ref. 35]** has shown that the restitution coefficient cannot to completely represented by a single value, being only active on the perpendicular velocity component and angle insensitive. Grant's observations are based on an experimental investigation of annealed 2024 aluminium, using dry air as the transport fluid; the highest impact velocity reported was 120 m/s. Grant's work showed that the coefficient is both angle dependent and that the parallel velocity component, in addition to the perpendicular velocity component, is reduced at impact.

Grant hypothesised that the parallel velocity component was reduced at impact due to the particles tendency to cut at the targets surface, as is experienced under erosive conditions. Further, surface discontinuities tend to interrupt the parallel velocity component. Grant found that the velocity of the particle at impact had little influence on both the parallel and perpendicular velocity components for the system tested. Grant also observed that the restitution coefficient was size independent for sand particles of the range 20 to 200 microns. This particle size range is that commonly found for produced sands

within the oil industry, see section 6.4.1 Assumptions made by Grant, which have been held by the present author, are that the particles are non-deformable, displaying no tendency towards plastic or elastic deformation. Further, the particle does not fragmentate at impact.

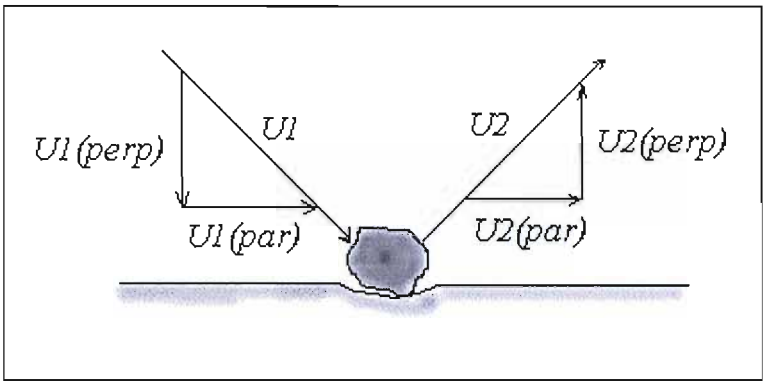

Figure 6-1 Velocity Components at Impact

One may conclude that the original coefficient of restitution held within CFX-F3D needs extension; allowing consideration of both the parallel velocity component at impact and the angle of impact. Due to the mechanism of parallel velocity attenuation (cutting), the hardness of the material will influence the degree of attenuation experienced; Grant [**Ref. 35**]. The greater the material hardness the lower the velocity attenuation experienced, with the parallel coefficient of restitution tending towards one. The perpendicular velocity component displayed slight variation with target material hardness. The perpendicular coefficient of restitution increased slowly with increasing material hardness, due to the reduced tendency to induce elastic deformation. Thus, in addition to Equation 6-18, we can propose the parallel coefficient of restitution as;

Equation 6-20

$$E_{par} = \frac{U2_{(par)}}{U1_{(par)}}$$

We must now revise Equation 6-19 to reflect the inclusion of the parallel coefficient of restitution.

Equation 6-21

$$U2 = E_{par}\left\{U1_{(par)}\right\} - E_{perp}\left\{U1_{(perp)}\right\}$$

Each angle of impact is known within the embedded FORTRAN, see section 7.2.1.3, allowing a power series to reflect the dependency of the coefficients of restitution on angle. That proposed by Grant for 2024 Aluminium impacted by sand particle of the size 20 to 200 microns has the form presented in Equation 6-22 and Equation 6-23.

Equation 6-22

$$E_{perp} = 0.993 - 1.76\alpha + 1.56\alpha^2 - 0.49\alpha^3$$

$$\text{Average } E_{perp} = 0.44$$

Equation 6-23

$$E_{par} = 0.988 - 1.66\alpha + 2.11\alpha^2 - 0.67\alpha^3$$

$$\text{Average } E_{par} = 0.79$$

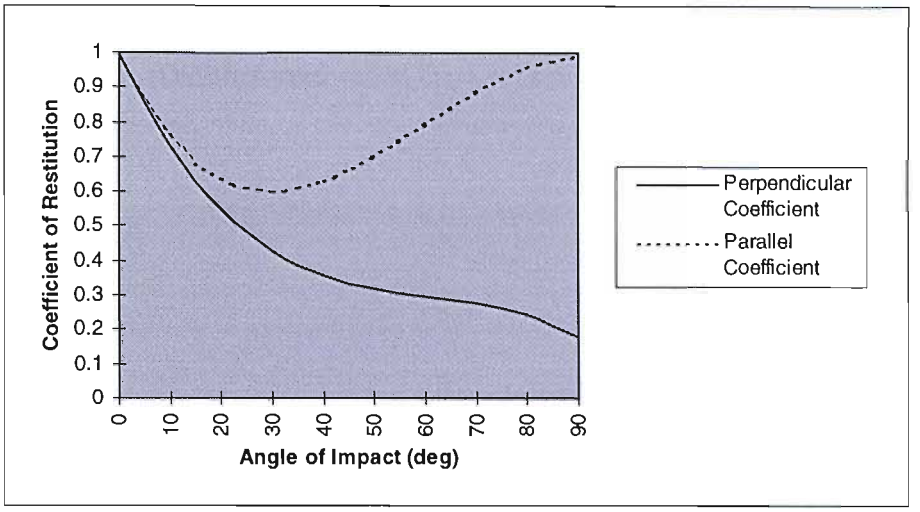

Figure 6-2 Perpendicular an Parallel Coefficient of Restitution for 2024 Annealed Aluminium

6.3.1.1 The Coefficient of Restitution for Differing Material Types

The advantage of *CFD* is that the flow domain must be defined, thus we can define regions of differing material types within the choke. Facility has been written into the embedded FORTRAN to allow such specification to be achieved, see section 7.3. Typically, we can define the trim of the choke to be tungsten carbide, whilst the body may be an AISI 1020. Naturally, the physical properties of these materials, including the coefficients of restitution, differ. As such, we need to obtain various coefficient values to capture the rebound characteristics of differing materials. These coefficients of restitution, as power series, are included within the embedded FORTRAN.

Improving upon Grant **[Ref. 35],** one may hypothesize as to values for the perpendicular and parallel coefficients for differing materials. Difficulties arise due to the lack of accurate information available in the literature. Those terms given to describe the coefficient values for steel and tungsten carbide are drawn from assumption regarding the 'likely' behaviour of those materials. Such assumptions are based simply on the relative hardness of the materials and the materials' flow stresses; see Table 2-1. Unfortunately, errors cannot be avoided due to the lack of factual data, however this best estimate approach for steel and tungsten carbide provide a significant advance in coefficient characterisation than that provided by CFX-F3D. An item of further work, beyond the scope of the present project, would be an improved correlation for the coefficient, generated through an experimental programme.

6.3.1.2 Carbon and Stainless Steel Coefficient of Restitution

Equation 6-24 and Equation 6-25 detail the rebound characteristics of a steel material, presenting the perpendicular and parallel coefficients of restitution respectively. Included within this group are the stainless type steels. Such an assumption may not be wholly accurate; however, work involving stainless steel materials within this project is limited. As such the effort of classification is not warranted due to

the slight variation experienced within the steel group of materials. Figure 6-3 shows the typical coefficient values for an AISI 1020 steel.

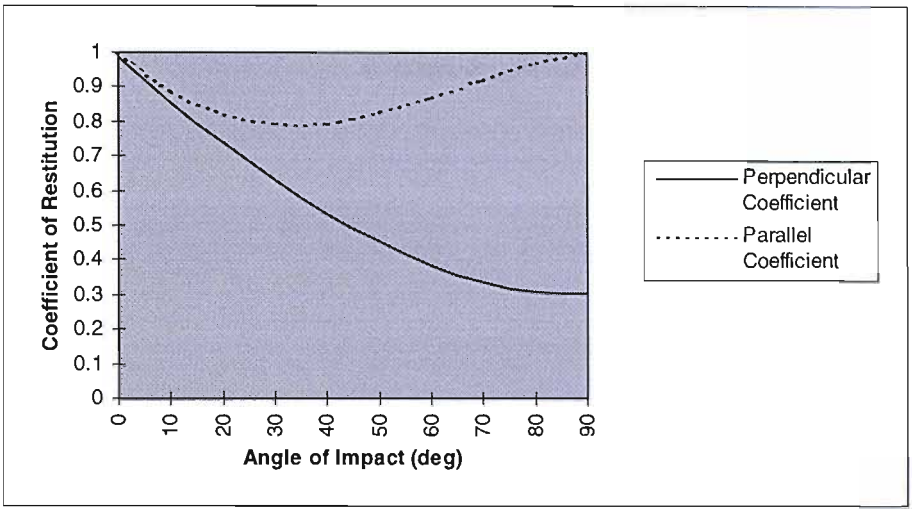

Figure 6-3 Perpendicular an Parallel Coefficient of Restitution for AISI 1020 Steel

The peak in parallel velocity attenuation is marked, occurring at an angle of approximately 30°. This peak in attenuation corresponds to the maximum erosion angle for such steel materials, see Figure 2-2 and Chapter 4. Furthermore, due to the relatively low flow stress of such steel materials, the attenuation of the perpendicular velocity is high when one approaches a normal angle of impact.

Equation 6-24

$$E_{perp} = 0.988 - 0.78\alpha + 0.19\alpha^2 - 0.024\alpha^3 + 0.027\alpha^4$$

$$\text{Average } E_{perp} = 0.55$$

Equation 6-25

$$E_{par} = 1 - 0.78\alpha + 0.84\alpha^2 - 0.21\alpha^3 + 0.028\alpha^4 - 0.022\alpha^5$$

$$\text{Average } E_{par} = 0.89$$

6.3.1.3 Tungsten Carbide Materials Coefficient of Restitution

Equation 6-26 and Equation 6-27 detail the rebound characteristics of a tungsten carbide material, presenting the perpendicular and parallel coefficients of restitution respectively. As with steel materials, the terms describe all material grades that fall within the tungsten carbide group. In this instance, such an assumption is warranted. Figure 6-4 shows the correlation for 6% cobalt tungsten carbide.

Here, one may observe, that due to the hardness of tungsten carbide, the parallel coefficient is very much suppressed; holding a mean value of 0.91. This value reflects the high resistance to cutting displayed by such materials, the majority of the parallel velocity attenuation stems from surface irregularities at the boundaries of carbide grains and the binder. The relatively high value for the perpendicular coefficient illustrates the lack of deformation, both plastic and elastic, that the material experiences.

Equation 6-26

$$E_{perp} = 0.998 - 0.59\alpha + 0.16\alpha^2 - 0.026\alpha^3 + 0.024\alpha^4$$

$$\text{Average } E_{perp} = 0.68$$

Equation 6-27

$$E_{par} = 1 - 0.49\alpha + 0.62\alpha^2 - 0.2\alpha^3$$

$$\text{Average } E_{par} = 0.91$$

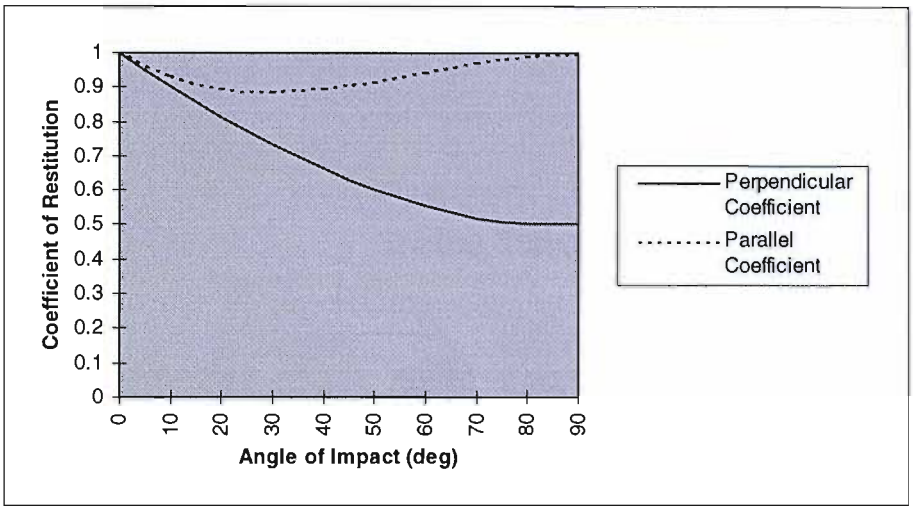

Figure 6-4 Perpendicular an Parallel Coefficient of Restitution for 6% Cobalt Binder Tungsten Carbide

6.3.2 Squeeze Film Effects

The near wall velocity of a particle is computed via the momentum argument from the transport fluid. CFX-F3D utilises wall functions to describe the near wall velocity gradient, thus avoiding the need to integrate the fluid transport equations right to the wall. See section 5.5.4. Integration to the wall would require very fine grids near the wall to resolve boundary layer effects, requiring much computational effort. However, the application of such wall functions may lead to near wall errors with regard to particle tracking due to poor resolution of the viscous sub-layer.

In liquid-solid erosion or where wet gas is the transport fluid, the viscous sub-layer at the wall significantly influences the erosion rate experienced. Where surfaces are wetted, surface tension effects act to attenuate the impact velocity of the particle, thus reducing the erosion experienced. However, through the application of wall functions within CFX-F3D, the critical near wall region is, in general, inadequately resolved for our needs. Figure 6-5 details the near wall interactions of the fluid and particle.

As the particle nears the wall, the particle must force a small volume of fluid out from beneath it, known as the squeeze film effect, where a pressure spike is generated beneath the impinging particle.

As the particle rebounds after impact, the fluid is drawn back into that region inducing a drag through the pressure gradient. Furthermore, each particle generates its own turbulent wake as it passes through the suspension. At rebound, in addition to the particle generating a new wake, the particle may pass through the original wake. Hence the drag imposed upon the particle in this region is high, with form drag effects strongly felt due to the squeeze film and skin drag effects felt due to the highly turbulent wake the particle must pass through. The viscosity of the fluid, the thickness of the sublayer and the density differential between fluid and particle influence the degree of attenuation.

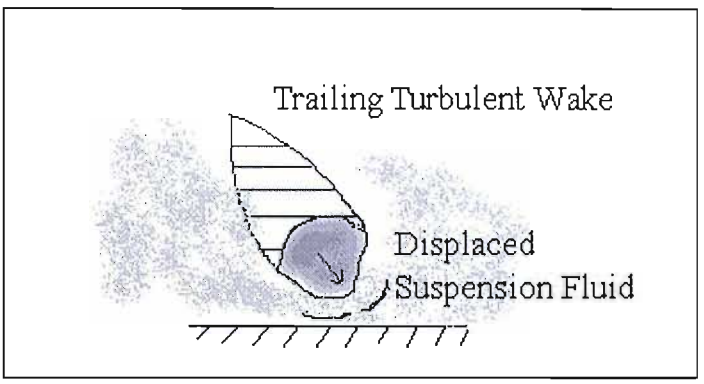

Figure 6-5 Near Wall Action of Particle

One has two options available to describe these near wall effects that are not well resolved by the transport equations of CFX-F3D. The coefficients of restitution may be set such that they are overly dissipative, thus accounting for squeeze film effects in liquid or wetted flows. However, as detailed in the previous section, the specification of the coefficients of restitution is an extremely complex tasks. As such, the additional handicap of consideration of squeeze film effects within the coefficients is not acceptable. The second option is the discrete consideration of the squeeze film effects, separate from the coefficients of restitution.

A squeeze film function has been included within the embedded FORTRAN of CFX-F3D, allowing the impact velocity and reflected velocity of the particle to be modified, reflecting these near wall effects. Care must be taken to develop a relationship which is suitably robust. Clark [**Ref. 21**] investigated this problem, presenting a solution to the squeeze film for incompressible Newtonian fluids. Through the application of the continuity equation, Clark presented a squeeze film retardation factor, considering the density differential between phases and the particle Reynolds number.

Equation 6-28

$$R_{vf} = \frac{a}{a+\xi} - 12\frac{\xi^2}{a+\xi}\frac{1}{\mathrm{Re}_{pp}}$$

where $a = 8.\left(\frac{2\rho_p}{\rho_g} + 1\right)$

$\xi = 10$. Experimentally derived empirical constant.

ξ, the squeeze film correction factor was derived by experimental work, whereby 230 to 750 micron glass beads, suspended in a water-glycerine mixture, were impacted onto a polished specimen at a number of angles. Impact velocities of 9.35 and 18.7 m/s were utilised [**Ref. 21**]. The energy dissipation within the squeeze film region was then determined from a comparison of energy transferred to the target, given the crater size, and kinetic energy of the particle, immediate to impact. The squeeze film retardation factor is then applied to the particle impact velocity as computed by CFX-F3D. Typical values for the retardation factor are within the region of 0.6-1. The particle Reynolds number is computed from the perpendicular component of the impact velocity.

Equation 6-29

$$\mathrm{Re}_{pp} = \frac{\rho_g . U_{perp} \theta_p}{\mu}$$

An interesting observations made within the paper presented by Clark, was that the squeeze film is only active over a short distance. This distance can be approximated to one-quarter of the particles radius. This observation supports the need to include squeeze film retardation factor within the base code of CFX-F3D, due to its inability to resolve this near wall region. An example of the Squeeze Film Retardation Factor, as it varies with perpendicular impact velocity, is presented in Figure 9-4.

6.3.3 Critical Particle Reynolds Number

An advantage of the work of Clark [**Ref. 21**] is that the critical particle Reynolds number is known. The critical particle Reynolds number denotes the minimum energy required by the particle to penetrate the squeeze film and inflict an impact which damages the target. The empirically determined critical particle Reynolds number can be shown to hold the form given in Equation 6-30; the test conditions are given within the previous section.

Equation 6-30

$$\mathrm{Re}_{cp} = \frac{12\xi^2}{a}$$

Within CFX-F3D it is possible for particles to became trapped within the boundary layer at the wall, due to the orientation of the velocity vectors. In such a situation the particles tend to bounce along the wall, producing many particle impacts. Such low energy impacts have no erosive potential, as such do not need to be considered within the erosion model. The availability of the critical particle Reynolds number provides a filter, whereby such low energy particles need not be considered. Thus, the critical particle Reynolds number is included with the embedded FORTRAN, any particle that does not satisfy this criterion is excluded from further considerations, allowing computational effort to be conserved.

6.4 Oilfield Sand Characterisation

The type and size of sand particle produced from an oil well will significantly influences the erosion experienced; see Chapter 2. As such, it is essential that erodent characterisation be undertaken in any erosive study; allowing the correct particle classification to be feed to the erosion models. Furthermore, the density of the sand influence the particle trajectory calculation via the density differential between phases. Thus, the parameters required within the *CFD* erosion model, allowing an accurate representation of the particle and material reactions, include;

1. the sand size distribution and mean.
2. the particle sharpness.
3. the sand density.
4. sand concentration or loading.

It is noteworthy that these parameters can vary between fields and even wells within fields, hence careful monitoring is required if an accurate erosion study is to be undertaken. The reader is referred to Chapter 9, where in support of an erosion investigation/simulation, a erodent analysis was undertaken.

6.4.1 Sand Size Distribution

The sand size distribution is required to set the distribution range within the command file of CFX-F3D. Here, one sets the upper and lower size limits and the number of sizes utilised between these limits. Figure 6-6 to Figure 6-9 present seize data from a number of sand sources, one may observe a size variation of between 40 and 600 microns. However, those particles occurring at the limits of the distribution range are few. As such it is more practical to utilise a limited distribution range, constructed on the mean sand sizes. In this instance the arithmetic mean is assumed to be the 50% cumulative weight of the distribution. Figure 6-13 details the typical size distribution of produced sand.

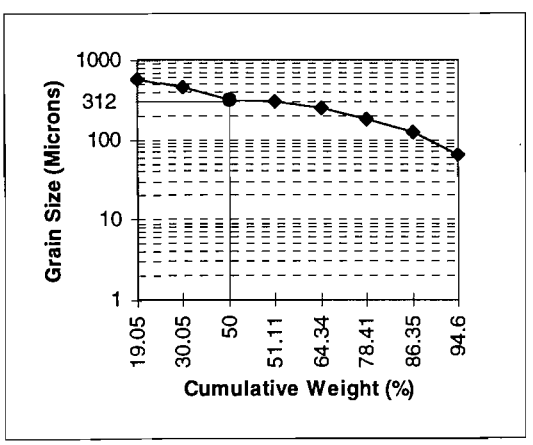

Figure 6-6 Sand Size Distribution (Candy Surge Drum)

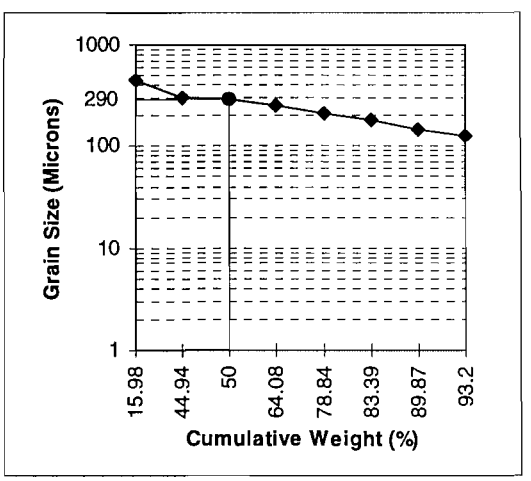

Figure 6-7 Sand Size Distribution (Boot of Ann Separator)

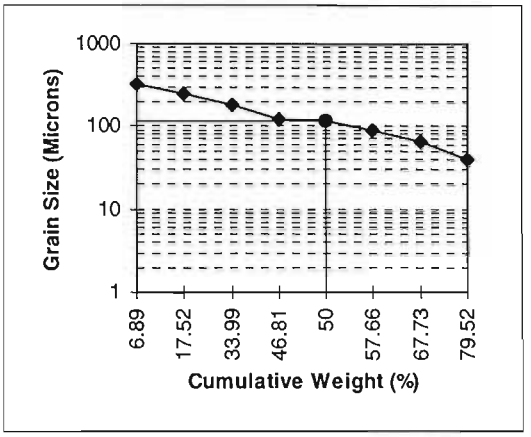

Figure 6-8 Sand Size Distribution (Candy Pump Suction Witches Hat)

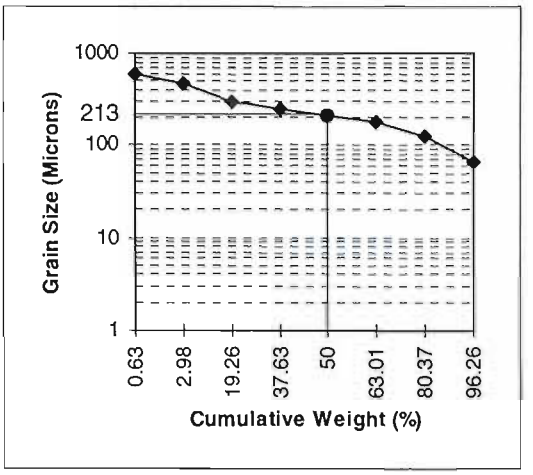

Figure 6-9 Sand Size Distribution (H.P. Vent Drum)

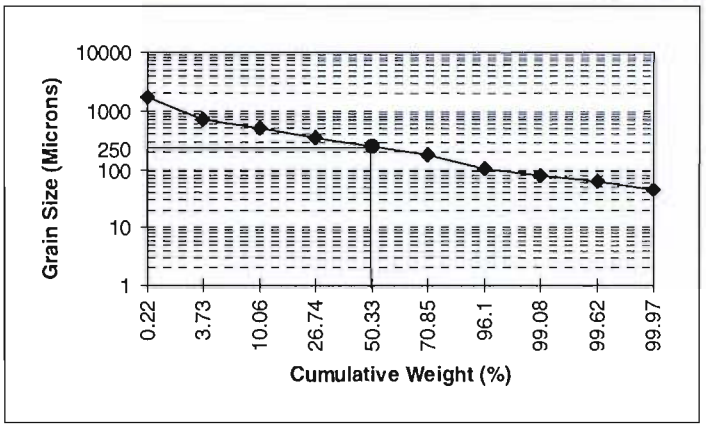

Figure 6-10 Sand Size Distribution (BP Forties Separator)

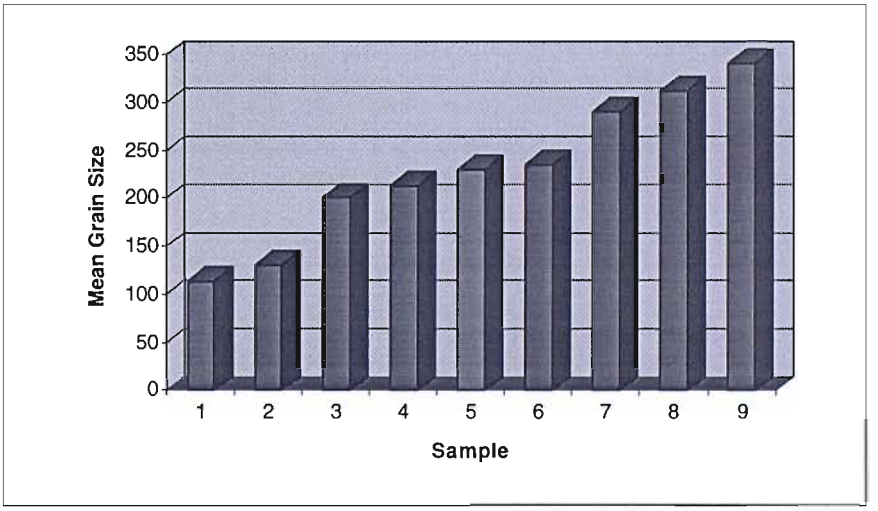

Sample 1 - Boot of Ann Separator.
Sample 2 - Forties Separator EX-V03.
Sample 3 - Forties MOL Pump Seal EX-CP04.
Sample 4 - Candy Surge Drum.
Sample 5 - Arithmetic Mean.
Sample 6 - Forties Separator FC61.
Sample 7 - Candy Pump Suction Witches Hat.
Sample 8 - Candy H.P. Vent Drum.
Sample 9 - Forties MOL Pump Seal with Magnetic Extract.

Figure 6-11 Mean Sand Size Distribution as used within CFX-F3D

Figure 6-11 details a collection of arithmetic means, obtained from the sources detailed. Here one may observe that the range of mean distributions is between 100 and 340 microns, having an average sand particle size of 229.3 microns. This sand distribution is the default used within the erosion model, with varying numbers of particle sizes utilised to determine the statistical confidence required. The greater the number of particle sizes, the greater the computational effort and statistical confidence. The range of sand distributions set directly effects the erosion prediction, it is essential to the overall accuracy of the erosion prediction, that the number of particle sizes be maximised.

6.4.2 Sand Particle Sharpness

The particle sharpness relates to the angularity of the particle, and its erosive potential. The greater the angularity, the greater the stress concentration effects generated and hence wear. See Chapter 4. Variations in particle sharpness, typically sharp and round, may result in an order of magnitude variance [**Ref. 45**] in the erosion rates experienced. Most sands produced from a well are roughly equiaxial; however there is considerable variation in the relative angularity depending on the reservoir rock. The erosion models of Hashish and Bitter both utilise a non-dimensional particle roundness factor to describe this angularity. This roundness factor is a simple description of the particle shape, derived due to the difficulties of identifying and quantifying the features of complex three-dimensional shapes. The factor is a measure of the perimeter and area of a two-dimensional projection of the particle, defined as the ratio between the actual area of projection and the area of a circle with the same maximum perimeter as the projection. See Figure 6-12. Here *Rf* can be shown by Equation 6-31.

Equation 6-31

$$Rf = \frac{4\pi A_p}{p_p^2}$$

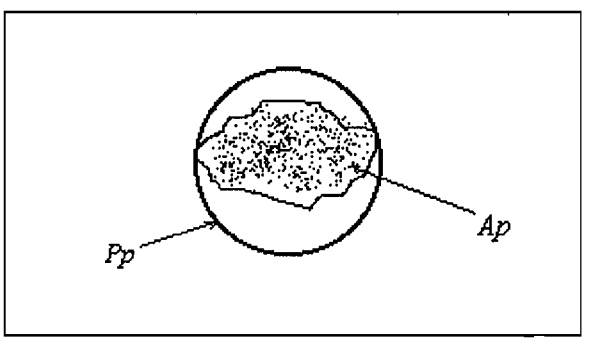

Figure 6-12 Definition of Particle Roundness Factor

The particle roundness factor utilised within the erosion models have a range of between 0.1 and 1; where 1 denotes a round particle. The greater the departure of the actual projected area from the perimeter area, the smaller the value of *Rf*. By averaging the values of *Rf* derived from the two-dimensional outlines of particles randomly orientated, an indication of the mean departure from

sphericity of three-dimensional particles can be gained. In the instance of oilfield sands, the majority of sand experienced has a mean departure from sphericity of $Rf = 0.5$. This is the default value used within the erosion models. However, due to the sensitivity of erosion to *Rf*, facility is available to vary the roundness factor to correspond to varying field conditions.

The traditional classification of particle shape is a simple verbal description. We may extend this description through the application of the roundness factor, providing an insight into the appropriate value to be applied. Table 6-1 provides an approximation of this comparison. Further description of the particle are available; however, the main classifications are shown here. Figure 6-13 details the typical sand shape, as produced by the Foinaven field in the West of Shetland region of the UKCS.

VERBAL DESCRIPTION	APPROXIMATE PARTICLE ROUNDNESS FACTOR
Rounded	0.9 - 1.0
Sub-Round	0.7 - 0.9
Sub-Angular	0.4 - 0.7
Angular	0.1 - 0.3

Table 6-1 Comparison Particle Description and Particle Roundness Factor

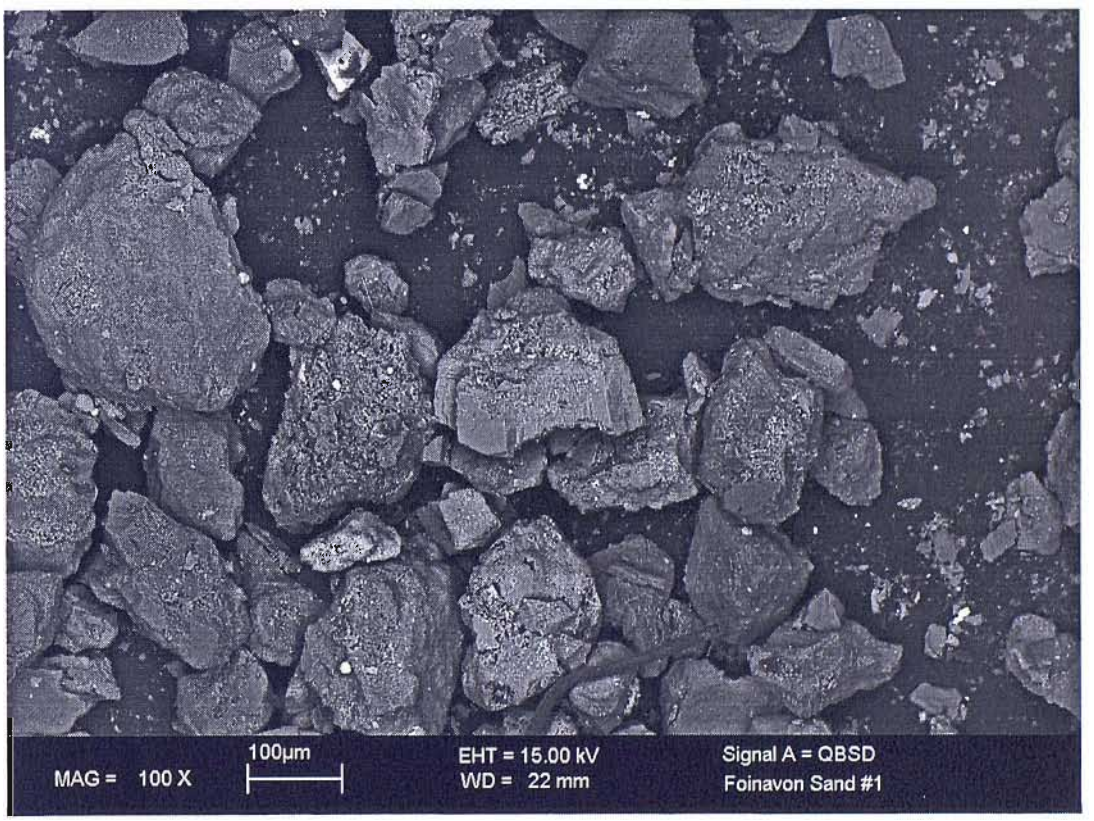

Figure 6-13 Foinaven Field Produced Sand Size and Sharpness

The particle size is known within the embedded FORTRAN of CFX-F3D. This particle size may then be used as a trigger to incorporate variations to the particle roundness factor. An interesting finding of the sand analysis, detailed in section 9.2.5, was that the sharpness of the sand varied with size. The general trend observed was that as the particle size decreased, the particle angularity increased.

6.4.3 Sand Particle Density

The particle density influences both the mass of the particle, given its diameter, and the density differential between phases. The particle mass represents the erosive potential of the particle; through the kinetic energy at impact and the number of particles represented by a given particulate mass flux.

The density differential between phases influences the trajectory calculations of the particle through the momentum argument. As such, from both an erosion and a particle trajectory viewpoint, it is essential that the particle density be correctly defined. Figure 6-14 details various samples of particle density. Note the relatively large variation of density. This variation is attributed to the structure of the reservoir rock, being field dependent. Before an erosion study can be undertaken, the density of the solids produced must be known. Additional complications arise in that any one reservoir may produce a varying particle composition from each well. The default sand density utilised is 2650 kg/m^3, however, facility is available to vary this value.

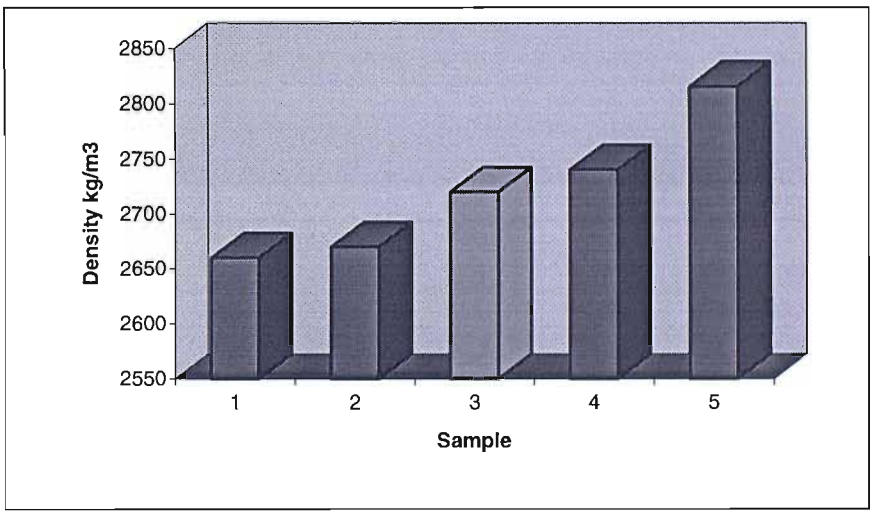

Sample 1 - Candy Surge Drum
Sample 2 - Candy Pump Suction Witches Hat
Sample 3 - Arithmetic Mean
Sample 4 - Candy H.P. Vent Drum
Sample 5 - Boot of Ann Separator

Figure 6-14 Mean Density of Solids Commonly Produced from the Reservoir

6.4.4 Sand Production Rates

The sand production rate has a major impact of the overall erosion experienced; simply through the mass of sand passing through the process system. However, sand production rates and operators reaction to sand, differs greatly between fields. Table 6-2 details the typical production rates for a

number of fields. The actual sand production rate is dependent upon the structure of the reservoir, the fashion in which the wells have been drilled, the manner in which the well is operated and the maturity of the well. Intrusive downhole techniques are available, which aim to reduce the sand production rate. Such techniques include gravel packing, where gravel is packed around the inlets to the riser. This packing acts as a crude filter, preventing large solids from being passed.

The normal unit of measure for sand production rates is pounds of sand per thousand barrels, PPTB. This somewhat quaint unit of measure is derived from the quantity of sand collected in the separator for a given flow rate, the thousand barrels. Part per million, by volume and by weight, is also used due to the low particle concentrations commonly experienced.

The philosophy of the operator regarding sand production differs greater through the various fields; Forties consider 20 PPTB to be serious. However, Venezuela and the Gulf of Mexico fields consider any concentrations below 0.02% by volume to be clean. The figure of 0.02% by volume relates to a sand production rate of 120 PPTB, or one barrel of sand arriving at the separator each day for a 5000 bpd well. This failing to appreciate levels of sand production stems from the methods used in its assessment. Shakeout centrifuge systems, principally used for water cut measurement, are utilised. A water cut of 0.02% is trivial, as such the sensitivity of such systems is insufficient to measure sand concentration. A much increased sample size is required to improve the systems accuracy to a usable state for sand.

FIELD	SAND LITRES/DAY	OIL BBLS/DAY	PPM BY VOL.	PPM BY WT	PERCENTAGE BY WT	PPTB
Forties A+E	311.5	133000	15.5	34.9	0.0035	9.3
Forties B	92	62000	9.8	22.1	0.0022	5.9
Forties C	98	42000	15.5	34.8	0.0035	9.3
Forties D	237	92000	17.1	38.4	0.0038	10.2
Ula (Worst)	353.5	12000	195.1	439.0	0.0439	116.7
Ula (Typical)	44.2	12000	24.4	54.9	0.0055	14.6
Venezuela	604	4000	1000	2250.1	0.225	598

Table 6-2 Typical Sand Production Rates

7. Development to the CFD Code to Enable Erosion Predictions

7.1 Introduction

In its basic form, CFX-F3D has no ability to predict erosion or even register a particle impact. The code simply produces a visual trace of the particles trajectory through the flow domain, with consideration given to particle impacts internally. To overcome such limitations, the author has substantially modified and developed the existing particle tracking routines held within CFX-F3D, embedding an erosion model and the subsequent numerical support for that model. Three source routines where supplied by AEA Technology which represented the particle tracking capabilities of CFX-F3D; including PARCAL, TRACK and BCSPAR.

The principal operations of these routines are as follows; PARCAL initialises the trajectory calculation, such as computing the number of starting positions and the number of particles each trajectory calculation represents, given boundary conditions supplied by the user. PARCAL then calls TRACK, allowing the trajectory of each particle within the flow domain to be calculated, given the momentum argument between phases. See chapter 6 for a description of the transport equations used. At a particle impact, TRACK calls the sub-routine BCSPAR. The original form of BCSPAR is such that it solely computes the reflected velocity of the particle ; which is subsequently passed back to the TRACK.

Through the modification of these sub-routines, the necessary parameters at particle impact can be determined, allowing erosion to be predicted and the resulting data visualised by surface plotting techniques.

7.2 The FORTRAN Routines, their Development, Requirements and Assumptions

Various predictive studies in the past have been aimed at the development of stand alone erosion models; see chapter 2. Each study sought to predict erosion rates based on a common core of variables, or manipulations thereof. As such the primary stage in the introduction of a *CFD* erosion model was the accumulation of these core variables for each particle impact event, including;

1) position of the particle impact.
2) velocity of particle at impact.
3) angle of particle at impact.
4) particle characteristics;
    - particle sharpness.
    - particle diameter.
    - density, mass of particle.

- Young's modulus of particle.
- Poisson's ratio of particle

5) specification of suspension fluid;

- viscosity.
- density.

6) declaration of the surface material type;

- Young's modulus of target.
- Poisson's ratio of target.
- Transverse rupture stress or yield stress of target.
- characteristic velocity component of target.
- deformation erosion factor of the target.

Within the basic form of CFX-F3D, limited data is supplied with regards to the particle movements, in the form of the x, y and z location of each particle as it passes through each control cell of the finite volume mesh. This particle movement data is not of a workable form, hence each of the core variables detailed, needed to be computed or declared within the three particle tracking FORTRAN routines discussed.

7.2.1 Supporting the Erosion Model - Calculation of Impact Event Data

As stated, that FORTRAN sub-routine performing the majority of the data calculation and manipulation was BCSPAR, it is this sub-routine that holds the erosion equations themselves. As such, all of the erosion variables had to be made available within this routine. Those variables held within the main structure of CFX-F3D, were passed to BCSPAR through either the common block facility, or the call argument at the head of each sub-routine. Those variables, not available in the common structure of CFX-F3D, had to be calculated individually within BCSPAR or one of the supporting routines. The following sections detail how each variable of interest was made available to the erosion equations.

7.2.1.1 The impact location

To predict the distribution of erosion, it was necessary for the location of the impact to be known. The position of the particle impact, in terms of its i, j and k location, was declared through the interrogation of the sub-routine TCUINT. TCUINT extracted the relevant information from the particle tracking array, held within the main structure of CFX-F3D. Further to the i, j and k location being known, it was necessary to determine the node or control cell number of each impact. The node number was required as address information for the surface plotting techniques. The reader is referred to Equation 7-3 and the related paragraph for details of how the node number was found and used.

7.2.1.2 The particle impact velocity, squeeze film and Reynolds number

The particle impact velocity components, *u*, *v* and *w*, were calculated within a sub-routine of TRACK, being passed to BCSPAR through the call argument. In addition to *u*, *v* and *w*, the perpendicular and parallel velocity components were also passed to BCSPAR. To ease the use of velocity components, the *speed* of the particle at impact was that used within the erosion model. The *speed* at impact was determined within BCSPAR, simply being the root-square of the velocity components; *u*, *v* and *w*. Further, to *speed* at impact being determined, the *perpendicular speed* at impact was also calculated. The *perpendicular speed* being of interest for squeeze film and critical particle Reynolds number.

Manipulations to the *speed* at impact were undertaken for liquid flows, or where a condensate occurs. The squeeze film retardation factor was computed within BCSPAR through consideration of the particle Reynolds number at impact; utilising Equation 6-30. The particle Reynolds number was computed by the *perpendicular speed* at impact. This retardation factor was then applied to the *speed* at impact, allowing squeeze film considerations to be made within the erosion model. Further, the retardation factor was utilised in the calculation of the reflected velocity components, else an over energetic particle would have been encountered at rebound.

The critical particle Reynolds number was also calculated within BCSPAR, being employed as a filter for low energy particle impacts that are non-erosive; enabling computational effort to be minimised. The critical particle Reynolds number allowed a threshold impact velocity to be established, below which erosion was assumed to be negligible. See Equation 6-30. If the Reynolds number at impact did not exceed the critical particle Reynolds number, then the impact was ignored by simply bypassing the erosion equations and subsequent data manipulation. The need for a threshold velocity arose when particles became entrapped in boundary layer regions, causing the particles to roll or bounce along the wall, when the velocity vectors of the flow field all point towards to wall.

7.2.1.3 The angle of impact

The angle of impact was calculated through the application of area vector considerations for each particle impact, see Equation 7-1. The vector components of the particle impact normal to the surface being computed within BCSPAR, giving areas in the three-dimensions, AREAX/Y/Z. The components of the area vectors being based upon the area of the cell face boundary, the face directions and the Jabcobian. AREASQ was then simply the sum-square of the area vectors. The flux, or dot product, was found by multiplying each of the vector components by its appropriate velocity component, i.e. U*AREAX, and summing over all the components. The angle argument is then;

Equation 7-1

$$\alpha = A\sin\left[ABS\left(\frac{Flux}{\sqrt{AREASQ} * Speed} \right) \right]$$

This angle was computed in radians, being referenced to the wall. Arccos can be used, as opposed to Arcsin, if the user requires the reference to be to the normal.

7.2.1.4 The particle characteristics

The density and diameter of each particle was set within the command file of CFX-F3D, i.e. the user interface. The mass flux of the particles was also set within the command file. The reader is referred to section 7.4 for the dealing with the mass flux and its influence on the erosion rate. PARCAL calculated the mass of individual particles, assuming that they are spherical. These variables were subsequently passed to BCSPAR, through the common block from CFX-F3D. Additional information, describing the particle characteristics, was set by the user within BCSPAR. The user defined database allowed information to be specified regarding the roundness factor of the particle, its Young's modulus and Poisson's ratio. These constants were then subsequently utilised by the erosion model.

7.2.1.5 The characteristics of the suspension fluid

The squeeze film retardation factor required knowledge of the fluid parameters, being the density and viscosity. This information may be passed directly from the main structure of CFX-F3D, or specified by the user within BCSPAR. The need for user specification arose from modelling gas condensate films at the wall. CFX-F3D, holds no information regarding such films, as such must be set explicitly within BCSPAR. If a bulk liquid had been specified, such as oil, then CFX-F3D was able to supply the required fluid parameters.

7.3 Declaring the Material Type of Individual Surfaces

In addition to declaring the particle impact characteristics to the embedded erosion model, one must also declare the material characteristics and constants used within the model. Difficulties arose as differing material types are commonly used within chokes, the trim may be a 6% cobalt binder tungsten carbide, whilst the body may be a AISI 1020 carbon steel. As such, there was a need to develop a technique whereby the material type of a surface could be defined. This declaration of differing material types was achieved by simply passing the face or patch name of each block face, set within the pre-processor, to BCSPAR. BCSPAR then recognised a series of unique face names, allowing areas of differing materials to be identified. In essence the face name simply denoted to the erosion model which constants and erosion parameters to extract from a database held within BCSPAR.

Figure 7-1 shows the trim area of a needle and seat choke, this area was given the face name TUNG6. The erosion model then recognised this area as tungsten carbide, whilst the remainder was assumed to be the default material, AISI 1020 Steel. If no face name details are provided, the code will predict erosion rates for the default steel. Those materials that are recognised by user FORTRAN, namely

BCSPAR, and declare to the erosion model are given by Table 7-1. The material parameters are detailed by Table 9-3.

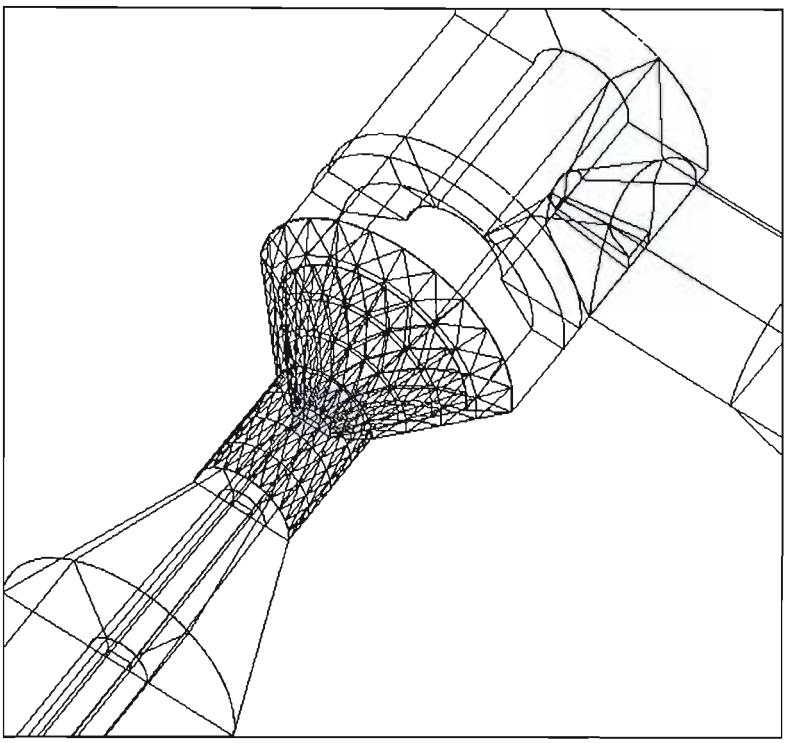

Figure 7-1 Declaring the Material Type of a Surface within a Geometry

PATCH NAME	MATERIAL
Default	AISI 1020 Carbon Steel
SSTL	17.4 pH Stainless Steel
TUNG6	6% Cobalt Binder Tungsten Carbide
TUNG11	11% Cobalt Binder Tungsten Carbide

Table 7-1 Materials Declared in BCSPAR

7.3.1 The Coefficient of Restitution and the Relationship of the Face Name

In addition to defining material and erosion parameters, the face name was utilised to denote the value of the coefficient of restitution; E_{par} and E_{perp}. Once the material type was declared, the form of the coefficient of restitution, given in section 6.3.1, was known. The correct coefficient value being determined from the relevant power series (Equation 6-24 to Equation 6-27), given the angle of impact and the material type. To include the parallel coefficient of restitution, those equations describing the reflected velocities of the particles had to be re-written, such that they held the form given by Equation 6-21. The original form of the reflected velocity equation (Equation 6-19) was also held within BCSPAR to ensure correct handling of particles at symmetry planes where the coefficient of restitution is assumed to be one. A filter loop was written into BCSPAR to ensure the correct form of the reflected velocity equation was utilised.

The patch type was also passed to BCSPAR. We know that symmetry planes are commonly utilised to simplify the flow solution; however problems arise due to their presence. To avoid erosion predictions being made for symmetry planes, a filter loop was included to ensure that symmetry planes were ignored by the erosion model. Further to the filter loop for symmetry planes, a 'no' filter loop, based on the face name, was written into BCSPAR, allowing certain surfaces to be removed from the erosion prediction at user request.

7.4 Embedding the Erosion Model within CFX-F3D

Once the core variables and erosion parameters had been declared, combined with the ability to distinguish the material type of individual surfaces within the flow domain, the erosion models of Hashish **[Ref. 37]** and Bitter **[Ref. 9]** were embedded within BCSPAR. Thus, providing the capability to predict *cutting* and *deformation* erosion, the reader is referred to Chapter 4 to review the equation forms. From Chapter 4, the structure of the erosion equations is seen to vary with the target material type; with regards to the characteristic velocity of cutting erosion, *Ck*, and the characteristic velocity of deformation erosion , *Dk*. To enable the equation forms to be varied, a similar approach to that described for declaring the material type was utilised; where, given knowledge of the face name, the appropriate equation forms could be selected. The total erosion experienced at each impact was then simply found by summing the contribution of each of the erosion models; providing, *Wt*, the total eroded volume at each particle impact (mm^3).

Each trajectory calculation was used to represents a number of particles. It would be impossible to simulate every particle entering the flow domain, as such the particle trajectory approach was adopted. The mass flux of individual trajectory calculations, PMASS, was determined within PARCAL; given the global mass flux specified on the inlet patch and the number of trajectory calculations to be made. The number of trajectory calculations was set by the user through the number of starting points and the number of particle sizes to be tracked. The individual trajectory mass flux was then passed to BCSPAR through the call argument; where, given the particle mass, the number of particles per second, NPART, that each trajectory calculation represents was found. NPART being used as a multiplying factor on *Wt*, giving the projected erosion per second (mm^3/sec);

Equation 7-2 $PROJ = Wt*NPART$

Further multiplying factors are normally applied depending on the time scale of erosion being investigated.

7.4.1 Additional Impact and Particle Data Calculated

Further to the speed, angle and eroded volume being determined for each impact event, additional impact data was calculated. This additional impact data was the particle kinetic energy and particle momentum at impact. The benefit of holding knowledge regarding such additional impact data was

the provision of a correlation relationship, enabling comparisons and observations to be drawn regarding the rate of erosion and the distribution of particle kinetic energy.

Particles that become trapped within boundary layer regions or backflow areas were killed by CFX-F3D, with the aim of minimising computational effect. If a significant number of particles were terminated in this fashion, the resulting erosion prediction would be incorrect. It was important that the termination cause of a trajectory calculation be known, enabling an assessment of the prediction accuracy to be made. To this end, a user file was created, providing provision to write data regarding the termination cause. A number of termination causes are inherent within CFX-F3D, including;

1. PARTICLE LEAVES FLOW DOMAIN.
2. TIME/SPACE ADVANCING SLOWLY - particle trapped within boundary layer region.
3. TIME LIMIT EXCEED.

The applicable termination cause was written to file, given a trigger held within TRACK. In support of the termination cause, the residence time of the particle within the flow domain was determined, providing a means whereby an appropriate time limit could be set. If a particle became trapped in a backflow region, hypothetically, it could continue to recirculate continuously. Those functions aimed at removing slow moving particles would be ineffective, as such a time limit must then be applied to handle such particles.

7.5 Data Manipulation of the Impact Event

Once the erosion and impact data had been determined, there was a requirement whereby the data could be manipulated and written to an output file for viewing by the user. To this end, the generation and utilisation of user files and user arrays or workspace areas was necessary.

The user files provided a means of outputting hard data regarding the impact event. The use of such user files requires that they only be open at the first particle impact, otherwise subsequent impacts would overwrite past data. To accommodate this requirement, a flag was set up which pointed to the first impact, allowing the user files to be opened at the appropriate time. Further to opening the user files, the file headers were only written at the first impact. A total of three user files were required, being named impact1-3, one generated within TRACK to provided information regarding the particle residence time and the termination cause, see section 7.4.1. Whilst two where generated within BCSPAR to detail the various impact variables and statistical analysis. The reader is referred to section 7.5.1 for a summary of the data written to file.

The use of user arrays arose through the discontinuous nature of BCSPAR. BCSPAR was only called by TRACK at each particle impact, once the reflected velocity and subsequent erosion predictions had

been made, BCSPAR was closed. As such the user array provided an area of permanent workspace, whereby data manipulation could be undertaken. Three user arrays were created within BCSPAR, VOL, SPD and VER; each array having two columns. VOL allowed the projected erosion to be manipulated, whilst SPD and VER dealt with the speed and angle at impact respectfully. The manipulation of these arrays provided the following parameters; the cumulative eroded volume, the average angle of impact and the average speed at impact.

To increase the value of the above parameters, the flow domain was broken down into three distinct areas; being the body, cage and plug/sleeve. The names in this instance refer to key components within the choke, see Chapter 3. However, the user may specify any combinations of names or areas as desired. The designation of differing areas within the flow domain was achieved through consideration of the face or patch name. See also 'Declaring the Material Type of Individual Surfaces', section 7.3. Here, an IF loop on the unique area names was recognised by the code, enabling the areas of the flow domain to be sorted through the component name. The following component numbers were applied; body (1), cage (2) and plug (3).

Once the components within the flow domain had been identified, the number of particle impacts to that component was also required. The impact number being the second address to the user arrays, the component numbers given in the previous paragraph being the first. The impact number was found through the generation of four integer counters, dealing with the overall number of impacts, the number of impacts to the body, the number of impacts to the cage and the number of impacts to the plug. Once again each counter was made active by an IF loop on the face name, used to designate the differing areas. The counters were given the names ICOUNT1-4.

All the required address information for the user arrays was now assembled, allowing the impact data to be written into the arrays. This followed the convention given in the example, here the eroded volume of the plug is being written to the array VOL. This convention was repeated for each of the component/variable combinations.

Equation 7-3 VOL(ICOUNT3,3) = PROJ

Data manipulation was achieved by summing each of the arrays for all components combinations, for every particle impact. Thus, providing a progressive assessment of erosion. Array summation was undertaken by a DO loop to the value of the individual component impact counters. The average values were found by simply dividing the summation through by the value of the appropriate impact counter. This data manipulation process enabled the following parameters to be assembled;

1) Number of particle impacts
   - body (ICOUNT1)

- cage (ICOUNT2)
- plug/sleeve (ICOUNT3)
- overall (ICOUNT4)

2) Average angle of particle impact (deg)
   - body (AVEA1)
   - cage (AVEA2)
   - plug/sleeve (AVEA3)

3) Average speed at particle impact (m/s)
   - body (AVES1)
   - cage (AVES2)
   - plug/sleeve (AVES3)

4) Cumulative eroded volume (mm3/hr)
   - body (SUM1)
   - cage (SUM4)
   - plug/sleeve (SUM7)

Furthermore, the total number of particle trajectories was known, allowing the average number of impacts per component to be found.

7.5.1 Summary of Erosion Data Contained in User Files

Three user files were created within BCSPAR and TRACK; impact1, impact2 and impact3. These user files contained the following information regarding the impact event. Each data item was written for ever particle impact.

1) termination cause and particle residence time (sec).
2) component impact counters; overall, body, plug/sleeve, cage.
3) particle number/number of particles tracked.
4) particle mass (kg) and diameter (m).
5) position of particle impact (x, y, z).
6) impact velocity components (u, v and w), (m/s).
7) speed at particle impact (m/s).
8) angle of impact (deg).
9) kinetic energy (J) and momentum at impact ($kgms^{-1}$).
10) the eroded volume at impact (mm^3).
11) Statistical analysis of the impact event.
    - the projected eroded volume for each component; body, plug/sleeve and cage (mm^3/hr).
    - average impact speed for each component; body, plug/sleeve and cage (m/s).
    - average angle of impact for each component; body, plug/sleeve and cage (deg).

7.6 Data Visualisation and Surface Plotting of Results; the User Interface

To ensure statistical confidence, it was essential that a large sample size be utilised. In this instance large is used to describe over 500 particles, which may result in greater than 3000 impacts. The greatest problem concerning such a large sample size was how to process and display the impact data. Originally, this data representation took the form of numerical user files, which simply listed all relevant data. Such an approach was acceptable for simple case studies, where no more than 100 particle impacts occurred. However, as the sample size increased with the increased complexity of the flow domain, this method becomes unpractical due to the time requirement.

A more efficient method was sought for impact and erosion data represented and processing; hence the development of surface plotting techniques. Such techniques allow complex 3-dimensional surface plots of the chokes' internals to be constructed. Coloured shading was utilised to differentiate the erosional and impact intensity and location within the choke. Such surface plots provided an excellent vehicle for the display and processing of large quantities of information in a format that was highly visual and relatively easy to understand. The surface plots facilitate rapid design optimisation of the choke via the visual and numeric interface with the user. Furthermore, as such surface plots are highly flexible, an incremental particle size distribution can be set. Here, the results of several runs can be combined, with each run having a differing particle flux, sharpness or size distribution. This approach provided improved control, allowing a wide size distribution to be analysed with fine increments. This was the approach utilised for the numerical investigation presented in Chapter Ten.

7.6.1 Surface Plotting Techniques

To minimise the development requirements necessary for the generation of surface plots, the existing graphics abilities of CFX-F3D were exploited. The use of such an infrastructure required the developer to gain access to the internal workspace and subsequently the output files of CFX-F3D, such that the user could write his or her own data to that file. As such, the four principal operations to generating surface plots were as follows;

1. Generating the workspace required.
2. Identifying and addressing the location of each impact.
3. Writing the impact and erosion data to the workspace.
4. Presenting the results.

The only modification to PARCAL was to provide access to workspace held within CFX-F3D, namely the scalar array. The main advantage of writing data to the scalar array was that all data held within the array was written to the dump file at the end of each run. Firstly, this provided a means to produce a graphical interface with the user, through the post-processor reading the dump file. Secondly, a re-start of CFX-F3D could be initiated from the dump file. In the instance of a re-start, data is already possessed by

CFX-F3D regarding previous erosion predictions, this data being subsequently added to or manipulated. This re-start facility related to the codes ability to combine the erosion predictions of several separate computational runs.

Originally BCSPAR did not have access to the scalar array, however this was a prime requirement, as the core erosion variables were computed within BCSPAR. The scalar array was passed from PARCAL to BCSPAR, via TRACK, by the calls to each subroutine. Within TRACK, the scalar array was extracted from the main workspace arrays of CFX-F3D, through the application of the GETADD subroutine. The main workspace array of CFX-F3D is very large, if the common area approach of FORTRAN programming were to be utilised, large numbers of common blocks, which are difficult to argument, would have to be passed through the code. To avoid this, GETADD was interrogated, returning the address of the workspace area of interest, in our case the scalar array. In addition to passing the scalar array amongst the subroutines, through knowledge of its address, it was necessary to dimension the array within BCSPAR. This dimensioning simply followed the scheme;

```
DIMENSION SCAL(NNODE,NPHASE,NSCAL)
```

Where the array, SCAL, was three columns wide; being dimensioned by the total number of nodes in the problem, NNODE; the total number of phases, NPHASE; and the total number of scalar variables set, NSCAL. These three parameters had to be passed to BCSPAR via the common block. NNODE and NPHASE were held internally within CFX-F3D, whilst NSCAL was specified by the user within the command file. See section 5.10. The advantage of utilising an array scheme for data visualisation was that one was not limited in the nature of the data that could be written to the dump file. One could simply increase the dimensions of the array to accommodate the variables of interest, by increasing the integer value of NSCAL. The syntax for specifying the number of scalars and the name of each scalar variable within the command file was as follows;

```
>> SET VARIABLE
   USER SCALAR1 = USRDCC ERODED
   USER SCALAR2 = USRDCC SPEED
   USER SCALAR3 = USRDCC ANGLE
   USER SCALAR4 = USRDCC KENERGY
```

The term USRDCC was an internal function of CFX-F3D that denotes that the data contained within each dimension of the scalar array was to be presented as surface plots.

In order that the distribution and intensity of the erosion be determined, the location of each discrete impact had to be known. The impact location was available within TRACK in terms of it's *i, j* and *k* co-ordinates, with these co-ordinates being passed through the common block to BCSPAR. However, for

data visualisation proposes, three dimensional co-ordinates were of little use due to the complexity of dealing with them. An improved approach was available through the gridding technique of finite control volumes used to describe the flow domain and the application of the scalar array. Here the flow domain was constructed of a number of discrete control volumes or nodes, each being uniquely number. The total number of nodes in the domain was that utilised in dimensioning the scalar array, i.e. NNODE. Figure 7-2 presents an extract of the surface grid used to describe a flow domain.

The particle impact locations; *i, j* and *k* co-ordinates, were converted into their unique node number, within BCSPAR, through the use of the following function.

Equation 7-4 INODE = IPCB+(K2-1)*NIB*NJB+(J2-1)*NIB+(I2-1)

Where; IPCB - details the block number scheme.

NIB - number of boundary nodes, *i* co-ordinates.

NJB - number of boundary nodes, *j* co-ordinates.

I2, J2, K2 - *i, j* and *k* co-ordinates.

This unique node number was then utilised to locate the particle impact given reference to the nodal numbering scheme of the flow domain; allowing the particle impact information to be addressed within the scalar array. Thus, in addition to the location of the impact; the impact velocity, the angle of impact, the kinetic energy at impact and the erosion contribution were known for each discrete impact. The contribution of every particle impact was then added to the scalar array through the use of the following generic term, held within BCSPAR;

Equation 7-5 SCAL(INODE,NPHASE,ISCAL) = Variable of Interest

Here INODE was given by Equation 7-4, being the unique address of the array. NPHASE was that phase of interest within CFX-F3D, given the default value of 1, whilst ISCAL was the scalar number of interest. Four distinct types of surface plots were available, denoted by the scalar number;

1. Distribution of and localised erosion rates, USRDCC ERODED.
2. Distribution of local particle impact speed, USRDCC SPEED.
3. Distribution of local particle impact angles, USRDCC ANGLE.
4. Distribution of local particle kinetic energies at impact, USRDCC KENERGY.

Such surface plotting techniques were highly effective, allowing large quantities of data to be processed and displayed. However, with such a large sample size it was reasonable to assume that more than one impact could be experienced at any one nodal location. To overcome such an occurrence, the total erosion was simply taken to be the summation of impacts at that nodal location, see Equation 7-6 for the syntax employed in this instance.

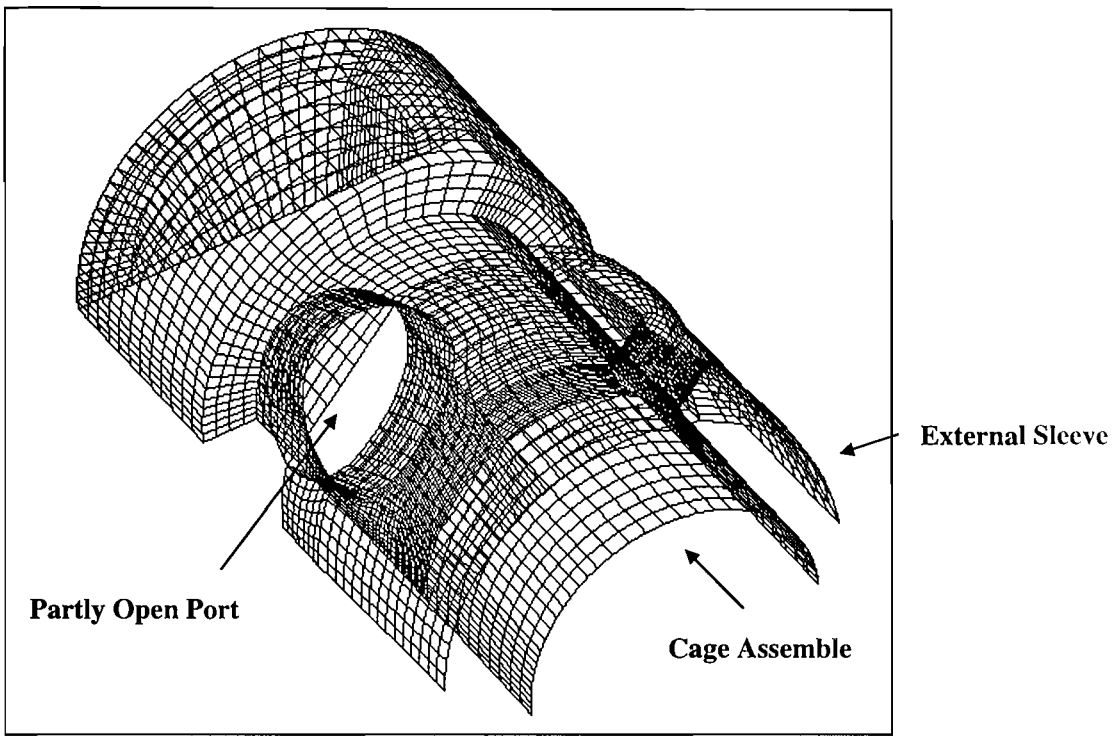

Figure 7-2 Extract of the Surface Grid of a Partly Open External Sleeve Choke

Equation 7-3 details PROJ. A similar approach was taken to determine the local kinetic energy at impact. Whilst the velocity of impact and the angle of impact at any one node was taken to be the average of particle impacts at that nodal location

Equation 7-6 SCAL(INODE,NPHASE,1) = SCAL(INODE,NPHASE,1)+PROJ

The post-processor of CFX-F3D, known as CFX-VIEW, holds a series of data plotting algorithms, which seek to produce surface plots through establishing common variable values over known nodal areas. A colouring scheme of six principal colours was then utilised to present the data in a sequential format, highlighting varying variable values across the internal surfaces of the chosen geometry.

As a cursory note, it was essential that in areas where rapid variation of erosion variables were experienced, the surface grid be sufficiently refined to accurately represent the erosion data. Through the scheme described above, erosion data was written to the centre of each surface node. As such coarse surface grids had failings in terms of accurate data visualisation and erosion representation.

7.7 Flow Diagram Depicting the Treatment of an Impact Event

A flow diagram has been presented, which deals with the underlying actions of predicting solid particle erosion and the subsequent data manipulation within BCSPAR. The flow diagram deals mainly with the modifications implemented within BCSPAR, briefly treating the contribution to the modelling process undertaken by PARCAL and TRACK.

The flow diagram is not intended to provide the reader with an exact description of the modelling process and contributing FORTRAN programming. Rather, the generic structure of the erosion modelling process is shown, to assist the readers understanding of the modelling process. Those readers interested in the exact details of the FORTRAN programming are referred to section 7.8, where an executive summary of each programming modification to BCSPAR, TRACK and PARCAL is made.

The details of how the turbulent flow field and particle trajectories calculates has not been dealt with here, the interested reader with referred to Chapters 5 and 6 respectively for such details.

7.8 Summary of Modifications to FORTRAN Routines

Detailed in the following section is a summary of all the modifications to the three subroutines of CFX-F3D. In total 44 major modifications have been detailed, minor modifications have been excluded on the grounds of triviality.

7.8.1 Subroutine PARCAL

1. Passing of workspace array in the argument call for TRACK (Real, Integer and Character)

7.8.2 Subroutine TRACK

1. Declaring the workspace array in the argument list of TRACK (Real, Integer and Character)
2. Creating common block (USRNNN); declaration of particle number, PDAT, patch type (CFAC), patch name (CFACP) and the I, J and K co-ordinates.
3. Creating common block (MLTGRD); declaration of grid details for scalar array (MLEVEL, NLEVEL, ILEVEL).
4. Dimensioning of the workspace array; WORK, IWORK and CWORK.
5. Setting up of LFIRST flag for opening a user file only on the first particle trajectory calculation.
6. Opening of 'impact3', user file containing information regarding particle residence time and trajectory termination cause.
7. Calling the subroutine GETADD to address the scalar array. Rather than passing large numbers of common blocks through the code, the address for the scalar array may be obtained by interrogating the GETADD subroutine.
8. The particle impact location I2, J2 & K2, is extracted from the trajectory tracking array (IPATH).
9. There are three calls to BCSPAR from TRACK. One, the coefficient of restitution equals unity. Two, the coefficient of restitution is non-unity. Three, turbulent particle dispersion is set. The argument list for each call is modified to included the following; the impact co-ordinates (I2, J2, K2), the workspace for the boundary node array WORK(JPNODB) and the scalar array WORK(JSCAL), and the particle mass flux (PMASS).
10. Write to 'impact3' user file, IF flag included to determine cause of trajectory termination.

11. Write to 'impact3' user file, particle number (NN) and particle residence time (T).
12. Format statements for detailing user file titles and number types.

7.8.3 Subroutine BCSPAR

1. Argument list for BCSPAR modified to include; the impact co-ordinates (I2, J2, K2) the workspace for the boundary node array WORK(JPNODB) and the scalar array WORK(JSCAL), and the particle mass flux (PMASS).
2. Declaring the character type of CFAC and CFACP, the patch type and patch name.
3. Creating common block (ADDIMS) for detailing the total number of phases (NPHASE) and the total number of scalar variables (NSCAL) in the problem.
4. Creating common block (RPART) for detailing the mass of the particle (AMDC) and the diameter of the particle (DIAM).
5. Creating common block (NIJKB) for detailing the nodal co-ordinates system, the number of boundary nodes in each dimension (NIB, NJB, NKB).
6. Creating common block (USRNNN); declaration of particle number, PDAT, patch type (CFAC), patch name (CFACP) and the I, J and K co-ordinates.
7. Creating user arrays for statistical analyses, (VOL, VER and SPD).
8. Setting up of LFIRST flag for opening two user files only on the first particle impact.
9. Setting up of four integer counters, for summating number of impacts to body/cage/plug/overall.
10. Save command to store the user arrays (VOL, VER, SPD) when BCSPAR returns to TRACK.
11. Determining the node number at impact, given the impact co-ordinates / nodal numbering scheme.
12. Generating constants for detailing fluid and particle characteristics, including;
    - particle density roundness factor.
    - Poisson's ratio and Young's modulus of particle.
    - fluid density and viscosity.
    - squeeze film constant (ξ).
13. Generating constants for detailing the properties of the target materials. Held in database within BCSPAR, which is IF looped by the patch name, to extract the correct data for each material type. Four material types held. Constants detailed include;
    - transverse rupture stress or yield stress.
    - Poisson's ratio and Young's modulus of target material.
    - deformation erosion factor.
    - cutting erosion factor, the velocity exponent.

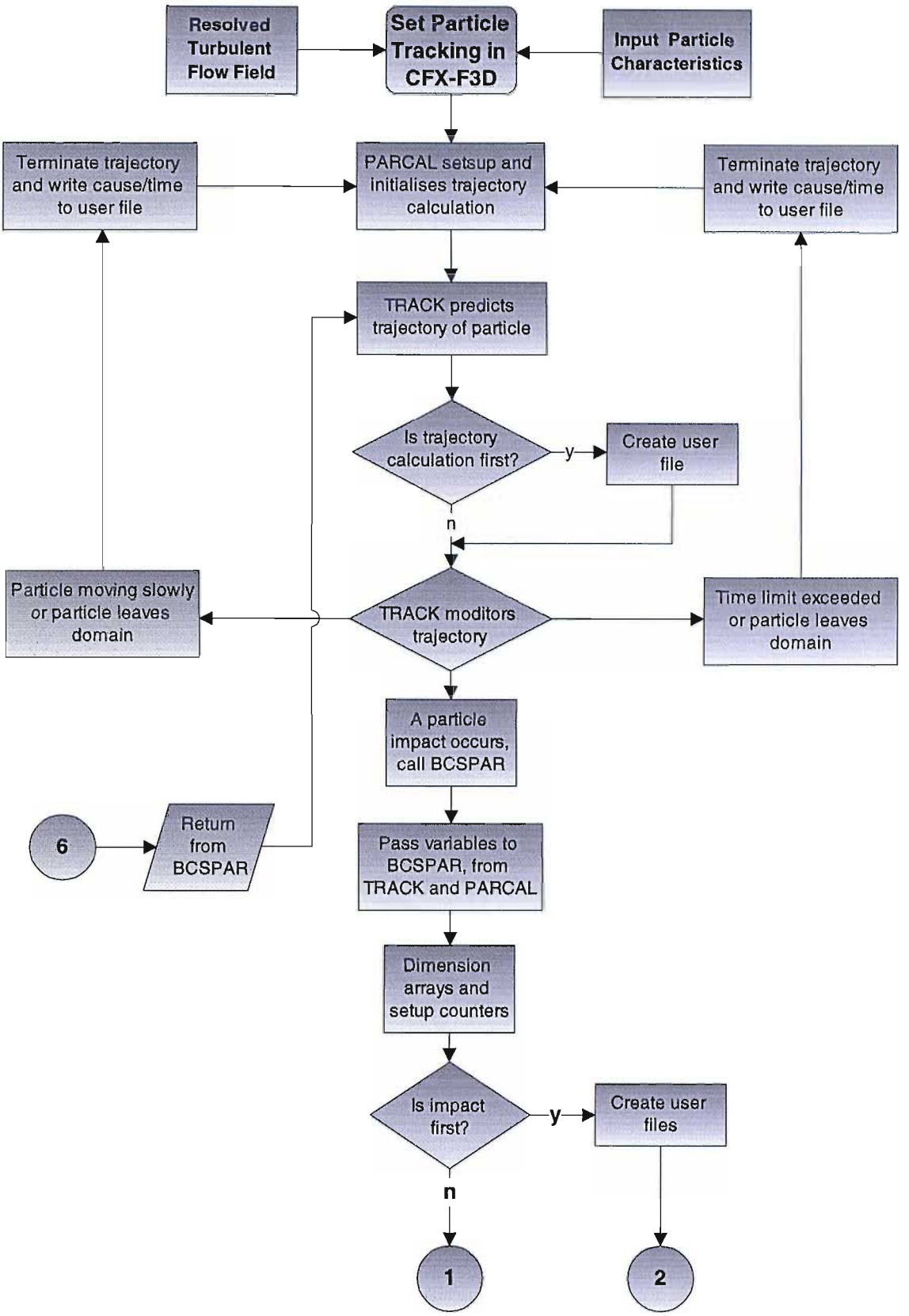
Resolved Turbulent Flow Field
Set Particle Tracking in CFX-F3D
Input Particle Characteristics
Terminate trajectory and write cause/time to user file
PARCAL setsup and initialises trajectory calculation
Terminate trajectory and write cause/time to user file
TRACK predicts trajectory of particle
Is trajectory calculation first?
y
Create user file
n
Particle moving slowly or particle leaves domain
TRACK moditors trajectory
Time limit exceeded or particle leaves domain
A particle impact occurs, call BCSPAR
6
Return from BCSPAR
Pass variables to BCSPAR, from TRACK and PARCAL
Dimension arrays and setup counters
Is impact first?
y
Create user files
n
1
2

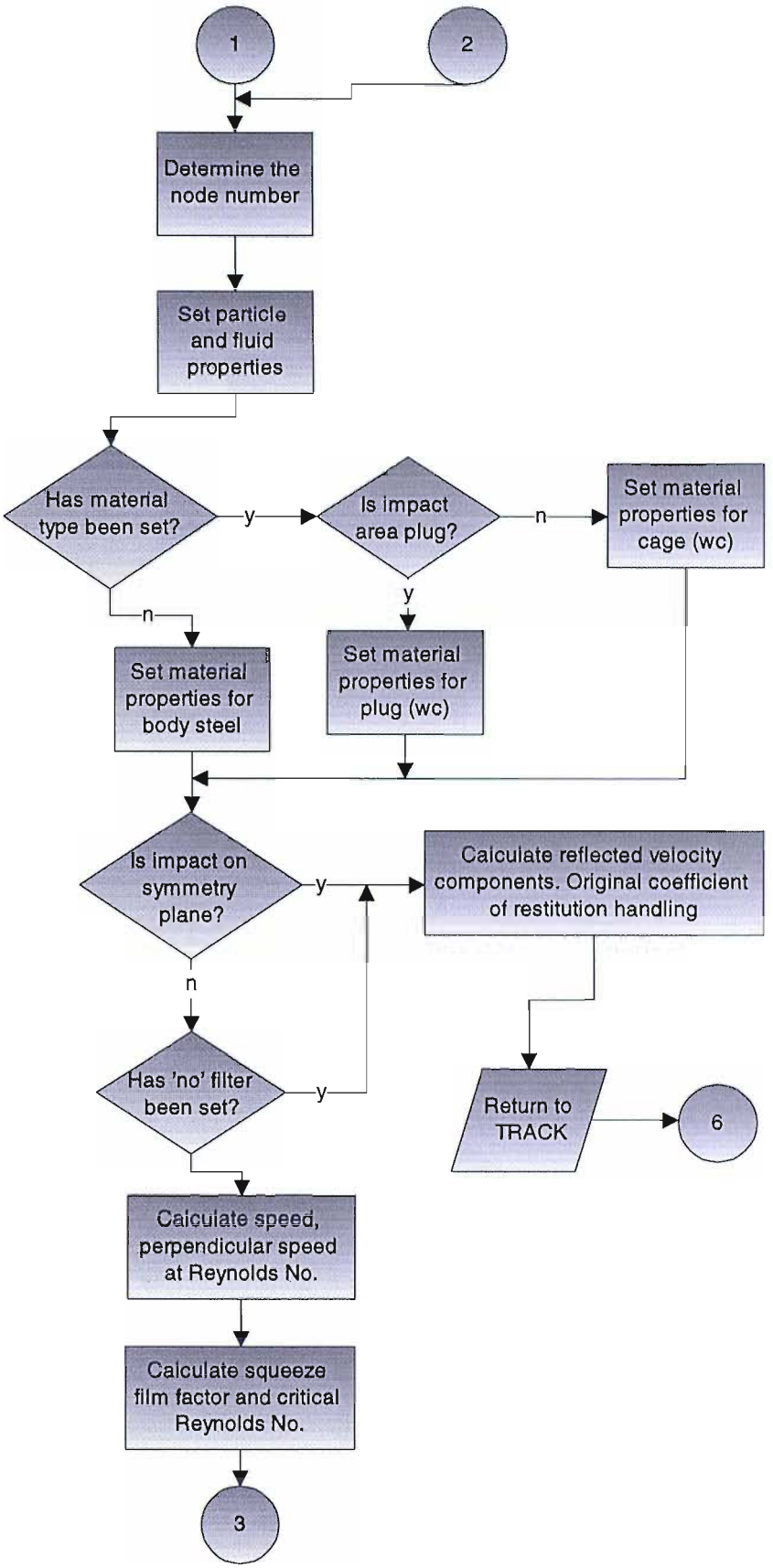
1
2
Determine the node number
Set particle and fluid properties
Has material type been set?
y
Is impact area plug?
n
Set material properties for cage (wc)
y
n
Set material properties for body steel
Set material properties for plug (wc)
Is impact on symmetry plane?
y
Calculate reflected velocity components. Original coefficient of restitution handling
n
Has 'no' filter been set?
y
Return to TRACK
6
Calculate speed, perpendicular speed at Reynolds No.
Calculate squeeze film factor and critical Reynolds No.
3

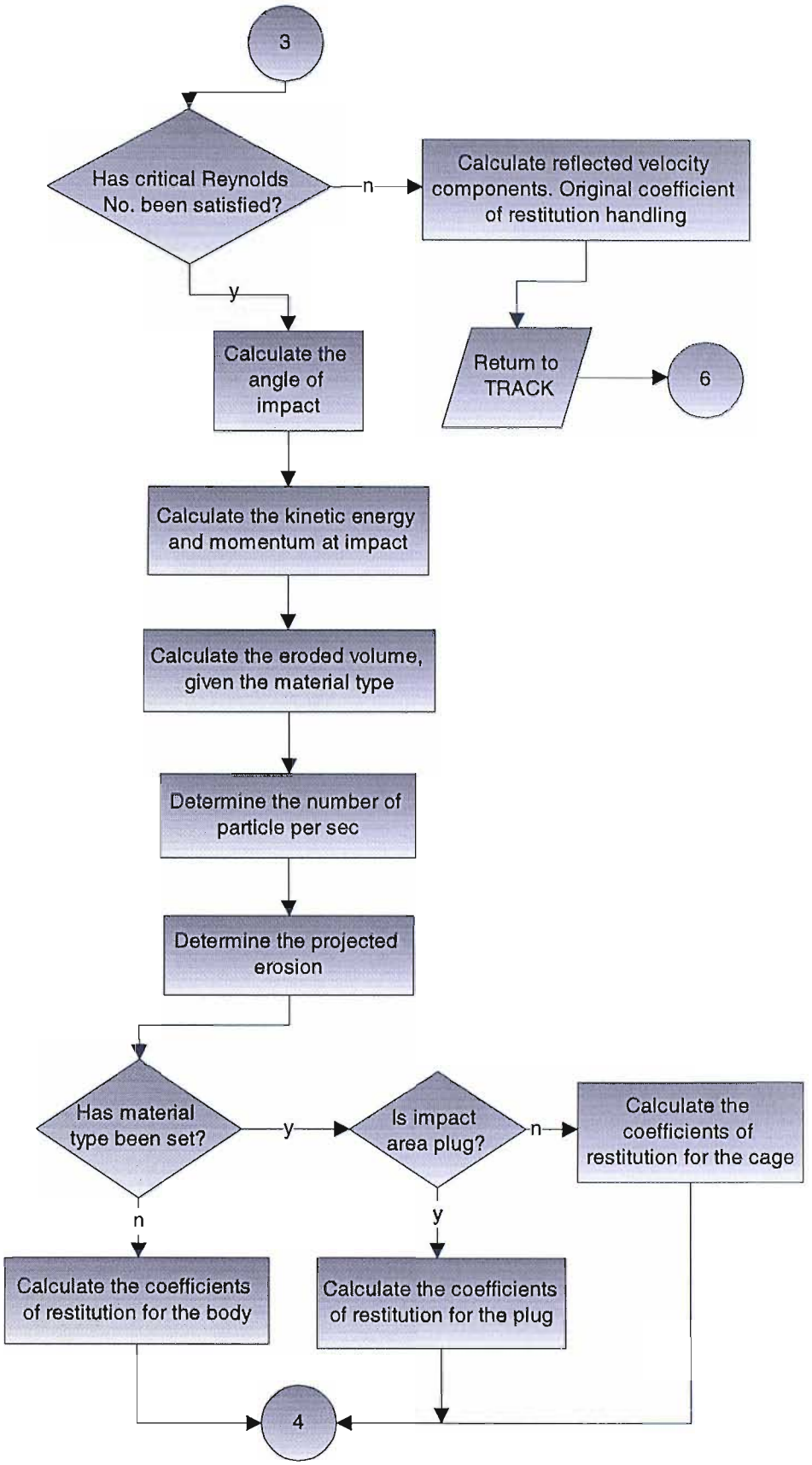
3
Has critical Reynolds No. been satisfied?
n
Calculate reflected velocity components. Original coefficient of restitution handling
y
Calculate the angle of impact
Return to TRACK
6
Calculate the kinetic energy and momentum at impact
Calculate the eroded volume, given the material type
Determine the number of particle per sec
Determine the projected erosion
Has material type been set?
y
Is impact area plug?
n
Calculate the coefficients of restitution for the cage
n
y
Calculate the coefficients of restitution for the body
Calculate the coefficients of restitution for the plug
4

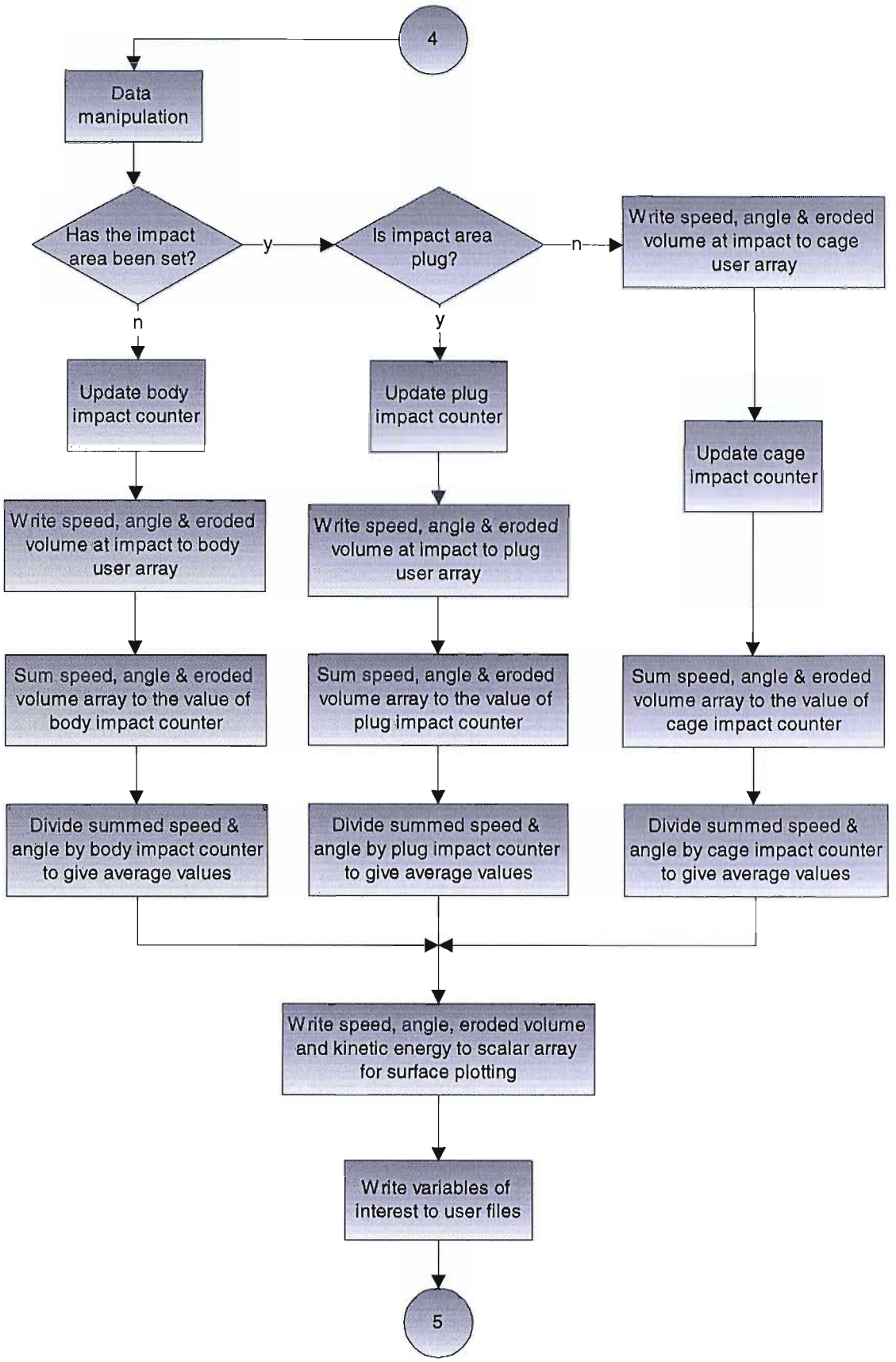
4
Data manipulation
Has the impact area been set?
y
Is impact area plug?
n
Write speed, angle & eroded volume at impact to cage user array
n
y
Update body impact counter
Update plug impact counter
Update cage impact counter
Write speed, angle & eroded volume at impact to body user array
Write speed, angle & eroded volume at impact to plug user array
Sum speed, angle & eroded volume array to the value of body impact counter
Sum speed, angle & eroded volume array to the value of plug impact counter
Sum speed, angle & eroded volume array to the value of cage impact counter
Divide summed speed & angle by body impact counter to give average values
Divide summed speed & angle by plug impact counter to give average values
Divide summed speed & angle by cage impact counter to give average values
Write speed, angle, eroded volume and kinetic energy to scalar array for surface plotting
Write variables of interest to user files
5

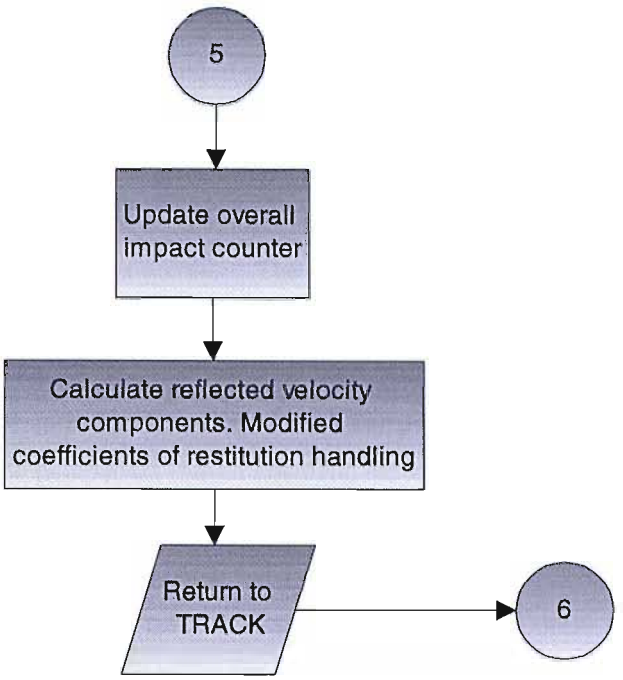

14. Creating two user files; 'impact1, impact2', on the first particle impact, given the true or false flag of LFIRST. Headings for user files printed.
15. Filter loop, generated by an IF loop on the patch type and name, to avoid erosion calculations being made for symmetry planes. Further, a 'no' filter loop is included to allow the user to switch off certain surfaces at request.
16. Speed at impact and perpendicular speed at impact calculated.
17. Calculating the squeeze film retardation factor and the critical particle Reynolds number, given consideration to the particle size, perpendicular impact speed, particle and fluid density and fluid viscosity.
18. IF Filter loop, based on the critical particle Reynolds number, aimed at minimising computational effect generated when particles become entrapped in the boundary layer. Impacts that do not satisfy the critical particle Reynolds number are ignored.
19. Calculating the particle impact angle, given the physical space and the velocity component at impact. Angle converted from radians into degrees.
20. Particle momentum and kinetic energy at impact calculated.
21. Eroded volume per impact calculated, through the embedded Bitter and Hashish equations. Total erosion found by summing the two products of the erosion equations. Volume converted to mm^3.
22. Number of particles per second (NPART), each trajectory calculation represents determined, given the particle mass flux (kg/s) and the mass of individual particles (kg).
23. Projected erosion (PROJ), given the eroded volume per impact and the number of particles each trajectory calculation represents. Scaled to provide the eroded volume per hour, (mm^3/hr).

24. The coefficient of restitution, parallel and perpendicular, is calculated by consideration to the material and impact angle. IF loop utilised to determine the material type given the patch name.
25. Data manipulation and statistical analyses undertaken for the three components; body (1), plug/sleeve (3) and cage (2). The projected erosion, the impact speed and the angle of impact are written to the user arrays; VOL, SPD and VER. The address for the arrays being the component impact counters and the component numbers. The component numbers are given above. The array combinations, nine in all, are summed utilising the DO loop facility, to the value of the individual component impact counters. The summed value of the projected erosion is written to the user file, 'impact2', presenting the cumulative erosion of each component. The summed impact angle and speed are averaged by the component impact counters, before being written to the user file. Thus, providing the average impact angle and speed for all components.
26. Each component impact counter is updated.
27. Write data to the scalar array for surface plotting. The array is address by the node number (INODE), the phase number (NPHASE) and the scalar variable number (1 to 4). Facility is provided to write the following variables for surface plotting;
    - projected erosion (mm^3/hr).
    - particle kinetic energy at impact (J).
    - particle impact velocity and angle (m/s and deg).
28. Writing data to the user files; the following data is available in either 'impact1' or 'impact2'.
    - component impact counters; overall, body, plug/sleeve, cage.
    - particle number/number of particles tracked.
    - particle mass (kg) and diameter (m).
    - position of particle impact (x, y, z).
    - impact velocity components (u, v and w), (m/s).
    - speed and angle of particle impact (m/s and deg).
    - kinetic energy (J) and momentum at impact ($kgms^{-1}$).
    - the eroded volume at impact (mm^3).
    - the projected eroded volume for each component; body, plug/sleeve and cage (mm^3/hr).
    - average impact speed for each component; body, plug/sleeve and cage (m/s).
    - average angle of impact for each component; body, plug/sleeve and cage (deg).
29. The overall impact counter is updated.
30. The reflected velocity components are calculated; given consideration to both the parallel and perpendicular coefficients of restitution for impacts that exceed the critical particle Reynolds number criterion. Original handling of the reflected velocity components occurs if the impact occurs at a symmetry plane or the critical particle Reynolds number has not been satisfied.
31. Format statements for the user files, i.e. headings and declaring number types.

7.9 Solution Techniques and Problems Experienced

The user or instruction manuals of CFX are designed such that, the everyday user is supplied with sufficient information to undertake moderate modelling activities. A failing of these manuals is their lack of support for the more advanced user. This fault propagated itself as a lack of detail regarding the internal structure of CFX-F3D. From the previous sections, one may understand that the ability to pass information within CFX-F3D was essential to the success of the CFD erosion model, where access to the core variables held within the common structure of CFX-F3D was required. To obtain this information, one needed to understand the naming or addressing schemes utilised within CFX-F3D, of which their are many. These addressing schemes are not clearly defined within the user manuals, leading to problems regarding data handling. The problem was two fold; firstly, the difficulties of acquiring the necessary data, secondly, the possibility of writing ones own data which was in dispute with a piece of CFX-F3D internal data. To avoid such a scenario, communications were made with AEA Technology; the authors of CFX-F3D.

At the end of the year 96, CFX-F3D was upgraded from its predecessor, CFDS-FLOW3D. The majority of the modifications between the two were cosmetic, whereby the names were changed. However, one major implication of the upgrade was a series of improvements to the particle tracking model, resulting in a re-write by AEA Technology of the particle tracking routines; PARCAL, TRACK and BCSPAR. The majority of my development work to the particle tracking routines had been undertaken with the old version, CFDS-FLOW3D, which now did not run on the new upgrade to CFX-F3D. As such, a considerable amount of time was spent upgrading my particle tracking routines to be compatible with the new version of CFX-F3D. This upgrade of my routines required the acquisition of the upgraded source routines from AEA Technology, followed by importing all of my modifications into these new source routines.

A software problem was identified with the old version of CFX, CFDS-FLOW3D. The bug propagated itself when the particle transport model was employed. The bug gave the appearance to the solver that a particle had passed through the solid walling of the flow domain. When this occurred the flow solver had no physical co-ordinates, in the form of a finite volume grid, upon which to base the particle trajectory calculation; invariably resulting in a core dump. This situation only occurred when a particle impinged at the intersection of a wall and an inter-block boundary, or at the intersection of two walls. AEA Technology produced a modification routine for the particle tracking model, in the form of an object file. This modification routine ensured that a consistent set of faces were shown to the particle solver, thus preventing particles from passing through a solid wall.

8. Numerical Investigation of Erosion & Control Choke Erosion

8.1 Introduction

This Chapter is concerned with presenting examples of the techniques developed in the previous Chapters, resourcing from each Chapter to provide an overview of how the prediction procedure is employed and the merits of simultaneous technique application.

Numerous examples and studies are tackled, demonstrating the versatility of the prediction procedure developed. These examples include a diversification into the realm of liquid droplet erosion; a pipe bend study whereby particle surface interactions are investigated; a sensitivity study to evaluate the key erosional influences for differing flow applications; the design evolution of a needle and seat choke; and a comparative study of the plug and cage type of choke design versus an external sleeve design.

This section is mainly concerned with gaseous flows, an analysis of the squeeze film retardation factor due to liquid flows is given in Chapter nine. Strictly speaking Chapter Nine should be read first as this Chapter deals with the validation of the erosion model utilised here within. However, it was convenient to the group the subject matter as given. Further to the numerical investigations presented here within, a detailed analysis which compares experimental and numerical erosion data is summarised in Chapter ten.

8.2 Modification to the Code to Facilitate Liquid Droplet Erosion Predictions

To demonstrate the flexibility of the erosion model developed, a study was undertaken whereby the solid particle erosion mechanics and associated particle trajectory support were adapted to facilitate the prediction of liquid droplet erosion. A case study is presented in the following section, which highlights the power of the techniques developed and it's adaptability.

The case study presented is of particular technical merit, as not only does it present the new concept of liquid droplet erosion, it also displays investigations of a non-typical flow configuration. In this instance the potential of utilising the Cameron CC40SR in reverse flow configuration was explored. A CFD investigation of the said choke was undertaken, giving vital information regarding both the flow stability & jet interactions in reverse flow configuration and the liquid droplet regime experienced.

The principal aim of the study was to quantify the risk associated with the presence of liquids in the gas stream and the resultant reaction of the choke body when exposed to an erosional attack. The main concern regarding the reverse flow configurations is that choke body must resist the full intensity of the erosional attack. The body naturally provides pressure containment, thus there is an

issue regarding loss of containment. The trajectories of liquid droplets, in addition to the turbulent flow field, were resolved for a compatible CC30 valve. Extrapolation to the sister CC40SR was then undertaken, allowing predictions as to the occurrence and relative intensity of any subsequent droplet erosion to be made.

The process conditions reported here within represent a collaboration between myself, Cameron (Ireland) Ltd and the BP Bruce Asset. The study was utilised to support a critical path discussion in the Phase II Development of the Bruce petroleum reservoir.

8.2.1 Summary of the Analysis undertaken and the Results Obtained from the Liquid Droplet erosion Study

As with solid particle erosion, the CFD code utilised within the study was CFX-F3D. Very similar modifications to the base code as that described in Chapter 7 were utilised. The code enabled a solution to be found regarding the turbulent flow field and droplets entrained within that flow field. The flow field was treated as a single phase fluid (wet gas), considered to be fully compressible. The Differential Stress closure model of turbulence, solved on a finite volume grid, was utilised to determined the flow field. A total of 275,000 grid cells were employed to describe the flow domain.

Appendix M Figure 5 to Appendix M Figure 13 present a pictorial record of the resolved flow field, giving details of the pressure and flow velocity distributions. Particular attention should be drawn to the vector direction and flow velocities induced by the aggressive pressure drop. In this instance a pressure drop of 192 bar induces gas velocities which approach sonic, Appendix M Figure 7. The jets generated by the trim are very pronounced, showing no indication of dissipating or diffusing before impacting with the choke body, Appendix M Figure 6. Appendix M Figure 8 to Appendix M Figure 13 are not intended to detail the peak flow velocities reached, rather the limits on the flow velocities depicted in the figures are intended to detail the lower range of flow velocities. This self imposed limit enables an enhanced insight into the flow activities within the body cavity. From Appendix M Figure 5 we may observe that the pressure drop occurs immediate to the trim.

Once the time-averaged flow field properties were resolved, the trajectories of the entrained droplets were calculated; being treated as a post-process event. Forces considered to be acting on the droplet included, the momentum argument from the transport fluid, isotropic turbulent dispersion and pressure gradient forces. No droplet-droplet interactions were assumed, enabling a solution to be sought through a Lagrangian frame of reference. Appendix M Figure 8 to Appendix M Figure 13 present the trajectories of a select group of droplets as they pass through the choke; see the constant lines overlaid with the velocity vector field of the fluid phase. The total number of droplets tracked was 324. We may have concluded from the aggressive flow field that droplet velocities would be

high. This conclusion was enforced by the subsequent droplet trajectory calculation. Whilst acceleration length are relatively short, a peak droplet velocity of 221 m/s was achieved; this relates approximately to 60% of the gas velocity.

The physical properties of the fluid and the system parameters, in terms of pressure drop, are summarised in Section 8.2.3. However, due to the difficulties of droplet measurements, no knowledge was held regarding the droplet size and liquid flux rates. To approximate the features of the droplets, a required input for the erosion model, the author referred to the work detailed [**Ref. 67**]. Through the application of Equation 8-1 and Equation 8-2, the droplet diameter range was determined. Equation 8-1 details the maximum size which is obtainable by a droplet in the fluid system under consideration, whilst Equation 8-2 denoted the average reduction in droplet diameter (due to break-up) as the droplet passed through the trim. Equation 8-3 supported the previous Equations. These are simply empirical correlation's derived by the authors of the above referenced paper.

Equation 8-1 $$\theta_{\max} = 5.96 - 0.0911 W_e$$

Equation 8-2 $$\frac{\theta_2}{\theta_1} = 0.6688 W_e^{-0.3977}$$

Equation 8-3 $$W_e = \frac{\rho_g U_{sg}}{\sigma_{st}}$$

The range of droplet diameters determined was of the region of 0.6-1.0 mm. The droplet flux rate was taken to be 1% of the fluid rate. However, this is simply a scaling function, which may be manipulated by hand if required.

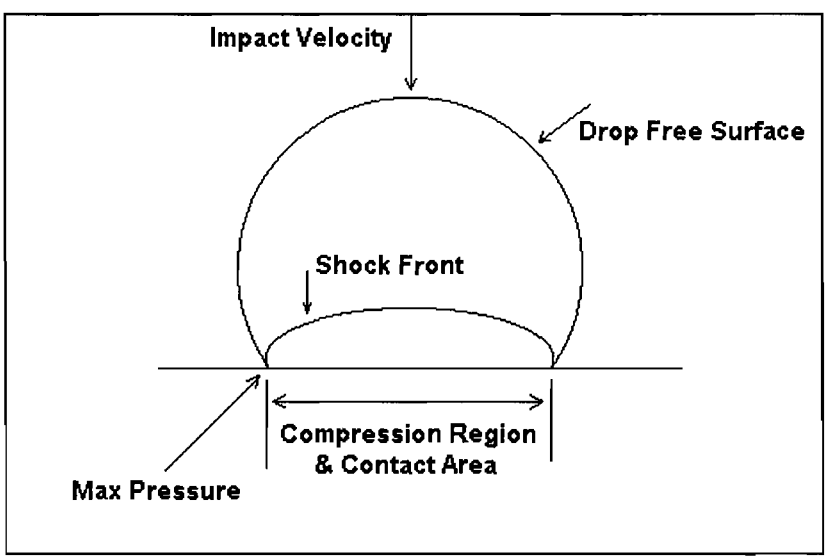

Figure 8-1 Consideration given to a Droplet Impact

Once the droplet parameters had been determined, a calculation regarding the erosion rate and erosive potential of each impact was made. The theory developed to achieve this calculation, centred upon water hammer theory. This is briefly explained by Figure 8-1; here a shock front is generated within the impacting droplet, causing a highly dynamic load to be passed to the target surface via the compression region of the droplet.

The magnitude of the dynamic load generated at impact was determined by Equation 8-4. The surface distribution and range of average droplet impact velocities, U_d, and average angles of impact, α, are depicted by Appendix M Figure 1 and Appendix M Figure 2 respectively.

Equation 8-4 $$D_L = 2\rho_d c_d \sin\alpha U_d$$

The effects of fatigue were assumed to be negligible in this instance, due to the difficulties associated with an accurate correlation. As such, erosion damage was assumed to only occur when the dynamic load applied by the droplet exceeded the yield stress of the target material. This relationship was determined by Equation 8-5, where the normalised erosion rate was simply the dynamic load supplied by the droplet over the yield stress of the target material. If N_{ER} was greater than 1, then erosion damage was assumed to have occurred. Appendix M Figure 3 details the surface distribution of normalised erosion rates, here the maximum value can be seen to be 1.23, occurring, as expected, directly oppose the flow ports of the trim.

Equation 8-5 $$N_{ER} = \frac{D_L}{\sigma_y}$$

The magnitude of the erosion damage induced at impact was determined through Equation 8-6; where the droplet diameter, droplet impact parameters and the speed of sound within the droplet were considered.

Equation 8-6 $$W_{td} = \frac{\theta_d U_d \sin\alpha}{c_d}$$

Due to the computational requirements, it was not possible to undertake a real time simulation of every droplet passing through the choke. A sample of 324 droplet trajectories was utilised. Here, the global mass flux of the droplets was set at 1% by wt; from this global mass flux an individual trajectory flux was determined. Simply the global mass flux was divided by the number of trajectory calculations made, in this case 324. Given the diameter of each droplet its mass was found, allowing the number of droplets each trajectory calculation represents to be determined. This number was then used as a multiplying factor on Equation 8-6, allowing the global erosion to be determined.

A summary of the results presented by Appendix M Figure 1 to Appendix M Figure 4 is given in Table 8-1. Here the choke has been broken down into its component parts, allowing an improved

understanding of the erosion process to be obtained. The main conclusion to be drawn from this summary is that whilst erosion is confined to the body, it is of a sufficiently high rate to warrant a note of concern regarding the potential scale of erosion damage and the mean time to failure. See Section 8.2.2 for a summary of observations and conclusions, and details regarding penetration rates and mean time to failure. It is important to note that the criterion for time to failure was the thickness of the overlay. A weld overlay coats the internals of the body to improve, primarily, the chokes corrosion resistance. A secondary effect of the overlay is an improved erosion resistance. Whilst pressure containment will not be compromised after the overlay has been eroded (the overlay thickness is approximately 3mm) the rate of any subsequent erosion/penetration will be accelerated due to the reduction in material performance.

Choke Component (Nickel Overlay)	Gas condensate Droplets Tracked	No. of Impacts	Projected Erosion (mm^3/hr)	Ave. Angle of Impact (deg)	Ave. Impact Velocity (m/s)
Body	324	3142	141.7	13.7	7.9
Cage	324	1152	0	3.4	33.8
Plug	324	97	0	31.5	10.7
Overall	324	4391	141.7	16.2	17.5

Table 8-1 Summary of Numerical Results for the Reverse Flow CC30.

8.2.2 Conclusions and Observations of the Liquid Droplet Erosion Study

The key conclusion to be drawn from the investigation is that erosion limitation activities will be required, due to the excessive droplet impact velocities generated by the **maximum pressure drop** expected for reverse flow gas injection through the CC40SR. As such it is recommended that the gas be either dried prior to injection or that the pressure drop, for wet gas, be limited to approximately **155 to 160 bar**. The threshold velocity for the onset of erosion should be avoided, limiting material loss effects to fatigue by repeated strike only.

1. It is strongly recommended that the gas be dried prior to injection, else droplet erosion is likely to occur for the maximum pressure drop expected in reverse flow configuration.
2. Recommended limit on pressure drop to avoid erosion by wet gas ~ 155 to 160 bar.
3. Wet gas presents an erosional hazard to the choke body due to the high flow velocities experienced across the trim.
4. Peak flow velocity of gas mixture, Mach 0.92 (Appendix M Figure 7).
5. Peak flow velocity of droplet, 221 m/s.
6. The dynamic loading imposed by an impacting droplet (0.6-1 mm diameter) is sufficient to exceed the yield stress of the Nickel Overlay.
7. The threshold droplet impact velocity for the onset of erosion occurs at 172 m/s for a 90° impact angle.
8. Peak droplet impact velocity 212 m/s, gave a Normalised erosion ratio of 1.23 (Appendix M Figure 3).

9. Predicted peak local erosion rate of 13.5 mm^3/hr, given a droplet flux rate of 1% by wt (Appendix M Figure 4).
10. Predicted peak penetration rate ~ 0.4 mm/hr. Predicted average penetration rate ~ 0.08 mm/hr.
11. Time to failure (given an Overlay thickness of 3.2 mm); Min ~ 8 hr, Ave. ~ 40 hr.
12. Erosion confined to body areas which experience direct jet impingement (Appendix M Figure 4).
13. The reverse flow configuration promotes the impingement of highly energetic upon the choke body.
14. Flow in body cavity is highly turbulent; however, relatively stable (Appendix M Figure 8 to Appendix M Figure 13).
15. Jets penetrates into the choke inlet, whilst in reverse flow configuration (Appendix M Figure 9).

8.2.3 Defining Conditions of the Liquid Droplet Erosion Study

The process conditions investigated represent the maximum pressure drop expected for reverse flow gas injection on the BP Bruce Phase II Development.

Thickness of 625 Nickel Overlay	- 0.125" (3.2 mm)
Yield Stress of Nickel Overlay, σ_y	- 75,000 psi (517.1 MPa)
Fluid Viscosity	- 0.047 cP
Fluid Temperature	- 20 °C
Choke Opening	- 28/64ths
Inlet Pressure	- 6960 psi (480 barg)
Outlet Pressure	- 4176 psi (288 barg)
Fluid Density at Inlet	- 332.6 kg/m^3
Fluid Density at Outlet	- 271.5 kg/m^3
Cp/Cv	- 1.26
Droplet Flux Rate	- 1 % by wt.
Droplet Size Distribution	- 0.6-1 mm
Number of Droplets Tracked	- 324
Speed of Sound in Water	- 1500 m/s

8.3 Evaluation of Key Erosion Influences; A Sensitivity Study

Here we seek to better our understanding of the mechanisms utilised within the erosion model and the influences that some of the key parameters have on the erosion modelling process. CFX-F3D and the modifications I have incorporated within the embedded FORTRAN allow the user to have several options as to how to solve the turbulent flow field and particle trajectories. The flow field can be solved through a number of closure models, whilst the Lagrangian particle trajectories can be treated with the following principal considerations; turbulent dispersion (providing stochastic tracking), modified coefficient of restitution and squeeze film retardation at impact. The effect of differing

modelling techniques will naturally be propagated to the erosion prediction, and it is the magnitude for this effect which is of interest here. In summary the erosional influences can be broadly grouped into three subsections;

1. Turbulence closure model (isotropic and anisotropic)
2. Particle size, concentration and shape.
3. Turbulent dispersion, coefficient of restitution and squeeze film effects.

Section 8.3.1 details the investigation of pipe bend erosion. This rather simplistic situation enabled the key influences of the erosion modelling process to be found. The findings of this initial study were subsequently carried over and elaborated upon to facilitate the complex analysis of erosion predictions within control chokes; section 8.4. The control choke investigated was of the needle and seat design; however, the findings of this study regarding erosional influences are equally applicable to all control choke designs.

8.3.1 Investigation of Erosion within a 90° Bend.

The studies presented in the following two sub-sections are supported by the experimental work of Bourgoyne [**Ref. 13**]. Section 8.3.1.1 details a sensitivity study aimed at evaluating key erosional influences at work, principally within simple bends, which have applicability within more complex geometries. The study emphasises those parameters which are of importance and the measures taken to ensure the accuracy of the CFD erosion model.

Section 8.3.1.2 draws upon the principal findings of the previous section, allowing a detailed analysis of the 90° bend to be undertaken. This section details the models ability to accurately depict the general patterns and erosional trends experienced experimentally.

8.3.1.1 A Sensitivity Study based on the 90° Bend

The study was based on a simple 1.5 times the diameter radius bend, having an internal diameter of 52 mm, the pipe material was a standard 1020 AISI carbon steel. Of interest was the reaction of the modified coefficient of restitution, see section 6.3, and the relationship of turbulent particle dispersion, see section 6.2.3. To ease the interpretation of results, the decision was made to neglect the influence of squeeze film retardation due to near wall liquid films, see section 6.3.2. To facilitate such a discussion, the suspension fluid selected was dry air.

Due to the simplicity of the geometry, the turbulence closure model utilised was the computationally advanced Differential Stress model. Additionally, the decision to utilise this model was driven by the author's interest in the influence of the turbulent dispersion forces on the erosion process, implying there was a requirement to provide the best possible resolution for the turbulent flow field. Whilst the

treatment of the turbulent dispersion of particles does not utilise the Reynolds stresses directly, the overall description of the turbulent flow field by this model is much improved over the isotropic closure models. A comparison of the relative performances of differing turbulence closure models is given in section 8.4.

A final interest which stemmed from the action of the turbulent dispersion model was the effect of particle size on the erosion process. To this end, two ranges of particle sizes were selected, being typical oilfield sands (100-500 microns) and oversized sands (650-1000 microns). The result of particle size ranges was that the total number of virtual particles that passed through the system altered, as the particle mass flux remained constant. See section 6.2. A uniform distribution across the inlet was utilised for the particles, with a total of 400 particles tracked. Four differing particle sizes were used within the range stated above. The average gas velocity was 32 m/s, whilst a particle loading of 112.7 kg/hr was employed.

TEST NO.	1	2	3	4
Pipe Material	Steel	Steel	Steel	Steel
Closure Model	DS	DS	DS	DS
Turbulent Dispersion	**Yes**	**No**	**Yes**	**No**
Modified Restitution	**Yes**	**Yes**	**No**	**No**
Squeeze Film Retardation	No	No	No	No
Suspension Fluid	Air	Air	Air	Air
Particle Type	Sand	Sand	Sand	Sand
Particle Roundness Factor	0.5	0.5	0.5	0.5
Particle Size Range (μm)	650-1000	650-1000	650-1000	650-1000
No. of Sizes	4	4	4	4
No. of Particles Tracked	400	400	400	400
Particle Flux (kg/hr)	112.68	112.68	112.68	112.68
Overall No. of Impacts	2487	2751	6993	7405
Impacts to Pipe	1334	1592	4604	4984
Impacts to Bend	1153	1159	2389	2421
Impacts per Particle - Pipe	3.34	3.98	11.51	12.46
Impacts per Particle - Bend	2.88	2.90	5.97	6.05
Projected Erosion - Pipe (mm^3/hr)	81.98	129.60	374.91	428.73
Projected Erosion - Bend (mm^3/hr)	614.55	849.31	804.65	1074.52
Normalised Erosion - Pipe (mm^3/kg)	0.728	1.150	3.327	3.805
Normalised Erosion - Bend (mm^3/kg)	5.454	7.537	7.141	9.241
Aver. Impact Velocity - Pipe (m/s)	13.68	13.64	24.69	24.64
Aver. Impact Velocity - Bend (m/s)	21.49	24.24	27.36	28.27
Aver. Impact Angle - Pipe (deg.)	8.24	9.10	2.55	2.83
Aver. Impact Angle - Bend (deg.)	20.45	20.39	10.37	10.41
Predicted Penetration Rate (mm/hr)	1.27	1.76	1.78	2.22
Observed Penetration Rate (mm/hr) [**Ref. 13**]	1.35	1.35	1.35	1.35
Error in Prediction (%)	**-5.9**	**23.3**	**24.2**	**39.2**

Table 8-2 Summary of Results obtained from Bend Analysis Sensitivity Study with Oversized Sand Particles

Table 8-2 and Table 8-3 present the results obtained from the bend study. Table 8-2 deals with oversized sand particles, whilst Table 8-3 deals with typical oilfield sands. The first twelve rows of each table detail the variable inputs into the erosion model. All variables are held constant except those discussed earlier; turbulent particle dispersion, coefficient of restitution and particle size range. Here we are concerned with obtaining that set of variables which generates the most accurate results.

Whilst each result of Table 8-2 and Table 8-3 is of interest, that which has most impact and is easiest to comprehend is the final line of each table, the Prediction Error based on the predicted and observed penetration rates. The observed rate being that found experimentally by Bourgoyne [**Ref. 13**]. Here a distinct trend has emerged for both the typically sized particles of Table 8-3 and the oversized particles of Table 8-2. Graphically this trend is clearly demonstrated by Figure 8-2, where the advantages of utilising the modelling techniques of stochastic particle tracking and the modified coefficient of restitution, developed by the author, are shown.

TEST NO.	5	6	7	8
Pipe Material	Steel	Steel	Steel	Steel
Closure Model	DS	DS	DS	DS
Turbulent Dispersion	**Yes**	**No**	**Yes**	**No**
Modified Restitution	**Yes**	**Yes**	**No**	**No**
Squeeze Film Retardation	No	No	No	No
Suspension Fluid	Air	Air	Air	Air
Particle Type	Sand	Sand	Sand	Sand
Particle Roundness Factor	0.5	0.5	0.5	0.5
Particle Size Range (μm)	100-500	100-500	100-500	100-500
No. of Sizes	4	4	4	4
No. of Particles Tracked	400	400	400	400
Particle Flux (kg/hr)	112.68	112.68	112.68	112.68
Overall No. of Impacts	2074	2210	3189	3516
Impacts to Pipe	950	1069	1699	1894
Impacts to Bend	1124	1141	1490	1622
Impacts per Particle - Pipe	2.38	2.67	4.25	4.74
Impacts per Particle - Bend	2.81	2.85	3.73	4.06
Projected Erosion - Pipe (mm^3/hr)	68.90	73.91	261.32	280.35
Projected Erosion - Bend (mm^3/hr)	714.41	729.82	820.84	888.42
Normalised Erosion - Pipe (mm^3/kg)	0.611	0.656	2.319	2.488
Normalised Erosion - Bend (mm^3/kg)	6.340	6.477	7.285	7.884
Aver. Impact Velocity - Pipe (m/s)	16.44	15.82	23.04	22.87
Aver. Impact Velocity - Bend (m/s)	22.28	22.73	26.20	26.51
Aver. Impact Angle - Pipe (deg.)	7.65	7.96	5.98	5.43
Aver. Impact Angle - Bend (deg.)	20.33	20.27	15.29	14.73
Predicted Penetration Rate (mm/hr)	1.47	1.51	1.72	1.84
Observed Penetration Rate (mm/hr) [**Ref. 13**]	1.35	1.35	1.35	1.35
Error in Prediction (%)	**8.2**	**10.6**	**21.5**	**26.6**

Table 8-3 Summary of Results obtained from Bend Analysis Sensitivity Study

From Figure 8-2 we may observe that the use of either turbulent dispersion or the modified coefficient of restitution resulted in a comparatively poor modelling performance, the extreme right hand column. However, one must consider that whilst this result may appear poor, it is in itself a testament to the robustness of the erosion model; in that it may be applied to any problem (in the models most basic form) and still produce acceptable results.

Improved accuracy is achieved if one utilises either turbulent particle dispersion or the modified coefficient of restitution. However, significant improvements in prediction accuracy are obtained when one couples both turbulent dispersion and the modified coefficient of restitution. **And it is upon the grounds of this study that it is recommended that this final solution to modelling be utilised at all times.** This conclusion is in agreement with the findings of Sato [**Ref. 76**], see the text based around Figure 2-7. Sato presented a comparison of stochastic and deterministic modelling, stating that stochastic[7] particle tracking gave the best fit to the experimental data.

Further to the principal observation made regarding the most efficient modelling technique, one may also comment upon several interesting phenomena relating to particle size effects. Here we may conclude that the particle size, and hence its momentum, has an influence on the resulting erosion through manipulation to the particle's trajectory.

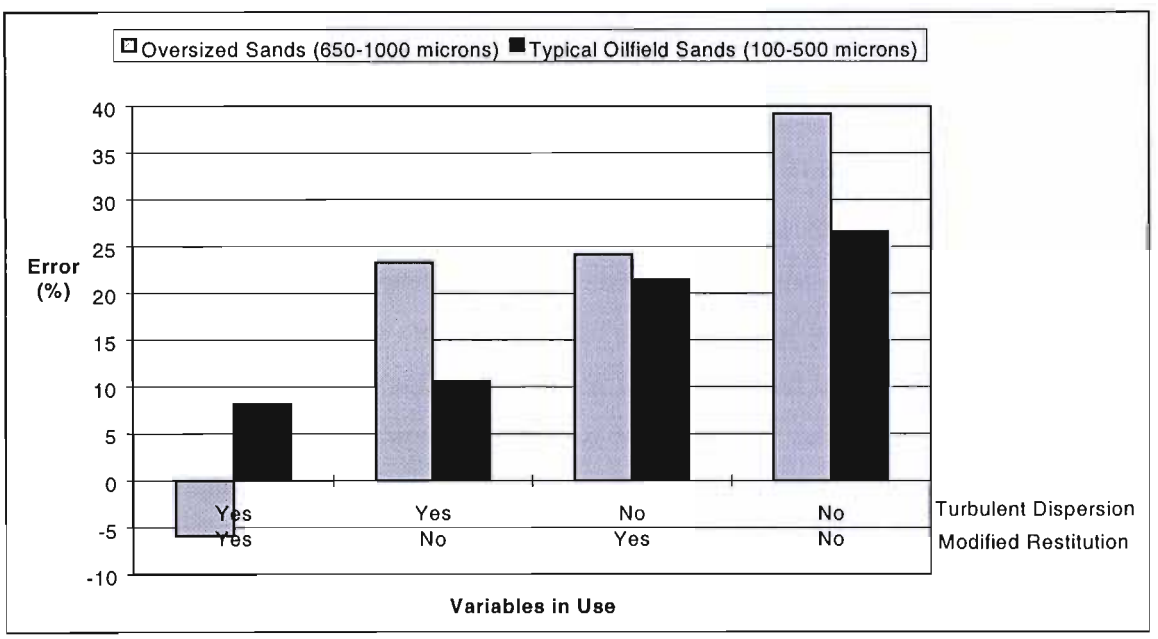

Figure 8-2 Summary of Bend Analysis Penetration Rate Error (%)

The trajectory of a typically sized particle (100-500 μm), is dominated by turbulent eddies within the flow. Here, the application of the modified coefficient of restitution slightly improves the erosion prediction, however, significant improvements are achieved by the utilisation of the turbulent

dispersion term. The particle is sized such that the momentum exchange from the turbulent eddies significantly influences the trajectory of the particle and hence the resulting erosion. The combination of modified coefficient of restitution and turbulent dispersion marginally improves the overall prediction accuracy, with wall effects being relatively insignificant for typically sized particles when compared with turbulence effects.

Oversized particles (650-1000 μm) display a tendency which suggest wall effects are progressively becoming more dominant. Here, the increased particle size, and hence momentum, tend to overcome turbulent eddies within the flow field, promoting a particle trajectory and erosion bias created by wall interactions. For oversized particles, the improved prediction accuracy offered by utilising the modified coefficient of restitution is of a similar magnitude than that provided by turbulent dispersion.

One may hypothesize that a further increase in particle size would result in an increased tendency towards wall effect dominated erosion, and the importance of accurately capturing the coefficient of restitution. Furthermore, the momentum of the particle could be increased through an increase in the mean trajectory velocity, with the influence of the turbulent dispersion term becoming progressively less as the particle velocity increases. It is important to note that an increase in particle velocity would be facilitated through an increase in the velocity of the carrier phase. Dependent upon the local fluid structure, this increased flow velocity would also promote turbulence intensity and hence particle dispersion. This situation implies that care is required in assessing such hypothesis, being considered on an individual basis through such relationships as density differential and carrier phase viscosity.

8.3.1.2 The Graphical Presentation of Erosion within a 90° Bend

Building upon the findings of the previous section, a graphical representation of the erosion experienced within 90° bends is presented here within; we utilise the same conditions as that used previously, with dry air being the motive force. The particle sizes of interest are the typical oilfield sands (100-500 μm), with full consideration given to the modified coefficient of restitution and turbulent dispersion; as recommended. Appendix M Figure 14 details the overall layout, the distribution and intensity of particle impact velocities. The flow field upstream of the bend is fully developed turbulent flow, resulting in little interaction between the wall and particles due to the axis-wise bias of the flow prior to the bend.

As the particles reach the bend, dual effects come to play upon the particles and their subsequent trajectories. Firstly, the particle's momentum allows the particles to escape the slip streams of the flow due to the change in direction, promoting particle impacts. The angle at which the particles impact varies, with a maxima of 54°; as detailed in Appendix M Figure 16. The non-uniformity in particle

[7] Within the body of this text the turbulent dispersion convention is utilised to describe stochastic particle tracking.

EROSION WITHIN A 50 MM, 1.5D RADIUS 90° BEND

Fluid - **Dry Air**
Average Gas Velocity - **32** m/s
Particle Size Range - **100-500** μm
No. of Particle Sizes - **4**
Particle Type - **Sand**
Particle Flux Rate - **112.7** kg/hr
Particle Roundness Factor - **0.5**

Figure 8-3 Surface Contour Plot of 90° Bend Particle Erosion Rate (mm^3/hr)

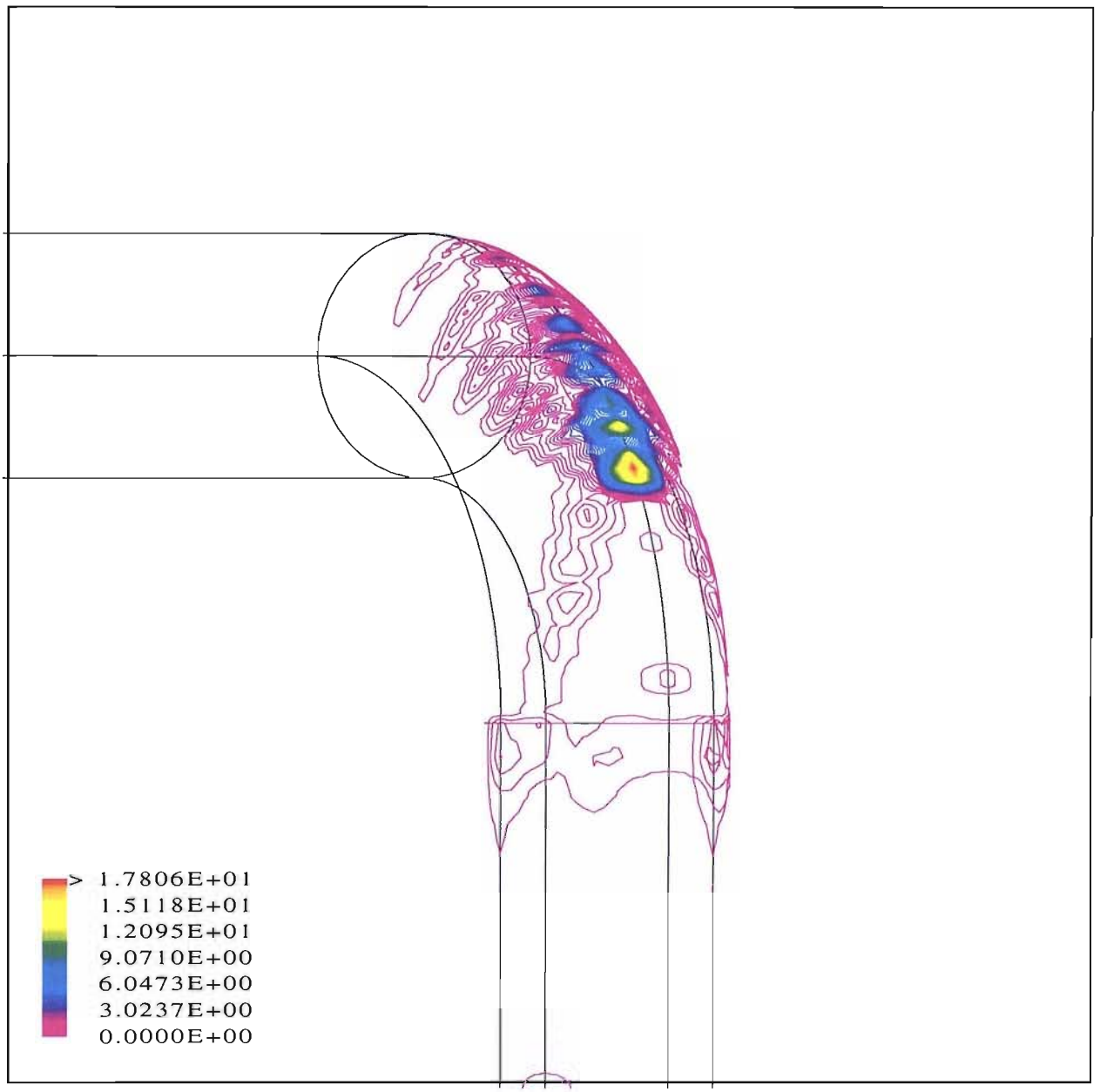

rebound, induced by the incident angle and the Particle Roundness Factor, produces a bias for subsequent impacts downstream of the bend. Secondly, the bend generates a turbulent region immediate to it. The effect of this turbulent region is to promote cross-axial turbulent eddies downstream of the bend, resulting in a tendency for downstream particle impacts.

The advantage of the CFD erosion model is its ability to highlight erosional patterns and trends. This capture of the erosional trend is clearly shown within Appendix M Figures 14-18, where the bend tends to 'channel' the particles into and out of the bends centreline. This channelling phenomenon is supported by the work of Burnett [**Ref. 17**] at the University of Greenwich, where detailed investigations of bulk solids handling equipment has been conducted. Here an erosional 'hotspot' is created, which results in bend puncture within an isolated region, Appendix M Figure 18 and Figure 8-4. From the above detailed modelling, the puncture region was predicted to occur upon the bends centreline at a radial angle of 48-50°. This observation is also supported by the work of Bourgoyne [**Ref. 13**], who reported a peak penetration rate at an angle of 48°.

The ability to accurately capture potential puncture point upon a bend is of value from an integrity viewpoint. Here, the critical location for ultrasonic mapping (non-destructive testing) of the pipe wall thickness can be pinpointed with a high degree of confidence, with the exact location being dependent upon the bend geometry, the process conditions and particle loading/type within the piping system.

8.4 Investigation of Erosion within a Needle and Seat Choke.

Further to the excellent findings of section 8.3.1, where the usage of turbulent dispersion and the modified coefficient of restitution terms were strongly identified as the provider of the best prediction accuracies, a more complex sensitivity study of a needle and seat choke was undertaken.

Here, the aims were similar to the previous sensitivity study, however, in this instance the additional element of utilising differing turbulence closure models was incorporated; namely the anisotropic Differential Stress Model and the isotropic k-Epsilon Model. To this end, the focus of this study was the influence of turbulence effects on particle erosion. Here consideration was only given to the turbulent dispersion term; whilst the modified coefficient of restitution was considered to be active and the squeeze film retardation term was considered to be inactive for each test. A discussion on the influence of the closure model, particle characteristics and turbulent dispersion is given in sections 8.4.2, 8.4.3 and 8.4.4 respectfully. A general discussion on the erosion trends observed for this type of choke is given in section 8.4.1.

The needle and seat geometry was chosen as it lends itself to this study via its relative simplicity and relevance to the problem. The simplicity facilitates an ease of erosion trend identification, whilst

generating a flow field which is both suitably aggressive and holds the fundamental flow feature commonly experienced in chokes. The dimensions for the needle and seat choke investigated were a reproduction of those produced by a leading choke manufacturer.

The choke had an inlet diameter of 3" (75mm) with a linear opening of 25%. The computational domain was constructed from 39 blocks, generating some 45,500 control cells. A symmetry plane was utilised to ease computational requirements. To ensure a good comparison with production chokes of this type, a 6% cobalt tungsten carbide was specified for the trim area. Figure 7.1 details those areas denoted as tungsten carbide within the geometry, whilst the remainder is an AISI 1020 carbon steel.

The sand particles were assumed to have a uniform distribution across the inlet, having a size range of 50-100 μm (small) and 150-200 μm (large). The size ranges were broken down into 6 size groups, in 8 μm increments. A total of 576 particles were computed for each test sequence, with a particle mass flux of 1% by wt. (1.78 kg/hr). The sand was assumed to be semi-sharp and non-spherical in shape, having a particle shape factor of 0.5 applied.

A difficulty in utilising a choke geometry to investigate the sensitivity of altering variables is that no factual data exist upon which to base any observations. However, our learning from the 90° bend case indicates that a certain set of solution parameters offers the best predicted results. If this set of solution parameters produces 'sensible' results, then it is reasonable assumption that these results may be utilised as the benchmark. In this instance, it was the variance generated by changing parameters that was of interest, not the accuracy of the prediction. Further, did varying the parameters have an impact on the erosional predictions. For simplicity dry air was specified, owing to the convenience of neglecting squeeze film effects.

NOTE REGARDING THE SOLUTION TECHNIQUE UTILISED

A total of eight test sequences were completed, where each test was broken into two individual runs, with the summation of these runs being the total for that test sequence. This test philosophy was utilised to make each sequence 'manageable', whilst capturing as much high resolution data as practical. The two flow fields were initially solved, utilising the above mentioned geometry and the two turbulence closure models, k-Epsilon and Differential Stress. Here, the convergence to a satisfactory solution was deemed to have been achieved after approx. 5000 iterations for each closure model.

Once the 'base' flow fields had been derived, the erosion predictions - under the conditions of interest - were solved as post processes. Here, the particle size, the usage of the turbulent dispersion term and the closure model were varied as appropriate. See tables 8-4 and 8-5 for a summary of the test

sequences. The test number is also marked up, as with a summary of the test conditions, on each of the supporting Appendix M Figures. See Appendix M Figures 19 to 67, where 20 to 22 denoted the staging through the flow field.

8.4.1 Erosion within Needle and Seat Chokes - General Observations.

Typical loadings of sand within the field are in the region of 40 wppm (0.004% by wt), see Chapter 6. In this instance, the sand loading was set at 1% by wt, being 250 times that which is considered 'normal'. Erosional failure of the outlet spool - under such excessive conditions - was deemed to occur within approx. 3 days. If the assumption that there is a direct relationship between sand loading and erosion is valid, then failure under typical field conditions would have occurred after approx. 2 years. This corresponds well with operating experience for this type of choke, allowing us to take confidence in the accuracy of the prediction.

Table 8-4 Comparative Study of Gas Driven Erosion in a Needle and Seat Choke (Small Particles).

GAS FLOW SMALL PARTICLES												
Test No.	1	1	**1**	5	5	**5**	2	2	**2**	6	6	**6**
Run No.	1	2	**Sum**	1	2	**Sum**	1	2	**Sum**	1	2	**Sum**
Closure Model.	K-E	K-E	**K-E**	DS	DS	**DS**	K-E	K-E	**K-E**	DS	DS	**DS**
Turbulent Dispersion.	Yes	Yes	**Yes**	Yes	Yes	**Yes**	No	No	**No**	No	No	**No**
Modified Restitution.	Yes	Yes	**Yes**	Yes	Yes	**Yes**	Yes	Yes	**Yes**	Yes	Yes	**Yes**
Squeeze Film.	No	No	**No**	No	No	**No**	No	No	**No**	No	No	**No**
Suspension Fluid.	Air	Air	**Air**	Air	Air	**Air**	Air	Air	**Air**	Air	Air	**Air**
Particle Size. (μm.)	50-75	75-100	**50-100**	50-75	75-100	**50-100**	50-75	75-100	**50-100**	50-75	75-100	**50-100**
No. of Particle Sizes.	3	3	**6**	3	3	**6**	3	3	**6**	3	3	**6**
Particle Loading. (% by wt.)	0.5	0.5	**1**	0.5	0.5	**1**	0.5	0.5	**1**	0.5	0.5	**1**
Sand Flux. (kg/hr.)	0.89	0.89	**1.78**	0.89	0.89	**1.78**	0.89	0.89	**1.78**	0.89	0.89	**1.78**
Total No. of Impacts.	2250	2366	**4616**	2242	2357	**4599**	2182	2351	**4533**	1978	2147	**4125**
No. of Trajectories.	288	288	**576**	288	288	**576**	288	288	**576**	288	288	**576**
Impacts per Particle.	7.81	8.22	**8.01**	7.78	8.18	**7.98**	7.58	8.16	**7.87**	6.87	7.45	**7.16**
Projected Erosion. ($mm^3/hr.$)	239.9	216.0	**455.9**	302.6	255.1	**557.7**	240.9	215.1	**456.0**	259.2	224.1	**483.3**
Erosion Intensity Index			**0.024**			**0.032**			**0.025**			**0.030**
Normalised Erosion Rate. ($mm^3/kg.$)	269.6	242.7	**512.3**	340.0	286.6	**626.6**	270.7	241.7	**512.4**	291.2	251.8	**543.0**
Ave. Impact Velocity (m/s)	30.80	29.05	**29.93**	30.70	29.20	**29.95**	30.85	28.85	**29.85**	31.20	29.64	**30.42**
Ave. Impact Angle (°)	27.03	27.50	**27.27**	28.04	27.70	**27.87**	27.62	27.80	**27.71**	28.16	27.73	**27.95**
Max Impact Velocity (m/s)	91.27	86.08	**91.27**	90.90	85.80	**90.90**	90.84	87.31	**90.84**	88.02	84.26	**88.02**

Appendix M Figures 26, 31, 36 and 41 denote the kinetic energy at impart or that energy transferred to the target surface for each test sequence. In the body annulus that energy transferred, hence erosion, is low, reinforcing the fact that this type of control choke is not prone to body erosion.

Table 8-5 Comparative Study of Gas Driven Erosion in a Needle and Seat Choke (Large Particles)

GAS FLOW LARGE PARTICLES												
Test No.	3	3	**3**	7	7	**7**	4	4	**4**	8	8	**8**
Run No.	1	2	**Sum**	1	2	**Sum**	1	2	**Sum**	1	2	**Sum**
Closure Model.	K-E	K-E	**K-E**	DS	DS	**DS**	K-E	K-E	**K-E**	DS	DS	**DS**
Turbulent Dispersion.	Yes	Yes	**Yes**	Yes	Yes	**Yes**	No	No	**No**	No	No	**No**
Modified Restitution.	Yes	Yes	**Yes**	Yes	Yes	**Yes**	Yes	Yes	**Yes**	Yes	Yes	**Yes**
Squeeze Film.	No	No	**No**	No	No	**No**	No	No	**No**	No	No	**No**
Suspension Fluid.	Air	Air	**Air**	Air	Air	**Air**	Air	Air	**Air**	Air	Air	**Air**
Particle Size. (μm.)	150-175	175-200	**150-200**	150-175	175-200	**150-200**	150-175	175-200	**150-200**	150-175	175-200	**150-200**
No. of Particle Sizes.	3	3	**6**	3	3	**6**	3	3	**6**	3	3	**6**
Particle Loading. (% by wt.)	0.5	0.5	**1**	0.5	0.5	**1**	0.5	0.5	**1**	0.5	0.5	**1**
Sand Flux. (kg/hr.)	0.89	0.89	**1.78**	0.89	0.89	**1.78**	0.89	0.89	**1.78**	0.89	0.89	**1.78**
Total No. of Impacts.	2542	2575	**5117**	2321	2296	**4617**	2559	2570	**5129**	2351	2292	**4643**
No. of Trajectories.	288	288	**576**	288	288	**576**	288	288	**576**	288	288	**576**
Impacts per Particle.	8.83	8.94	**8.88**	8.06	7.97	**8.02**	8.89	8.92	**8.90**	8.16	7.96	**8.06**
Projected Erosion. (mm^3/hr.)	187.3	166.5	**353.8**	173.1	144.8	**317.9**	178.0	157.9	**335.9**	168.5	141.1	**309.6**
Erosion Intensity Index			**0.028**			**0.022**			**0.029**			**0.023**
Normalised Erosion Rate (mm^3/kg.)	210.5	187.1	**397.5**	194.5	162.7	**357.2**	200.0	177.4	**377.4**	189.3	158.5	**347.9**
Ave. Impact Velocity (m/s.)	25.55	24.00	**24.78**	25.35	24.40	**24.88**	24.96	24.31	**24.64**	25.37	24.76	**25.07**
Ave. Impact Angle (°)	28.38	27.16	**27.77**	28.07	28.18	**28.13**	27.58	26.58	**27.08**	27.83	27.56	**27.70**
Max Impact Velocity (m/s)	64.64	63.62	**64.64**	68.40	65.12	**68.40**	63.78	60.84	**63.78**	67.51	64.45	**67.51**

Due to the radial entry of the particles to the choke body, the particles have a tendency to pass to the rear of the annulus cavity before flowing through the trim section. This situation is assisted by the large annulus volume and the fact that the flow in this area is relatively benign/turbulence free (see Appendix M Figure 19 and 23); leading to little energy transfer between phases. This focusing of the particles due to the geometry - similar to that noted by the pipe bend analysis (section 8.3.1.2) - induces a biased particle concentration. This high concentration results in a greater transfer of energy to the target surface in one particular location, as denoted by the increased area of shading on the 'left' side of the taper, resulting in an erosional 'hotspot'. See Appendix M Figure 26.

Field experience supports such an erosional tendency, where a common trend would be the 'cutting' of the needle/seat in one particular location. Here, the particle bias in one location initiates the erosional attack at that point. Once the erosion is established, a continued channelling of particles occurs within the wear site, thus accelerating the localised erosion further.

This flow biasing is also propagated downstream of the trim. The concentration of particles at the 'back' of the annulus cavity are 'picked-up' by the jets generated through the choking action, see Appendix M Figures 19 to 22. The particles are accelerated jet wise, resulting in an erosion 'hotspot' where the jet/particles impinges upon the opposite walling of the outlet spool. This effect is clearly shown by Appendix M Figure 26.

In this instance, the situation is further exasperated by the geometry of the choke itself. The taper angle upon the needle is such that accelerated particles impinge with the outlet walling immediately downstream of the outlet spool expansion piece. This geometric combination ensures that the particles retain their high velocity due to the constricted area of the outlet spool followed by the expansion spool; which maintains the velocity of the carrier phase through the expansion of this compressible fluid. Section 8.5 discusses a method whereby the aggressive nature of this geometry can be refined to prolong the service life of the component.

In addition to the retention of high particle and carrier fluid velocities, the taper geometry is such that the particle impact angles within the outlet spool are at their most aggressive from an erosional viewpoint. The target material in the outlet spool is an AISI 1020 carbon steel, from our knowledge of such materials, their poorest erosion resistance is at an angle of 20 to 30°. The average impact angle within the outlet spool is of a similar magnitude (Appendix M Figure 35), thus ensuring, rather perversely, that erosion is maximised. This observation is common for both particle sizes. Conversely, the impact angle within the annulus cavity is high, here the material is once again the AISI 1020, however at high impact angles this materials erosion resistance is significantly improved.

Appendix M Figures 34 details the particle impact velocities. Here we may observe that the velocities within the annulus cavity are relatively low, however those velocities experienced within the trim area and outlet spool are high. This observation is supported by the maximum impact velocities quoted in Tables 8-4 and 8-5. The large particles (150-200 μm) impact at velocities upto 68 m/s, whilst the small particles (50-100 μm) impact at velocities upto 91 m/s. Further, the high impact velocities are seen to be propagated far downstream due to the high density differential between phases, resulting in significant erosional damage in the outlet spool due to the coupling of the low incident angles, as discussed above. Here, the erosional attack is at least an order of magnitude higher than that experienced across the trim due to the material characteristics.

The trim and the constricted outlet spool were assumed to be a 6% cobalt tungsten carbide (Figure 7.1). This material is able to resist low angle cutting erosion due to its high hardness, see Chapter 4. Whilst the impact velocities within the trim area are high, the angles of impingement are low (Appendix M Figure 34 & 35). The result is minimal erosion across the trim area of the choke, Appendix M Figure 37.

We may conclude that due to both material effects and the geometry of the flow domain that erosion within the outlet spool is significant for all of the test sequences. See Appendix M Figures 27/28 (Test 1); 32/33 (Test 2); 37/38 (Test 3); etc. This failing is well documented for this type of choke, being heightened further by the localised erosion generated by the particle biasing. No further discussion as to the details of each test sequence will be made here due to the repetition that that would impose. The reader is referred to Sections 8.4.2 to 8.4.4, Appendix M Figures 19 to 67, Tables 8-4 & 8-5 and the general comments made above, which are valid for all test cases.

8.4.2 Turbulence closure model; The Isotropic or Anisotropic Approach.

The turbulent flow field was solved for dry air using the two principal closure models, the *k*-Epsilon model and the Differential Stress model. In each case an identical flow domain was utilised, including the grid construction. Interest in the closure model arises through the underlying assumptions of the models, i.e. anisotropic and isotropic turbulence. Through the inclusion of the Reynolds stress tensors, the Differential stress model is able to compute three-dimensional turbulence, whilst the *k*-Epsilon model is limited by its isotropic Reynolds stress assumption. (i.e. $\tau_{xx} = \tau_{yy} = \tau_{zz}$). This variance in the computed turbulence structure is passed to the particle trajectory calculation via the turbulent dispersion term[8] (See section 6.2.3) and hence the resultant erosion.

Furthermore, due to the variance in the underlying assumptions of the two closure models, the resultant fully converged flow fields - the velocity vectors - hold differing structures. It is also noteworthy that effects such as the tendency of the *k*-Epsilon model to over predict turbulent dispersion influences the predicted flow field. The variance in the predicted flow fields (velocity contours and turbulent kinetic energy) of the *k*-Epsilon and the Differential Stress models may be observed in Appendix M Figures 19 to 23 and 44 to 47 respectively.

From Appendix M Figures 19 and 44 we may note that the velocity contours of the Differential Stress model were more developed than those of the *k*-Epsilon model; with the jetting in the outlet spool being better defined. Appendix M Figures 23 and 47 details the turbulent kinetic energy for each of the closure models. The kinetic energy predicted by the *k*-Epsilon model could be seen to be very rapidly attenuated. This reinforces the observation made above regarding the know tendency of the *k*-Epsilon model to over dissipate energy.

[8] It is important to note that the structure of the turbulent particle dispersion function, utilised within CFX-F3D, does not differ between turbulence closure model. Furthermore it is only the *k* term output from the closure model that is employed by the dispersion function. The Reynolds tensors computed by the Differential stress model do not directly impact the resultant turbulent dispersion affected upon the particles.

Whilst the turbulence intensity immediate to the trim was large for the *k*-Epsilon model, this quickly diminished as one traversed downstream. The result of this overall lower turbulent kinetic energy, *k*, (when compared with the Differential Stress model) was that the associated turbulent dispersion acting upon the particles was also lower. As such, those particles which were affected by turbulent dispersion (sub 150 μm in size), experienced a higher number of impacts when subjected to the flow field computed by the Differential Stress model. The high localised turbulence intensity enabled the turbulent dispersion term to become active through a reduced particle momentum, exciting particles perpendicular to the streamlines and hence into the walling. Further discussions as to turbulent dispersion will be given in section 8.4.3.

Due to the lower energy jet predicted by the k-Epsilon model, wall effects tended to dominate, promoting a tendency for the jet to remained partly attached to the walling. This encouraged particle-wall interactions and a tendency for large particles to strike the walling. Those particles excited by the 'centralised' jet predicted through the Differential Stress model, which were not acted upon by turbulent dispersion (greater than 150 μm in size), tended to be accelerated along the centre-line of the outlet spool.

No further discussion of the influence of the closure models will be given here. However, one may readily conclude that the selection of the correct closure model is essential due to its influence on the erosion process through the underlying assumptions. Upon the grounds of the above discussion, I recommend the usage of the Differential Stress over the *k*-Epsilon model due to its superior flow field resolution characteristics.

8.4.3 The Influence of Turbulent Dispersion, Particle size and Concentration.

As detailed previously, within this study we were only concerned with the influence of turbulent dispersion upon the erosion process, including the effect of particle size and concentration. As such the effects of the squeeze film and coefficient of restitution were neglected.

As mentioned in section 8.4.2, the underlying turbulent flow fields calculated by the differing closure models impacts the predicted erosion. The main findings as to this effect may be summarised by the following discussion.

The number of impacts per particle was relatively constant, Table 8-2 and Table 8-3, with the general trend being an increase in the number of impacts as the particle size was increased and turbulent dispersion did not act upon the particle. As noted previously, an increase in particle sizes tended to increase the tendency towards particle wall interactions and the importance of the coefficient of

restitution. The particle size also influenced the number of impacts when the particle was subjected to turbulence dispersion, allowing us to reach an important conclusion regarding the turbulence closure models, the predicted turbulence and the interactions with particles.

It was noted that when the k-Epsilon model was tested for its sensitivity towards the turbulent dispersion function - both small and large particles - the difference between the number of particle impacts was minimal. This allowed us to conclude that the k-Epsilon model did not adequately resolve local turbulence such that it was passed to the erosion process via the turbulent dispersion function. See tests 1, 2, 3 & 4 of Table 8-2 and Table 8-3.

Through the improved predictive capabilities of the Differential Stress model, when the impact frequency of small particles was tested for its sensitivity towards turbulent dispersion, a marked difference was noted (test 5 & 6 of Table 8-2). However, this situation was not replicated for the large particles (tests 7 & 8 Table 8-3). One could then conclude that the Differential Stress model adequately resolved the local turbulence, with the large particle not being acted upon by the dispersion term due to the increased particle momentum associated with the increased size. This resulted in a particle trajectory/erosion process which was dominated by particle-wall interaction for the large particles, whilst the small particles were eclipsed by turbulent dispersion effects.

This last observation is in agreement with the closing comments of section 8.3.1.1, where it was hypothesised that either an increase in particle size or it's trajectory velocity could cause the erosion process to revert from being turbulent dispersion dominated to wall effect dominated. Furthermore, the mean particle velocity influences the particle size at which the transition from wall dominated to dispersion dominated erosion occurs. For the example of section 8.3.1.1, it was noted that particle above 650 μm had an erosion process which was wall effect dominated, whilst those below 500 μm were dispersion dominated. For the example presented above, the particle size at which the transition from dispersion to wall dominated erosion occurred at 150 μm.

This suppression in the transition point occurred due to the increased mean particle velocity. The bend example experienced a peak impact velocity of approx. 30 m/s, whilst for the needle and seat example the impact velocity were as high as 90 m/s. Through the increased particle velocity, the particles momentum was increased, and hence the particles ability to break the influence of the turbulent dispersion function and the tendency towards wall dominated erosion. In the instance of the k-Epsilon model, the predicted turbulence was markedly lower than that of the Differential Stress model, as such the reactive force predicted by the dispersion function was lessened, hence even the small particles (50-100 μm) were wall effect dominated due to the model's inadequate resolution of localised turbulence.

Such observation are further supported if one gives consideration to the eroded volume, Figure 8-4. Here the predicted erosion for the k-Epsilon did not vary between cases; small and large particles with or without turbulent dispersion. However, in the instance of the Differential Stress model, the variance between the predicted erosion for small particles, with and without turbulent dispersion, was marked; whilst no significant difference could be reported for the large particles.

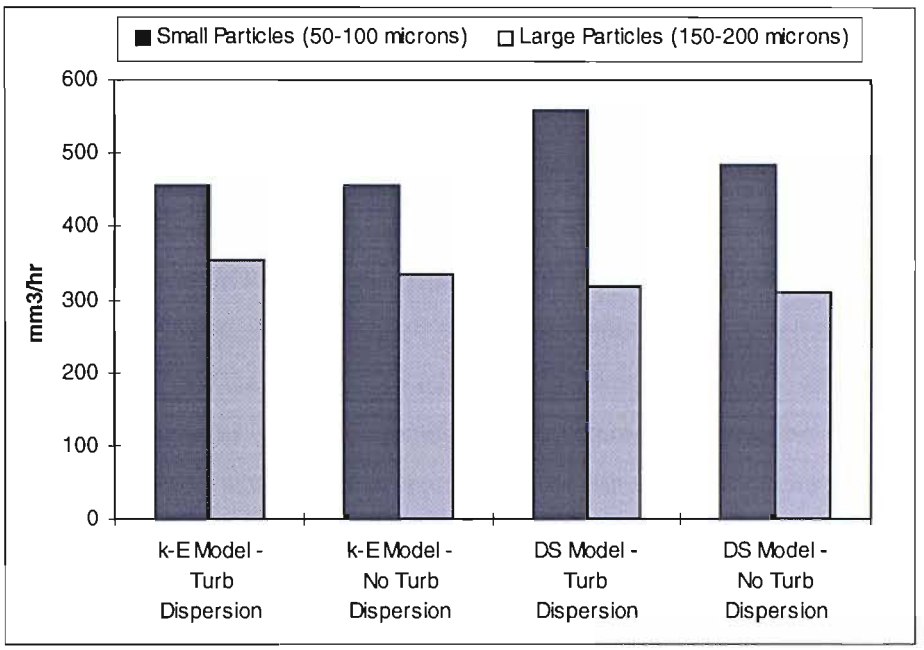

Figure 8-4 Summary of Needle and Seat Choke Erosion Rates

In it interesting to note, Figure 8-4, that the eroded volume predicted by the small particle was the greater. A conclusion as to this occurrence is that the number of particles which represents a sand flux of 1.78 kg/hr was significantly greater for the small particles. The result being that whilst the small particles would result in less erosion (under identical impact condition) then that of the large particles, their numbers biased the erosion prediction. Furthermore, due to the lesser momentum of the small particles, they were easier to excite; resulting in higher impact velocities (peak and mean). See Appendix M Figures 48 and 58. This situation was duplicated in the bend example - section 8.3.1.1 - where like tests, using the Differential Stress model and turbulent dispersion, resulted in the smaller particles predicting the greater eroded volume.

The erosional intensity index, being defined as the local erosion rate over the global erosion rate, gave an indication of the localised intensity of the erosional attack. The greater the index, the greater the localised erosion or 'hotspoting'. From this index the Differential Stress model, operated with turbulent dispersion, gave the most intense attack (test 5). This coincides with our finding that it was this test case - turbulent dispersion being active - where some turbulence effect was acting to drive the particles into the walling at an isolated location. The remaining test case where all wall interaction

dominated, generating an improved particle distribution in the outlet spool and a reduced erosional intensity index.

One may close with the affirmation that the erosion process can be defined as being dominated by either wall interactions, and the associated coefficient of restitution, or turbulent dispersion generated by the flow field. The mass and velocity of the particle, coupled with the resolution quality of localised turbulence, influence the transition point between the two processes. Further, the 'best' prediction results are achieved through the usage of the Differential Stress model and the turbulent dispersion function for particle tracking.

8.5 Investigation of Erosion within a Needle and Seat Choke; A Design Evolution.

From the discussion of section 8.4.1 we understand that the original needle and seat choke design is susceptible to excessive erosion in the outlet spool. This situation arises through the aggressive interaction of the walling and the particles. To mitigate the erosional hazard one must either eliminate the particles from the process stream or minimise their interactions with the walling. The later approach is undertaken here, whereby the design is evolved with the sole purpose of limiting erosion within the outlet spool.

An advantage of the CFD erosion model is that many and innovative approaches to erosion limitation by design can be investigated in a cost effective environment; avoiding the need for hard prototyping. Modifications to the flow domain, such as contouring, and the subsequent re-gridding of that structure can be undertaken in half a day. The solution of the flow field, prediction of erosion rates and interpretation of result would occupy a day. Thus, turn around between design modifications can be achieved in approx. 2 days, allowing the optimum solution to be sought rapidly.

To facilitate compatibility throughout the evolution process, the process conditions and particle loading characteristics remained constant, being identical to those utilised for Test case 3 quoted in Table 8-5 i.e. the k-Epsilon closure model was employed with turbulent dispersion of the particles active. Further, the global dimensions and material characterisation of the chokes, such as inlet/outlet diameters, were identical. As an initial discussion on a design evolution, that area experiencing the highest erosion attack is the outlet spool. Here one may specify a tungsten carbide wear sleeve; however, its length would have to be many pipe diameters, resulting in a cumbersome and costly solution.

A more appropriate approach would be the optimisation of the trim area and constricted outlet spool, ensuring that impact velocities are attenuated rapidly. One approach would be the extension of the constricted outlet spool and the shortening of the needle taper; thus promoting particle wall interactions

in constricted outlet spool. Particle impact velocities in the outlet spool would be lower through the promotion of aggressive particle-wall interactions within the tungsten carbide region of the constricted outlet spool. Furthermore, the diameter of the constricted outlet spool could be increased to ensure that fluid and particle velocities attenuate rapidly as they move away from the trim area. Care is required to ensure pressure recovery is not excessive, or cavitation may occur.

The above approach is somewhat negative in its foundation, as here one is promoting particle-wall interaction for the purpose of attenuating the particle velocity by energy transfer to the walling, albeit an area of walling which, to some degree, is constructed for such practice. A more sound approach would be to limit the particle-wall interactions in the first instance. Following this design methodology of mitigating particle-wall interactions, the particle acceleration length was minimised and the trim profile such that no sudden variations in flow direction occurred. This profiling was achieved by decreasing the head diameter of the needle, increasing the taper length of the needle, eliminating the constricted outlet spool and increasing the length of the expansion taper in the outlet spool. For liquid flows, the extended expansion taper removed concern regarding cavitation through controlled pressure recovery. A penalty incurred by the profiling was an increased choke size, however this penalty was deferred by the enhanced erosional characteristics of the evolution design.

Appendix M Figures 68 to 71 details the refined geometry - compared with original design (Appendix M Figure 19) - and the flow field induced by that geometry operating under the boundary conditions imposed. The peak flow velocities induced are comparable at 313 m/s, however the main difference is in the reaction of the jets as they emerge from the trim section, and the turbulence that this promotes. Appendix M Figure 72 details the evolution turbulent kinetic energy, whilst Appendix M Figure 23 details that of the original design. Immediately one may observe a reduction in the turbulence intensity due to the profiling. Furthermore, the jets of the evolution design remain attached to the wall due to the low angle of divergence in the outlet spool.

This adhesion of the jets to the wall by the localised shear stresses promoted a stable flow field which did not have the pertinacity to 'throw' particles at the walling. This stability was in contrast to that induced by the original design, where the jets were unattached and promoted cross-streamline transfers of the particles, and hence particle-wall interactions, due to the localised instabilities and turbulence intensities. An additional benefit of the jets remaining attached to the walling was that particles entrained within the jets had a tendency to be excited stream-wise with the jets, and hence parallel to the wall, as opposed to perpendicular to it. This minimised the particle impact angles in the outlet spool, as can be seen by Appendix M Figure 74 where the mean impact angle is 15°. A comparison with the impact angles of the original design (Appendix M Figure 35) enables one to understand the merits of profiling.

It is noteworthy that whilst the attachment of the jets to the walling eased the overall erosion problem, the evidence of particle biasing may still be observed (as discussed in section 8.4.1) with 'hotspoting' in the outlet spool as per the original design. This is to be expected as the observation made in section 8.4.1 are still valid for this test case.

The mismatch of the tapers upon the needle and the seat parts of the trim enabled the acceleration length of the particles to be minimised; via a restriction in the jet length within the trim area. A comparison of Appendix M Figure 68 and 19 allows one to note that the peak jetting velocity is only achieved at the very end of the taper for the evolution design, whilst the original design experiences peak velocities along the entire length of the choking gap between the needle and seat. This allowed the acceleration length to be reduced by approximately half over that of the original design, with a comparable reduction of the particle impact velocities in the outlet spool. From Appendix M Figures 73 and 34 we may observe that the evolution design experienced impact velocities of the order of 32 m/s in the outlet spool, whilst for the original design these impact velocities were as high as 60 m/s.

As a result of the reduced impact angles and velocities of the evolution design, a reduction in the erosion induced of approx. an order of magnitude, from that of the original design, was achieved. Appendix M Figures 37 & 38 show that the original design experienced peak erosion rates of 9.8 mm^3/hr, whilst from Appendix M Figures 76, 77 and Figure 8-5 we may observe that this has been driven down to 1.4 mm^3/hr. A significant gain, allowing the choke's life to be extended and cost savings realised.

This simple example highlights the merits of the CFD erosion model, allowing design evolution to be conducted quickly and at minimal cost to the operator. A further benefit of the code is that specific erosion problems experienced within the field can be investigated in detail. Such detailed investigations allow solutions to be achieved, promoting the overall efficiency of the process system.

8.6 Investigation of Erosion within Cage Type Chokes; A Comparative Study.

Due to the qualitative nature of the data output from the erosion model, both graphical and numerical, design evolution work can be undertaken. A progression of this design evolution work is the model's ability to answer one of the most commonly sighted question within the erosion arena of control chokes; being 'which choke design offers the best erosion resistance ?'. However, this question is then quickly followed by what is only common sense; 'will I then get a choke which has an excellent erosion performance, but will fail through another mechanism ?'. Figure 1-3 summaries the failure mechanisms which concerns operators.

EROSIONAL TRENDS OF A EVOLUTION NEEDLE AND SEAT CHOKE (K-EPSILON MODEL)

Particle Type - **Sand**
Particle Roundness Factor - **0.5**
Particle Flux Rate - **1** % by wt.
Number of Particle Sizes - **6**
Particle Size Range - **150-200** μm
Turbulent Dispersion - **Yes**

Figure 8-5 Surface Contour Plot of Needle & Seat Choke Particle Erosion Rates (mm3/hr)

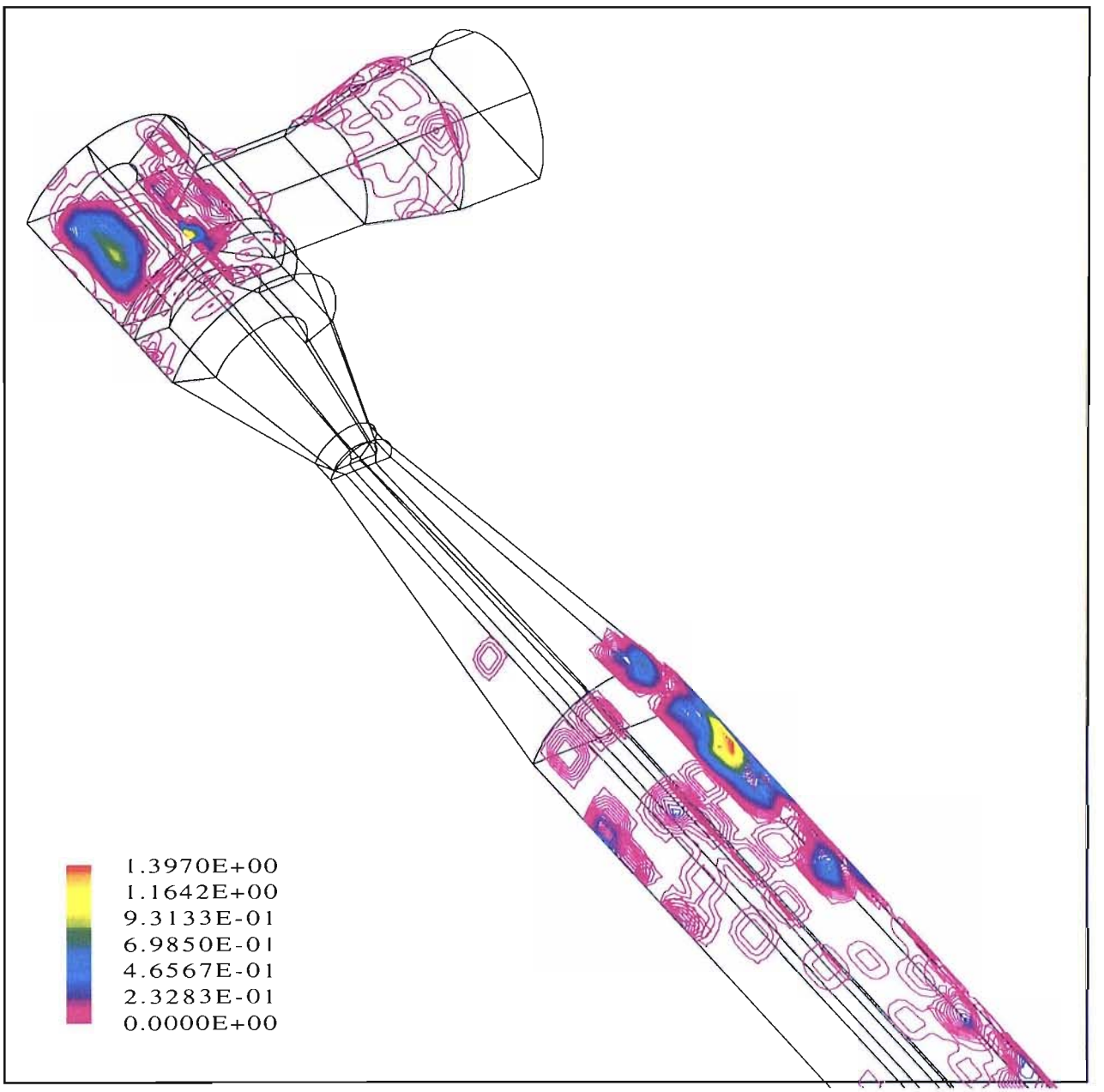

In truth you cannot answer the first question if you cannot ensure the customer that your product will have the durability to be reliable. As such it is a compromise that results, whereby the choke must have a good erosion performance, but must also be sufficiently durable to deliver good all-round performance. Personal experience shows that choke operators are happy to live with erosion, what is a concern is if this erosion becomes unstable or unpredictable. The choke manufactures have responded to this with the cage type chokes. These chokes enable a more uniform erosion pattern to be achieved, with the durability to deliver reliable operation for a number of years.

A further consideration is then, if a particular cage choke design has been identified, is this observation then applicable to all operating regimes and subtle variations in the design style of the trim, i.e. the port configurations. The answer is no, and to enable the best understanding to be presented, a detailed study has been undertaken, whereby a number of carriers and particle sizes have been investigated. A plug and cage and a external sleeve design were considered within the study. To allow a comparison of results, the chosen port configuration was relatively simple, with the cross-sectional area presented to the flow held constant for both trim types. The trim design considered was a four port configuration, as shown by Appendix D - external sleeve and cage choke.

The external sleeve design was modified, such that the external sleeve was changed out for an internal plug, enabling the external choking action to be swapped to an internal action. The inclusion of the internal plug removed the cavity above the cage associated with the external sleeve design and increased the annulus area. Appendix M Figures 78 to 120 present both of the computational geometries and the findings of the study. Note the differences between the external and internal designs centred upon the trim area. Furthermore, the positioning of both the external sleeve and internal plug was such that the larger upper port was 50% covered, allowing the interaction of the sleeve and plug to be modelled. As per convention, a symmetry plane was utilised to ease computational effort, as such only two ports have been presented in each case.

Two carrier types were considered, being a crude oil and a wet gas, with a turbulent flow field calculation being made for each design type. This resulted in a total of four flow fields, upon which the trajectory calculations were performed as a post process. To promote consistency, the closure model utilised for all four flow field calculations was the differential stress model. The same convergence criterion for the closure models was utilised in each case. The solution of the flow fields was found to be problematic, particularly for the crude oil carrier. The transport equations associated with such a non-compressible fluid are rigorous, care being required to arrive at a sensible solution. Here, the active application of such solution aids as under-relaxation factors and deferred corrections were a necessity. See section 10.2.2 for further details as to the resolution of non-compressible flow field within choke type geometries.

Appendix M Figures 78 and 99 present the velocity flow field for the external sleeve design, whereby oil and then gas were considered respectively. A more detailed representation was made for the plug and cage design, where Appendix M Figures 87 to 89 dealt with an oil carrier, whilst Appendix M Figure 109 to 111 considered a gas carrier. An extraction of the turbulent kinetic energy associated with the various flow field is given by Appendix M Figures 90, 100 and 112. A summary of the process conditions is provided in the above mentioned Appendix M Figures, including a description of trim type. From the plug and cage representations it is noted that the velocities were similar, for both carrier types. This situation was intended, enabling a like comparison between both carrier and choke types to be achieved.

This particular design style utilised a disproportionate port arrangement, whereby two mutually opposite ports impinged upon themselves in two different planes, with the ports of the two planes being of differing sizes. This configuration lead to flow instabilities - including cyclonic effects in the outlet - and the tendency for the larger upper port to dominate the smaller lower port, even with the larger port partially covered. These effects are detailed through Appendix M Figures 87 to 89, the carrier being the non-compressible oil. Note the creation of dual jets in the outlet spool, where the jet from the smaller port could not penetrate into the mid flow and was deflected back into the walling where it remained attached. This phenomenon created a high velocity region at the wall, with velocities of the order of 45 m/s. The compressible solution utilised for the gas carrier generated similar effects, Appendix M Figures 109 to 111, however in this instance the jets merged to become a single high velocity region impacting upon the walling.

These observations emphasized the importance of port selection, and the requirement to ensure the ports are balanced. The design philosophy of such cage type chokes is that the jets created by the ports will impinge upon themselves in the centre of the outlet spool and hydrodynamic energy will be destroyed through a combination of turbulence and diffusion. The aim is to minimise frictional effects associated with the walling. However, the positive impingement of the jets upon themselves requires careful control of the jets shape and form. If only two large jets impinge upon themselves, they can bypass one another resulting in the effect reported above, this also occurs if the jets are disproportionate in size. If the other extreme is utilised and many small jets are employed, i.e. 12, the spray curtain created is of such an energy level that diffusion effects cannot sufficiently dissipate the associated energy and the jets deflected off one another to strike the walling. The optimum port configuration[9] is reputably four ports per plane. Here, the jets are sufficiently sized to positively impinge upon themselves, whilst the four jets per plane reduce the tendency for the jets to rotate and bypass one another.

[9] Comments supplied courtesy of the Copper Cameron Corporation, being based upon experimental work.

A further consideration is the tolerance applied to each port. If the alignment is poor, the jets can bypass one another and impinge upon the walling. Furthermore, the progression of erosion can de-centralise a jet, again allowing the jet to bypass the oncoming jet and impinge the walling.

Appendix M Figures 78 and 99 detail the velocity contours - both carriers - for the external sleeve design. Again, the disproportionate nature of the jets is noted, with the tendency for the large port to dominate the smaller port and generate a high velocity flow at the walling. However, in the instance of the external sleeve design, the flow in the trim area was complicated by the cavity created above the cage. See Appendix D. The flow into this cavity was limited for the incompressible oil case due to stagnation effects, with some backflow tendencies noted. The cavity assisted with hydrodynamic energy dissipation, by shifting the dissipation mechanism away from frictional towards turbulence and diffusion, thus partially reducing the velocities at the walling.

In the case of the gas carrier, the compressibility assumption allowed a much increased inflow into the cavity above the cage, Appendix M Figure 99 and Figure 8-6. The dominance of the large port is further emphasised in this instance, and the impingement of the flow into the top of the sleeve noted. This is a known failure mechanism for the external sleeve design, whereby upflow impinging on the sleeve top can cut through the sleeve, resulting in loss of control. A further complication is the inclusion of pressure balance ports on the sleeve top, if the balance ports coincide with the impingement site, erosion is channelled by the balance ports and failure of the stem can occur. This can be particularly problematic as tungsten carbide is not utilised in the stem construction, only as a protective tablet at the top of the sleeve.

The flow fields enable a number of trajectory calculations to be completed. To provide an arduous duty, emphasis should be placed upon the high pressure drop utilised, being at 50 bar. The material composition of the choke was considered to be tungsten carbide for all trim components, whilst the body was a carbon steel. Table 9-3 details the empirical constants utilised within the erosion model. A total of eight erosion simulations were completed, with each simulation being constructed of two runs. This approach allowed a more representative study to be undertaken, with Table 8-6 and Table 8-7 detailing the results of the simulations for both the choke and carrier types. In addition to the carrier type, the size of the particles were altered to investigate the size relationship.

Each of the trajectory calculations utilised the turbulent dispersion term, the modified coefficient of restitution and the squeeze film function. It was assumed that the gas phase was wet with a condensate layer at the wall, hence the application of the squeeze film function in this instance. A total of 392 trajectory calculations were made for each simulations, with the particulate flux assumed to be 5.14

FLOW FIELDS WITHIN CAGE TYPE CONTROL CHOKES

Fluid - **Wet Gas**
Inlet Diameter - **75** mm
Port Diameters - **12.5** & **25** mm
Taper Angle on Sleeve - **15°**
Choke Opening - **75** %
Pressure Drop - **50** Bar
Mass Flow Rate (Gas) - **140** kg/hr

Figure 8-6 Velocity Contour Plot of External Sleeve Control Choke (m/s)

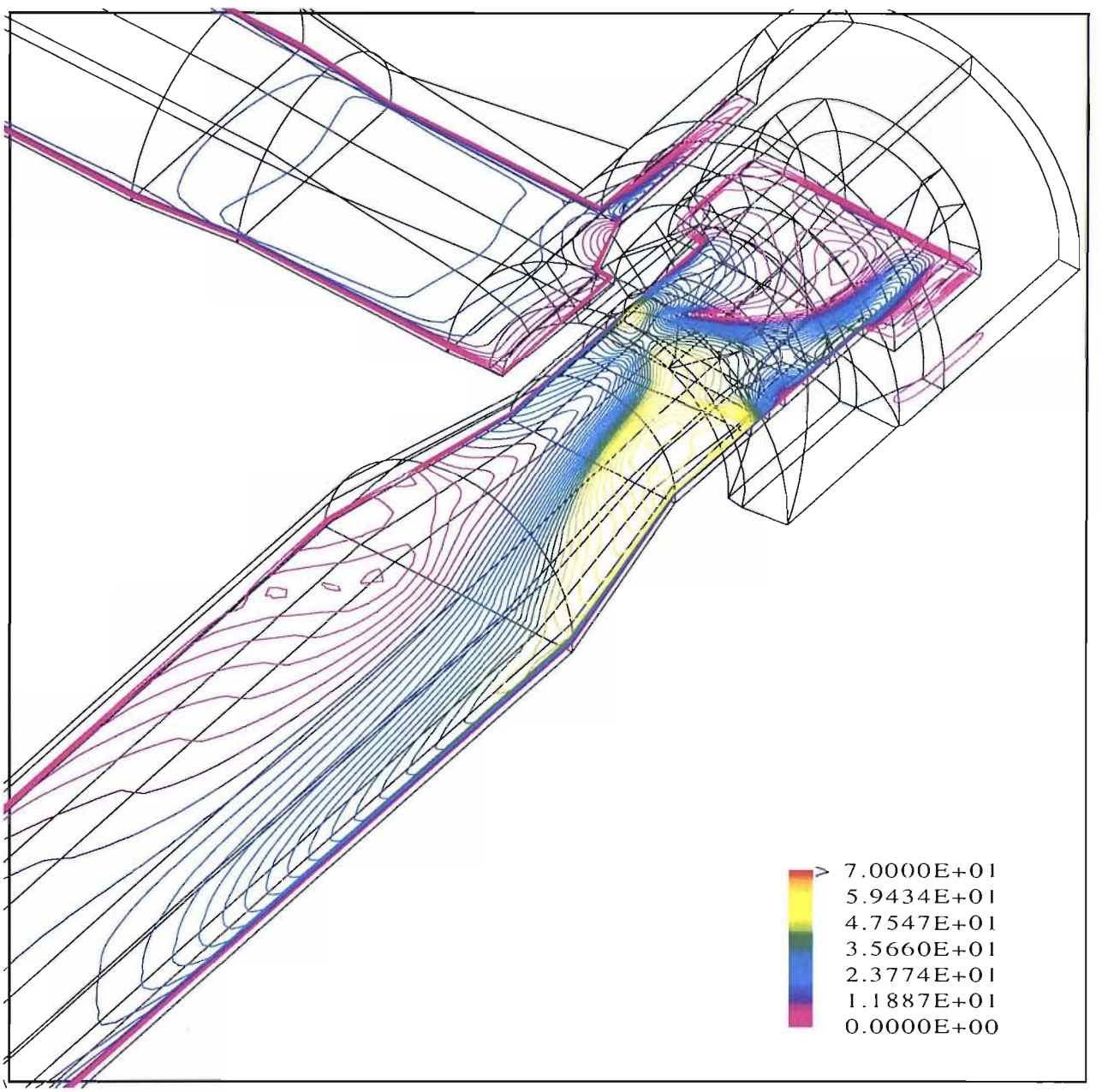

kg/hr in all cases. A small and large particle size convention was employed, whereby the small particles ranged from 75-165 μm, whilst the larger particles were sized from 170-260 μm. Seven and eight particle sizes were described between each of the size bands, whilst the particle roundness factor was held constant at 0.5.

Appendix M Figures 79 to 82 detail the impact characteristics of the external sleeve design, with an oil carrier and small particles, Test 1. The Appendix M Figures summarise the particle impact velocity, the impact angle, with two representations of the predicted erosion. This presentation scheme was utilised in all cases and subsequent reference will be limited to the test number and the referring Appendix M Figures. From Appendix M Figure 79, a focused area of particle impacts is noted in the outlet spool, at the divergence point. This site relates to the dominance of the large port and the tendency for the particles to be routed through this port. The port was positioned near the radial inlet of the choke and tended to act as a sink for the majority of particles entering the annulus cavity. Other impact sites were noted at the ports, with a peak impact velocity of 15 m/s recorded. The impact angle at the focus site was approximately 35°, whilst the average impact angle for the trim was found to be 43.5°. See Table 8-6 for further statistical data.

Appendix M Figures 81 and 82 detail the predicted erosion. Confirming the observation made via Appendix M Figure 79, that site of peak erosion was reported opposite the large port. This erosional site was problematic in that the divergence of the outlet spool denoted the transition from a tungsten carbon to a steel based material, further heightening the erosional attack. The reported localised erosion was of the order of 8.7 $x10^{-2}$ mm^3/hr, being predominantly centred within the outlet spool. Thus, it was recommended that a wear sleeve be fitted to the outlet, or the design be modified such that this erosional site be removed from the steel based outlet spool.

Appendix M Figure 83 to 86 provide details of Test 3. What was apparent from Appendix M Figure 83 was that the number of impact events had increased over the smaller particle size of Test 1. This effect is clearly summarised by Table 8-6, whereby we consider the number of impacts per particle for Test 1 and 3. Here we note the increase from 4.1 at 75-120 μm to 8 at 215-260 μm. This increase was related to the squeeze film effect and the improved ability of the larger particles to contact the walling. Furthermore, as a result of the increased particle mass, the momentum possessed by the larger particles was increased. This implied the mean trajectory velocity and hence the impact velocity were reduced through a reduced momentum transfer from the carrier phase. We note the average impact velocity decreased from 5.7 m/s at 75-120 μm to 3.5 m/s at 215-260 μm. Furthermore, the average impact angle decayed from 48.1° at 75-120 μm to 39.7° at 215-260 μm.

LIQUIDS	EXTERNAL SLEEVE SMALL PARTICLES			EXTERNAL SLEEVE LARGE PARTICLES			PLUG & CAGE SMALL PARTICLES			PLUG & CAGE LARGE PARTICLES		
Test No.	1	1	**1**	3	3	**3**	2	2	**2**	4	4	**4**
Run No.	1	2	**Sum**	1	2	**Sum**	1	2	**Sum**	1	2	**Sum**
Turbulent Dispersion	Yes	Yes	**Yes**	Yes	Yes	**Yes**	Yes	Yes	**Yes**	Yes	Yes	**Yes**
Modified Restitution	Yes	Yes	**Yes**	Yes	Yes	**Yes**	Yes	Yes	**Yes**	Yes	Yes	**Yes**
Squeeze Film	Yes	Yes	**Yes**	Yes	Yes	**Yes**	Yes	Yes	**Yes**	Yes	Yes	**Yes**
Fluid	Oil	Oil	Oil	Oil	Oil	Oil	Oil	Oil	Oil	Oil	Oil	Oil
Particle Size	75-120	120-165	**75-165**	170-215	215-260	**170-260**	75-120	120-165	**75-165**	170-215	215-260	**170-260**
No. of Particle Sizes	4	4	**8**	4	3	**7**	4	4	**8**	4	3	**7**
Particle Con'tion (Wppm)	26.84	26.84	**53.68**	26.84	26.84	**53.68**	26.84	26.84	**53.68**	26.84	26.84	**53.68**
Total Sand Flux (kg/hr)	2.57	2.57	**5.14**	2.57	2.57	**5.14**	2.57	2.57	**5.14**	2.57	2.57	**5.14**
Total No. of Impacts (Body)	539	840	**1379**	872	630	**1502**	515	667	**1182**	728	486	**1214**
Total No. of Impacts (Trim)	266	215	**481**	251	541	**792**	200	230	**430**	224	275	**499**
Overall No. of Impacts	805	1055	**1860**	1123	1171	**2294**	715	897	**1612**	952	761	**1713**
No. of Particles Tracked	196	196	**392**	196	147	**343**	196	196	**392**	196	147	**343**
Impacts per Particle (Body)	2.750	4.286	**3.52**	4.449	4.286	**4.38**	2.628	3.403	**3.02**	3.714	3.306	**3.54**
Impacts per Particle (Trim)	1.357	1.097	**1.23**	1.281	3.680	**2.31**	1.020	1.173	**1.10**	1.143	1.871	**1.45**
Impacts per Particle	4.107	5.383	**4.74**	5.730	7.966	**6.69**	3.648	4.577	**4.11**	4.857	5.177	**4.99**
Projected Erosion (Body)	1.100	2.059	**3.16**	2.016	1.943	**3.96**	1.055	1.474	**2.53**	1.760	1.798	**3.56**
Projected Erosion (Trim)	0.148	0.106	**0.25**	0.086	0.109	**0.19**	0.142	0.164	**0.31**	0.115	0.102	**0.22**
Projected Erosion (mm^3/hr)	1.248	2.165	**3.41**	2.102	2.052	**4.15**	1.197	1.638	**2.83**	1.875	1.900	**3.77**
Norm. Erosion Body (mm^3/kg)	0.428	0.801	**0.61**	0.784	0.756	**0.77**	0.411	0.574	**0.49**	0.685	0.700	**0.69**
Norm. Erosion Trim (mm^3/kg)	0.058	0.041	**0.05**	0.033	0.042	**0.04**	0.055	0.064	**0.06**	0.045	0.040	**0.04**
Norm. Erosion (mm^3/kg)	0.486	0.842	**0.66**	0.818	0.798	**0.81**	0.466	0.637	**0.55**	0.729	0.739	**0.73**
Aver. Impact Vel. (Body)	4.391	4.004	**4.20**	3.568	3.379	**3.47**	4.365	3.913	**4.14**	3.644	3.507	**3.58**
Aver. Impact Vel. (Trim)	6.988	6.112	**6.55**	5.432	3.643	**4.54**	8.067	7.125	**7.60**	5.749	4.373	**5.06**
Aver. Impact Velocity (m/s)	5.690	5.058	**5.37**	4.500	3.511	**4.01**	6.216	5.519	**5.87**	4.697	3.940	**4.32**
Aver. Impact Angle (Body)	51.19	48.74	**49.97**	46.02	43.52	**44.77**	51.87	49.04	**50.46**	45.22	43.00	**44.11**
Aver. Impact Angle (Trim)	45.11	41.78	**43.45**	38.05	35.84	**36.95**	42.38	39.56	**40.97**	35.09	31.10	**33.10**
Aver. Impact Angle (deg)	48.15	45.26	**46.71**	42.04	39.68	**40.86**	47.13	44.30	**45.71**	40.155	37.050	**38.60**
Peak Impact Velocity (m/s)	14.73	11.73	**13.23**	10.04	9.71	**10.04**	15.46	13.27	**14.37**	11.84	10.08	**10.96**

Table 8-6 Summary of Numerical Investigation into Plug & Cage and External Sleeve Erosion via a Liquid Carrier

WET GAS	EXTERNAL SLEEVE SMALL PARTICLES			EXTERNAL SLEEVE LARGE PARTICLES			PLUG & CAGE SMALL PARTICLES			PLUG & CAGE LARGE PARTICLES		
Test No.	5	5	**5**	7	7	**7**	6	6	**6**	8	8	**8**
Run No.	1	2	**Sum**	1	2	**Sum**	1	2	**Sum**	1	2	**Sum**
Turbulent Dispersion	Yes	Yes	**Yes**	Yes	Yes	**Yes**	Yes	Yes	**Yes**	Yes	Yes	**Yes**
Modified Restitution	Yes	Yes	**Yes**	Yes	Yes	**Yes**	Yes	Yes	**Yes**	Yes	Yes	**Yes**
Squeeze Film	Yes	Yes	**Yes**	Yes	Yes	**Yes**	Yes	Yes	**Yes**	Yes	Yes	**Yes**
Fluid	Wet Gas	Wet Gas	**Wet Gas**	Wet Gas	Wet Gas	**Wet Gas**	Wet Gas	Wet Gas	**Wet Gas**	Wet Gas	Wet Gas	**Wet Gas**
Particle Size	75-120	120-165	**75-165**	170-215	215-260	**170-260**	75-120	120-165	**75-165**	170-215	215-260	**170-260**
No. of Particle Sizes	4	4	**8**	4	3	**7**	4	4	**8**	4	3	**7**
Particle Con'tion (% by wt)	1.85	1.85	**3.7**	1.85	1.85	**3.7**	1.85	1.85	**3.7**	1.85	1.85	**3.7**
Total Sand Flux (kg/hr)	2.57	2.57	**5.14**	2.57	2.57	**5.14**	2.57	2.57	**5.14**	2.57	2.57	**5.14**
Total No. of Impacts (Body)	479	746	**1225**	1045	887	**1932**	393	561	**954**	691	612	**1303**
Total No. of Impacts (Trim)	707	724	**1431**	833	607	**1440**	500	547	**1047**	601	447	**1048**
Overall No. of Impacts	1186	1470	**2656**	1878	1494	**3372**	893	1108	**2001**	1292	1059	**2351**
No. of Particles Tracked	196	196	**392**	196	147	**343**	196	196	**392**	196	147	**343**
Impacts per Particle (Body)	2.444	3.806	**3.13**	5.332	6.034	**5.63**	2.005	2.862	**2.43**	3.526	4.163	**3.80**
Impacts per Particle (Trim)	3.607	3.694	**3.65**	4.250	4.129	**4.20**	2.551	2.791	**2.67**	3.066	3.041	**3.06**
Impacts per Particle	6.051	7.500	**6.78**	9.582	10.163	**9.83**	4.556	5.653	**5.10**	6.592	7.204	**6.85**
Projected Erosion (Body)	4.654	3.945	**8.60**	2.879	2.697	**5.58**	3.565	3.875	**7.44**	3.562	3.024	**6.59**
Projected Erosion (Trim)	4.079	2.527	**6.61**	1.969	1.584	**3.55**	2.247	1.636	**3.88**	1.262	1.120	**2.38**
Projected Erosion (mm^3/hr)	8.733	6.472	**15.21**	4.848	4.281	**9.13**	5.812	5.511	**11.32**	4.824	4.144	**8.97**
Norm. Erosion Body (mm^3/kg)	1.811	1.535	**1.67**	1.120	1.049	**1.08**	1.387	1.508	**1.45**	1.386	1.177	**1.28**
Norm. Erosion Trim (mm^3/kg)	1.587	0.983	**1.29**	0.766	0.616	**0.69**	0.874	0.637	**0.76**	0.491	0.436	**0.46**
Norm. Erosion (mm^3/kg)	3.398	2.518	**2.96**	1.886	1.666	**1.78**	2.261	2.144	**2.20**	1.877	1.612	**1.74**
Aver. Impact Vel. (Body)	10.31	7.50	**8.90**	5.60	5.09	**5.34**	11.16	9.02	**10.09**	7.37	6.22	**6.79**
Aver. Impact Vel. (Trim)	14.06	11.07	**12.57**	9.15	8.53	**8.84**	15.39	12.70	**14.05**	10.41	9.92	**10.17**
Aver. Impact Velocity (m/s)	12.19	9.28	**10.73**	7.37	6.81	**7.09**	13.28	10.86	**12.07**	8.89	8.07	**8.48**
Aver. Impact Angle (Body)	23.54	25.12	**24.33**	24.77	25.43	**25.10**	25.25	23.42	**24.34**	23.89	24.55	**24.22**
Aver. Impact Angle (Trim)	48.18	47.09	**47.64**	47.25	46.05	**46.65**	45.90	43.92	**44.91**	45.35	44.41	**44.88**
Aver. Impact Angle (deg)	35.86	36.11	**35.98**	36.01	35.74	**35.88**	35.58	33.67	**34.62**	34.62	34.48	**34.55**
Peak Impact Velocity (m/s)	28.78	27.77	**28.78**	20.58	19.22	**20.58**	23.35	25.87	**24.61**	17.90	16.73	**17.90**

Table 8-7 Summary of Numerical Investigation into Plug & Cage and External Sleeve Erosion via a Wet Gas Carrier

The reduced impact angle was again in response to the squeeze film effect. The squeeze film function only considered the perpendicular velocity component at impact. To enable the particle to contact the walling, the perpendicular component must be of a suitable magnitude - dependent upon the particles momentum - to break the squeeze film. As the particle size increased, the associated momentum increased, allowing the particle to strike the walling at a lower perpendicular velocity or angle. The phenomenon described was noted for all simulation, when the particle size was increased.

Appendix M Figures 85 and 86 denote the predicted erosion. The erosive trending was very similar to that noted by Test 1, and the same comments apply, however in this instance the localised erosion was greater at 1.3E-01 mm^3/hr. This observation was also confirmed via Table 8-6, where the projected erosion was noted at 3.4 mm^3/hr for Test 1, whilst Test 3 presented an erosional rate of 4.2 mm^3/hr. The reasoning for this increased erosion prediction with particle size was explained through an average particle mass increase of 83 % between the size groupings, whilst the average impact velocity was only diminished by 25 %.

Appendix M Figures 91 to 94 detail the findings of Test 2. Appendix M Figure 91 summarises the impact velocities, being supplemented by Table 8-6. Here we note that the impact velocities were higher than that delivered by the external sleeve design of Test 1, both average and peak. This phenomenon relates to the close confines of the controlling surfaces, implemented by the internal choking action of the plug and cage design. Furthermore, as commented upon previously, via Appendix M Figure 78, the external sleeve design did reduce the near wall velocities of the flow field, promoting a tendency for the particle to decelerate prior to impact. Given that the structure of the flow field was similar to that generated by the incompressible external sleeve design, the domination of the larger port was once again apparent, with the impingement site opposite this port clearly shown. In addition to the location of this impingement site, the impact angles were of a similar magnitude as that reported in Test 1, i.e. 35°.

The structure of the resulting erosion - Appendix M Figures 93 and 94 - was again similar to that of Test 1, with the peak localised erosion rate reported as 8.8 $x10^{-2}$ mm^3/hr. However in this instance the erosional damage to the divergence of the outlet spool was more marked, whilst additional damage had been done to the inner walling of the cage, note the erosional area under the small port. From Table 8-6 we perceive that whilst the overall projected erosion was reduced by the plug and cage design, that erosion experienced by the trim was increased.

Appendix M Figures 95 to 98 summarise the final liquid simulation, Test 4. Once again the findings were as per the previous liquid simulations, with the large port dominating the smaller, producing the characteristic erosional hotspot upon the divergence of the outlet spool. The average impact velocity

and angle were both noted to decay, whilst the projected erosion increased in line with the comments made as per Appendix M Figure 85 and 86. Akin to that of Test 2, the overall projected erosion was comparably reduced to that of the like external sleeve case, however the erosion damage induced to the trim was increased.

From Appendix M Figure 98 we note that the erosional damage to the outlet was spread over an extended area when compared to that generated by Test 2. This observation was also valid for the large particles versus the smaller particles of Test 3 and 1. No conclusive hypothesis can be given for this occurrence, however it should be emphasised that the given the limited number of trajectory calculations made per simulation - a necessity of the extensive nature of the study - the statistical confidence can only be stated as moderate.

Appendix M Figures 101 to 104 present the details of Test 5. What is indisputable is that the utilisation of a gas carrier very much increased the interactions with the walling. Here both the average and peak impact velocities were markedly increased over that generated by the oil carrier. If we consider both the oil and gas simulations as a whole, the average impact velocity was increased from 4.9 to 9.6 m/s, whilst the peak impact velocity jumped from 12.2 to 22.9 m/s. Furthermore, the particle wall interactions within the annulus area were heightened, this effect is particularly apparent from Appendix M Figure 102. Given the relatively benign conditions of the annulus, and high density differential between phases, the particles readily escaped the slipstreams of the flow field, impacting the walling and generating erosional damage to the annulus cavity, Appendix M Figures 103 and 104.

The erosional damage to the annulus above the cage ports is actually a field reported erosion mechanism, whence the choke has large ports. Here, the drawdown caused by the large ports is of such an intensity that an annulus shaped inflow jet is generated. This annulus jet impinges upon itself above the port and the resultant impingement reaction generates a jetting action upon the annulus walling. This phenomenon is only active with compressible fluids, as the stagnation effects of incompressible liquids mitigates this tendency. The solution is to either decrease the port size such that the inflow effect is limited, else increase the size of the annulus cavity to diffuse such tendencies.

Again, the dominance of the large port generated an erosional area upon the opposite walling. However, for a gas carrier, the erosional site was directly opposite the large port as opposed to the divergence site of the outlet spool observed with the oil carrier, Appendix M Figure 103. Furthermore, an additional erosion area was created in the outlet spool, whereby the divergence ceased and the outlet become parallel. The reasoning for this secondary erosional site was explained through Appendix M Figure 99, where the high velocity jet generated by the large port was shown to remain attached to the walling. The peak localised erosion rate was reported at 3.3 $x10^{-1}$ mm^3/hr, or an

increase of 74 % over that of Test 1. This observation is supported by Table 8-7, where the overall projected erosion was 15.2 mm^3/hr. Note that with a gas carrier, the ratio of erosion between the trim and body was comparably reduced from that of a liquid carrier, reason being the ability of the particles to directly traverse the trim given the increased density differential.

Appendix M Figures 105 to 108 detail the findings of Test 7. The erosional locations were very similar to that reported by Test 5, were the erosional damage was focused upon the trim opposite the large port, the outlet spool immediately after the divergence and the annulus walling above the large port. In addition to the erosional damage to the area above the port, additional damage was done to the annulus where a number of particles escaped the sink that was the large port and passed to the smaller rear port. To avoid the sink effect of the large port, the particulate momentum had to be of a sufficient magnitude. This momentum magnitude was only possible with the larger particles in the gas carrier phase, however the resultant of this excess particulate momentum in the annulus was addition damage to the walling.

Akin to the observations made for the oil carrier, the average impact velocity was noted to decay with increased particle size, Test 5 and 7 of Table 8-7. However, the increased particle size resulted in a diminished projected erosion, being in contrast to the oil carrier, where an increase was projected. The reasoning for this was two fold. Firstly, given the increased density differential between the phases with a gas carrier, the reduction in average impact velocity was more marked. The increased particle size produced a 38 % reduction in impact velocity for an oil carrier, whilst a 44 % reduction was noted for the gas carrier. Further, the average impact angle was noted to diminish with increasing particle size for the oil carrier. The implications of this was that the reduced angle promoted an increased cutting erosion effect within the body, and hence an increase in the projected erosion. However with the gas carrier, the average impact angle remained static with an increasing particle size, allowing the projected erosion to diminish in line with the decaying impact velocity. The impact angle remained static given the enhanced ability of the particle to cross streamlines with the increased density differential.

Appendix M Figure 113 to 116 present the findings of Test 6, the plug and cage simulation operating with wet gas. Here, we note that whilst the average impact velocity was increased over that generated by the external sleeve of Test 5 (Table 8-7) the number of impacts to the trim was reduced, allowing the projected erosion to the trim to be reduced from that of Test 5. The overall projected erosion was 11.32 mm^3/hr, whilst that of the trim was 3.88 mm^3/hr. The erosional trends were similar to that of the external sleeve, however given the increased variation in the flow field presented by the use of a compressible continuous phase, some subtleties existed. The location and form of the erosional sites opposite the large port and immediately after the divergence were the same, however the annulus

erosion had been manipulated by the increased annulus area, offered by the plug and cage design. This increased area allowed additional particles to bypass the sink that was the large port and impact the walling, resulting in the smaller particles contributing to annulus erosion in this instance.

Further to the erosional site immediate to the divergence, an additional site was created upon the opposite walling, Appendix M Figure 115. This site related to the close confines of the plug and cage design, and the deflection of the particles by the plug. Given that the drag or attenuation characteristics of the gas carrier were poor, the particulate momentum enabled the particles to traverse the slipstreams of the flow and impact upon the opposite walling. The peak localised erosion was reduced from that presented by Test 5, being 2 $x10^{-1}$ mm^3/hr.

Finally, Appendix M Figure 117 to 120 summarise the findings of Test 8. Inline with the findings of Tests 5 and 7, the particle impact velocity and projected erosion were both seen to diminish, with increasing particle size (Table 8-7). Again the particle impact angle remained independent of particle size. The erosional trending was similar to that report by Test 6, however the influence of the increased particle size was clearly seen in the outlet spool. Similar to Test 6, the close confines of the plug, caused particle to be deflected across the slipstreams of the flow field and impact upon a number of sites within the outlet spool. This effect was heightened over that reported by Test 6, given the increased particle size and hence momentum. The peak localised erosion rate was 7.6 $x10^{-2}$ mm^3/hr, or a reduction of 62 % over the smaller particles.

8.6.1 Conclusions as to Erosion within Cage Type Chokes

Thus one may conclude and comment upon a number of observations. Here, the design type did not significantly influence the underlying mechanisms of erosion. The principal influences were those generated by the carrier type and the particle size, being related to such effects as squeeze film and density differential between phases. One may summarise these phenomena loosely as Table 8-8.

LIQUID CARRIER			
For an increased particle size	Increased erosion rate	Decreased particle impact velocity	Decreased particle impact angle
GAS CARRIER			
For an increased particle size	Decreased erosion rate	Decreased particle impact velocity	Static particle impact angle

Table 8-8 Summary of Particle Characteristics

If we now consider the relative performance of the differing choke designs, summating the particle sizes to enable comparisons to be drawn on the carrier and choke types, Table 8-9. The difference between the two choke styles, with respect to projected erosion, was relatively small in real terms. The biggest variations arose through the properties of the continuous phase, with the gas carrier being significantly more erosive than the oil carrier. This observation was expected, with the difference

being some 70 % for the external sleeve, whilst 67 % was noted for the plug and cage. Unfortunately these representations were for ideal fluids, i.e. fully or incompressible. The reality is that the carrier will be a multiphase mixture, possessing a combination of properties that place it somewhere between the two bounding conditions presented. However, the simulations undertaken provide a good insight into the likely erosional rates and locations.

COMPARISON SUMMARY	EXTERNAL SLEEVE LIQUID	PLUG & CAGE LIQUID	EXTERNAL SLEEVE GAS	PLUG & CAGE GAS
Test No. Summation	1 & 3	2 & 4	5 & 7	6 & 8
Closure Model	DS	DS	DS	DS
Turbulent Dispersion	Yes	Yes	Yes	Yes
Modified Restitution	Yes	Yes	Yes	Yes
Squeeze Film	Yes	Yes	Yes	Yes
Fluid	Oil	Oil	Wet Gas	Wet Gas
Particle Size	75-260	75-260	75-260	75-260
No. of Particle Sizes	15	15	15	15
Particle Con'tion (Wppm)	107.36	107.36	7.4	7.4
Total Sand Flux (kg/hr)	10.28	10.28	10.28	10.28
Total No. of Impacts (Body)	2881	2396	3157	2257
Total No. of Impacts (Trim)	1273	929	2871	2095
Overall No. of Impacts	4154	3325	6028	4352
No. of Particles Tracked	735	735	735	735
Impacts per Particle (Body)	3.95	3.28	4.38	3.12
Impacts per Particle (Trim)	1.77	1.28	3.92	2.86
Impacts per Particle	5.72	4.55	8.30	5.98
Projected Erosion - Body (mm^3/hr)	7.118	6.087	14.175	14.026
Projected Erosion - Trim (mm^3/hr)	0.448	0.522	10.159	6.265
Projected Erosion (mm^3/hr)	7.566	6.609	24.334	20.291
Erosion Intensity Index (local/global)	0.0283	0.0280	0.011	0.0131
Norm. Erosion Body (mm^3/kg)	0.692	0.592	1.379	1.364
Norm. Erosion Trim (mm^3/kg)	0.044	0.051	0.988	0.609
Norm. Erosion (mm^3/kg)	0.736	0.643	2.367	1.974
Aver. Impact Vel. (Body)	3.836	3.857	7.124	8.440
Aver. Impact Vel. (Trim)	5.544	6.329	10.702	12.105
Aver. Impact Velocity (m/s)	4.690	5.093	8.913	10.273
Aver. Impact Angle (Body)	47.37	47.28	24.72	24.28
Aver. Impact Angle (Trim)	40.20	37.03	47.14	44.90
Aver. Impact Angle (deg)	43.78	42.16	35.93	34.59
Peak Impact Velocity (m/s)	11.64	12.66	24.68	21.26

Table 8-9 Summary of Plug & Cage Versus External Sleeve Erosion Performance

We also note the differences in impact velocities and angles between phases, whereby the impact velocity generated by the gas carrier was some 49 % greater than that of the liquid carrier, at 9.6 m/s for both choke styles. Given this increased impact velocity, the average impact angle experienced by the gas carrier was much reduced from that of the liquid carrier at 24° for the body. This related to the perpendicular convention utilised within the squeeze film function.

The impact characteristics and projected erosion between design types were similar, Table 8-9. General observations may conclude that the impact velocities to the bodies were relatively constant, whilst the plug and cage design exhibited an increase impact velocity to the trim, over that of the external sleeve. This increase related to the close proximity configuration utilised in the plug and cage design, whilst the external sleeve attempted to remove the controlling surfaces from the high velocity jetting regions. The product of these observations was that the projected erosion rates for the body were similar, however the erosional rates of the trim varied. Reasoning would dictate that as the impact velocities were the highest for the plug and cage design, that the erosion rates for the trim would be the greatest for this design. This was indeed true for the liquid carrier, however not the case for the gas carrier, Table 8-9.

This phenomenon related to the density differential between phases, the particulate drag and the design of the trim. Whilst the plug and cage design promoted high velocity impacts at the trim, its design was such that particles were readily ejected from the trim area to traverse downstream, causing some damage to the outlet spool. However, in the case of the external sleeve design - operating with a gas carrier - the high density differential retained the particles to the trim area, undergoing many impacts and hence erosion. The increased impact tendency of the external sleeve design is noted through Table 8-9.

To summate the projected erosion rates between the two choke types were relatively similar, however we must then consider the implications of this erosion upon the controllability and performance of the choke. The essence of the external sleeve design is that its purpose is erosion resistance, at the expense of flow capacity or Cv. Given that the controlling surfaces - the sleeve - are removed from the high velocity jetting regions, its ability to withstand erosion are excellent. From a comparative viewpoint the external sleeve design is able to withstand approximately 4.5 times the erosive damage than that capable with the plug and cage design, see Figure 9-6. Given that the erosion rates were predicted to be similar in this study, the external sleeve design would be expected to have a service life 4.5 times greater than that offered by the plug and cage when operating under purely erosive duties.

Here stands the question mark, the external sleeve design is know to have a debatable robustness, and incidences have been cited in the field whereby the tungsten carbide flowcage has scattered. Furthermore, the flowcage can only be supported at one end, generating cantilever associated difficulties. Given that the choking occurs externally to the cage, the cage cannot have a protective sleeve fitted around it, as is the case with the plug and cage design. Figure 1-1 details such a sleeve, whilst the sleeve is eroded, the underlying cage is serviceable and able to deliver continued

performance. The cage of the external sleeve design is know to fail through a number of mechanisms including, poor shrinkfit at the flowcage base giving rise to harmonics problems, impact by produced debris from the well and impact by liquid slugs.

The first problem is a manufacturing associated difficulty and should be avoidable with greater care. However, given the continued pressure to reduce emissions to atmosphere, many wells are now being cleaned-up through the operational facilities, as opposed to being flared upon the drill rig. Debris can then be expected, which may result in excessive loads being applied to the cage, and the subsequent failure of that component. An alternative is to have a dedicated clean-up choke - typically of a needle and seat design - to be changed out post clean-up, however this is only possible with topsides facilities. Given the increased reliance on subsea developments to reduce costs, especially in the maturing UK continental shelf area, the choke of choice has become the plug and cage.

Operators are not willing to support the costs associated with a catastrophic cage failure subsea, hence the robust plug and cage design is utilised. Whilst the limitations in terms of erosion resistance are recognised, the erosional rates are understood and controllable. These observations are supported by the author, and it is recommended that the plug and cage be utilised subsea, whilst the external sleeve be utilised topsides, where the change-out costs are manageable and warrant the additional exposure related to this design. Such recommendations are general, and the specifics of each application should be fully understood prior to the selection of a design type.

9. Experimental studies to evaluate the *CFD* Erosion Model

Experimental studies within the project focused on two main subject areas. Firstly the validity of the erosion model was assured by the correlation of the model against flat sample experimental data, as collected through the water-sand slurry test facility housed within the Erosion Corrosion Research Consultancy at the University of Southampton. Secondly, full valve erosion testing was completed on a number of choke configurations, valving kindly supplied by Copper Cameron Ltd and ABB Kent Introl Ltd. The high pressure flow loop test facility at BP Sunbury was utilised for this sequence of water-sand erosion tests under simulated field conditions. This dual approach allowed each of the key stages within the erosion modelling process to be investigated, with techniques being identified that ensured accurate predictions from the erosion model.

NOTE REGARDING TURBULENT CLOSURE MODEL VALIDATION

The erosion model and the particle trajectory calculation on which it is based relies upon an accurate prediction of the turbulent flow field, including the structure of that flow field. However, due to the lack of accurate data detailing this structure, it is difficult to quantify the ability of the closure model to accurately capture the flow field. A related discussion is given in section 8.4.2, whereby it is argued that due to this lack of quantifiable data we are reduced to selecting the best practice for any solution scheme.

In general we select the Differential Stress model and assume that this model will generate the best results. To provide slight justification for this assumption we can complete any number of gross validation tests, whereby the pressure drop across the valve - or a similar parameter - is modelled. An example of this is presented in Table 9-1[10] where the pressure drop is calculated.

3 INCH CONTROL CHOKE	MEASURED DATA	PREDICTED DATA
Fluid	Water	Water
Valve Opening	12.5 mm	12.5 mm
Inlet pressure	2700 kN/m^2	2700 kN/m^2
Pressure Drop	*98 kN/m^2*	*120 kN/m^2*
Flow Rate	1700 l/hr	1700 l/hr
Temperature	40.5 °C	40.5 °C

Table 9-1 Comparison of Measured and Predicted Flow Data.

However, this does not give us an indication of the accuracy with which the turbulent structure has been resolved, being that which influences the erosion process through the trajectory calculation. Such gross validation tests are relatively redundant in the field of model validation, with a more comprehensive investigation being required to improve our understanding of the turbulent structure within such control valves. Here laser Doppler or a similar technique would need to be completed on

[10] Data provided courtesy of the Copper Cameron Corporation.

the innumerable combinations of control chokes/choke openings/fluid properties. This task is beyond the scope of this study, as such we are reduced to the best practice approach with regards to the solution scheme, leaving to others the task of developing the turbulence closure models.

9.1 Evaluation of Empirical Erosion Constants

From Chapter 4 we understand that to accurately model erosion we must be able to accurately capture all terms/mechanisms relating to both the target material and the erodent. To an extent this has been achieved through the development of the characteristic velocities for both the cutting and deformation erosion mechanisms, terms C_k and D_k. However, as one may appreciate the intricacies of the overall erosion process cannot be entirely captured by terms such as the material yield stress or other simplistic measures. To ensure the model holds the correct form for any number of materials/erodent combinations we are reliant upon empirical constants which force the models content into the correct form.

This section is concerned with assessing the two empirical constants which are embedded within the erosion model, being 'n' the cutting erosion factor and 'E_f' the deformation erosion factor. Here a number of common materials utilised within control chokes were studied under a range of impact conditions, with the model being tailored to best fit the measured data. The measured data was obtained through mass loss measurements, Figure 9-1, shows a schematic view of the slurry erosion rig employed. Here we are solely concerned with water driven erosion.

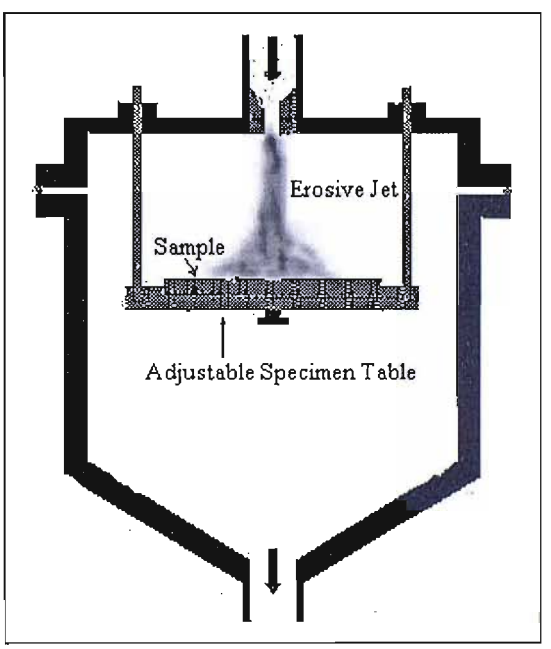

Figure 9-1 Slurry Erosion Rig Schematic.

Whilst facilities were available to characterise air driven erosion, this exercise was deemed to be outwith the scope of this work. The reasoning for this decision being that water was utilised as the carry fluid for the full valve erosion testing (having very similar impact characteristics as those generated by the erosion

rig), whilst others at the University of Southampton were working in the field of air driven erosion. Further, neither water or air fully represents the multiphase hydrocarbon system experienced within oil production facilities, thus we are forced to extrapolate to this situation for either case. Thus, to limit the required work load only water driven erosion was investigated.

The system under test was a fully submerged water driven case, utilising a 5.9 mm diameter nozzle to produce a slurry jet that impinged upon a flat specimen, with the typical test duration being one hour. The system was closed loop with a slurry pump continuously circulating the carrier fluid and the erodent. The sand concentration was varied between 2.0 and 2.5 % by wt, whilst the sand utilised for the test was Redhill 50, having an average size of 235μm. The density of sand was taken to be 2650 kg/m^3, with the sand assumed to be semi-sharp. The liquid flow rate in each case was 45 ltr/min or 430 bpd. The stand-off distance between the centre-line of the nozzle and the flat specimen was varied between 22 and 30 mm. The angle between the nozzle and the specimen was varied between 30 and 90 degrees in 15° increments. These test conditions and findings have been summarised in Table 9-2.

It is important that clarity is assured regarding the erosion testing of flat samples, and how a meaningful correlation can be made from such testing for surfaces that hold a curvature. Here the differing test angles of the samples (15° increments) was utilised to induce a variance in the impact angle, which would normally be forced through the structure of the flow field or the local curvature of the target surface. One could argue that the subtle differences propagated by a target which is or is not flat would influence the mechanism of erosion, i.e. the extent of cutting experienced Figure 4-10. However, this is unlikely to be the case due to the working scale of erosion, whereby the effective tip diameter of the impacting particle is many times smaller than the typical radius of curvature of a target. Thus, we assume the curvatures effect of the target to be negligible in all cases.

To allow the empirical constants of the erosion model to be tuned, the entire erosion system, as shown by Figure 9-1, was modelled using the *CFD* erosion model; given the process conditions summarised in Table 9-2. The fluid velocity contours for angles ranging from 90° to 45° are detailed by Appendix N Figures 121 to 124. Here we may observe that as the impact angle decreases the jet has a tendency to spread along the target, generating an elongated erosion scar. This situation is further compounded by variance in the erosion regime as the angle differs, where the peak erosional angle for steel is at approximately 75°. After several computational iterations for each material tested, the erosion constants were suitably tailored to allow confident predictions to be made. Table 9-3 details the empirical erosion constants generated through experimentation.

Figures 9-2 and 9-3 detail the resulting erosion profiles produced for both the measured data and the erosion predictions (constructed through the derived empirical constants) for both AISI 1020 carbon steel

and 6% cobalt binder tungsten carbide. The measured data was assumed to be the average value for each test conducted under those conditions. Here, the classical erosion profiles of a ductile (steel) and a brittle (tungsten carbide) material are observed, as discussed in detail in section 4.1. The correlation between the measured and predicted is good in each case, which is to be expected given that the model was tailored to give the best data fit. However, the point of most importance is that the correlation over the entire range of impact angles is consistent, thus demonstrating the benefits of the dual equation approach presented in Chapter 4.

Material	Liquid Flow Rate (l/m)	Sand Size (μm)	Sand Loading (% by wt)	Stand-off Distance (mm)	Angle (deg)	Duration (min)	Mass Loss (mg)	Average Mass Loss (mg)	Predicted Mass Loss (mg)
AISI 1020	45	235	2.5	30	90	60	629.4		
AISI 1020	45	235	2.5	30	90	60	677.5		
AISI 1020	45	235	2.5	30	90	60	589.9	*632.3*	*617.5*
AISI 1020	45	235	2.5	30	75	60	697.6		
AISI 1020	45	235	2.5	30	75	60	809.7		
AISI 1020	45	235	2.5	30	75	60	933.4		
AISI 1020	45	235	2.5	30	75	60	862.6	*825.8*	*849.1*
AISI 1020	45	235	2.5	30	60	60	803.2		
AISI 1020	45	235	2.5	30	60	60	748.9		
AISI 1020	45	235	2.5	30	60	60	694.3	*748.8*	*758.5*
AISI 1020	45	235	2.5	30	45	60	399.5		
AISI 1020	45	235	2.5	30	45	60	622.8		
AISI 1020	45	235	2.5	30	45	60	492.6	*505.0*	*518.0*
AISI 1020	45	235	2.5	30	30	60	362.4		
AISI 1020	45	235	2.5	30	30	60	438.1		
AISI 1020	45	235	2.5	30	30	60	493.2	*431.2*	*420.3*
Boart S6	46	235	2.0	22	90	60	104.5		
Boart S6	45	235	2.0	22	90	60	96.1		
Boart S6	45	235	2.0	22	90	60	97.3	*99.3*	*98.5*
Boart S6	45	235	2.0	22	75	60	101.2		
Boart S6	45	235	2.0	22	75	60	90.12		
Boart S6	45	235	2.0	22	75	60	85.26	*92.2*	*94.6*
Boart S6	45	235	2.0	22	60	60	76.9		
Boart S6	44	235	2.0	22	60	60	81.1		
Boart S6	45	235	2.0	22	60	60	71.9	*76.6*	*78.1*
Boart S6	45	235	2.0	22	45	60	57.8		
Boart S6	45	235	2.0	22	45	60	53.5	*55.7*	*54.2*
Boart S6	45	235	2.0	22	30	60	29.3		
Boart S6	45	235	2.0	22	30	60	34.1	*31.7*	*29.4*
Boart S11	43	235	2.0	22	90	60	99.4		
Boart S11	43	235	2.0	22	90	60	95.8		
Boart S11	43	235	2.0	22	90	60	97.5	*97.6*	*97.3*
Boart S11	43	235	2.0	22	75	60	84.85		
Boart S11	44	235	2.0	22	75	60	92.33		
Boart S11	44	235	2.0	22	75	60	88.67	*88.6*	*93.1*

Table 9-2 Summary of Slurry Test Conditions and Comparison with Predictions.

PARAMETER	1020 AISI CARBON STEEL	17.4 PH STAINLESS STEEL[11]	6% COBALT BINDER TUNGSTEN CARBIDE	11% COBALT BINDER TUNGSTEN CARBIDE[12]
'n' Cutting Erosion Factor (Hashish)	2.8	2.8	3.0	3.05
'E_f' Deformation Erosion Factor (Bitter)	1.9E+10	4.4E+10	1.38E+11	1.34E+11
Yield Stress (MN/m^2)	320	470	N/A	N/A
Transverse Rupture Stress (GN/m^2)	N/A	N/A	3.0	3.38
Young's Modulus (GN/m^2)	207	213	624	568
Poisson's Ratio	0.293	0.27	0.21	0.22

Table 9-3 Derived Empirical Erosion Constants and Material Parameters.

An interesting observation, which cannot be fully supported due to the lack of data, is the difference between the differing grades of tungsten carbide. Here, the erosion rate for the two grades of tungsten carbides at 90° is very similar, however as the impact angle decreases (75°) the 11% binder out performs that of the 6% binder, see Table 9-2. One hypothesis for this occurrence is that due to the increased binder content of the 11% grade, the carbide particles have an increased adhesion strength within the matrix than that generated by the 6% grade. This results in a reduced tendency for the carbide particles to be knocked out of this matrix at this impact incidence.

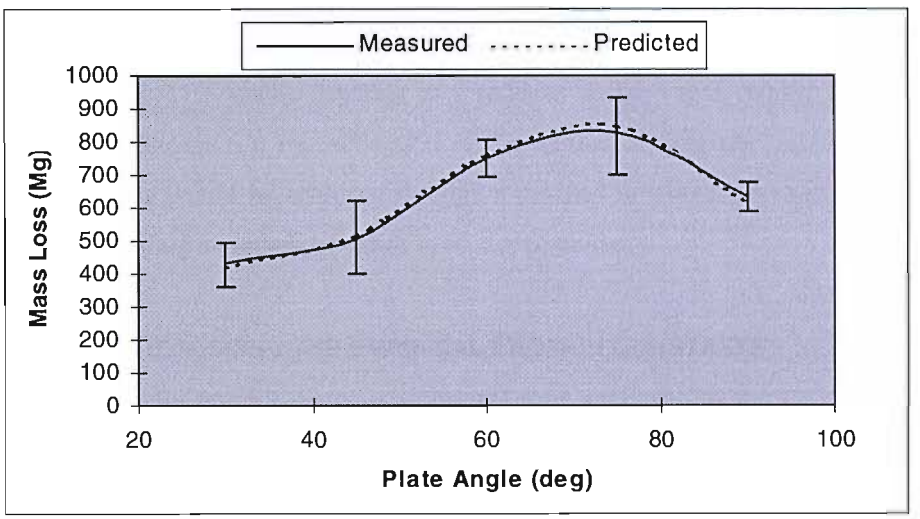

Figure 9-2 Comparison of Predicted Erosion Rates for AISI 1020 Steel

[11] The empirical constants for stainless steel were not derived experimentally. Here, the constants where extrapolated from carbon steel - given the variance in gross parameters - and validated through the full valve erosion simulation presented in Chapter 10.

[12] Only two impact angles (90° and 75°) where utilised to derive the empirical constants for 11% tungsten carbide due to time constraints. Here the structure of the lower impacts angles were assumed to mirror those of the sister 6% tungsten carbide. This assumption is valid for tungsten carbide do to the classical deformation erosion profile that it holds. See Figure 9-3.

Whilst at 90° the prominent erosion mechanism is crushing of the carbide particles, hence the binder content has little influence at this angle and the similarity between the two grades.

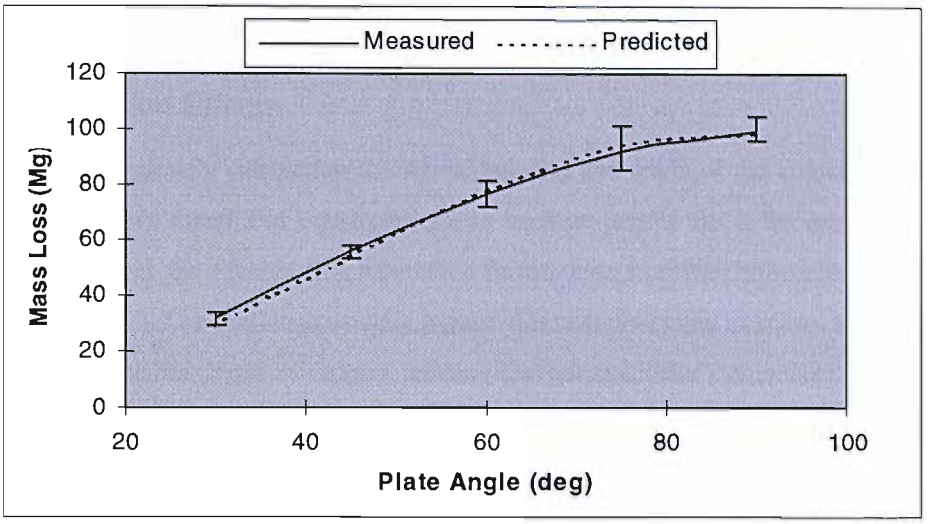

Figure 9-3 Comparison of Predicted Erosion Rates for BOART S6 Tungsten Carbide.

One may further hypothesize that as the impact angle is reduced below 75°, the 6% grade will start to outperform the 11% grade. The argument for this being that at such low impact angles there is insufficient energy to knock the carbide particles out of the matrix. Here, the prominent erosion mechanism is a progressive cutting/undermining of the binder, resulting in the loosening/loss of the carbide particles with time. Hence, due to the decreased binder content, the area of attack of the 6% grade is lower than the 11% grade, resulting in a reduced attrition rate. Whilst the current author believes the above statement is a true reflection of the erosion of tungsten carbide (for the limited range detailed), benefits would be achieved through a detailed investigation to supplement the data already collected, including an increased range in binder contents.

NOTE OF CONCERN REGARDING THE EMPIRICAL EROSION CONSTANTS

It must be clarified that the empirical erosion constants were generated by the study of a water slurry jet impinging upon a flat surface. Caution is required when applying these constants to other erosion regimes; i.e. where the carrier fluid is other than water. The erosion prediction is essentially based upon the energy with which the particle arrives at the targets surface. This suggests that provided the relative energy with which the particle impacts the target is of a similar magnitude, the erosion constants will be valid. Emphasis is thus placed upon the accuracy of the trajectory calculation and the content of the squeeze film retardation term. See section 9.1.1.

The assumption that the constants are valid for any carrier breaks down when the difference between the validation case and test case energy of impact becomes great. Typically, when one is investigating very high energy impacts, as induced by a high velocity air or gas jet, such effects as an increased rate

of localised melting of the target, tends to invalidate the empirical constants generated by the relatively low energy case presented here. Thus further work is required is ensure the applicability of the erosion model to the wider spectrum of erosion modelling. However, in the instance of choke model investigation - provided the carrier is liquid - the constants are valid.

9.1.1 Squeeze Film Effects

The importance of accurately calculating the arrival velocity and angle of the erodent upon the target surface has already been noted. For liquid carriers, an intrinsic part of this is the correct correlation of near wall effects through the squeeze film retardation factor, these near wall effects have been discussed in detail in section 6.3.2. The need to accurately capture this near wall layer increases as the impact angle decreased. The diminished angle of impact reduces the perpendicular component of the impacting velocity - the parallel component becoming dominant - and hence the particles ability to strike the target.

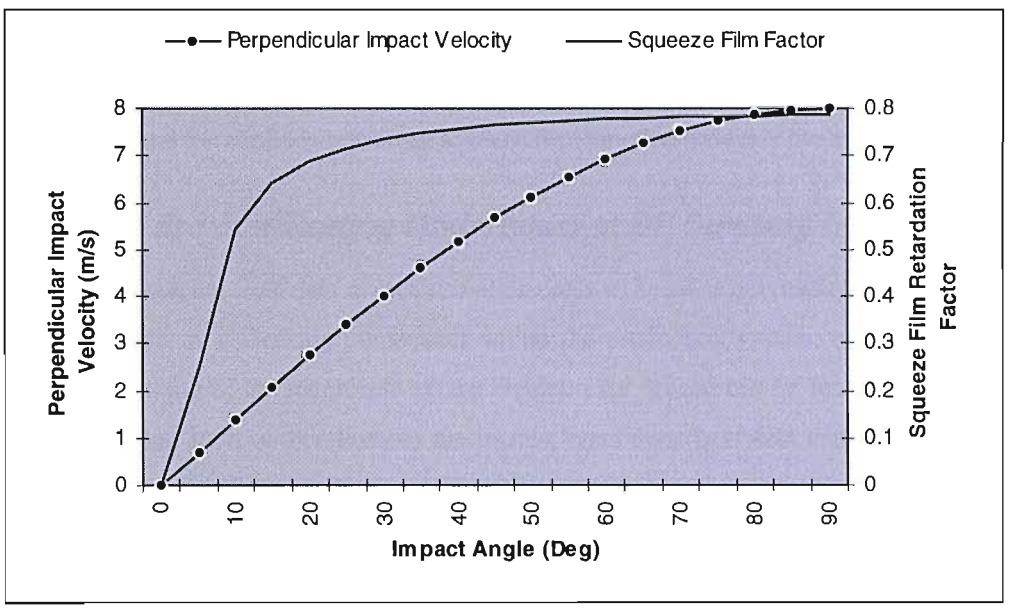

Figure 9-4 Slurry Jet Squeeze Film Retardation

The squeeze film retardation factor is calculated via the perpendicular particle Reynolds number, Re_{pp}, (Equation 6-29), which is determined through the perpendicular impact velocity, i.e. a function of the particle impact angle. Figure 9-4 details the relationship between the angle of impact, the squeeze film retardation factor and the perpendicular velocity component of the slurry case presented above (the standard correlations of section 6.3.2 were utilised). In each case the particle impact speed was assumed to be 8 m/s, with a particle size of 235 μm. The particle impact angle was varied between 0 and 90°, resulting in a range of perpendicular impact velocities between 0 and 8 m/s. There is a sudden decrease in the squeeze film factor as the angle of impact drops below 35°, whereby the particle cannot penetrate the viscous boundary layer of the carrier fluid.

To test the applicability of the squeeze film function, the empirical constants of erosion were fitted to the data for the 90° impact angle only. The simulation for the remaining impact angles were then run, in the hope that an understanding of the squeeze film effect could be acquired. This exercise was only partly successful due to the dual equation approach utilised within the erosion model. At an impact angle of 90°, only the deformation element of the erosion model was active, thus the erosion rate for the subsequent angles was under-predicted as only the deformation erosion factor, E_f, could be fitted. For carbon steel, this under-prediction was substantial at the lower angles due to the dominance of the cutting mechanism in these regions.

Encouragement was provided by the prediction obtained for tungsten carbide. The deformation mechanism was prime through the majority of the impact angles, resulting in a relatively small under-prediction across the impact range; of the order of 20 to 30% depending upon the impact angle. This promoted the belief that the squeeze film function was correct in both size and form, with the shortfall in prediction accurately being accountable through the lack of a cutting mechanism correlation within the erosion model. The introduction of the cutting mechanism yielded the excellent results reported by both Figure 9-2 and 9-3 and the confidence that the squeeze film function provided the best solution.

9.2 Full Valve Erosion Testing Undertaken at BP Sunbury

Qualitative experimental or field data of erosion within control chokes is not readily available. The choke is viewed very much as a working component within the production system, being treated as such. Whilst an understanding of the magnitude of any erosion experienced can be readily obtained through observations, coupling such observations to the process conditions is at best tentative. Here measures such as the sand concentration, production rates or the pressure drops across the choke are not logged with any confidence, leading to inherent error within any modelling process due to assumptions.

To facilitate validation of the entire erosion modelling process within a complex geometry such as a choke, reliable quantifiable data needs to be made available; which encompass all parameters. To this end, full valve erosion testing was undertaken on two donated control chokes; under strictly regulated conditions. The two chokes were generously supplied by Copper Cameron Ltd and ABB. Kent Introl Ltd. for erosion testing within the high pressure flow loop facility at BP Sunbury. I must give my sincere thanks to ABB and Cameron for their support of this project.

Detail drawings and dimensions of the ABB and Cameron chokes are presented in Appendix N Figure 125 and 126. The ABB choke employed multiple stages to manage the pressure drop, whilst the Cameron valve utilised a single stage. This fundamental difference rendered ranking of performance between choke manufactures invalid.

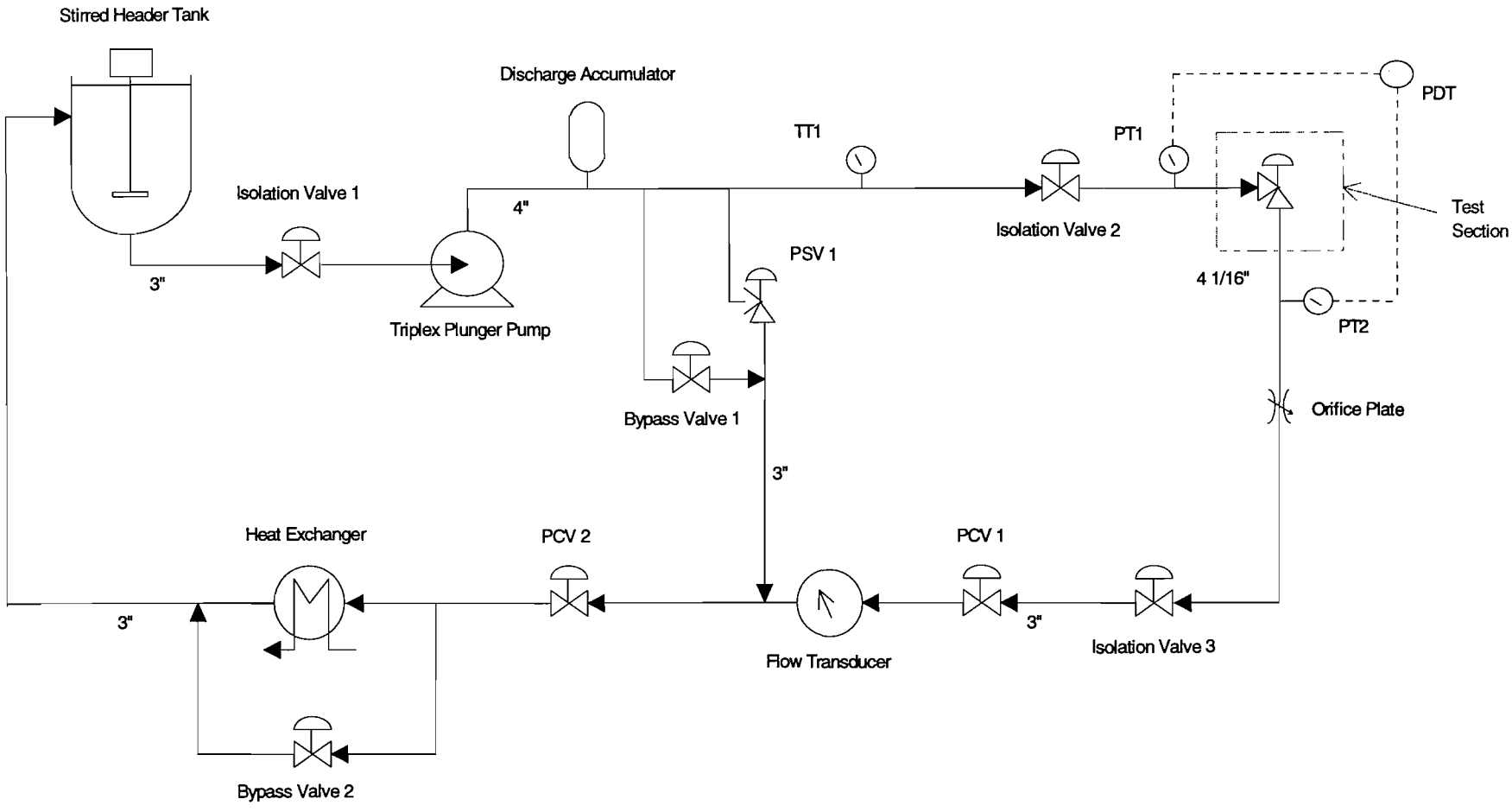

Figure 9-5 Schematic of BP Sunbury High Pressure Flow Loop Test Facility

Figure 9-5 shows the basic arrangement of the valve test facility; designed to simulate field conditions. The flow loop was of a closed design, feed by a stirred header tank which ensured any solids remained suspended. The control chokes were mounted within the test section and through which the test fluid was circulated by a diesel engine driven Schumberger triplex pump, originally designed as a cement pump. Appendix N Pictures 1 & 2 give an indication of the flow loop configuration and mounting position of the test chokes. The process routing was such that Bypass Valve 1 and the pressure relief valve (PSV1) were closed, forcing all of the flow through the test section. If there was a requirement to reduce the flow rate within the test section, Bypass Valve 1 could be opened to a nominal setting to allow a proportion of the flow to bypass the test valve.

Process control itself was provided by the test choke (see section 9.2.2 for further details) and through modulation of the pump speed via the gearing select of the gearbox and the rpm of the diesel engine. Back pressure on the downstream of the choke - to avoid cavitational influences on the modelling - was provided by both the orifice plate and PCV2. In this instance PCV1 was not utilised, being left wide open for the duration of the testing. The discharge to the stirred header tank was at atmospheric conditions, leading to concerns regarding erosion of the downstream pressure control equipment; further details can be found in section 9.2.2.

The test fluid was water, a concern was noted that due to the relatively low viscosity of water, the suspended solid could drop-out if the flow velocity was sufficiently low. See section 9.2.4 and Chapter 10 for further discussion on gravitational effects. To this end, the usage of polymer viscosifier within the carrier water was investigated. However, it was deemed that the cost and increased difficulty of operations utilising such a additive would not be justified. Between each test the flow loop was drained to enable the introduction of a fresh charge of sand, thus requiring the addition of the viscosifier for each test and an expense incurred.

	OPERATING PARAMETERS
TEST FLUID	Water. 0.5 - 1.5% by weight quartz sand, Forties distribution.
PRESSURE	100 - 5000 psig (7 - 345 barg)
PUMP DISCHARGE	270 gal/min at 1000 psig (1227 l/min at 69 barg) 100 gal/min at 2000 psig (455 l/min at 138 barg) 50 gal/min at 5000 psig (227 l/min at 345 barg)
TEMPERATURE	Ambient at 70°C.
TEST DURATION (Material Dependent)	Approx. 50% loss of pressure drop. Or 3 hour test duration.

Table 9-4 Operating Parameters of the High Pressure Flow Loop

Table 9-4 broadly summaries the operating parameters of the test rig, including typical pump discharge rates and pressures. The test duration may appear to be excessive, with testing being terminated after a 50% reduction in the pressure drop. However, it was found that as the chokes were supplied 'new' a

degree of the pressure drop loss was attributed to cleaning-up the newly machined surfaces of the trim. The termination of the test after a 10% loss in the pressure drop was found to result in 'rounding or profiling' of the control surfaces, leading to difficulties in accurately quantifying the location and intensity of any erosional attack. Whilst quantifiable data was required from the test, excessive erosion renders comparative work with the numerical model extremely complicated due interaction between the erosion scars of the trim and the flow field.

	CAMERON CC30	ABB. KENT INTROL SERIES 74'
FLANGE DIAMETER	3"	2"
FLOW CONTROL	Equal %	Equal %
PRESSURE DROP STAGES	1	2
STEM TRAVEL	1.375"	1.125"
DESIGN *Cv*[13]	30	8.5

Table 9-5 Control Choke Types Tested in Erosion Loop

The chokes tested were the Copper Cameron CC30 equal percentage plug and cage type and the ABB. Kent Introl Series 74 equal percentage plug and cage, as summarised by Table 9-5. One body for each choke was supplied, with a number of trims set combinations provided, Table 9-6. The chokes were originally supplied with the stainless steel trim set in the Cameron valve, whilst the ABB. valve housed the Stellite trim. Following each test the valves were completed stripped and refurbished prior to re-assembly with a differing trim set. During each refurbishment the condition of the choke body - including the sealing surfaces - was assessed for erosion damage.

	CAMERON CC30	ABB. KENT INTROL SERIES 74'
TRIM MATERIALS, INCLUDING BOTH PLUG AND CAGE.	Three of 17.4 PH Stainless Steel. One of 6% cobalt binder Tungsten Carbide.	Two of cast Stellite. One of 6% cobalt binder Tungsten Carbide. One of the ceramic Partially Stabilised Zirconia (PSZ).
BODY MATERIALS.	One of AISI 1020.	One of AISI 1020.

Table 9-6 Control Choke Material Combinations Tested

9.2.1 Test Philosophy

A number of choke testing philosophies were available. However, the underlying purpose of the testing was to provide quantifiable data upon which the erosion model could be tested. This led to a number of testing restrictions, which would not normally be considered as best practice in the industry. The prime consideration was whether the choke was to be adjusted during the test. To enable model validation it was important that the choke opening remained static. Further to the choke opening, the flowrate through the choke and hence the pressure drop across it should remain constant from a validation viewpoint. If the choke were to be adjusted during the test, each variance in the

[13] A definition of *Cv* is given by Appendix E.

choke opening would require an update to the model. The flow domain would require re-mapping with additional iterations of the flow field calculation and the particle trajectory/erosion prediction. This was an untenable situation due to the workload requirements generated via the re-mapping and re-modelling process incurred for each choke movement; of which there could be many in a three hour test.

However, the progressive closing of the choke on erosion of the controlling surfaces is the recognised best practice. The reasoning being that the process conditions should not vary with time, the delivery pressure from the reservoir and the operating parameters of any downstream equipment - such as the separator - will remain constant. Thus, the control choke should be progressively closed in (assuming a constant flow rate) to provide the desired pressure drop from reservoir/well head conditions to downstream process equipment conditions.

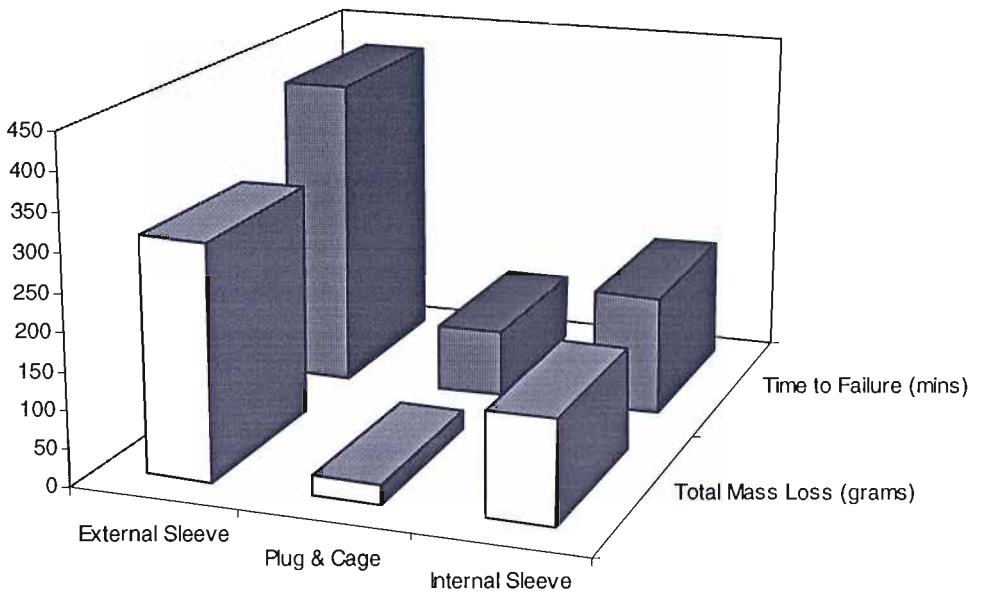

Figure 9-6 Time to Failure Comparison Generated via a Constant Pressure Drop Erosion Testing Approach

An example of such a testing approach is provided by Figure 9-6[14], here the flow rate and the pressure drop across the control choke were held constant, at 100 gpm (7.6 l/s) and 1500 psi (103 bar). The chokes were progressively closed-in until loss of flow control was experienced. When the choke could no longer generate the required pressure drop the choke was deemed to have failed and the test was terminated. Essentially, loss of flow control occurred when the plug/sleeve of the choke closed against the seat, however due to the extent of the erosion damage, the desired pressure drop characteristics could not be achieved due to the absence of further choke adjustment.

[14] Details of the testing have been limited due to the commercial nature of the findings and the legal implications.

The most striking feature of this figure is that the external sleeve design significantly outperforms the other chokes under these conditions, of the order of 4.5 times over the plug and cage type design. As such, one may conclude that for heavily erosive duty the external sleeve design is the choke of choice. However, following the discussions of section 8.6 one can appreciate that there are additional influences which affect the performance/longevity of the choke. Historically, the specification of the external sleeve for highly erosive duties can lead to trim failure through shatter, not erosion. As highlighted in section 3.4.3, problems occur if the well is producing solid of a significant size or generating very large liquid slugs due to an inherent weakness within the trim design.

Thus, in contrast to the above discussion the testing was conducted at a fixed choke opening to provide ease of model validation. Further to this conclusion, options upon the optimised flow rate/pressure drop/choke opening had to be reached. Here, the decision was made that two testing regimes should be incorporated into the test program, being broadly summarised as small choke and large choke opening or high pressure and low pressure testing. See Table 9-7.

	HIGH PRESSURE	LOW PRESSURE
SUPPLY PRESSURE	1520 psig (105 barg)	800 psig (55 barg)
PRESSURE DROP	840 psi (58 bar)	430 psi (30 bar)
FLOW RATE	100 igpm (7.6 l/s) 4100 bpd	175 igpm (13.3 l/s) 7200 bpd
Cv	3.5	8.5

Table 9-7 Summary of Testing Regimes

Given that the choke opening was fixed, pump operations required careful consideration. The pump speed was initially set to give the desired flow rate and pressure drop characteristics for the given choke opening. As erosion of the choke progressed the pressure drop characteristics were altered, with a reduction in the delivery pressure of the pump. This caused the pump to move down its discharge curve, resulting in a increased flowrate for the pump speed and reduced ΔP across the choke. From a validation viewpoint, the ideal situation would be that both the flowrate and the pressure drop be held constant. However this was against the nature of the experimentation, where the stated purpose was the collection of quantifiable data. This statement could only be achieved through the introduction of surface damage and hence variances in the pressure drop.

Thus a compromise was required, whereby one had to sacrifice either a constant flowrate or pressure drop across the choke given the need for a fixed choke opening. Both approaches were utilised, with either the pump speed being increased to maintain a constant pressure drop, or backed out to enable the flowrate to remain constant for the duration of the test. The preferred method was the constant flowrate

approach, with 7 of the 8 tests being conducted in this manner. The reasoning for this being that the resultant erosion from the constant flowrate case was better defined and more suited to the purpose of model validation. The constant pressure drop case gave a tendency towards gross erosion damage, which was difficult to interpret.

A requirement of data for model validation is that the conditions under which it has been obtained be held constant, including the target surface. This statement is contrary, and a compromise is required. If the induced erosion is of a relatively low intensity, the conditions will have been held constant, however the confidence in that data and usage in driving the validation exercise is limited. In contrast, if the damage is gross then conditions will have changed excessively and the data is of little value also. The target surface will have been eroded significantly from the original, and parameters such as angle of particle impact cannot be quantified.

Two low pressure/high flow tests were completed - one being of constant pressure drop - with the remaining six being of the high pressure drop case. The high pressure drop case was preferred as the erosive response of a choke is more pronounce at small opening, where the interaction of the plug and the impinging flow field is maximised through the close confines of the controlling surfaces. This enabled a more accurately defined erosion pattern within the choke through the promotion of localised attack. The low pressure/high flowrate approach was required to provide an understanding of the choke opening.

The preference for the high pressure/low choke opening approach to testing was also related to the flow capacity, or *Cv*, of the ABB. Kent Introl valve being limited to 8.5. This implied that the high flowrate test would require the valve to be wide open, generating an unrealistic test case scenario. An additional cause for the preference towards the low choke opening test was that of mapping or constructing the computational flow domain. The geometric blocking strategy for the inclusion of all of the flow ports within the cage would at best have been extremely complex, if at all possible. This would have lead to considerable difficulties in achieving a reliable solution for both the flow field and erosion prediction.

The target sand loading was 1% by wt., utilising a Forties mix. This loading was deemed most appropriate as the erosion rate was sufficiently accelerated to provide a realistic time scale for testing, whilst the loading was low enough to provide an inter-particle spacing which ensured particle-particle interactions were largely avoided and hence their impact on the erosion mechanism. The Forties mix was arrived at by a combination of Redhill sands, having the composition; 25% Redhill 50, 50% Redhill 65 and 25% Redhill 110. The synthetic mix was employed for the sake of ease. Whilst actual produced Forties sand could have been easily sourced, the sand would have required cleaning to remove hydrocarbons and possible LSA scale.

9.2.2 Test Procedure

A basic outline of the test procedure used follows. Great importance was placed upon consistency of results, requiring care to be taken at each of the test stages due to the complexity associated with the flow loop and the impact of these complexities upon the erosion process. The tests were broken down into three key operations;

1. Inspection and assembly of choke components.
2. Erosion test and condition monitoring.
3. Disassembly and inspection of the choke components.

Operation	Step	Keypoints
1. Inspection and assembly of choke components.	a) Weight all trim components prior to assembly.	• Measurement accuracy limited by mass of some components.
	b) Note any machining or construction defects which may influence the erosion process.	• Special attention to be given to orientation of ports. Machining marks to be finished if felt to impact erosion mechanism.
	c) Assembly choke components as per manufacturers guidelines. Utilise a new seal set for each re-assembly, four of in total.	• Mark orientation of plug to the inlet of choke for reference.
	d) Fit choke to the test section of the flow loop, if not already done so. Stoke test the choke to confirm operability then set opening to desired setting. Lock choke in position.	• CC30 low pressure test - 40/64ths. • CC30 high pressure test - 28/64ths. • ABB high pressure test - 25%.

Operation	Step	Keypoints
2. Erosion test and condition monitoring.	a) Once choke installation is complete, introduce a fresh charge of water to the flow loop.	• Loop to be filled via the stirred header tank to ensure loop is fully primed with water. Charge volume approx. 1000 lt.
	b) Confirm loop is leak tight. Start diesel engine via compressed air starter and allow engine to warm at idle.	• Monitor coolant and oil temperatures via the control suite.
	c) Confirm all loop valving is configured correctly, and all instrument feedback is live.	• Isolation valves 1/2/3 - open. • Bypass valve 1 - closed. • Bypass valve 2 - open. • PSV1 - closed. • PCV1 - fully open. • PCV2 - managing discharge to atms.
	d) Initiate PI data logger on supporting PC and confirm action of archiving system.	• If data logger is not archiving the pressure, flow or temperature data, abort test.
	e) Engage gearing to pump and increase engine revs to allow the target flow rate to be achieved, as confirmed by the flow transducer.	• High pressure - 100 igpm / 58 bar ΔP. • Low Pressure - 175 igpm / 30 bar ΔP. • 5 gears available. Gear selection is dependent on the target pump discharge pressure / flow and engine revs. For the conditions experienced here the 3rd gear is optimal in terms of engine speed.

Operation	Step	Keypoints
	f) Once target flowrate and pressure drop achieved, confirm operability and stability of set up. If happy that test conditions are good, add a fresh charge of Forties mix sand to the stirred tank.	• Given that a proportion of the previous test sand is held up in the flow loop, the volume of fresh sand added per test is adjusted to reflect this. The optimal additional volume was found to be 4 kg.
	g) Initiate cooling water spray curtain.	• Careful that you don't get wet feet....
	h) Allow fresh sand to fully circulate the loop, approx 10 mins, then collect a 1 lt. sample of carrier fluid to assess particle loading.	• A minimum of 3 sand loading samples to be taken during the test, at equally spaced times. For the 3 hour tests 5 sand samples to be taken. • On collection of the sand samples, filter the solids from the carrier and oven dry prior to weighting for loading analysis.
	i) Monitor flowrate, temperature and pressure drop across the test choke via instrumentation, manually adjust pump speed by throttling the drive engine as necessary.	• The engine speed should be adjusted if the flow transmitter fluctuates by more than 4 gpm. • Confirm condition of pump set via control suite instrumentation throughout test.
	j) Once the test criterion has been satisfied terminate the test. The drive engine should be throttled back and neutral gear selected prior to stopping the engine.	• Test criterion being a 50% reduction in pressure drop across the choke or a test duration of 3 hours.

Operation	Step	Keypoints
	k) Closed down spray curtain facility and cease data logger on the PI system.	• Back-up archived data.
	l) Open drain point on bottom of stirred tank and allow flow loop contents to discharge to drains.	• Collect large sand sample from base of stirred tank - approx 1 kg - for sand attrition analysis. • Hose clean stirred tank for fresh charge.
3. Disassembly and inspection of the choke components	a) Once flow loop is drained and confirmed as depressurised - via vent point on choke body -, break out bonnet connections on the choke and remove the complete trim assembly as per manufactures guidelines.	• It is preferred that the choke/trim be disassembled in situ do to the risk associated with the removal of the entire choke. • The choke body is only to be removed to test the choke of other manufacture. • Note any abnormalities when disassembling the trim - such as sand packing - and note the orientation of the trim relative to the inlet.
	b) Closely inspect the in situ choke body for any signs of erosion damage and confirm it's integrity for subsequent tests.	• Specific attention should be paid to the outlet spool, with any signs of damage being recorded pictorially.
	c) Compete detailed analysis of all trim components and store for future reference.	• Analysis to include mass loss and pictorial records of erosion sites and directional influences.

9.2.3 Flow Loop Preparedness

I was fortunate in that the flow loop was in a near state of readiness, having been moth balled for only a relatively short period. Given the technical support of the BP technicians at Sunbury, the engine, pump, flow loop hardware and the instrumentation-control-logging systems of the loop were re-commissioned.

The engine and the pump itself required little work as prior to testing phase the engine's two cylinder heads had been rebuilt following operational difficulties. Initial commissioning runs upon the engine/flow loop highlighted a number of difficulties, including erratic instrumentation feedback and rapid heating of the test fluid within the closed loop. In response to the erratic instrumentation feedback, the calibration of the pressure and flow transducers was confirmed and corrected as necessary. However, this did not resolve the pressure pulsations difficulties. The cause was traced to a failed discharge accumulator, whereby the bladder of the accumulator had ruptured. A time delay occurred whilst a replacement bladder was sourced and fitted, with the accumulator being padded to the nitrogen pressure; in this instance 80 barg or 80% of the typical discharge pressure of the pump.

Due to containment issues the heat exchanger was bypassed for the duration of the testing via Bypass Valve 2. This lead to difficulties with overheating of the equipment, more specifically the pump, due to the thermal energy created through the choking and pumping processes within the closed loop. The pump tripped itself when a temperature of 70°C was reached. Initial testing indicated that this overheating would be problematic for the extended duration tests, as such an alternative method of cooling the flow loop was devised. Here a rather crude spray curtain arrangement was rigged, whereby the flowloop was deuced with cold water using an irrigation hose fastened to the piping. This proved to be effective in managing the thermal equilibrium of the loop, with a stability point reached at approximately 60-65 °C.

As commented upon in the above section, a concern regarding the test loop was the erosion of the downstream pressure control equipment, required to generate a backpressure upon the choke.. The decisions was made to introduce an orifice plate which was not in the original flow loop configuration, as detailed by Figure 9-5. The orifice was design by the author, constructed and installed within the test loop. A simple schematic is show by Figure 9-7.

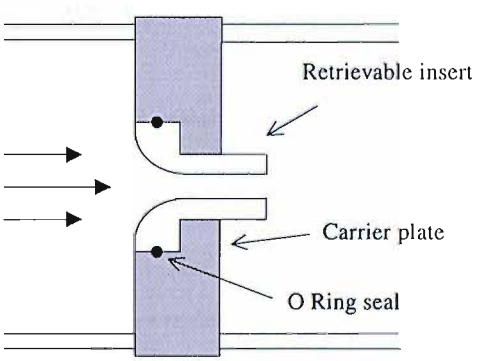

Figure 9-7 Orifice Plate Schematic

The design philosophy was to enable easy change-out of the orifice if severe erosion should occur. Here the central insert was retrievable, such that the requirement for duplicate carrier plates was removed. The whole assembly was simply bolted into the pipework at a ring tight joint, given the carrier plate thickness was only 25 mm and there was sufficient 'flexibility' in the pipework to allow installation. The entire assembly was constructed on site from an AISI 1020 steel.

The orifice was sized such that it offered a high degree of protection to PCV2, taking the majority of the pressure drop to the atmospheric conditions of the stirred tank. For the two test regimes, being anticipated to generated inlet pressures to the orifice of 20 barg for the high flow and 45 barg for the low flow, orifice diameters of 18 and 12 mm were utilised. These orifice diameters generated calculated pressure drops of 16.8 and 37.4 barg given flow rates of 175 & 100 igpm (13.3 and 7.8 kg/s) respectively. The orifice plates were sized using a simple one-dimensional analysis derived from Bernoullis equation, having the form;

Equation 9-1

$$\Delta P = \left\{ \left(\frac{a_1}{a_{vc}} \right)^2 - 1 \right\} \frac{\rho V_1^2}{g}$$

Where the area of the *vena-contracta* is given by $a_{vc} = C_c a_2$, the coefficient of contraction, C_c, being dependent upon the orifice profile.

Given the concerns regarding erosion, the orifice plate was modelled by the CFD erosion model prior to the erosion testing phase of the project. This allowed the profile of the orifice to be tailored such that the expected erosion was minimised. The process conditions selected for this modelling work, including the considerations given to the particulate phase, are summarised by Appendix N Figures 127 to 130. This summary also provides the dimension ratios of the orifice taper which were arrived at to provide the best erosion resistance. The iterative design step to achieve this optimal solution are not been discussed. Appendix N Figure 127 details the flow structure across the orifice, whilst Appendix N Figures 128 to 130 depict the projected particle impacts and resulting erosion.

As has been established as the solution technique of choice, the Differential Stress model was utilised to capture the flow structure, whilst the particle treatment included recognition of turbulent dispersion, the modified coefficient of restitution and squeeze film effects.

The distinct benefits of the design evolution upon the taper profile are realised from Appendix N Figure 130. Here, the assumed flow rate was 200 igpm or 54.5 m^3/hr, for the specified 1.0% by wt particle flux a total of 545 kg of sand was passed in the hour. However, for this very large particle flux, the predicted erosion did not exceed 1 mm^3/hr. If we apply the concept of normalised erosion in this instance, that found for this example is 0.0014 mm^3/kg of erodent. The significance of this figure can be understood

when one considers the typical normalised value for control choke undertaking liquid duty, being of the order of 0.75 to 2.0 mm^3/kg of erodent. This is further exemplified when one considers that the material utilised for the orifice plate was a standard carbon steel, which has relatively poor erosion performance when classified along side materials commonly found in process control equipment.

The excellent performance of the orifice was demonstrated throughout the erosion testing, where no significant erosion damage was noted upon the orifice, one being utilised for all of the high pressure testing; having a duty time of 12 hr 39 min, passing a total of 347.9 m^3 of carrier and 3538 kg for erodent. The only indications of damage were those generated by the corrosion of the carbon steel due to its water duty.

9.2.4 Test Conditions, Observations and Results Summary

As discussed previously eight full valve erosion tests were completed, with the philosophy behind the testing regimes presented. For ease of convention the tests were number from one to eight, Table 9-8.

Test	1	2	3	4	5	6	7	8
Manufacture and Choke	Cameron CC30 EP 17.4 pH SS	Cameron CC30 EP 17.4 pH SS	Cameron CC30 EP 17.4 pH SS	Cameron CC30 EP 6% WC	ABB Series 74 Stellite	ABB Series 74 Stellite	ABB Series 74 6% WC	ABB Series 74 PSZ
Test Type	High Flow	High Flow	Low Flow	Low Flow	Low Flow	Low Flow	Low Flow	Low Flow

Table 9-8 Summary of Test Conditions.

Each of the tests followed the procedure detailed in section 9.2.2. and the conditions and findings have been summarised by Table 9-9. Table 9-9 presents both the measured mass loss for each of the trim components and the volume loss, such that cross material comparisons can be made. A numerical interpretation of the results has been provided by Table 9-11.

Prior to reporting on the tests individually, it is important to reaffirm that both manufactures choke bodies were examined in detail after each test. In all cases no visible signs of erosion were noted other than polishing. The Cameron body passed 2263 kg of sand, whilst the ABB body passed 2346 kg of sand. Credit must be given to each manufacturer for delivering a choke which contained erosion to the trim components, under arduous liquid duty. However, it is important that the reader be aware that this statement is only in support of liquid duty. A gaseous carrier will develop differing conditions in the trim/downstream areas and one cannot say with confidence that the design presented here will perform as well under gas or even multiphase duties.

Test 1 - Cameron CC30 Stainless Steel. High Flow (Constant Choke ΔP)

The first test was principally utilised to gain an understanding of the operational performance of the flow loop and the erosive response to the conditions established for the testing, this learning was

essential to the successful testing of subsequent chokes. It is of interest that whilst the BP Sunbury flow loop facility had been available for a number of years, it had been under-utilised and lessons learnt from previous tests had not been carried forward in detail.

The main feature of this test was that it was outwith the subsequent tests, here the philosophy of constant ΔP across the choke was utilised. At the time of the first test it was unclear whether the constant flowrate or ΔP across the choke approach to testing was the method of choice, given this uncertainty the decision to proceed with the constant ΔP was made. The test was conducted under the high flow - low pressure - regime, with a choke opening of $40/64^{ths}$. The summarised conditions are presented in Table 9-9, derived in part from Appendix N Figure 131, the logged data over the period of the test. This logged data included the volumetric flowrate, the upstream and downstream pressures, the pressure drop across the choke, the carrier temperature and the calculated Cv. Three sand samples taken throughout the test found the sand loading to be 0.82 % by wt. giving a calculated total mass of sand passed at 823 kg for a test duration of 120 mins. The test was completed in parts, here the overheating problems discussed in 9.2.3 were first realised. The pump-set tripped on high temperature after 35 minutes, the loop was allowed to cool and the remaining 85 minutes of testing completed.

From Appendix N Figure 131 it can be seen that there were spikes in the logged data. These surges related to instabilities in the pump-set generated by pushing the pump to the limits of it's operational envelope. In terms of tests consistency such surges are undesirable and have lead to doubts regarding the applicability of the data to the validation case.

The initial ΔP across the choke was 23 bar, giving a volumetric flow rate of 160 igpm. Upon erosion of the controlling surfaces the pump speed was progressively increased, generating a final volumetric flowrate of 220 igpm. However the ΔP across the choke had fallen to 16 bar at test termination. The cause for failure to maintain the constant ΔP found its grounding in the hydrodynamic efficiency of the choke. The hydrodynamic efficiency of the choke, or the rate of energy dissipation, decreased with erosion. As commented on previously the chokes were supplied new, the initial period of erosion testing - approx 30 mins - resulted in the profiling of the controlling surfaces, i.e. a rounding of the sharp edges on the cage and plug. This profiling progressively decreased the chokes hydrodynamic efficiency through a reduction in the turbulence and diffusion losses associated with sharp edges. The result of this effect was that the flowrate through the choke needed to be significantly increased to maintain the energy dissipation rate and hence the pressure drop. This demand for a significant increase in the flowrate exceeded the performance capabilities of the pump set and the constant ΔP criterion was not met. This situation was compounded by the fact that the test was operated under the high flow regimes.

RESULT SUMMARY	CAMERON 17.4 PH	CAMERON 17.4 PH	CAMERON 17.4 PH	CAMERON 6% WC	*ABB STELLITE 6*	ABB STELLITE 6	ABB 6% WC	ABB PSZ
TEST NUMBER	1	2	3	4	*5*	6	7	8
DURATION (mins)	120	27.5	75	187	*63*	60	187	187
CHOKE OPENING	40/64^{ths}	40/64^{ths}	28/64^{ths}	28/64^{ths}	*25%*	25%	25%	25%
AVER. FLOW (igpm)&(kg/s)	183.1 (13.94)	157.6 (12.0)	104.2 (7.88)	100.3 (7.64)	*100.3 (7.64)*	100.3 (7.64)	99.9 (7.61)	99.7 (7.6)
INITIAL PRESSURE DROP (bar)	23	31	48	58	*48*	56	59	59
FINAL PRESSURE DROP (bar)	16	14	26	36	*24*	20	31	36
AVER. PRESSURE DROP (bar)	16.4	19.4	33.3	40.2	*31.2*	27.4	37.8	39.3
AVER. INLET PRESSURE (barg)	50	56	93	103	*100*	100	110	105
AVER. TEMP (°C)	53.6	23.4	36.2	57.2	*45.2*	47	62.9	72.8
FORTIES MIX	✔	✔	✔	✔	✔	✔	✔	✔
AVER. SAND LOAD (% by wt.)	0.82	1.16	0.58	1.16	*0.88*	0.999	1.024	1.096
TOTAL MASS OF SAND PASSED (kg)	823	248	206	986	*254*	283	874	935
MASS LOSS OF PLUG (mg)	14000	6000	6500	3600	*1900*	1700	500	200
MASS LOSS OF SEAT (mg)	✗	✗	✗	✗	*1260*	1220	380	90
MASS LOSS OF FLOW CAGE (mg)	8100	3600	2000	2350	*23240*	18340	11800	2740
MASS LOSS OF CARRIER (mg)	✗	✗	✗	✗	*15000*	800	3400	2300
MASS LOSS OF SLEEVE (mg)	✗	✗	✗	1150	✗	✗	✗	✗
VOLUME LOSS OF PLUG (mm^3)	1795	769	833	248	*225.1*	201.4	34.44	34.5
VOLUME LOSS OF SEAT (mm^3)	✗	✗	✗	✗	*149.3*	144.5	26.2	15.5
VOLUME LOSS OF FLOW CAGE (mm^3)	1038.5	461.6	256.4	161.9	*2752.9*	2173	812.7	472.4
VOLUME LOSS OF CARRIER (mm^3)	✗	✗	✗	✗	*1776.8*	102.6	435.9	294.9
VOLUME LOSS OF SLEEVE (mm^3)	✗	✗	✗	147.4	✗	✗	✗	✗

Table 9-9 Summary of Full Valve Erosion Testing.

Further to the failure to meet the pressure drop demand, the erosion generated by the constant ΔP approach was excessive. Here the energy dissipation rate was maximised through the philosophy of constant ΔP, the resultant erosion was gross in nature. This is verified through Appendix N Picture 11 and 12 where one may observe the erosion damage. From a validation viewpoint the erosion data generated by this test was of little value due to the extent of the damage, rending the controlling surfaces grossly removed from the original. In addition to the damage to the plug, of the order of 1795 mm^3, the cage also experienced damage, of the order of 1039 mm^3. Of the Cameron tests, test 1 was

that which experienced any significant damage to the cage. Figure 9-8 and Appendix N Picture 11 details the erosion around the cage ports and the complete erosion of one of the step from one of the ports. See Appendix N Figure 126 for details of the choke configuration.

Clarity should be made of the flow cage configuration. The flow cages of the stainless steel Cameron chokes were constructed such that they mimicked that of the tungsten carbide valve. To support and protect the tungsten carbide flow cage there was a stainless steel carrier sleeve, with a step in port size between the carrier sleeve and flow cage. These components of the trim are labelled as 5A and 5B on Appendix N Figure 126. To ensure consistency this arrangement was duplicated for the stainless steel chokes, where the flow cage and outer sleeve were constructed as a single piece stainless steel 'flow cage' with the same geometric configuration, including the step change in port diameter. Table 9-9 details how the tungsten carbide Cameron valve could be split into the sleeve and the flow cage, whilst the stainless steel valve could only be represented as the flow cage.

The cage erosion occurred due to the gross erosion of the plug. As the plug eroded, those surfaces which were providing flow control shifted from the plug to the cage, giving rise to cage centred and not plug erosion. This test is the only Cameron case where this shift has been noted, with subsequent tests producing plug focused erosion only.

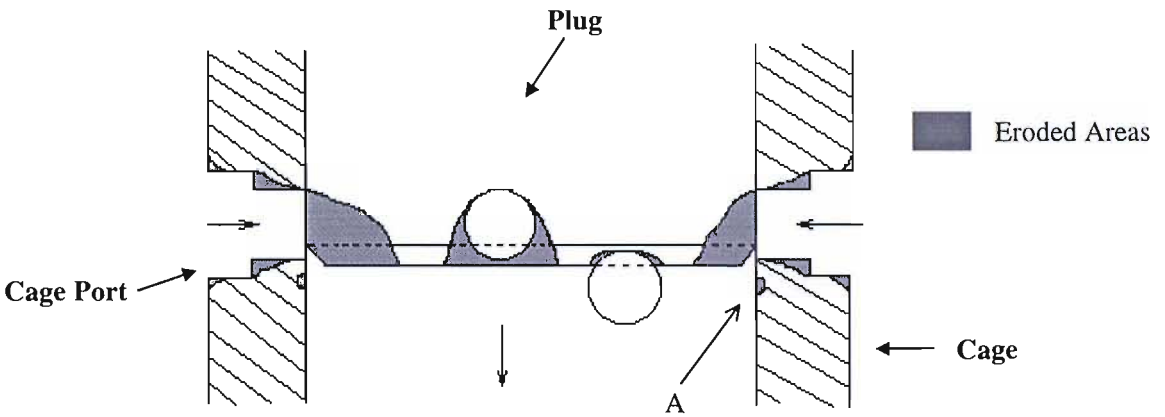

Figure 9-8 Simplified Representation of Erosion within the Stainless Steel CC30

From Appendix N Picture 11 it is noted that the erosion of the plug, and to an extent the cage, is non-uniform. The reasoning for this has been addressed in section 10.1. Figure 9-8 presents a simplified view of both the cage and plug erosion, including the profiling of the ports. Note that only 4 of the 24 ports in the flow cage have been included for clarity. It is of interest that the most aggressive erosion on the plug was induced by ports which had very little original overlap with the plug. The ports shown have a diameter of 4.8 mm, hence the overlap was of the order of 0.6 mm. This close overlap generated very intensive wall-fluid interaction and much accelerated erosion. Furthermore, prior to eroding, the seat angle on the base of the plug interacted with the jets generated by the overlapping ports, causing the jet to be reflected back into the inter walling of the cage. This actions caused a 1

mm deep crescent shaped erosion scar to be formed on the inter wall, as noted by 'A'. If the flow cage had been constructed of a material with a lessor erosion resistance than the plug, this reflection action could have resulted in through erosion of the flow cage.

Test 2 - Cameron CC30 Stainless Steel. High Flow (Constant Flow)

Given the finding of the first test regarding operational performance of the pump-set and the erosive response of the choke, the decision was made whereby the test method of choice be the constant flowrate approach. Due to the inconsistency of data generated by the first test and the gross erosion induced, the conditions of the first test were reproduced to provide workable data. The conditions and findings of this test are presented in Table 9-9 and Appendix N Figure 132. The average sand loading was found to be 1.16%, or a total of 248 kg of sand passed.

The learnings of test 1 indicated that to avoid gross erosion damage, the test duration needed to be shortened. In response the target test duration was deemed to be 45 minutes. However, the test was terminated after 27.5 minutes due to difficulties with the pressure transducers. The feedback from the transducers was becoming progressively more erratic, and it was felt that at the risk of lessening the value of the data collected, the test should be suspended and the rogue pressure transducers re-calibrated. Isolation valves 2 and 3 were closed and the trim assembly removed without a complete drain down of the flow loop. The reason for this was that given the short duration of the test, if the erosion to the trim set was found to be within limits, the test could be re-established (upon re-calibration work) and data collected regarding the progressive nature of the erosion. However, upon removal of the trim, the erosion damage was found to be extensive, and the test terminated.

Appendix N Picture 12 details the damage to the plug. The volume loss from the plug was found to be 769 mm^3, whilst the volume loss from the flow cage was 462 mm^3. The biasing of the erosion around the plug is noted, and the reader is again referred to section 10.1. In this instance the erosion to the flow cage was much reduced to that of test 1, with the shift to cage centred erosion being avoided due to the shortened duration. The damage to the cage was limited to a rounding of the ports, following a similar pattern to test 1, including the reflection erosion scarring on the inter wall of the flow cage. In association with test 1, the high flow tests required the choke to have a greater opening than the low flow case, $40/64^{ths}$ as opposed to $28/64^{ths}$. This resulted in an higher number of ports being laid open to the erosive flow, and a higher erosion rate of the cage over the low flow cases due to the increased exposure area. 20 of the 24 ports were involved in flowing for the high flow case, whilst only 12 were utilised for the low flow case. See section 9.2.4.1 for further discussions on the erosive relationship.

Erosion was initially rapid prior to the removal of sharp edges and the controlling surfaces of both the cage ports and the plug, the erosion then becomes relatively steady state as the profiling continues and

the erosion scarring is propagated. This statement can be confirmed through a comparison of test 1 and 2 data, see Table 9-10. Test 2 undergoes a much accelerated erosion rate than that of test 1, as test 2 was still operating in the incubation period of erosion scar development. This is also confirmed from Appendix N Picture 12 whereby the erosion scarring of test 1 is further developed than test 2. The normalised erosion rates gave consideration to the particle loading in addition to the test duration.

TEST	1	2
Test Duration (mins)	120	27.5
Volume loss to Plug (mm^3)	1795	769
Volume Loss to Cage (mm^3)	1038.5	461.6
Plug Erosion Rate (mm^3/min)	15	28
Cage Erosion Rate (mm^3/min)	8.7	16.8
Normalised Plug Erosion Rate (mm^3/min/% by wt.)	18.3	24.1
Normalised Cage Erosion Rate (mm^3/min/% by wt.)	10.6	14.5

Table 9-10 Test 1 and 2 Erosion Rates

Test 3 - Cameron CC30 Stainless Steel. Low Flow (Constant Flow)

Test 3 was the first of the low flow - high pressure - tests. The choke had an opening of 28/64ths and the test duration was 75 minutes. Table 9-9 and Appendix N Figure 133 details the conditions and findings of the test. Given that the short duration test 2 had been terminated prematurely and the flow loop only partly drained, no additional sand was added as it was felt that attrition of the residual sand would be minimal. This resulted in a low sand loading for the test of 0.58%, or 206 kg of sand passed.

The volumetric flow rate was maintained at approx 100 igpm (average 104 igpm), resulting in an initial ΔP across the choke of 48 bar, dropping to 26 bar on erosion of the controlling surfaces. Difficulties were experienced with the data logging system, and the data reported by Appendix N Figure 133 is a manual interpretation of the online data. As such small errors should be expected in this reported data. However, test 3 was the first test where one may observe the decline in the pressure drop profile as erosion progressed. As the flowrate was held constant, the pressure drop profile reports directly the progression of erosion to the controlling surfaces. The profile was relatively steep initially as the incubation period of erosion was experienced, the shift to a steady state linear profile occurred after approx. 40 minutes of testing. The data supports the statement made in test 2, where it was noted that erosion is initially rapid as the sharp edges are profiled and the erosion scars are established, declining to a steady state processes as the erosion scars and profiling actions are extended.

The erosion damage to the cage was limited 256 mm^3, with the scarring being a profiling of the step in the ports and the 'crescenting' of the inter wall due to the seat angle on the plug, as reported in test

1. The plug experienced intensive jetting, with the recorded volume being 833 mm^3 (Appendix N Picture 12). This intensive jetting, far in excess of that noted in the previous tests, was generated via the large pressure drop across the valve acting on small ports within the flow cage. The active ports diameter in this instance was 3.2 mm, as opposed to the 4.8 mm reported for the high flow cases. The velocity associated with such a intense jet was very high, and the erosion resistance offered by a steel material inadequate for such service. See Figure 10-1 for a simplified view of the plug erosion.

A defect in the placement of a port in the flow cage generated an additional erosion site on the plug. One port of the zone immediate above the plug - the first zone shutoff by the plug - was positioned too low, resulting in an overlap action similar to that reported by Figure 9-8. This erosion site can be seen on Appendix N Picture 12 - top of plug - where there are two erosion sites. The left site is set back further from the main erosion site and is that generated by the port overlap which should of been shutoff. This overlap also caused severe 'crescenting' erosion on the inter wall of the cage. The erosion biasing on the plug is also very apparent and the reader is again referred to 10.1.

Test 4 - Cameron CC30 Tungsten Carbide. Low Flow (Constant Flow)

Test 4 utilised the tungsten carbide configuration for the CC30. The test duration was extended 187 minutes, clearly demonstrating the improved erosion resistance that is offered by this material specification. The test was completed at a constant rate of 100 igpm and a choke opening of 28/64ths. Four sand samples were taken over the period, giving a sand flux of 1.16 % by wt. or a total mass of sand passed of 986 kg, the largest quantity of sand passed by any of the choke configurations. Appendix N Figure 134 and Table 9-9 provide a summary of the test conditions and findings.

Given the flowrate, the initial ΔP across the choke was 58 bar, dropping to 36 bar upon completion of the test. It is of interest that given the same choke opening and flowrate, the stainless steel CC30 generated an initial pressure drop of 48 bar. Whilst a proportion of this drift was attributed to the measurement difficulties of test 3, the port positioning defect - noted above - was that highlighted as the chief contributor. A 10 bar variance is a significant value, demonstrating clearly the emphasis which must be placed on consistency for such validation exercises. It is also noteworthy that the 'softer' grade of material, such as stainless steel in the Cameron case and Stellite for the ABB case, tended to generate lower ΔP then the tungsten carbides and Partially Stabilised Zirconia. This must be associated to the hardness of such materials, and the interactions of the sharp edges in the close confines of the cage ports.

Appendix N Figure 134 details the process conditions, including a summary of the decline in ΔP across the choke as erosion progresses. As with test 3, the incubation period for the tungsten carbide valve was approximately 35 minutes prior to steady state erosion being achieved. The rate of ΔP decline was then

linear for the remaining test duration. From Appendix N Figure 134, one can also note the steps changes in delivery pressure from the pump - inlet pressure - as the speed of the pump-set was backed out to accommodate the declining hydrodynamic performance of the choke through erosion. This effect is also noted on the ΔP across the choke, however it has been hidden on the downstream pressure through the orifice plate and PCV2.

The erosion damage to the two part flow cage and carrier sleeve was minimal. The stainless steel carrier experienced erosion of the order of 147 mm^3, related to a profiling of the ports only. The tungsten carbide flow cage experienced erosion of the order of 161.9 mm^3, again related to profiling of the ports. The eroded volumes were low, given the mass of sand passed and the test duration. Appendix N Picture 12 and 14 detail the erosion scarring to the tungsten carbide plug, including the relation of the choke inlet. The jetting action, related to the differential pressure across the valve and small port diameter, was of the same intensity as that in test 3. Through the superior erosion resistance of tungsten carbide, the eroded volume was limited to 248 mm^3. The erosion pattern propagating was of a similar configuration to that developed on test 3, with a biased distribution also present.

Given that there was only one pressure balance port[15] on the plug of the tungsten carbide CC30, a stagnation zone was generated in the void above the plug, see Appendix N Figure 126. The jets emerging from the flow cage impinged upon themselves in the centre of the outlet spool, this set up a pressure gradient in the pressure balance port and hence a stagnation zone. The stainless steel valves had four equally spaced pressure balance ports - removed from the centre of the plug - thus ensuring that the void remained flushed, see Appendix N Picture 12. As the test valves were installed horizontally, the tungsten carbide design allowed sand to back flow into the stagnation zone, causing the void to become tightly packed with sand. See Appendix N Picture 15. This sand packing prevented the valve from being opened further, much reducing the capacity of the choke. This situation is not acceptable from an operations viewpoint, and upon raising my concerns as to the usage of a single pressure balance port, the design has been revised to accommodate further pressure balance ports, thus ensuring that the void is self flushing.

Given the excellent nature of the data collected through this test and the good balance of erosion damage, the Cameron tungsten carbide CC30 was utilised as the validation benchmark for the CFD model. The reader is referred to Chapter 10 for further details as to this test and the validation process. Given the similarity of test 3, a limited validation case was also completed for the stainless steel CC30.

Test 5 - ABB Series 74 Stellite 6. Low Flow (Constant Flow)

[15] Pressure balance ports are commonly utilised to equalise the pressure differential across the plug or sleeve. This allows the opening torque on the hand wheel or actuator to be minimised.

The ABB valve has a far greater complexity than that of the Cameron choke, a schematic of the trim configuration is detailed in Figure 9-9. The flow direction is out to in, with a series of galleries utilised to provide communication between the ports and hence introduce multiple stages. The flow cage is constructed of an inner and outer cage, which is normally shrunk fitted together. The flow cage sits atop of the seat, with both the flow cage and the seat being held by the carrier, the carrier being constructed from a stainless steel, to protect the cage from shock loading and potential shatter. The plug is only active on the inner flow cage, with the remaining two stages - outer cage and carrier - acting as positive restrictions. Through specific attention to the gallery arrangement, the routing of the flow can be controlled to the upper or lower galleries by the plug position, allowing a more even pressure drop between the stages to be achieved.

The complete ABB trim set is detailed by Appendix N Picture 5, whilst the carrier and the choke body is presented by Appendix N Picture 3. Detail drawing of the ABB valve configuration are presented in Appendix N Figure 125.

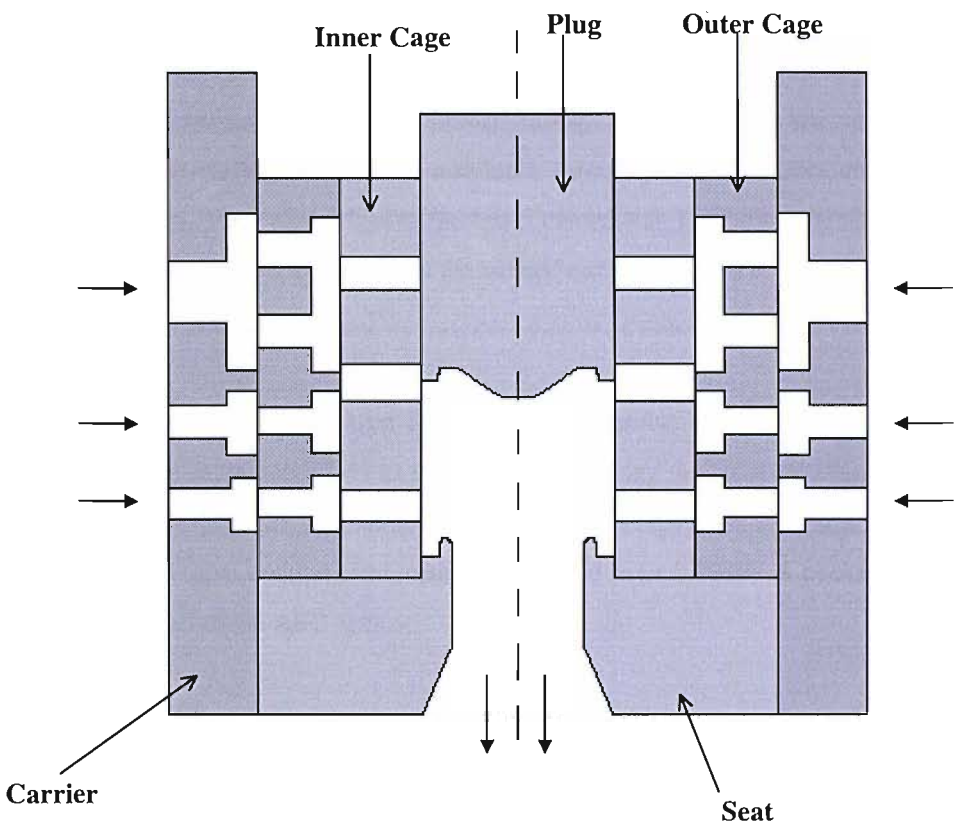

Figure 9-9 Trim Configuration within the ABB Series 74

Data from test 5 has been included as reference for completeness, however it is void due to design difficulties associated with the fluid type. See Table 9-9 and Appendix N Figure 135. The history of the ABB valve-set was that it was developed for duty in the BP Pompano - Gulf of Mexico - project, being applicable to this test case due to a similar Cv. The service of the choke was prominently high

pressure gas, as such the trim configuration had been designed for this. The design philosophy involved a small port sizing for the carrier, progressively increasing in size through the outer and inner cages to accommodate the expansion of gas as the pressure was reduced. This information had not been made available to the author on testing of this ABB trim configuration, and it was found that catastrophic erosion of the outer cage and gallery spacing between the carrier and the outer cage resulted.

The majority of the pressure drop occurred across the undersized carrier stage, promoted by the flowing of an incompressible liquid through a trim designed for compressible fluids. Very intensive jetting was established by the carrier and the damage to the Stellite outer flow cage is noted by Appendix N Picture 8. The volume loss to the flow cage was found to be 2753 mm^3. It must be highlighted that the inclusions of this test in the data set was meant only as an example of the importance of correctly sizing the choke for the duty expected of it. Failure to do so can result in the rapid failure of the product and reputation issues for the manufacture, which in most cases could be avoided through improved communication and knowledge sharing between parties.

In response ABB redesigned the stainless steel carrier assembly, such that it was applicable to the incompressible duty utilised for the BP Sunbury testing. The port sizing was increased, allowing the choking action to be shifted to the outer and inner flow cages, which were constructed of a higher specification material. The volume loss to the test 5 carrier was 1777 mm^3, being reduced to 103 mm^3 (test 6) by the redesign. Note in both cases the carrier was constructed of stainless steel and underwent the same duty, Table 9-9.

Test 6 - ABB Series 74 Stellite 6. Low Flow (Constant Flow)

Test 6 employed the same conditions as that of test 5, utilising the redesign stainless steel carrier. The test conditions and findings are summarised by Table 9-9 and Appendix N Figure 136. The flowrate was held constant at 100 igpm and the sand loading was found to be 0.999%. A choke opening of 25% was utilised for this and all of the ABB tests.

The initial ΔP generated across the choke was 56 bar, however this rapidly decayed to a final ΔP of 20 bar. The 'incubation' period of erosion noted previously was limited to approx. 15 minutes before steady state erosion was established, Appendix N Figure 136. It is of interest that test 5, due to the action of the undersized carrier, generated a ΔP profile which was much flatter, Appendix N Figure 135. The reasoning for this lays in the wall-fluid interactions. The hydrodynamic efficiency of the ABB choke was governed to a large extent by frictional losses generated by the walling. The design configuration of test 5 was such that the majority of the pressure drop occurred across the carrier stage, whilst it was distributed across all three stages in test 6. The hydrodynamic losses for test 5 were chiefly generated by

turbulence and diffusion effects caused by the high intensity jetting across the carrier. However, test 6 was reliant upon frictional losses across all three stages for energy dissipation - as intended through design - having a much increased susceptibility to port profiling and loss of sharp edges, hence a rapid decline in ΔP.

Given the ABB dependency on frictional losses, particle wall interactions are encouraged. These interactions are commonly of a low energy level if contained within the galleries of the flow cage, however if the trim is constructed from a material of relatively poor erosion resistance - Stellite - the resultant erosion can be severe. In this case the flow cage (inner and outer) experienced a volume loss of 2173 mm^3. The erosion damage to the flow cage is detailed in Appendix N Picture 5, 9 and 10. From Appendix N Picture 10, one notes that there was no jetting damage to the outer cage - as with test 5 Appendix N Picture 8 - related to the redesign of the carrier.

Appendix N Picture 9 details the erosion damage to the inner cage. Here it is evident that jetting from the outer cage has occurred in the lower galleries (also see Appendix N Picture 5) and that profiling of the ports has been extended beyond that found for the Cameron tests. This port profiling loosely follows the schematic of Figure 9-10 where a 'tear drop' erosion scar was commonly generated. This scar profile related to the close confines of the galleries between the flow cages, where the tortuous flow path imposed many changes in momentum. Due to a 90° change in momentum immediate to the ports, a low angle of incidence erosion regime was established, thus promoting a tendency towards tear drop erosion. This situation was further extenuated through the relative softness of Stellite and its ductile erosion characteristics. This key-way profiling of the ports was also noted on the outer flow cage, where the close confines of the carrier gallery established a similar erosion phenomena, Appendix N Picture 10.

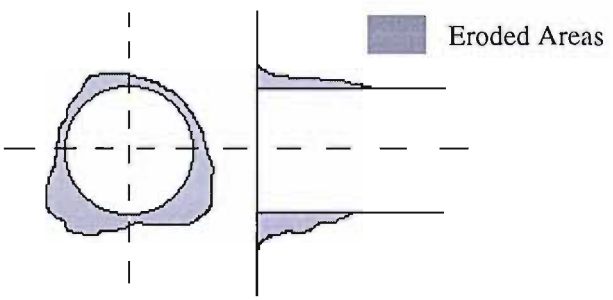

Figure 9-10 Summary of Erosion Damage to ABB Flow Cage Ports

The ABB design, through it utilisation of frictional losses, was heavily focused towards cage centred erosion. This was confirmed by the limited erosion damage to the plug, reported as 201 mm^3. Appendix N Picture 7 presents the typical erosion damage to the Stellite plug. Here one notes the action of jetting on the deflection cone at the base of the plug and the cutting of the plug where the ports overlapped. It should be emphasised that the damage was limited, given the direct impingement

situation established, being a testimony to the hydrodynamic performance of the multistage cage design and its ability to dissipate energy efficiency.

The ABB design also incorporated a removable seat, as shown by Figure 9-9 and Appendix N Figure 125. The volume loss of the seat during test 6 was 145 mm^3. The erosion damage is presented Appendix N Picture 6, where the damage was limited to an 'ellipsing' of the seat edge. The ellipsed shape coincided with the eroded areas on the defection cone of the plug, as shown by Appendix N Picture 6.

Test 7 - ABB Series 74 Tungsten Carbide. Low Flow (Constant Flow)

Both tests 7 and 8 utilised the conditions employed for the tungsten carbide CC30 test, test 4. The test duration was 187 minutes, the flowrate was held constant at 100 igpm and the choke opening fixed at 25% as summarised by Table 9-9 and Appendix N Figure 137. A total of 5 sand samples were taken during the test, finding the average sand loading to be 1.02 % by wt. The redesign stainless steel carrier was utilised for the test and the test was conducted in two parts, to allow feeding of the testers..

The initial ΔP across the choke was 59 bar, declining gradually to 31 bar at test termination. The reported 'incubation' period of erosion was much extended in this case with time to steady state erosion being approximately 50 mins. Such a performance had been expected due to the excellent erosion characteristics offered by tungsten carbide type materials. The hydrodynamic efficiency of the ABB choke was generated predominantly through frictional effects, the hardness of tungsten carbide limited the profiling action on the cage ports, as reported by Figure 9-10. Such profiling was found to be active at a low angle of incidence, being outwith the peak erosion rate of tungsten carbide. However, through the jetting action into the gallery cavities, a direct impingement situation was generated. The angle of this gallery jetting coincided with the peak erosion rate of tungsten carbide. Whilst the jetting did not advance profiling of the ports - and a loss of ΔP - a marked volume loss of the flow cage was noted at 813 mm^3.

Appendix N Picture 4 presents the trim set for the tungsten carbide ABB choke. Flow cage erosion was chiefly limited to damage within the inner cage gallery. The two flow cages were shrunk fitted together, meaning that no pictorial record of the erosion scarring could be made. The damage to the outer cage was limited to profiling of the ports, which was minimal in nature and did not demonstrate the key-way type of erosion produced by test 6. Little erosion damage was generated upon either the plug or seat, the eroded volumes being 34 mm^3 and 26 mm^3. The erosion patterns on the plug and the seat were similar to that of the test 6 - Appendix N Pictures 7 and 6 - albeit of a much diminished intensity.

It is noteworthy that due to the hydrodynamic efficiency of the flow cage, the jetting intensity in the outlet spool was low and no damage induced on the inner wall of the inner flow cage. Thus avoiding the 'crescenting' erosion which was commonly reported for the Cameron chokes.

Test 8 - ABB Series 74 Partially Stabilised Zirconia. Low Flow (Constant Flow)

Test 8 employed the same conditions as tests 4 and 7, testing the ceramic material Partially Stabilised Zirconia. Again the flowrate was held constant at 100 igpm with the choke opening fixed at 25%. The test duration was 187 minutes and the average sand loading 1.1 % by wt. Similar to test 7, the test was conducted in two parts. Finding of the test and process conditions are summarised by Table 9-9 and Appendix N Figure 138. No picture is included of the PSZ trim-set due to the similarity with the tungsten carbide, and the reader is referred to Appendix N Picture 4 for a geometric impression.

The initial ΔP across the choke was 59 bar, declining to 36 bar on test termination. The decline profile was similar to the tungsten carbide test, with an erosional 'incubation' period of approximately 40 minutes. The same observations apply to test 8 as those noted for test 7 regarding the ΔP profile. It is noteworthy that the inlet pressure to the choke, for both ABB tests 7 and 8, held up well given the declining hydrodynamic performance of the chokes. If one compares test 4 with these tests, one can appreciate that the inlet pressure decline is mark for the Cameron choke. This was related to the difference in dissipation techniques utilised between each manufacture, with the turbulence/diffusion method utilised by Cameron lacking the hydrodynamic efficiency to sustain the inlet pressure upon the progressive loss of the controlling surfaces. This observation was supported by the pump-set speed, being lower for test 4 than that of either tests 7 or 8.

The erosion generated upon the PSZ trim components was very similar to that reported for test 7. Profiling of the ports in the flow cage was minimal, and the majority of the 472 mm^3 volume loss could again be attributed to the direct jetting phenomena in the gallery cavities. No pictures are available, as the inner and outer cages were shrunk fitted together. This eroded volume was markedly lower then that displayed by the tungsten carbide valve. This relates to the improved erosional characteristics of the PSZ material under a near perpendicular impingement situation. The plug and seat erosion was minimal, with the recorded volume losses being 35 mm^3 and 16 mm^3. The eroded volume and pattern of the plug was identical to that experienced for the tungsten carbide valve, however the seat erosion was reduced, albeit with the same basic pattern. Again this reduced seat erosion related to the excellent near perpendicular erosion characteristics of PSZ.

For tests 7 and 8 a discrepancy was noted in the volume loss of the stainless steel carrier, being recorded as 436 mm^3 for test 7 whilst only 295 mm^3 for test 8. No apparent reasoning could be found to describe this occurrence, with all process conditions being very similar, Table 9-9. A possible hypothesis may

relate to the geometric tolerance in the carrier gallery, and how a reduced gallery volume could lead to increased particle wall interactions. Furthermore, a machining defect in the gallery walling may have allowed cross gallery flow, generating a wormhole erosional effect at the weakness. It should be reinforced that whilst best endeavours have always been applied in an improved understanding of erosion, the erosion process itself is a chaotic phenomenon, possessing the ability to throw-up curiosities.

9.2.4.1 Discussion on Full Valve Testing Erosive Relationship

Table 9-11 provides a numerical interpretation of the erosion data summarised by Table 9-9. The data presented here is intended to complement that detailed in Table 9-9, giving meaning to the recorded volume losses by consideration of factors such as test duration, mass of sand passed and particulate loading. Three concepts have been introduced; the normalisation of volume loss against mass of sand passed, the normalisation of volume loss against test duration and particulate flux, and interpretation of ΔP against both sand passed and test duration.

RESULT SUMMARY	CAMERON 17.4 PH	CAMERON 17.4 PH	CAMERON 17.4 PH	CAMERON 6% WC	*ABB STELLITE 6*	ABB STELLITE 6	ABB 6% WC	ABB PSZ
TEST NUMBER	1	2	3	4	*5*	6	7	8
Mass Passed Erosion Rate - PLUG (mm^3/kg)	2.18	3.1	4.04	0.25	*0.87*	0.71	0.04	0.037
Mass Passed Erosion Rate - CAGE (mm^3/kg)	1.26	1.86	1.24	0.16 *sleeve (0.31)*	*10.84 carrier (17.8)*	7.68 *carrier (8.0)*	0.93 *carrier (1.43)*	0.51 *carrier (0.82)*
Mass Passed Erosion Rate - SEAT (mm^3/kg)	×	×	×	×	*0.59*	0.51	0.030	0.017
Mass Passed Erosion Rate - OVERALL (mm^3/kg)	**3.443**	**4.962**	**5.288**	**0.565**	***19.307***	**9.263**	**1.498**	**0.874**
Volumetric Erosion Rate - PLUG ($mm^3/min/\%$ by wt)	18.4	24.1	19.1	1.1	*4.1*	3.36	0.18	0.17
Volumetric Erosion Rate - FLOW CAGE ($mm^3/min/\%$ by wt)	10.6	14.5	5.9	0.74	*49.7*	36.3	4.24	2.3
Volumetric Erosion Rate - OVERALL ($mm^3/min/\%$ by wt)	**29.0**	**38.6**	**25.0**	**2.5**	***53.8***	**39.7**	**4.4**	**2.5**
Pressure Drop Erosion Rate (psi/kg) - (kPa/kg)	0.12 (0.85)	0.99 (6.85)	1.55 (10.68)	0.32 (2.23)	*1.37 (9.45)*	1.84 (12.72)	0.46 (3.20)	0.36 (2.46)
Pressure Drop Erosion Rate (psi/min) - (kPa/min)	0.85 (5.83)	8.96 (61.80)	4.25 (29.33)	1.71 (11.76)	*5.52 (38.09)*	8.70 (59.98)	2.17 (14.97)	1.78 (12.30)
NORMALISED AVERAGE	**8.35**	**13.38**	**9.02**	**1.27**	***20.00***	**14.88**	**2.13**	**1.38**

Table 9-11 Summary of Normalised Erosion Rates - Full Valve Erosion Testing.

Each of these concepts have been applied to the various trim components, allowing hypothesis to be constructed regarding material and design performance. The normalised average is simply a summation of the three normalising concepts, aimed at providing a balanced interpretation. The reader is reminded that test 5 is included for reference purposes only, due to the carrier difficulties discussed previously. No further consideration shall be given to this test.

The most apparent observation of Table 9-11 is one that has been commented upon previously, the Cameron choke exhibited plug focused erosion, whilst the ABB product displayed cage centred erosion. Again the reasoning for this lays in the hydrodynamic principle utilised by the various chokes, with the Cameron product relying upon turbulence and diffusion effects in the outlet spool - hence plug erosion - whilst the ABB valve chiefly employed frictional losses across the flow cage. If we consider the mass passed normalised rate, the average plug value for the Cameron valve was 2.4, whilst the ABB value was limited to 0.3. In contrast, the average Cameron cage value was 1.1, with the ABB valve being 3.0. This observation was also supported by volumetric erosion rate.

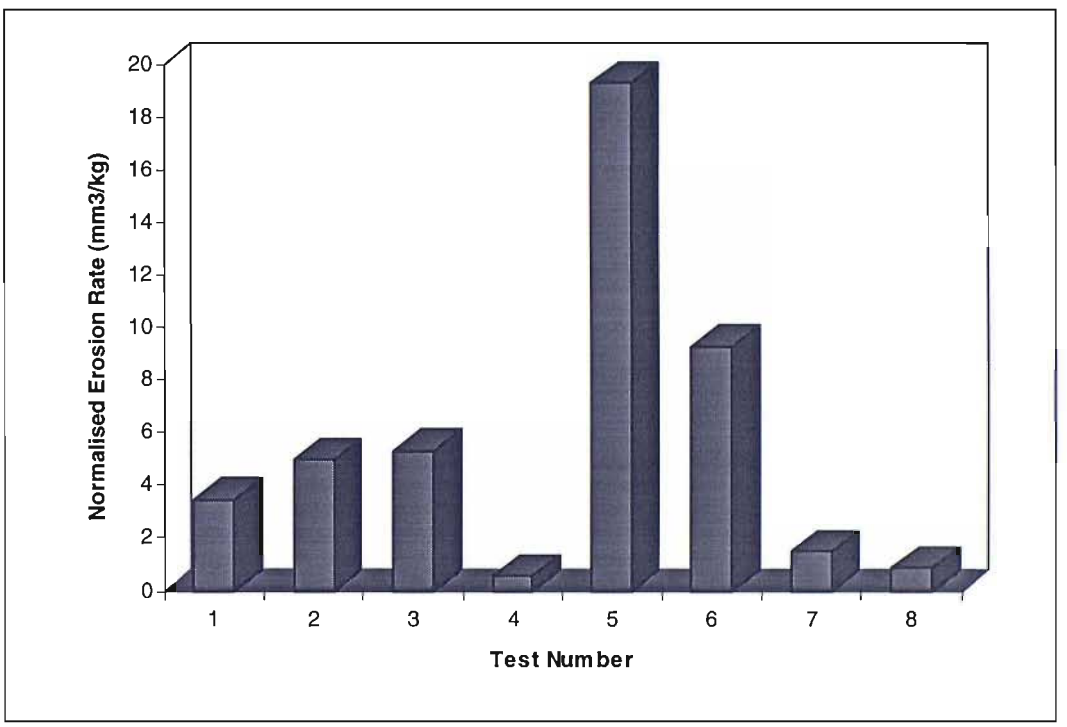

Figure 9-11 Massed Passed Normalised Erosion Rate (mm3/kg)

The normalisation process allows us to consider material properties and the influence of the testing regime. Figure 9-11 and Figure 9-12 detail the overall normalised erosion rate for both the mass approach and the volumetric approach. The relative performance of the materials is noted, with the higher specification tungsten carbide and PSZ materials outperforming the stainless and Stellite materials. For like testing - the low flow conditions of tests 3, 4, 6, 7 and 8 - the Cameron tungsten carbide provided an order of magnitude improvement in erosion performance over that offered by the

stainless steel (tests 3 and 4). Similarly the ABB tungsten carbide offered 6 times the erosion performance than Stellite 6, whilst the PSZ material demonstrated an order of magnitude improvement than the Stellite 6 (test 6, 7 and 8).

The tungsten carbide material utilised for both the ABB and Cameron valves was a 6% cobalt grade, as such one would expect a similar erosion rate for both test 4 and 7. This was demonstrated to an extent, however the variance could be attributed to the differing erosional regimes generated within the valve types. The ABB product relied predominately upon fluid-wall interactions, hence it is just that the normalised erosion rate be higher than those generated by the Cameron valve. Through this observation, one could conclude that given the erosion rate of the Cameron valve was the lower, this product provided the best erosional characteristics through design. However, one must consider the location of that erosion. The erosion of the Cameron valve was focused upon the plug, that component providing control. Gross erosion to the plug can result in rapid loss of control, as was discussed through Figure 9-6. Whilst the erosion rate to the ABB valve was higher, that erosion was focused upon a non-critical component - the flow cage - in terms of flow control. Erosion to the plug was limited, hence the operating life for the ABB valve was expected to be good.

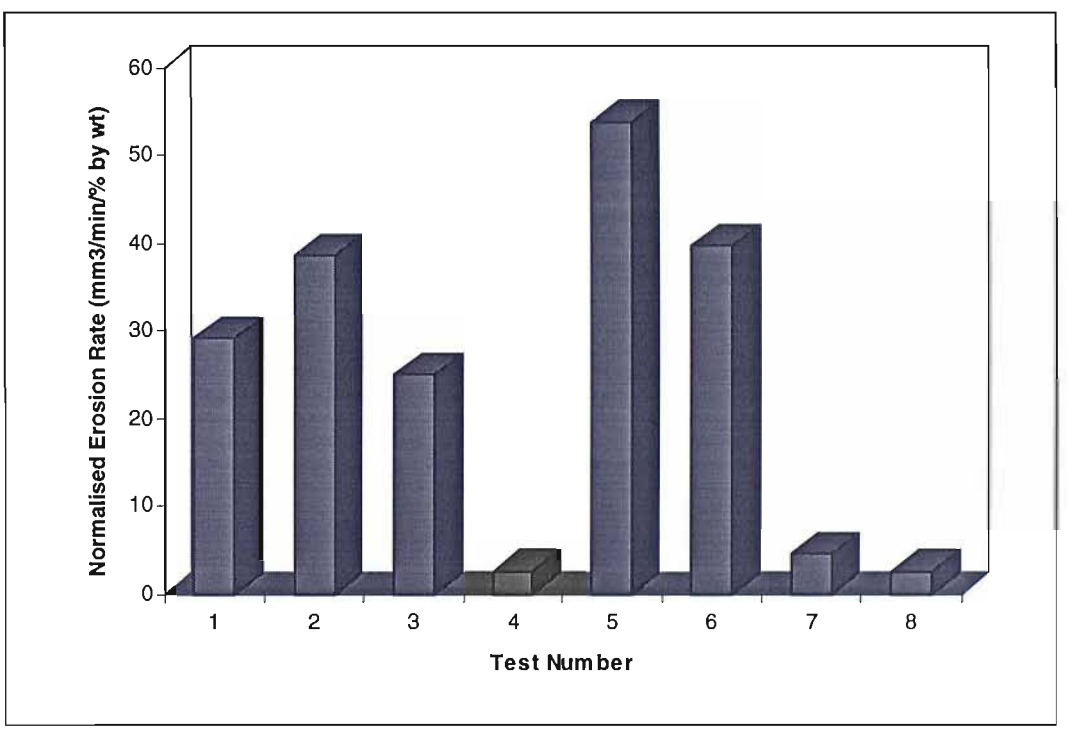

Figure 9-12 Volumetric Normalised Erosion Rate (mm3/min/% by wt)

The ceramic PSZ displayed excellent erosion characteristics, giving twice the overall erosion performance offered by ABB tungsten carbide, test 7 and 8. This improvement related to the high-friction (wall dominated) erosional regime generated through the ABB design, which exploited the excellent characteristics of PSZ. The Vickers hardness of PSZ was lower than that offered by the 6%

cobalt tungsten carbide at 1120 kg/mm^2 - Table 2-1 - with both being in excess of that inherent to sand, 750-1200 kg/mm^2. However the fracture toughness of PSZ was greater than the 6% carbide, at 12-15 MN/m$^{3/2}$ as opposed to 10.4 MN/m$^{3/2}$. Given that the particle impacts within the cage galleries were of relatively low impact energies and high angle of incidences (except the port profiling process discussed in Figure 9-10) the erosional process was governed by fatigue effects through the many particle wall interactions of the gallery cavities. The fracture toughness of the PSZ material was in excess of that displayed by the 6% carbide, hence the PSZ material provided improved fatigue and erosion characteristics under the wall dominated flow regime established within the ABB valve.

The design philosophy of the Cameron valve was contra to that of the ABB valve, generating high intensity jets that impinged upon the controlling surfaces. Given this scenario, it was anticipated that if the PSZ material were applied to the Cameron application it performance would be poorer than that offered by the tungsten carbide. As such, the reader is made aware of the importance of selecting a material which is best for that individual application. This material selection is reliant upon knowledge of the process conditions, which can be difficult to arrive at.

9.2.5 Sand Attrition Analysis

The test environment was of a closed loop design, as such a degree of sand attrition was expected. The testing procedure call for sand samples to be taken throughout the test duration to assess the mean sand loading, monitoring for sand drop. Given a knowledge of when the sand sample were taken, a mean attrition rate could be arrived at and applied to the modelling work described in Chapter 10. Sieve analysis was conducted upon the samples to allow the size distribution to be quantified. This distribution is presented by Figure 9-13, whereby the baseline Produced Forties and Redhill Mixes are presented for reference; the sieve sizes are also detailed by the figure.

The main focus of the work was upon the attrition after 3 hours, however it can be seen that even after 1 hour of circulation significant levels of attrition were experienced, with a marked shift towards the smaller sizes. This is most noticeable in the 300 μm plus category, where the large particles are easily fractured into smaller components, thus bolstering the percentage splits in the smaller size distributions. This tendency is further repeated by the 3 hour test, where the preference towards the smaller sizes is further extenuated. Here, those particle in the 300 μm plus category have all but been eliminated. For the three hour tests the mean distribution of Figure 9-14 was found for application within the erosion modelling of Chapter 10.

An SEM investigation was undertaken on the one hour Stellite sand samples, the outputs are shown in Appendix N Pictures 16 to 18. For reference, the scale line on each of the pictures is 1000 μm. Here samples were taken at 20, 40 and 60 minutes to monitor the progressive attrition of the sand due to the

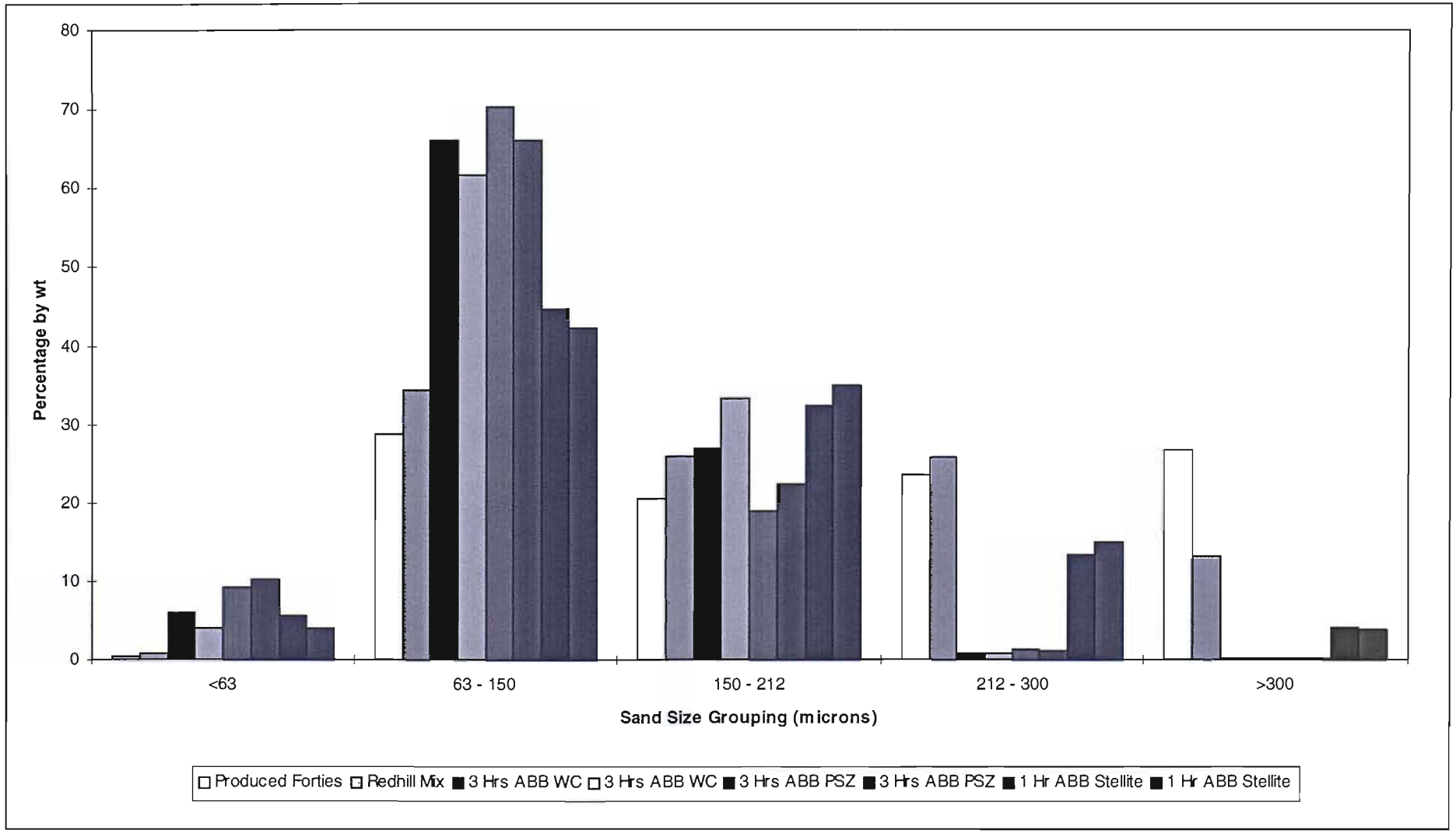

Figure 9-13 Sand Attrition Experienced Under Full Valve Erosion Testing

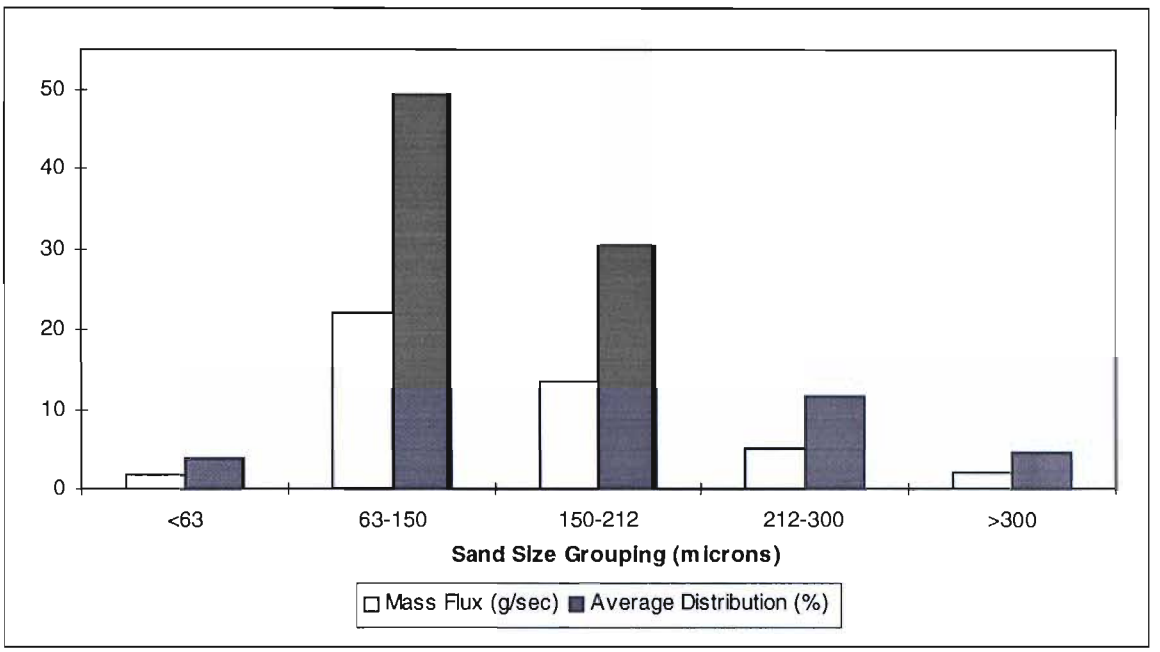

Figure 9-14 Sand Distribution Utilised within the Numerical Erosion Modelling

ongoing circulation. The main conclusion being that there appeared to be little attrition of the sand during the first 40 minutes, Appendix N Pictures 16 and 17. However, after 40 minutes the impacts experienced were of sufficient number and intensity to exceed the fracture toughness of the sand. This led to attrition of the sand and the introduction of fines, as noted by Appendix N Picture 18. This observation is reinforce by Figure 9-13, the one hour Stellite tests, where one can note a tendency towards fines after one hour of circulation.

An additional observation, was that the underlying shape or sharpness of the sand altered with attrition or a reduced particle size. The attrition trend noted was that as the sand became abraded, those areas of the particle which broke away at the fissures and defects within the sand formed splinters and angular fragments. This tendency resulted in an increase in the mean angularity of the small particles or fines, i.e. below 150 μm, Appendix N Picture 18. To include consideration of this effect within the modelling work undertaken, the particle roundness factor applied to each size band was altered to best reflect the mean angularity of that size range. Following the convention introduced by section 6.4.2 and utilising the SEM investigation as the basis, the following roundness factors were arrived at, Table 9-12.

SIZE GROUP (μm)	< 63	63 - 150	150 - 212	212 - 300	> 300
PARTICLE ROUNDNESS FACTOR	0.35	0.4	0.52	0.55	0.6

Table 9-12 Particle Roundness Factors Utilised

9.2.6 Conclusions to Full Valve Erosion Testing

The full valve erosion testing completed at BP Sunbury was most successful. The testing provided both excellent stimulus with which to drive the model validation activities of Chapter 10, and an insight into the material and design characteristics within complex choke geometries. This test data included a good understanding of the attrition characteristics of the sand utilised within the flow loop. The erosional test data of the Cameron Stainless Steel CC30 - test 3 - and Tungsten Carbide CC30 - test 4 - were carried forward and applied to the CFD model, allowing the material parameters incorporated within the model, in addition to the particle trajectory correlations, to be investigated.

10. Comparison of Numerical and Experimental Erosion Studies. Erosion Model Validation

This Chapter deals with the simulation and validation of the complete erosion model upon live test data. Such activities were completed for both the Cameron Tungsten Carbide CC30 and the Stainless Steel CC30. To conserve effort only the physical dimensions of the choke were model, to the inlet and outlet flanges. Whilst this presented a less complex solution, a number of issues had to be closed out prior to commencing with the simulation, including the possibility that external influences were at work upon the erosion process within the test chokes.

10.1 Gravitational Influences upon the Erosion Studies

From the findings of the previous Chapter, it was apparent that a biasing process was at work upon the erosion mechanisms within the test chokes. All of the Cameron test chokes had displayed a tendency towards this biasing process, calling for a study to be completed to enable one to better understand its effect and implications on the erosion modelling undertaken. Appendix N Picture 12 and Figure 10-1 summarise the biasing effect. The reader is reminded that the test chokes were installed horizontally, as shown by Appendix N Picture 1, 2 and 3. It is of interest that the Cameron valves displayed flow biasing, whilst this was not present in the ABB valves, due to their complexity.

Figure 10-1 shows a simplified slice through the Cameron Stainless Steel choke, test 3, whereby the central circle is the plug, detailing the location and intensity of the erosion scarring in relation to the choke inlet. The gravity vector is also shown for reference. Note that only the erosion scars generated by those ports that overlapped - directly impinged upon - the plug are shown.

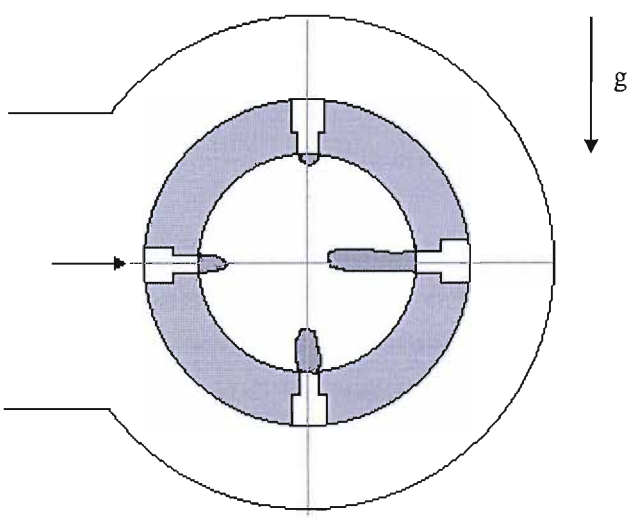

Figure 10-1 Erosional Scarring upon the Stainless Steel Copper Cameron Plug.

Here one notes that the erosion was distributed non-concentrically around the trim, the scarring indicated that the intensity of the attack was most pronounced at the bottom and the rear of the trim. The stimulus for this study was then to determine if this effect was generated solely by the radial position of the choke inlet or whether pre-conditioning in the upstream pipework was evident. The importance of this knowledge being the ability to quantify the extent of any external influence at work, or to conclude that the boundaries of the flow domain were sufficient to capture this flow biasing, i.e. it was a choke generated effect and the entry to the choke was uniform, in terms of both the liquid and particulate phases.

One would expect a degree of flow biasing to occur due to the radial inlet, with gaseous flows - and their entrained solids - impinging directly on the trim at entry whilst liquid flow bypassed the trim, to impinge upon itself at the rear of the flow or trim cavity prior to passing through the trim. Due to the viscosity of liquids, a proportion of the entrained particles would be carried with the continuous phase to the rear of the flow cavity. However in this instance the effect was marked and non-uniform. If indeed this liquid effect was prominent, then there would have been an even split between the erosion induced upon the 'top' and 'bottom' sections of the trim. Thus, it was felt that pre-conditioning was the dominant effect, with the particulate phase being pre-described through the upstream geometry.

A CFD simulation of the upstream pipework for the Cameron test chokes was completed to enable the nature of this pre-conditioning to be described. Appendix O Figure 139 shows the 10 metres of pipework simulated and the inter spool piece spacing, i.e. pipework flanges. The direction of flow was from the left to the bottom of the page, with the exit from the pipe being the immediate entry to the choke. The fluid was assumed to be water, the volumetric flow 100 igpm (7.8 ltr./s) and the entry to the pipe fully developed flow. It was evident from the Figure that any disturbance induced by the pipe bend had sufficiently diminished prior to arrival at the choke, and that the turbulence generated by the flange connections was negligible. Thus, the assumption that the entry to the choke section was fully developed turbulent flow was valid.

This observation lead to an investigation of the particulate phase and the possibility of particle segregation due to gravitational effects. The volumetric flow rate was relatively low given the pipeline nominal diameter (100 mm), coupled with the moderate density differential between phases of 2.6 times. Appendix O Figures 140 and 141 detail the particle volume fraction along the pipeline - converted to % by wt. - where the entry was assumed to be a uniformly distributed 1% by wt. (a particle volume fraction of 3.75×10^{-3}). It was shown that due to the action of the gravitational vector, working on the relatively low carrier phase velocities of approx. 2 m/s, that a marked stratification of the particulate phase distribution occurred. It is also interesting to note that boundary layer effects are

active on the particulate phase, with a tendency for higher particle volume factions in near wall regions, as shown by Appendix O Figure 141.

These observations correlate well with the findings of the Cameron erosion testing, whereby the flow biasing is explained by the gravitational stratification of the particulate phase on entry to the choke. Here, the sand preferentially routed to the bottom of the flow cavity due to its positioning on entry to the choke, promoting the erosion in the 'bottom' of the trim. Furthermore, through the momentum of both the carrier and particulate phases the sand had a tendency to pass the 'very bottom' port and arrive at the 'rear' port, whereby it was forced through the 'rear' port due to the impinging flow which had passed over the top of the flow cavity. Thus, the erosional hotspot observed at the rear of the trim was set-up by a local increase in the particulate concentration, generated through gravitational stratification along the entry pipeline.

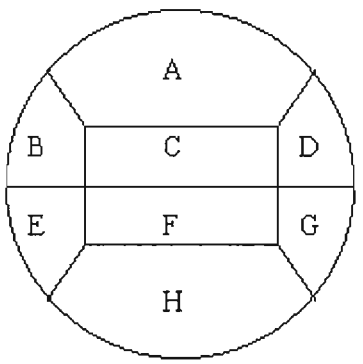

Figure 10-2 Inlet Area Convention

It was necessary to pass this learning of external influences to the erosion simulation, to secure prediction confidence. The finding of Appendix O Figures 140 and 141 were simplified using the convention described by Figure 10-2. This convention was in unison to the blocking strategy utilised to construct the CC30 flow domain, allowing accurate detailing of the particle inlet conditions via the inlet patches.

Area	% by wt.	Weighting Fraction	Mass Flux Cal 1 300-385 µm (g/s)	Mass Flux Cal 2 212-300 µm (g/s)	Mass Flux Cal 3 150-212 µm (g/s)	Mass Flux Cal 4 63-150 µm (g/s)	Mass Flux Cal 5 20-63 µm (g/s)	Mass Flux Total 20-385 µm (g/s)
A	0.5	0.063	0.26	0.65	1.69	2.74	0.21	5.55
B	1.1	0.138	0.57	1.42	3.71	6.03	0.47	12.20
C	0.7	0.088	0.36	0.90	2.36	3.84	0.30	7.76
D	1.15	0.144	0.60	1.49	3.88	6.31	0.49	12.75
E	1.2	0.150	0.62	1.55	4.04	6.58	0.51	13.31
F	0.8	0.100	0.42	1.03	2.70	4.39	0.34	8.87
G	1.2	0.150	0.62	1.55	4.04	6.58	0.51	13.31
H	1.35	0.169	0.70	1.74	4.55	7.40	0.57	14.97
			4.15	**10.34**	**26.96**	**43.88**	**3.40**	**88.73**

Table 10-1 Particle Inlet Distribution for Tungsten Carbide CC30 Simulation.

Table 10-1 summarises the distribution of particle mass fluxes for each of the inlet patches - A to H - with the highest particle loading being at the bottom and where boundary layer effects were

prominent. The % by wt. column was found using the 1 % distribution of the bend analysis. This information was then used to weight each of the simulations runs and assign mass fluxes for each patch as detailed by the Cal 1 to Cal 5 columns. The final column summaries the total mass flux passing through each inlet patch or area. Table 10-1 summarises the particle inlet distribution for the tungsten carbide CC30, a similar exercise was completed for the stainless steel CC30 - test 3 - using a total sand flux of 45.7 g/s, however this has not been reported. For a more detailed description of the solution techniques utilised for the CC30 simulation, the reader is referred to the following section.

As noted in the first paragraph of this section, the flow biasing phenomena was limited to the Cameron valves. In part this is due to the complexity of the ABB product, whereby the tortuous paths that the flow followed had a tendency to break any flow stratification effects. However, the chief reasoning for the ABB avoidance was the entry pipework to the choke. From Appendix N Pictures 1 and 3 one can note the difference in the entry pipework between the two valve types. The ABB valve required a reducer to be constructed - having a nominal diameter of 50 mm - to accommodate a reduced flange connection on the choke. This reducer accelerated the flow to the choke, mixing the stratified flow, such that the particulate entry to the choke was relatively uniform. Time restrictions prevented a *CFD* analysis from being conducted to prove this hypothesis, however given the severity of the reducer, localised turbulence was high and a intensive mixing action established.

10.2 Solution Techniques Utilised to Drive the CC30 Erosion Simulation

Prior to a full discussion upon the comparison of test data with that found through simulation, a description of the solution techniques utilised will be provided, including the difficulties experienced and the limiting assumptions of the model.

The reader is reminded that two validation exercises were undertaken. The basis for these simulations was the erosional data collected via the Cameron CC30 Stainless Steel full valve erosion test and the Tungsten Carbide test. These tests are named as test 3 and 4 in Chapter 9.

In relation to other numerical simulations, the turbulent flow field was resolved for a single flow domain. This turbulent flow field was then utilised as the basis for various post-process particle trajectory simulations and hence erosion calculations, whereby parameters such as particle size and flux rate were varied. The material types specified for the various trim components was also varied as described by the valve type - i.e. stainless steel or tungsten carbide - and the orientation of the gravitational vector was altered to represent the valve arrangement. Given this detail of simulation, a total of 15 particle trajectory calculations were completed, in addition to the simulations required to resolve the turbulent flow field.

10.2.1 Construction of the CC30 Flow Domain

Given the complexity of the CC30 geometry, significant effort was required to generate and grid the flow domain. The complexity of generating the CC30 flow domain and problems associated with its blocking strategy are exemplified in section 5.1.2.1. The *CFD* interpretation of the CC30 flow domain is presented in Figure 5-1, including the individual block arrangements. This flow domain is an exact reconstruction of the actual valve tested and the reader is referred to Appendix N Figure 126 for detail drawings of the valve. It should be noted that a symmetry plane was utilised to ease the computational effort, whilst the geometry only extended to the inlet and outlet flanges of the valve[16]. The argument for the symmetry plane was along the centre line of the inlet and outlet spools, dividing the trim area into two symmetric parts.

Further to Figure 5-1, Table 5-1 provides a summary of the geometric features. Of most interest here is the number of blocks and grid cells utilised to describe the flow domain, being 547 blocks and 274056 computational cells. As mentioned, such figures represent a considerable effect in describing the flow domain. It should be noted that advances are at foot whereby the limitations and difficulties analogous to generating a flow domain through the finite volume gridding method, and its dependence upon formal blocks, are being phased out. The introduction of unstructured gridding techniques should ease this situation considerably, however at the time this project was completed, the complex physics associated with particle trajectory calculations was not available.

Through the application of the patch naming technique - section 7.3 - the material type of the trim area was specified. This material specification involved the individual naming of some 200 odd patches, with the material types specified as per Table 10-2.

COMPONENT	Tungsten Carbide Simulation	Stainless Steel Simulation
Body (including inlet / outlet spools and annulus cavity)	AISI 4130 Carbon Steel	AISI 4130 Carbon Steel
Sleeve	17.4 pH Stainless Steel	17.4 pH Stainless Steel
Flow Cage	6% Cobalt Tungsten Carbide	17.4 pH Stainless Steel
Plug	6% Cobalt Tungsten Carbide	17.4 pH Stainless Steel

Table 10-2 Summary of Choke Materials

The choke opening was specified through the full valve erosion testing at 28/64^{ths}. The flow cage of the CC30 was divided into six zones - A to F - with 4 mutually opposite ports in each zone. The progression in port size for each zone can be summarised as per Table 10-3.

[16] Provision was provided in the outlet spool whereby the flow could achieve fully developed flow prior to exiting the flow domain. This requirement is a pre-requisite to accurate flow field calculations.

ZONE	A	B	C	D	E	F
PORT SIZE (MM)	3.2	3.2	3.2	4.8	4.8	11.6

Table 10-3 Summary of Port Sizing

Given the opening of 28/64^{ths}, the first three zones of ports were found to be open, with zone C impinging directly onto the seat angle of the plug, as summarised by Figure 10-3. This geometric configuration was model, with a total of 6 ports being incorporated within the flow domain. Note, as a symmetry plane was utilised, only half of the geometry was constructed.

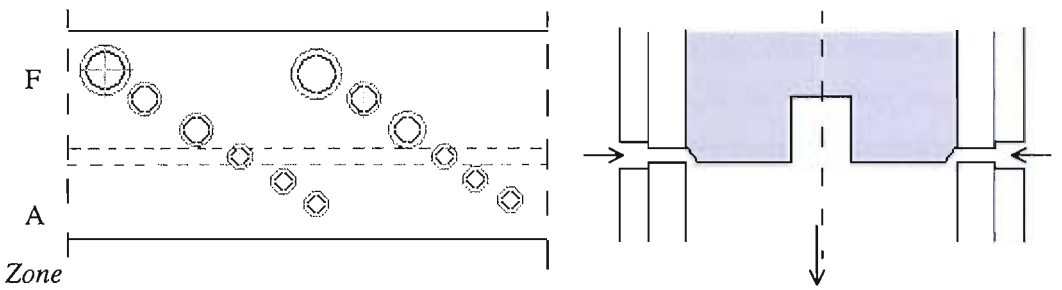

Figure 10-3 Port Configuration and Plug Overlap of the CC30

A difficulty associated with the use of the symmetry plane to simplify the flow domain, was the positioning of that plane and how to best treat the ports. From Appendix N Pictures 13 and 14 - those tests utilised for the validation study - it can be seen that the ports of zone C (that which generated the most severe jetting erosion) were lined up with the inlet. This can be seen by the top image of Figure 10-4. The construction of this geometry was attempted, however due to the inclusion of 7 ports (2 of which were partial) the complexity of the blocking strategy was found to be in excess of the author's ability. To enable a solution to be effected, the porting configuration was rotated by 15° and the symmetry plane (dotted line) positioned such that no partial ports were experienced.

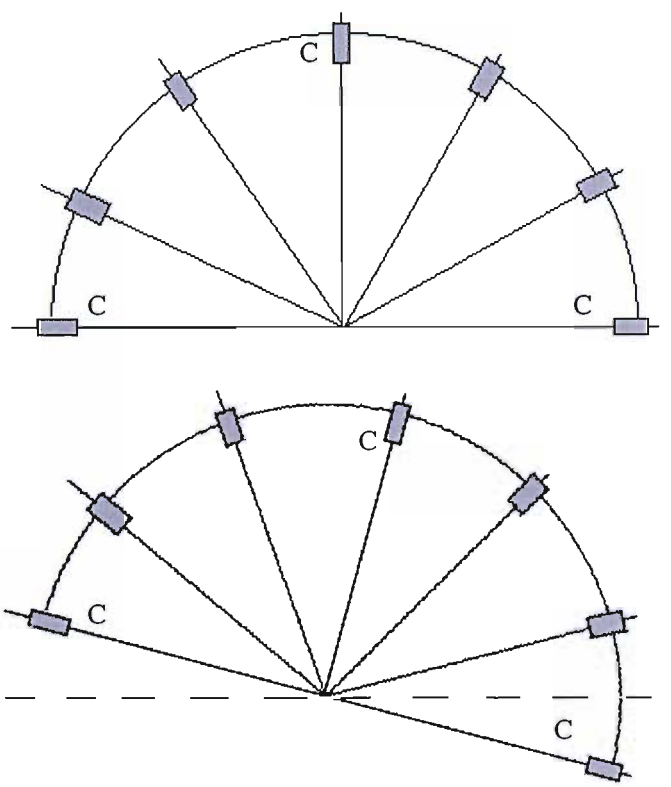

Figure 10-4 CC30 Symmetry Plane Positioning

This approach allowed a practical blocking strategy to be developed, whereby the symmetry plane convention was held, whole ports were treated and the overall number of ports considered was reduced to 6. The treatment of partial ports was found to be particularly troublesome for the gridding algorithm. Such difficulties related to the non-symmetric geometry that such partial ports presented and the integration of such non-symmetric blocks into the overall blocking scheme. The implementation of such an approach for the symmetry plane necessitated a compromise and the recognition that the solution scheme was not wholly correct. However, this approach was the only method to progress the solution.

Section 10.1 presented the arguments which related to the erosional biasing around the plug of the CC30. From such arguments it was apparent that the flow domain would require treatment in two parts, the convention used being the 'top' and 'bottom' halves of the symmetry plane. To minimise effort and accelerate solution times a number of assumptions were made. The turbulent flow field was assumed to be independent of gravitational effects, allowing a single solution to be achieved which was applicable to both the top and bottom simulations. Furthermore, to avoid the requirement to reconfigure the port orientation (and the subsequent re-blocking and re-gridding), the same flow domain was utilised for both the top and bottom simulations. To enable this solution approach, the gravitational vector was simply rotated through 180°.

Whilst such an approach avoided the need to construct a second flow domain, an error was introduced in terms of the port location, in particular those ports of zone C. As discussed in Figure 10-4, the ports had been skewed by 15° to enable the blocking strategy to be realised. The application of the symmetry plane - which mirrored the flow domain between the top and bottom simulations - compounded this error. Figure 10-5. If we consider the top half (dotted line is the symmetry plane), then the true convention of the symmetry plane describes the ports of the bottom zone C as ***C****.

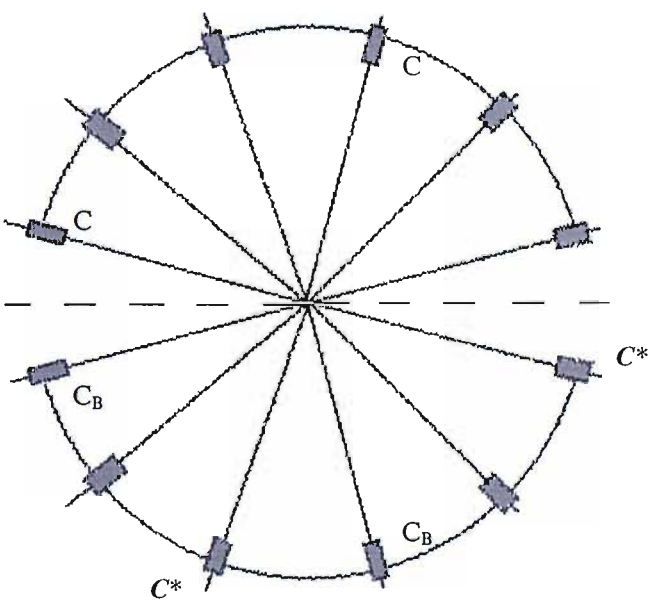

Figure 10-5 Symmetry Plane Application

However, through the rotation of the gravitational vector, the bottom half was presented as a mirrored image of the top, and C_B represents the positioning of the bottom ports of zone C within the *CFD* simulation. Again, this convention was not strictly correct, however the recognition and acceptance of such allowed the solution to be significantly accelerated and additional work to be undertaken, in

the form of the stainless steel simulation. The value of this additional work was deemed to greater then that demonstrated by the time consuming grid reconstruction process.

10.2.2 Resolving the Turbulent Flow Field

The turbulent flow field was resolved through the application of the Differential Stress closure model, acting upon an incompressible fluid. The conventions and form of the closure model utilised was that standard to CFX-F3D, with the model being found to provide adequate resolution of the flow field. A total of 2000 iterations were utilised in the solution scheme, with convergence being demonstrated after some 1800 + iterations. Through the use of the 2000 iteration criterion and the total number of control cells employed to describe the flow domain, some 6.5 billion calculations were required to generate the turbulent flow field. The CPU time necessary to deliver such a large number of calculations was considerable, hence the drive to provide one flow field which catered for all of the particulate solution scheme assigned.

An example of the command file utilised to drive the CC30 simulation is presented in Appendix F. The logic of the command file is not strictly correct as the example presented was that employed to drive the particle trajectory calculations. However, the solver data and stability aids utilised to provide a solution are summarised. It is noted that the application of both deferred correction and false time steps on the K and Epsilon terms was required to generate the flow field. It was found that if the standard solution scheme of CFX-F3D was utilised, the solution grew unstable as the diffusion term would become oversized. The severe jetting associated with the flow field tended to promote divergence in the terms dealing with the creation and dissipation of turbulent kinetic energy, and the solution would run away with itself. In addition to the usage of the deferred correction and false time steps stability aids, mild under relaxation factors were also applied.

Further to convergence difficulties associated with the severe jetting across the trim, the classification of the continuous phase as an incompressible fluid exasperated the numerical instabilities. The transport equations utilised to describe an incompressible fluid are most rigorous, meaning that sensitivities to numerical imbalances, caused by momentum change, are high. Such sensitivities result in an increased tendency towards solution divergence then that generated by a compressible solution.

The boundary conditions applied were fully developed turbulent flow at inlet and exit, with the assumption of no slip at the wall upheld. This required the treatment of the wall function (Appendix G) and a particular problem relating to inter-block boundaries. Given that 574 blocks were required to construct the flow domain, that algorithm which connected blocks to one another failed on occasion. This failure resulted in an inter-block boundary being assigned as a virtual wall, as opposed to a flow path. The presence of such virtual walls, which consisted of a plane of cells, within the internals of the

flow domain caused extreme difficulties in arriving at a converged solution due to the massive shear stress induced and the associated oversizing of the diffusion term. The great difficulty of such inter-block problems was that they were transparent during the grid construction phase. Their presence could only be hypothesised about when one experienced convergence difficulties.

Such convergence difficulties were initially noted and one had to interrogate in turn each of the 1348 inter-block boundaries. Once those boundaries most at fault were corrected, a limited simulations runs was undertaken - through the heavy application of stability aids - and the remaining boundaries at fault become visible via results interpretation. Section 10.3.1 presents a further discussion.

10.2.3 The Trajectory Calculation and Erosion Prediction

The approach utilised for the trajectory calculation has been introduced in section 10.1. To confirm, through the application of the symmetry plane and the influence of gravitational vector upon the erosion process, simulations of the top and bottom halves of the CC30 were considered separately. To facilitate accurate detailing of the particle entry conditions, the inlet area was sub-divided into regions, as summarised by Figure 10-2. The top tungsten carbide CC30 simulation utilised the particle fluxes presented as A, B, C and D - Table 10-1 - whilst the bottom utilised E, F, G and H.

The sand distribution analysis of section 9.2.5 found the distribution and concentrations between the sizes to be varied. To enable such a wide particle sizing to be accurately considered, a number of progressive trajectory calculations were made. CFX-F3D evenly distributes the particle sizing and particle flux rate over the minimum and maximum particle size specified, given the number of particles to be consider and the overall mass flux. If this approach were utilised to drive the solution, such that a single trajectory calculation was made for the particle range of 20-385 μm and mass flux of 88.73 g/s, the particulate distribution would be wholly incorrect.

To enable an accurate particle distribution and loading to be specified, a total of 5 trajectory calculations was made for each simulation. Each trajectory calculation considered 288 particles, giving the total number of particles utilised to describe the erosional process as 2880. Two complete simulation sequences were utilised to predict the overall eroded volume. A summary of the particle size ranges (and mass flux starting points) considered is given in Table 10-1. Three particle sizes were specified for each size band, giving the largest inter-particle size spacing at 29 μm. The use of progressive trajectory calculations incurred additional computational effort, however the approach provided both an accurate description of the particulate distribution and an insight into the erosional contribution generated by each particle size range. In addition to the description of the particle size and loading, the particle shape was manipulated as a function of particle size; section 9.2.5.

The solution method required to undertake multiple trajectory calculations was relatively straight forward. The turbulent flow field generated previous was utilised to set the 'initial guess' function within CFX-F3D. The trajectory calculation was then undertaken for each size range, with the dump file originally created by the flow field calculation being progressively populated with the particulate surface plotting data developed by the author. See Chapter 7 for details of this surface plotting data and how the dump file was modified to accommodate this additional information through the use of the scalar array function. The data generated via the user file interface - section 7.5.1 - was correlated and has been presented by Table 10-4 and Table 10-5.

Following the recommended best practice of Chapter 8, both turbulent dispersion of the particulate phase and the modified coefficient of restitution was utilised. The standard form of the turbulent dispersion function was employed, whilst the author derived correlations of section 6.3.1 were incorporated for the coefficient of restitution. The specification of the material type enabled the model to apply the correct form of the restitution correlation, i.e. steel or tungsten carbide. Further, the squeeze film retardation factor was included within all of the particle trajectory calculations, see sections 6.3.2 and 9.1.1. Here the recommended correlation for the squeeze film constant operating under water duty was applied, i.e. 10. The gravitational vector was utilised at all times, with the orientation being altered to reflect the simulation argument.

It should be noted that the assumption was made that the momentum coupling between the carrier and particulate phases was not bi-directional, i.e. the momentum was only transferred from the carrier to the particulate phase. This assumption was a requirement of the erosional prediction process, whereby the bi-directional coupling of the carrier and particulate phases required an iterative solutions scheme, which would of significantly increased the complexity of handling user specified data within CFX-F3D. This assumption of non bi-directional transfer was deemed valid through the relatively low particulate loading, the particulate loading of 1% by wt (0.4% by vol.) did not significantly impact the structure of the turbulent flow field, given the low sensitivity of the carrier to such effects.

This approach to the trajectory calculation realised excellent results, with the standard drag correlations of CFX-F3D found to deliver good consistency, i.e. Equation 6-4. The trajectory calculation of the CC30 simulation initially proved to be problematic, due to a tendency for the particles to hang-up. To ensure an excessive amount of CPU time is not consumed in completing a trajectory calculation, a number of triggers are available within CFX-F3D to terminate the calculation. These triggers include the maximum time a particle is to spend within the flow domain, the maximum time a particle is to spend in a control cell or the minimum fraction of a control cell crossed. If any of these criterion are not held, such as a particle becomes trapped within a backflow region or is catch within the boundary layer at the wall, the trajectory will be terminated and <u>not</u> restarted. If a

significant number of trajectories are terminated in this manner, the particle loading can be removed from that originally specified.

The use of the default values for the triggers summarised was found to result in an unacceptable number of trajectories being terminated for the CC30 simulation. The particles tended to become stationary or near-stationary, causing the trajectory to be terminated through the minimum fraction of cell crossed criterion. This near-stationary tendency was associated to the volumetric flowrate and the step within the ports of the flow cage. The body of the CC30 valve tested was standard, however, the trim set had been sized for the specific application of erosion testing. This combination lead to an oversized annulus cavity for the choke and the resultant low flow velocity in this area, promoting particle drop-out under gravitational effects.

However, the main trajectory termination problem was associated with the step in the flow cage ports. The particles would roll along the outer curvature of the sleeve/flow cage until arrival at a port, the particles would then be entrained in the fast flowing stream until the step was reached. The vector field around the port steps was such that the particles tended to be driven into the corner of the step, where they could not ready escape from this dead zone. This effect is detailed in Appendix O Figure 157, where the termination of the particle trajectories in the port area is noted.

To minimise the problems associated with the port step such that the trajectory termination rate was controlled, the grid sizing around the ports was restructured, allowing an improved velocity vector resolution to be realised. Whilst this approach did not fully remove the termination tendency, the improved resolution enabled a less aggressive vector field to be presented to the particles, better managing the trajectory progress in the port area and a reduction of the wall effect. Furthermore, the minimum fraction of cell crossed term within CFX-F3D was reduced for all of the trajectory calculations. This action - coupled with the restructured/reduced cell size - allowed an acceptable compliance with the requested flux rates to be achieved as an extended particle tracking duration was enabled. The minimum fraction of cell crossed was reduced to 1.00E-03.

The erosion prediction element of the trajectory calculation was well accomplished, with the only problems being minor details relating to sizing of the computational array and ensuring sufficient work space was available to treat the many particle impacts. This strong performance stood in testimony to the robustness with which the *CFD* erosion model had been constructed and its applicability to the extremely complex example presented here within. The experimentally derived correlations presented by Table 9-3 were used within the erosion model.

10.3 A Comparison of the CC30 Numerical and Experimental Results

10.3.1 The Turbulent Flow Field and Trajectory Calculation

The turbulent flow field and particle trajectory calculations for the CC30 were delivered using the techniques described through sections 10.2.2 and 10.2.3. Appendix O Figures 142 (Figure 10-6) to 153 provide a summary of the turbulent flow field, whilst Appendix O Figures 154 to 158 detail a selection of particle trajectories within the flow domain. The reader is reminded that a single flow field was prepared, independent of gravitational effects and applicable to all trajectory applications.

The simulation utilised the following process conditions whereby the fluid was classified as incompressible water, flowrate 7.64 kg/s, temperature 57.2°C, inlet pressure 90 barg and pressure drop between the boundaries of the flow domain 40.2 bar. Through the specification of the pressure drop, the flow field was forced to provide a good correlation with that measured experimentally. An alternative approach would have been to specify only the inlet pressure and the flowrate, allowing the code to predict the pressure drop. However, such an approach would have introduced an additional error source and was deemed inappropriate given the focus upon erosion validation, not an assessment of the prediction capabilities of the Differential Stress model.

The application of the pressure drop within the flow calculation, required an appropriate value to be arrived at. The difficulty of specifying this value related to the erosion experienced within the choke and resulting variance in the pressure drop throughout the test. The initial ΔP was 58 bar declining to 35 bar at test termination, whilst the average ΔP was 40.2 bar (Appendix N Figure 134). If the initial ΔP were to be incorporated within flow calculation, the resultant flow velocities would be excessive. Thus, the average ΔP was utilised in support of the trajectory calculation.

Due to the associated difficulties, no data was collected upon which either the turbulent flow field or the particle trajectory calculation could be validated. As such the proceeding discussion are limited to observation made solely upon the simulation work.

Appendix O Figure 142 (Figure 10-6) to 144 present the velocity contours along the centre line or symmetry plane. These figures provide an excellent summary of the general flow field established within the CC30, when operating under the regime detailed above. Appendix O Figures 145 to 148 provide horizontal slices through the geometry, at 5 mm intervals from the centre line. Here the velocity vectors are shown, allowing an impression to be gained regarding the orientation of the jetting flow and the resultant interactions. Appendix O Figures 149 to 152 are similar to the previous Appendix O Figure selection, however in this instance the projection of the slices was vertical.

The Flow Field within the CC30 Equal Percentage Control Choke

Fluid - **Water**
Inlet Diameter - **75** mm
Choke Opening - **28**/64ths
Port Diameter & Number of Zones Exposed - **3.175** mm & **3**
Plug Edge - **Taper at 60°**
Inlet Pressure - **58** Barg
Pressure Drop - **40.2** Bar
Fluid Temperature - **57.2** °C
Volumetric Flow Rate - **7.64** kg/s

Figure 10-6 CC30 Velocity Contour Plot Along Centre Line (m/s)

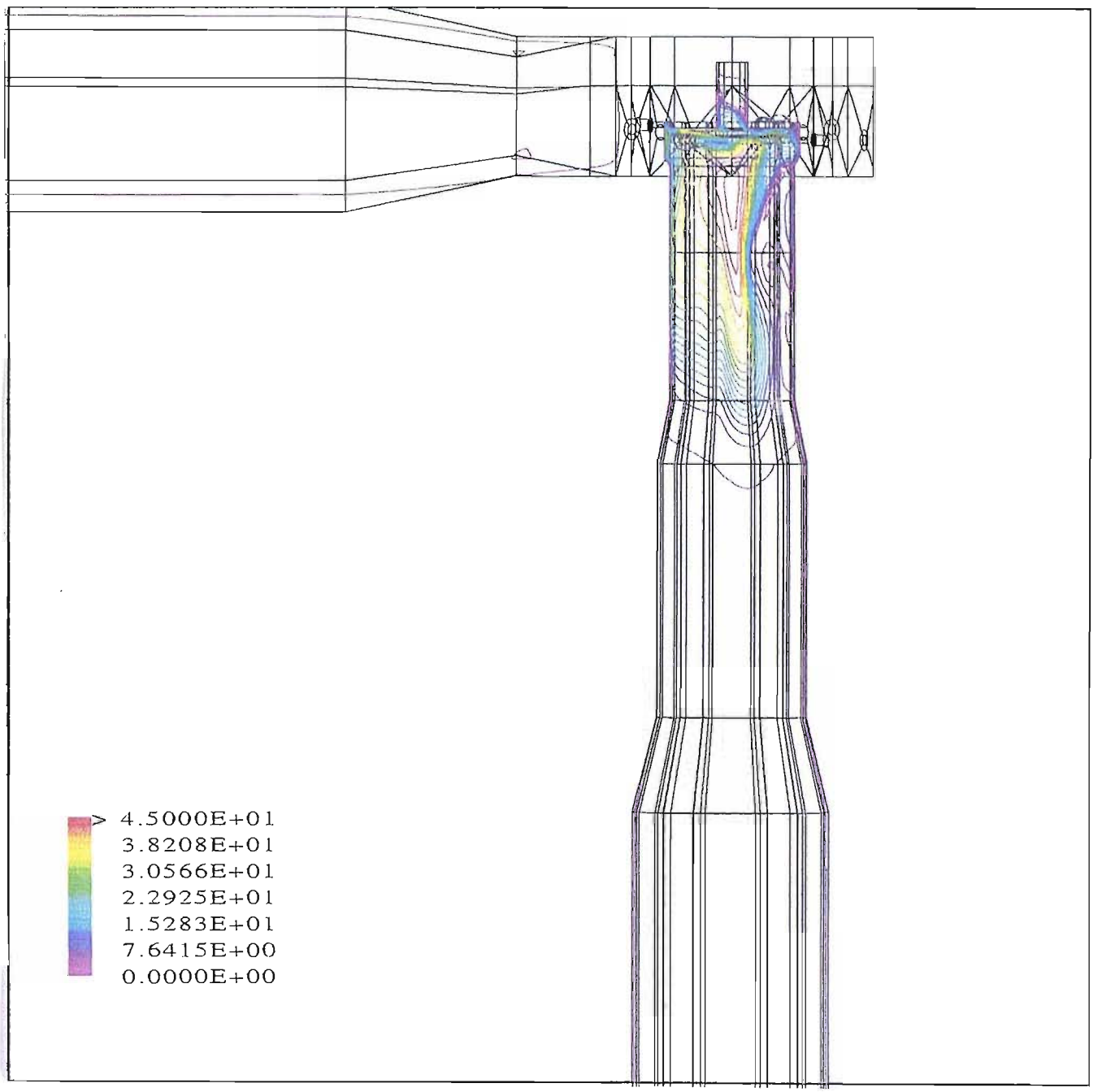

The peak predicted flow velocity for the carrier was 133.5 m/s. A range of velocity scaling has been utilised within the Appendix O Figures, with the capping of some Figures at 45 and 80 m/s to enable greater low velocity detail to be presented.

A number of flow features have been presented by the simulation, which have been confirmed by the experimental testing. From Appendix O Figures 142 to 145 a large backflow region is noted in the outlet spool along the centre line. The region was formed through the biased inflow into the outlet from the annulus cavity. Due to the radial inlet of the choke body and the high pressure drop scenario generated, the flow had a tendency to flow over the top of the trim, impinging upon itself at the rear of the annulus cavity. Here a slight pressure increase was noted, forcing the jetting intensity to be higher at the rear of the trim, and hence the backflow region was formed through a slight unbalance of the jetting momentum. This backflow scenario was propagated through the combination of choke opening and ΔP, an increase in choke opening would result in a lowered ΔP and the breaking of this backflow tendency by a promotion of a more uniform inflow from the annulus cavity.

Whilst the near-wall backflow region has been highlighted, the intensity of the re-circulation was relatively low at approximately 5 m/s and mainly parallel to the wall. The walling in this region was tungsten carbide, and the erosional damage was expected to be minimal. This was confirmed through the erosion testing, where no damage was noted in the outlet spool. Further to the backflow region, the outlet spool was devoid of damage due to the well defined manner of the exit flow. Here one may observe that the high velocity flow of the outlet spool was confined to the centre axis - Appendix O Figures 146 to 148 - avoiding highly energetic particle-wall interaction and erosion.

One anomaly was that presented by Appendix O Figure 146. A limited high velocity region is shown at the walling (left of outlet). This anomaly was driven by the small re-circulation zones near the face of the plug and interactions with the vector flow of the above and below region (Appendix O Figures 147 and 145). This effect was believed to be short lived, relating to the solution scheme and convergence criterion utilised. Further to this anomaly, some jetting was noted on the seat angle of the flow cage. The velocities and approach angles associated with such jetting were low and little erosional threat was presented to the seat given its construction from tungsten carbide.

The near plug region is where jet interactions were maximised and the majority of the hydrodynamic work took place. This resulted in high velocities across the plug face and much small scale interactions, including re-circulation zones and near chaotic flows (Appendix O Figure 146 and 149). This high hydrodynamic workload via the creation and destruction of turbulent kinetic energy is summarised through Appendix O Figure 153. The highly turbulent region is confined to the near plug area, with little propagation into the outlet spool. The only extension of turbulent energy into the

outlet is that generated by the backflow region discussed previously. This confinement of the highly turbulent region is advantages from a containment viewpoint, however much load is placed upon the controlling surfaces and rapid loss of control could be anticipated.

An interesting phenomenon not previously anticipated was the flow around the taper angle of the plug, where a small cavity was formed between the plug and the inner wall of the cage. A radial flow was established in this cavity, emulating from the impingement of the zone C ports upon the taper angle of the plug, see Appendix O Figure 152. The flow in this area was anticipated to be near stagnant due to the proximity of a large pressure sink - the outlet spool - and the expected tendency for the flow to preferentially route in that direction. However, due to the hydrodynamic workload of the near plug area the flow was backed up in the cavity causing it to adopt the radial direction. The radial flows around the plug cavity where energetic at + 25 m/s.

This effect can be problematic if the plug and cage are poor fitting. In the case of the CFD simulation, the gap between the plug and the cage was considered to be zero and hence the strong tendency to radial flow. However, actual chokes carry a tolerance between the plug and cage to enable the sliding movement. Through the confinement of the flow to the plug taper cavity, by the proximity of the hydrodynamic workload, a tendency for flow into the gap between the plug and cage can be established. The rates of any such flow will be extremely low, however if the carrier phase is heavily contaminated with solid fines, the gap can become packed off with solids, causing the plug to gall upon movement.

As commented upon in section 9.2.4, the tungsten carbide design suffered from sand packing in the pressure balance port. The reasoning for this is noted through Appendix O Figure 145, where the flow into the pressure balance port (cylindrical section sunk into the plug) is clearly visible. The use of a single pressure balance port - centrally position - prevents the cavity above the plug from being flushed and the resultant sand packing occurred.

Finally, the flow within the annulus cavity was benign, given the low volumetric flowrates analogous to the testing regime. This effect was further emphasised by the use of effectively an oversized body for the *Cv* capacity of the trim. The body of the CC30 was an off the shelf unit, whilst the trim was a reduced capacity unit aimed specifically at the arduous application presented by the erosion testing. Further to the low annulus velocities, Appendix O Figures 149 to 152 detail the approach velocities to the cage ports and the acceleration of the flow through these ports. The acceleration induced by the outer port is clearly visible, in addition to the resultant high velocity impingement upon the inner port. This energetic impingement was associated with the rounding of the port steps reported through the erosion testing, and in some cases the subsequent washing out of these inner ports completely.

The particle trajectory component of the erosion prediction was straightforward, with Appendix O Figures 154 to 157 providing a particle trajectory and velocity summary, whilst Appendix O Figure 158 details a representative sample of the particle trajectory and size summary. It is noted that the peak particle velocity achieved was 127 m/s. Due to the confusion associated with many overlaying particle trajectories an exemplary particle trajectory was extracted and presented in Appendix O Figure 157. The peak particle velocity in this case was 100 m/s, immediately downstream of the flow port. The particle is seen to impact the step in the port, at approximately 35 m/s, before passing across the outlet spool - due to the flow biasing reported previously - to impinge upon the opposite walling of the flow cage. The particle decelerated rapidly in the relatively low velocity area of the exit, resulting in a low energy (non damaging) impact with the walling.

This scenario was repeated many times as each particle was individually tracked through the flow domain. Appendix O Figure 155 (Figure 10-7) provides an overall summary of the near trim particle trajectories. Here, through the action of the turbulent dispersion term, the particles in and around the trim area had highly confused trajectories. It was only those particles entrained within the high velocity central region of the outlet spool that held true trajectories, a number of high velocity particles were also noted to impinge the walling to the left of the flow cage. It was only these high velocity impacts which held a damaging potential to the outlet spool. The many other impacts in the outlet spool were the result of the turbulent dispersion term. This implied that for the action of the turbulent dispersion term to be active, due to the density differential between phases, the momentum (and hence the velocity) held by these particle was low. Thus, the erosive potential of such particles was minimal when consideration was given to the squeeze film effect.

Those ports which overlap with the plug - one and four in a clockwise direction - were those which experienced the lowest particle velocities, as noted through Appendix O Figure 155 (Figure 10-7). Through the choking action of the interaction with the plug, the particle velocities across the ports were held to approximately 95 m/s, whilst those ports removed from the plug enabled the particles to be accelerated to the peak velocity of approximately 125 m/s. However, the damage yield by the impingement of a particle at or near 95 m/s was severe, even at the advantageous impact angles experienced, i.e. removed from the peak erosion rate for tungsten carbide (perpendicular).

Finally, the high velocity particle trajectory across the face of the plug are observed. These high velocity particle were responsible for the channelling effect across the plug face noted through the discussions of section 9.2.4 and Appendix N Picture 12.

PARTICLE TRAJECTORIES WITHIN THE TUNGSTEN CARBIDE CC30 CONTROL CHOKE

Particle Type - **Sand**
Particle Loading and Flux Rate - **1.16** % by wt & **88.7** g/s.
Particle Roundness Factor - **0.5**
Number of Particle Sizes and Total Number of Particles Tracked - **20** & **1440**
Particle Size Range - **20-385** μm
Turbulent Dispersion - **Yes**
Modified Coefficient of Restitution - **Yes**
Squeeze Film Retardation - **Yes**
Gravity Vector Set - **Yes**

Figure 10-7 Particle Trajectories and Trajectory Velocities within the CC30 (m/s)

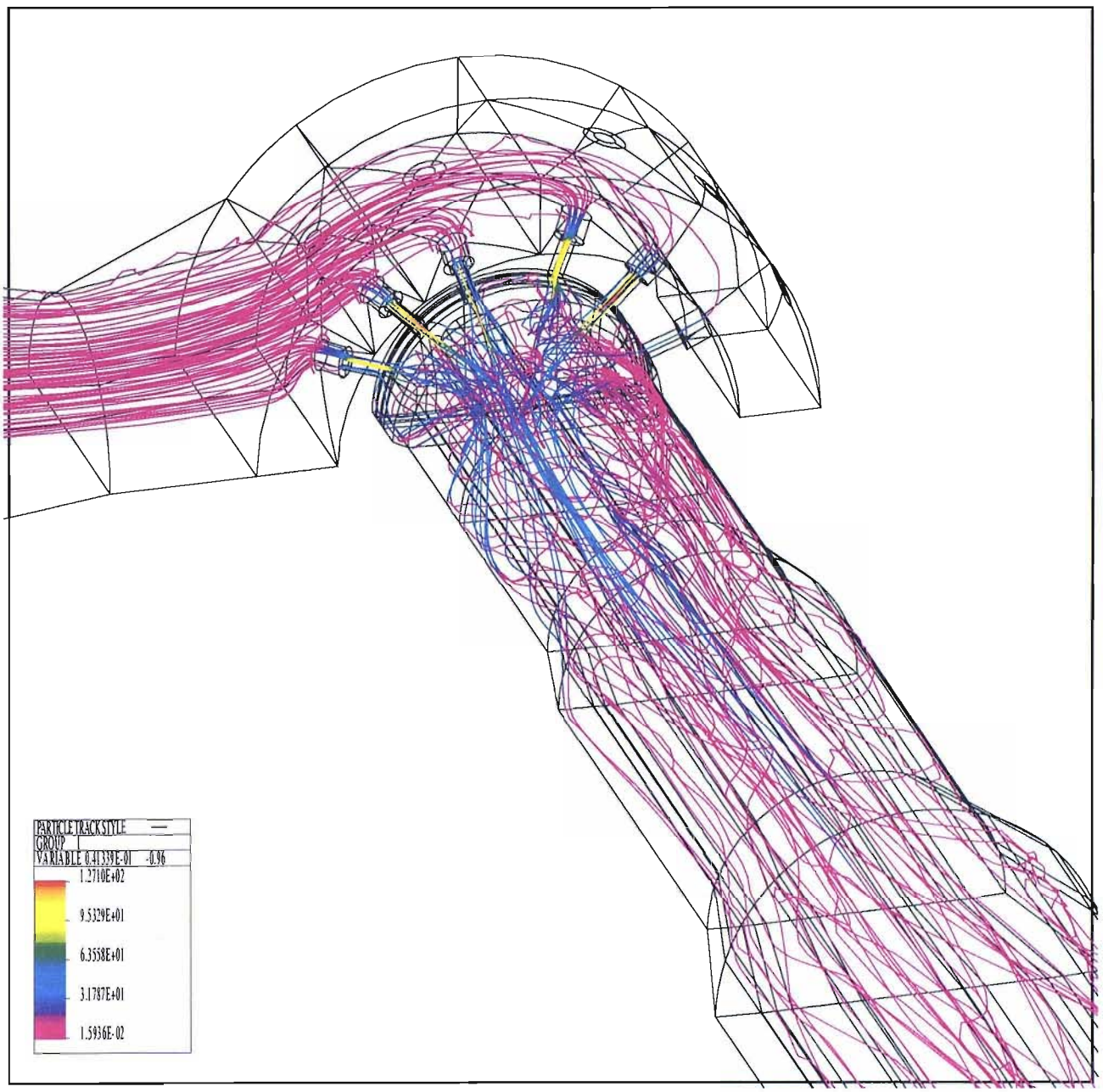

10.3.2 The Tungsten Carbide CC30

As commented upon previously, the flow domain was divided through the application of a symmetry plane to enable computational convenience. However, as a result of flow biasing by gravitational effects, separate trajectory and erosional simulations were required for both the top and bottom sections. Table 10-4 presents a summary of both the top and bottom simulations for the tungsten carbide CC30, including the process conditions considered. Appendix O Figure 159 to 168 (Figure 10-8) present the findings of the top simulations, whilst Appendix O Figure 169 to 175 present the findings for the bottom simulation. The reader is once again reminded that a total of five trajectory and erosional calculations were made for each simulations - see section 10.2.3 - implying a total of ten calculation routines were required to resolve the overall erosion prediction. The sand loadings utilised for each calculation sequence are presented through Table 10-1.

The benefit of the multiple trajectory calculation sequence was that the progression and weighting of erosion for each particle size and loading was noted. Extractions from the progressive trajectory calculations have been presented in the Appendix O Figures, whilst Table 10-4 provides an entire sequence summary. Discussion will be made separately for the top and bottom simulation sequences.

The progressive impact velocities of the top calculation sequence are presented by Appendix O Figures 159 to 161, being the impact velocities after the 2^{nd}, 4^{th} and final sequences. It was noted that the impact velocity decreased with diminishing particle sizes. The reasoning for this was the addition of subsequent impacts to the data array, providing the normal distribution for the entire particle size range. Particles in the range 212-300 μm, were able to break the squeeze film at the walling, thus delivering the highest impact velocities. The larger particles of the 1^{st} calculation sequence were more able to break the squeeze film at the wall, however, their mass was such that their acceleration - via momentum exchange from the carrier - was limited given the short acceleration lengths presented.

This ability of the largest particles to overcome boundary layer effects is clearly summarised in Table 10-4, where this particle size generated the highest number of particle impacts. These impacts were centred upon the sleeve - outer cage - where the influence of the gravitational vector was sufficient for the particles to break the squeeze film and contact the walling. The average impact velocity upon the sleeve for this particle size was low at 2.87 m/s, markedly less with the diminished particle sizes. The reduction of particle size presented a marked reduction in the number of particles contacting the walling, whereby only 38 particle impacts were recorded for the 20-63 μm. This effect was related to the squeeze film and the momentum requirement upon the particle to break the film, as the particle size and mass diminished, the impact velocity must increase. The benign flow in the annulus cavity could not readily supply the required levels of excitations, hence the rapid reduction in impacts.

EROSION CHARACTERISTICS OF THE TUNGSTEN CARBIDE CC30 CONTROL CHOKE

Particle Type - **Sand**
Particle Size Mass Flux - **88.7** g/s.
Particle Roundness Factor - **0.5**
Number of Particle Sizes and Total Number of Particles Tracked - **20** & **1440**
Particle Size Range - **20-385** μm
Turbulent Dispersion - **Yes**
Modified Coefficient of Restitution - **Yes**
Squeeze Film Retardation - **Yes**
Gravity Vector Set - **Yes** Simulation Section - **CC30 Top**

Figure 10-8 Tungsten Carbide CC30 Particle Erosion Rate, Complete Calculation Sequence (mm2/hr)

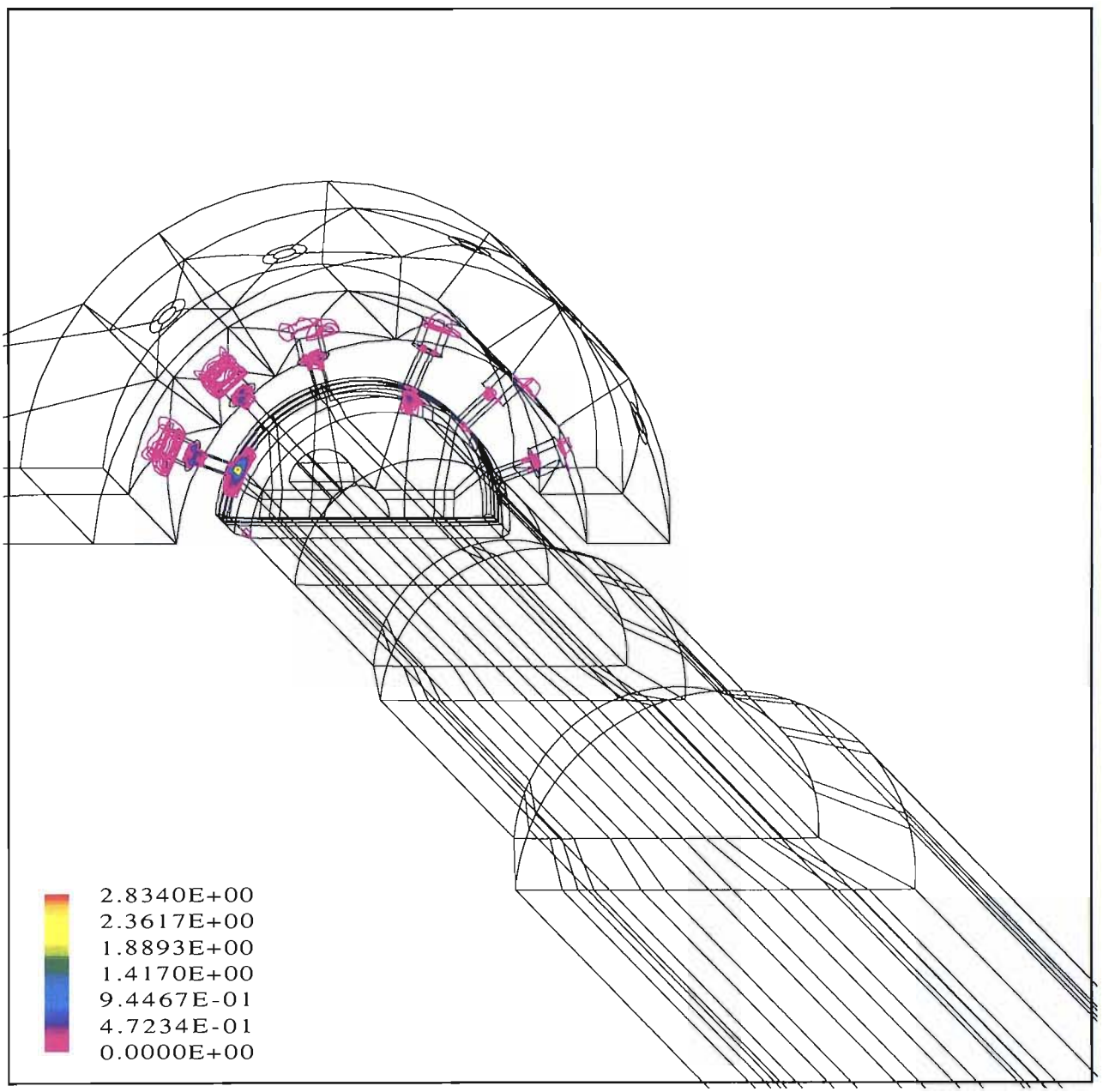

This squeeze film effect can be further explored through consideration of the impacts to the plug. The plug lends itself to such comparison via a relatively uniform number of impacts across the entire size range. Figure 10-9 presents both the average impact velocity and the normalised erosion rate of the plug. The impact velocity can be seen to increase with diminishing particle size, until the 20-63 μm size was reached. Here, the trajectory velocity of the particle was the greatest, however the squeeze film was most active upon this particle size, resulting in the decayed impact velocity. Conversely, the large particles do not achieve the trajectory velocities of the smaller particles through the drag relationship, however their mass enables them to effectively break the squeeze film.

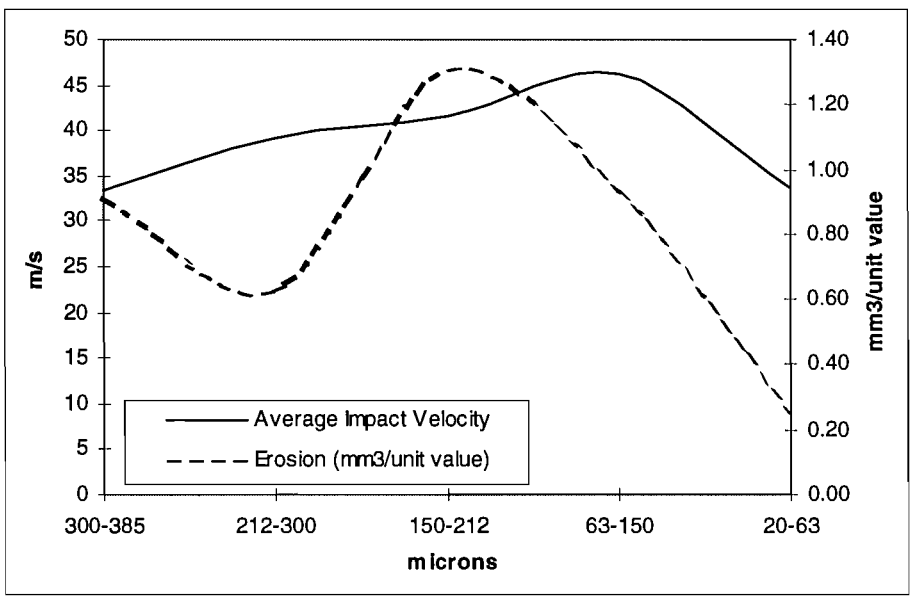

Figure 10-9 Predicted Impact Velocity and Erosion Rate of the CC30 Plug

Given the squeeze film, it was those particles of size 63-150 μm that achieved the highest impact velocities. However, through a comparison of the normalised erosion rates it was the 150-212 μm particles which were the most erosive. Whilst the impact velocity was not the highest for this particle size, the particle mass factor within the erosion equations - Chapter 4 - favoured the larger and heavier particles. This observation was also presented in Table 10-4.

Appendix O Figure 160 presents the impact velocities after the 4th calculation sequence. The impact velocity was slightly reduced from that of sequence 2, whilst Appendix O Figure 161 presents a summary of the completed sequence. The distribution of particle impact provided good representation with that found experimentally, where the distinctive erosion scaring upon the tungsten carbide plug correlated well with the sites of peak impact velocities, see Appendix N Picture 14. This is noted via Appendix O Figure 161, erosional sites were created upon the plug where the 1st, 2nd and 4th ports impinged (clockwise direction).

Calculation Number	1	2	3	4	5	Total
Material - Sleeve/Cage/Plug	ss/wc/wc	ss/wc/wc	ss/wc/wc	ss/wc/wc	ss/wc/wc	ss/wc/wc
Test Duration (min)	187	187	187	187	187	187
Aver. Flow Rate (l/s)	7.64	7.64	7.64	7.64	7.64	7.64
Aver. Pressure Drop (bar)	40.2	40.2	40.2	40.2	40.2	40.2
Aver. Fluid Temperature (degC)	57.2	57.2	57.2	57.2	57.2	57.2
Aver. Particle Flux (% by wt)	1.16	1.16	1.16	1.16	1.16	1.16
Mass Flux (g/s)	4.15	10.34	26.96	43.88	3.4	88.73
Total Mass of Sand Passed (kg)	44.82	111.67	291.17	473.90	36.72	958.28
Particle Size (μm)	300-385	212-300	150-212	63-150	20-63	20-385
No. of Particles Tracked	576	576	576	576	576	2880
Gravity Vector Set	Yes	Yes	Yes	Yes	Yes	Yes
Turbulent Dispersion Set	Yes	Yes	Yes	Yes	Yes	Yes
Min. Fraction of Cell Crossed	1.00E-03	1.00E-03	1.00E-03	1.00E-03	1.00E-03	1.00E-03
ξ Squeeze Film Constant	10.00	10.00	10.00	10.00	10.00	10.00
Fluid Viscosity (kg/ms)	0.004807	0.004807	0.004807	0.004807	0.004807	0.004807
Fluid Density (kg/m^3)	984.6	984.6	984.6	984.6	984.6	984.6
Particle Impacts to Sleeve	2534	1191	617	244	38	4624
Particle Impacts to Cage	902	837	1374	366	184	3663
Particle Impacts to Plug	48	40	39	36	48	211
Total Number of Impacts	3484	2068	2030	646	270	8498
Erosion Rate, Sleeve (mm^3/hr)	3.304	6.716	15.942	20.922	0.378	47.26
Erosion Rate, Cage (mm^3/hr)	2.618	12.722	20.558	29.668	1.480	67.05
Erosion Rate, Plug (mm^3/hr)	3.778	6.456	35.198	40.904	0.846	87.18
Overall Erosion Rate (mm^3/hr)	9.700	25.894	71.698	91.494	2.704	201.49
Aver. Impact Velocity, Sleeve (m/s)	2.87	3.16	3.94	4.24	4.17	3.68
Aver. Impact Velocity, Cage (m/s)	9.68	8.83	6.07	12.69	17.28	10.91
Aver. Impact Velocity, Plug (m/s)	33.37	39.20	41.52	46.20	33.64	38.79
Peak Impact Velocity (m/s)	47.07	68.32	59.88	64.72	47.57	64.72
Aver. Impact Angle, Sleeve (deg)	20.13	25.71	36.09	55.64	80.41	43.60
Aver. Impact Angle, Cage (deg)	17.27	21.18	29.88	28.76	27.45	24.91
Aver. Impact Angle, Plug (deg)	23.54	23.44	24.89	29.97	22.12	24.79
Peak Impact Angle (deg)	75.67	71.89	71.89	71.89	82.59	82.59
Projected Erosion, Sleeve (mm^3)	9.91	20.15	47.83	62.77	1.13	141.79
Projected Erosion, Cage (mm^3)	7.85	38.17	61.67	89.00	4.44	201.14
Projected Erosion, Plug (mm^3)	11.33	19.37	105.59	122.71	2.54	261.55
Projected Erosion, Overall (mm^3)	29.10	77.68	215.09	274.48	8.11	604.47
Peak Local Erosion (mm^3)	0.213	0.941	1.883	3.652	3.670	3.670
Erosion Intensity Index (local/global)	0.00732	0.00882	0.00585	0.00612	0.00607	0.0061
Norm. Erosion, Sleeve (mm^3/kg)	0.221	0.180	0.164	0.132	0.031	0.148
Norm. Erosion, Cage (mm^3/kg)	0.175	0.342	0.212	0.188	0.121	0.210
Norm. Erosion, Plug (mm^3/kg)	0.253	0.173	0.363	0.259	0.069	0.273
Norm. Erosion, Overall (mm^3/kg)	0.649	0.696	0.739	0.579	0.221	0.631
Impacts per Particle, Body	8.80	4.14	2.14	0.85	0.13	3.21
Impacts per Particle, Cage	3.13	2.91	4.77	1.27	0.64	2.54
Impacts per Particle, Plug	0.17	0.14	0.14	0.13	0.17	0.15
Impacts per Particle, Overall	12.10	7.18	7.05	2.24	0.94	5.90
Cameron CC30 6% WC.	**Sleeve**	**Cage**	**Plug**	**Overall**		
Measured Erosion (mm^3)	147.4	161.9	248	557.3		
Prediction Error	-4.0 %	19.5 %	5.2 %	7.8 %		

Table 10-4 Summary of Copper Cameron Tungsten Carbide Simulation - Test 4

Such impacts upon the plug ranged from 47 to 68 m/s, dependent upon the particle size accelerated across the trim. The reader is reminded that the philosophy utilised to construct the flow domain required the ports to be rotated by 15° to accommodate the blocking strategy.

The impact velocities upon the cage were focused around the ports, and in particular the step within the ports. Again, this correlated well within the experimental findings, where profiling and washing out of the port set was reported. Impact velocities upon the step were as high as 30 m/s. An impact site was noted within the outlet spool, having impacts velocities of sub 10 m/s. This area related to the large backflow region created within the outlet spool, due to the flow biasing phenomena noted previously. The average impact velocities for the sleeve, cage and plug were found to be 3.68, 10.91 and 38.79 m/s. The sleeve encompassed the outer cage, to the step, whilst the cage represented the step and inner cage.

Appendix O Figures 162 and 163 present the particle impact angles for the completed calculation sequence. The peak impact angle noted was 82°, whilst the average impact angles for all components was low, bar the sleeve when exposed to small particles. As has been commented upon previously, it was only those particles which possessed sufficient momentum to break the squeeze film which contacted the walling. The statement should be further expanded in that for the squeeze film calculation only the perpendicular component of the impact velocity was considered. Hence, the small particles only contacted the sleeve when the approach angle was acute due to the benign flow conditions within the annulus cavity. The average impact angles for the sleeve, cage and plug were 43.6, 24.9 and 24.8°.

The impact angle upon the cage - in the area around the port step - was high, with impacts at angles upto 65°. This relatively high value, coupled with the impact velocities of approximately 30 m/s, resulted in an arduous service. High impact angles were also noted at entry to the ports within the flowcage. The impact angles upon the seat angle of the plug where somewhat reduced at 25-30°. However, whence such angles were paired with the high impact velocities, again the service was arduous. The impact angle presented by the plug exploited the optimum erosive characteristics of the tungsten carbide material, unfortunately this angle coincided with the poorest erosion resistance of the stainless steel plug investigated subsequently.

Appendix O Figures 164 to 168 present the progressive erosion rates predicted for the tungsten carbide CC30, ranging from the 2nd calculation to the completed sequence. Here we note the principal erosion sites as the entrance to the ports of the flowcage, the step within the ports and seat angle of the plug. As expected the most aggressive erosion was that induced upon the seat angle of the plug. This was confirmed through the full valve erosion testing, Appendix N Picture 12, where good correlation

was found for the mass loss and penetration rate. The predicted penetration rate was 4.2 mm, or a localised erosion rate of 2.8 mm^3/hr, whilst that delivered erosion testing was 4.9 mm. Further, erosion was noted upon the plug where the zone B ports cut across the face of the plug, see Appendix M Figure 26 and Figure 10-3. This second erosion site upon the plug was predicted through the erosion model, however the extent of the erosion was comparably under-predicted, see Appendix O Figure 164 and 165[17].

A possible reason for this was the relatively small number of particles utilised to describe the many particles passed through the test choke. Here a total of 2880 trajectory calculations were made, scaled to provide the correct overall sand loading. However, if one assumes the mean particle size to be 150 μm (Figure 9-13) then the total number of particles actually passed during the test was 2.1×10^{11}. Such a ratio implies that whilst the salient features were captured, smaller underlying details were not readily predicted. To an extent this did not overly concern the author, as it is the salient features which are gross in terms of erosion, and are those likely to induce loss of containment and/or flow control.

The profiling of both the entrance to the ports and the washing out of the step within the flowcage were accurately captured. Whilst the damage at the entrance to the ports of the flowcage is glaring, the extent of that damage was limited and the reader's attention is brought to the scale for representation, whereby interrogation reveals that the damage relates solely to profiling erosion. The damage to the port step was markedly increased over that predicted at the entrance. The reader is reminded that in this case, the reduction in port diameter signified the transition from a stainless steel to a tungsten carbide. Even with this transition, the erosion damage to the step area was marked, with a reported localised erosion rate of approximately 1 mm^3/hr.

As one browses through Appendix O Figure 164 to 168 it is apparent that the basic structure of erosion did not significantly alter with the variance in particle size. This was to be expected, as the flow field was such that any subtleties induced by particle size were destroyed by it's aggressive nature, i.e. the localised and intense jetting established. For example, a less aggressive flow field may have propagated an increased turbulent dispersion tendency for the smaller particles. In this case the main relation of varying particle size was the erosional contribution made by that particle grouping.

The erosional contribution made by the particle groupings to each component is summarised by Table 10-4, under the heading projected erosion. The summary presented through the table reinforced that which was presented graphically, with the progressive contributions given. Furthermore the peak

[17] As one progresses through the calculation sequence, the zone B erosion sites upon the plug appear to diminish. These erosion sites do not disappear, they are simply not represented by the requirement to increase the scale as the predicted eroded volume increased with subsequent calculation sequences.

localised erosion is provided. Before a comparison is made of the prediction and experimental erosion data, comments will be made of the bottom simulation.

The bottom simulation for the tungsten carbide CC30 is summarised via Appendix O Figures 169 to 175. In this instance, the graphical representation were limited to the completed calculation sequence. The attention of the reader is brought to the discussions made in section 10.2.1, whereby the application of the symmetry plane approach required a compromise to be made regarding the porting orientation of the bottom simulation. Appendix O Figures 169 and 170 present the particle impact velocities. What is immediately apparent from these graphics was that the spread of particle impacts in the lower portion of the geometry was greater than that of the top simulation. This occurrence was related to the application of the gravitational vector, promoting the tendency for the particle to strike the walling of the outlet. In the case of the top simulation, the gravitational vector drove the particle toward the centre axis and the symmetry plane.

This observation is very much reinforced by the graphical representation of the particle impact angle, as summarised via Appendix O Figures 171 and 172. Again the increased tendency towards particle impacts is immediate apparent when a comparison is made with the top simulation, Appendix O Figure 163. However, such impacts were driven by gravitational effects, as such the impact velocities were low at sub 14 m/s, whilst the impact angles were all below 30°. These relatively low impact velocities implied that whilst an impact event was common in the outlet, the erosional effect associated with the impacts were limited. This is confirmed via Appendix O Figures 173 to 175 where no marked erosion of the outlet spool was noted. Again, this observation was validated via the erosion testing, where no erosion was noted in the outlet, bar polishing associated with the sheer volumes of sand passed.

The particle impact velocities and angles, in addition to the predicted erosion rate, were similar to that established by the top simulation, with the erosional focus being sited at the entrance to the ports in the flowcage, the port steps and the seat angle upon the plug. However, in this instance it was the rear most port (4^{th} in an anticlockwise direction) which generated the greatest erosion upon the plug, Appendix O Figure 173. Furthermore, that step most removed from the inlet (6^{th} in an anticlockwise direction) was that which experienced the greatest erosion. This observation was in agreement with that phenomenon noted through the erosion testing, where the incoming sand had a tendency to pass to the rear of the body cavity before passing through the trim, Appendix N Picture 12.

It is of interest that the highest impact velocity were recorded for the forward - that nearest the choke inlet - seat angle upon the plug, at 83 m/s. It was believed that this indication was a spurious event, whereby one of the small particles (20-63 μm) was overly excited. However, the bulk of the particles

passed these forward ports, preferentially routing to the rear ports to promote the increased erosion of these rear ports. The forward port experienced a localised erosion rates of 1.8 mm^3/hr, whilst the rear port experienced a rate of 3.6 mm^3/hr. This higher rate is in comparison to the peak erosion rate of 2.8 mm^3/hr for the top simulation, and hence the excellent representation of the generic erosion scarring noted via Appendix N Figure 12.

A final comment upon the nature of the predicted erosion is that whilst the form was not exactly as noted in the erosion testing (the characteristic crescent scarring as reported through Figure 9-8) the phenomenon was captured by the simulation. Here erosion generated by the reflection of the flow, from the seat angle of the plug, back into the inner walling of the flowcage was predicted. Whilst difficult to decipher in the graphic representations, Appendix O Figures 168 and 174 summarise this phenomena.

Good comparison was found between the erosion predicted and that found experimentally. These results were extremely encouraging from a validation viewpoint and confidently affirmed the ability of the erosion model. From Table 10-4 we can assess the prediction accuracy, with the overall error being reported at 7.8%, whilst the error for the sleeve, cage and plug was -4.0%, 19.5% and 5.2% respectively. The predicted eroded volumes were 141.8, 201.1 and 261.6 mm^3 for the sleeve, cage and plug. That particle size which generated the highest erosion rates for all components was the 63-150 μm grouping. The related to both the particle loading of this grouping and the high average impact velocities experienced.

Such accuracies were excellent, with the slight over-predictions of the cage and plug being related to the manner in which the progression of erosion was treated. Within the model, the overall eroded volumes were factored from the instantaneous erosion rates, with no consideration given to the transient nature of erosion in terms of surface deformation. As such the erosion prediction was excessive, being based upon an original or static geometry, as opposed to a transient one. As any such profiling or deformation occurs to the target surfaces, the erosion rate will be reduced until a relatively steady state erosion rate is achieved, as discussed in Chapter 9. The transient nature was not capture and is a recommendation regarding further work.

Furthermore, the over-prediction of the cage was also related to the step, and the previously stated trajectory calculation difficulties whereby the particles become hung-up upon the step - see section 10.2.3 - causing repeated particle impacts and hence an excessive erosion prediction.

10.3.3 The Stainless Steel CC30

Appendix O Figures 178 to 186 present the findings of the stainless steel CC30 simulation. A slightly differing solution style was utilised in the instance of the stainless steel model. Here, only one calculation sequence was undertaken, being the top, as opposed to the top and bottom of the tungsten carbide CC30. Such an approach was instigated due to a limited time resource, requiring an assumption to be implemented regarding the treatment of the particle loading and the extrapolation of erosion. As discussed in section 10.1 the particle loading at entry to the flow domain was manipulated such that a good representation of the gravitational effect could be arrived at.

The split for the sand loading between the top and bottom entry sections - Figure 10-2 - was found to be 43 % to 57 % respectively. This weighting was then utilised to extrapolate the overall stainless steel erosion rate from the top simulation only. The assumption was proven valid from the findings of the tungsten carbide simulation, where the erosional weighting between the top and bottom was found to be of a similar magnitude. Such a weighting factor was also confirmed through all of the experimental workings undertaken on the CC30 valve.

The trim material of the stainless steel valve called for a differing treatment for the restitution coefficient than that applied for the tungsten carbide case, see section 6.3.1, implying that the trajectory calculations would differ. Appendix O Figures 176 and 177 exemplify the trajectory calculation made for the stainless steel case. Through the increased absorption characteristics of steel based materials over the likes of tungsten carbide, the peak trajectory velocity achieved by the stainless steel simulation was lower than that of the tungsten carbide simulation. Here, the peak velocity was 124.6 m/s whilst the tungsten carbide case achieved 127.1 m/s.

Appendix O Figures 178 to 181 presents the progressive calculation sequences for the particle impact velocities. The basic structure of the impacts was relatively static for all the particle sizes considered. However, for this top simulation, there appeared to be a tendency for the particle size to influence which port the particles preferentially routed to. The reasoning for this being that the larger and heavier particles - under gravitational effects - dropped out earlier than the smaller particles due to the relatively benign conditions in the annulus. As these particles dropped out, they preferentially routed to those ports nearest the inlet, whilst the smaller particles are conveyed to the rear ports. This effect is detailed in Appendix O Figures 178, 179 and 180, where the magnitude of the shading for the rear ports increases notably with a diminishing particle size. This effect was also noted in the tungsten carbide simulation, Appendix O Figures 159, 160 and 161. Furthermore, the flow biasing effect was also noted, whereby an area of particle impingement was noted in the outlet spool, Appendix O Figure 181.

Calculation Number	1	2	3	4	5	Total
Material - Sleeve/Cage/Plug	ss/ss/ss	ss/ss/ss	ss/ss/ss	ss/ss/ss	ss/ss/ss	ss/ss/ss
Test Duration (min)	75	75	75	75	75	75
Aver. Flow Rate (l/s)	7.88	7.88	7.88	7.88	7.88	7.88
Aver. Pressure Drop (bar)	33.3	33.3	33.3	33.3	33.3	33.3
Aver. Fluid Temperature (degC)	36.2	36.2	36.2	36.2	36.2	36.2
Aver. Particle Flux (% by wt)	0.58	0.58	0.58	0.58	0.58	0.58
Mass Flux (g/s)	2.14	5.33	13.90	22.64	1.7	45.70
Total Mass of Sand (kg)	9.63	23.99	62.55	101.88	7.65	205.7
Particle Size (μm)	300-385	212-300	150-212	63-150	20-63	20-385
No. of Particles Tracked	288	288	288	288	288	1440
Gravity Vector Set	Yes	Yes	Yes	Yes	Yes	Yes
Turbulent Dispersion Set	Yes	Yes	Yes	Yes	Yes	Yes
Min. Fraction of Cell Crossed	9.00E-03	9.00E-03	9.00E-03	9.00E-03	9.00E-03	9.00E-03
ξ Squeeze Film Constant	10.00	10.00	10.00	10.00	10.00	10.00
Fluid Viscosity (kg/ms)	0.004807	0.004807	0.004807	0.004807	0.004807	0.004807
Fluid Density (kg/m^3)	984.6	984.6	984.6	984.6	984.6	984.6
Particle Impacts to Body	26	7	3	0	0	36
Particle Impacts to Cage	1758	1501	982	621	175	5037
Particle Impacts to Plug	60	25	37	45	30	197
Total Number of Impacts	1844	1533	1022	666	205	5279
Erosion Rate, Body (mm^3/hr)	0.356	0.000	0.000	0.000	0.000	0.36
Erosion Rate, Cage (mm^3/hr)	28.036	52.064	76.826	60.244	1.378	218.55
Erosion Rate, Plug (mm^3/hr)	63.920	63.620	276.990	320.806	1.816	727.15
Overall Erosion Rate (mm^3/hr)	92.312	115.684	353.816	381.050	3.194	946.06
Aver. Impact Velocity, Body (m/s)	2.84	1.06	1.17	0.00	0.00	1.01
Aver. Impact Velocity, Cage (m/s)	7.45	8.33	10.19	11.09	13.97	10.21
Aver. Impact Velocity, Plug (m/s)	31.86	38.55	46.13	42.96	27.26	37.35
Peak Impact Velocity (m/s)	45.03	55.94	64.94	77.37	53.84	64.72
Aver. Impact Angle, Body (deg)	36.87	33.73	37.57	0.00	0.00	21.63
Aver. Impact Angle, Cage (deg)	24.61	22.85	27.50	31.88	40.80	29.53
Aver. Impact Angle, Plug (deg)	25.41	25.48	26.56	29.04	22.03	25.70
Peak Impact Angle (deg)	74.56	71.89	71.89	73.87	76.12	82.59
Projected Erosion, Body (mm^3)	0.45	0.00	0.00	0.00	0.00	0.45
Projected Erosion, Cage (mm^3)	35.05	65.08	96.03	75.31	1.72	273.19
Projected Erosion, Plug (mm^3)	79.90	79.53	346.24	401.01	2.27	908.94
Projected Erosion, Overall (mm^3)	115.39	144.61	442.27	476.31	3.99	1182.57
Peak Local Erosion (mm^3)	2.110	5.578	15.757	23.557	25.633	25.633
Erosion Intensity Index (local/global)	0.01829	0.02145	0.02244	0.01999	0.02168	0.0217
Norm. Erosion, Body (mm^3/kg)	0.00	0.00	0.00	0.00	0.00	0.00
Norm. Erosion, Cage (mm^3/kg)	0.17	0.32	0.47	0.37	0.01	1.33
Norm. Erosion, Plug (mm^3/kg)	0.39	0.39	1.68	1.95	0.01	4.42
Norm. Erosion, Overall (mm^3/kg)	0.56	0.70	2.15	2.32	0.02	5.75
Impacts per Particle, Body	0.09	0.02	0.01	0.00	0.00	0.03
Impacts per Particle, Cage	6.10	5.21	3.41	2.16	0.61	3.50
Impacts per Particle, Plug	0.21	0.09	0.13	0.16	0.10	0.14
Impacts per Particle, Overall	6.40	5.32	0.13	0.16	0.10	0.14

Cameron CC30 SS.	Cage	Plug	Overall
Measured Erosion (mm^3)	256.4	833	1089.4
Prediction Error	6.1 %	8.4 %	7.9 %

Table 10-5 Summary of Copper Cameron Stainless Steel Simulation - Test 3

Table 10-5 provides the summary of the stainless steel simulation. As commented upon, the overall erosion was extrapolated through the weighting factor. However, the particle impact characteristics - such as average impact velocity - are reported for the top simulation only. Furthermore, the flowcage of the stainless steel CC30 was a one piece, as opposed to the sleeve and cage of the tungsten carbide model. This meant that the entire flowcage was numerically considered as a single piece item, allowing a numerical summary of the body to be made. One notes that it was only the large particles (>150 μm) which were able to impact the walling of the body, including both inlet and outlet spools. The intensity and frequency of such impacts were limited and posed no erosional threat. The average impact velocity was approx. 1 m/s and the projected erosion 0.45 mm^3. The average impact velocities for the other CC30 components are also summarised by Table 10-5.

Appendix O Figure 182 details the particle impact angles, completed calculation sequence. The peak impact angle noted was 72°, with the higher angles being centred upon the entry to the flow cage and the step within the ports. Reinforcing the comments made through the description of the tungsten carbide simulation, the impact angle upon the seat angle of the plug was approximately 25-30°. Such an angle represents the optimum attack for a steel base material, hence the gross erosion damage depicted in Appendix M Figure 13, where the severe jetting is noted. Table 10-5 presents the average impact angles for each component within the choke, here we note the relationships between particle size and component. Such relationships included the squeeze film effect upon the cage, whereby the diminishing particle size required an increased impact angle - and perpendicular velocity - to contact the walling. This effect was also confirmed through both the impact velocity and the number of particle impacts to the cage.

Appendix O Figures 183 to 186 (Figure 10-10) summarise the predicted erosional damage after 3, 4 and the completed calculation sequence. Again, we note the accuracy of the prediction erosion structure when compared to that found experimentally, Appendix N Picture 13. Here the erosion was centred upon the entry to the ports, the port steps and the plug, with the same biasing effect as that noted by the tungsten carbide simulation. A comparison of the intensity of the erosional attack is noted between that found for the tungsten carbide and the stainless steel simulations. Such a variance allows the excellent characteristics of a tungsten carbide material to be displayed, whereby after the 3^{rd} calculation sequence the peak localised erosion for the stainless steel simulation was 9 mm^3/hr, however this was limited to 1.7 mm^3/hr for the tungsten carbide. Further, upon the completion of the calculation sequence this variance was extended to 17.8 mm^3/hr and 2.8 mm^3/hr respectively. The attention of the reader is brought to Table 10-4 and Table 10-5 where the normalised erosion for each component is summarised, allowing the relative material performances to be gauged, including the influence incurred by the averaged impact angles and velocities.

EROSION CHARACTERISTICS OF THE STAINLESS STEEL CC30 CONTROL CHOKE

Particle Type - **Sand**
Particle Size Mass Flux - **88.7** g/s.
Particle Roundness Factor - **0.5**
Number of Particle Sizes and Total Number of Particles Tracked - **20** & **1440**
Particle Size Range - **20-385** μm
Turbulent Dispersion - **Yes**
Modified Coefficient of Restitution - **Yes**
Squeeze Film Retardation - **Yes**
Gravity Vector Set - **Yes** Simulation Section - **CC30 Top**

Figure 10-10 Stainless Steel CC30 Particle Erosion Rate, Complete Calculation Sequence (mm2/hr)

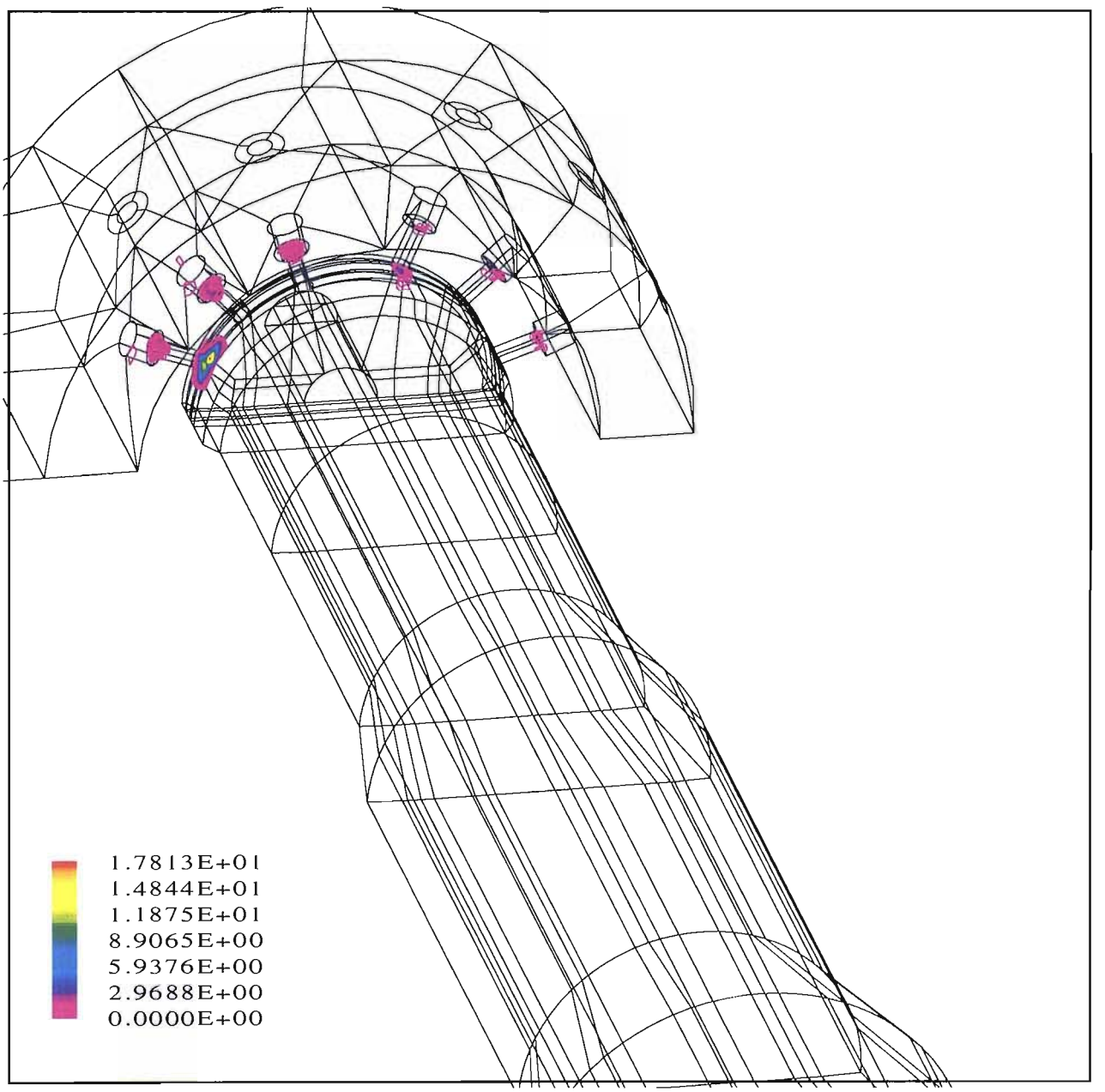

One note of interest relating to the erosion upon the plug was that the 'spread' adjacent the ports appeared to be much increased over that found experimentally. This phenomenon occurred due to the assumption within the model that the surface was non-deforming. The experimental case saw the jetting scar being created relatively quickly, this scar tended to produce a channelling effect that limited the spread of the erosion scarring. Such a phenomenon was not captured by the erosion model. Again, the predicted erosion damage to the zone B ports was limited, the reasoning for this being the same as that stated for the tungsten carbide simulation, however in this instance the scarring observation is further exasperated by the intensity of the erosional attack.

Table 10-5 presents both the predicted erosion rate and the projected erosion for each component. Here we note that that particle grouping which contributed the most to the overall erosional damage was the 63-150 μm. However, the cage experienced the greatest erosional damage from the 150-212 μm group. Such differences related to the mass flux specified and the number of particle impacts experienced for each size grouping, whereby the larger particles were more able to impact the cage.

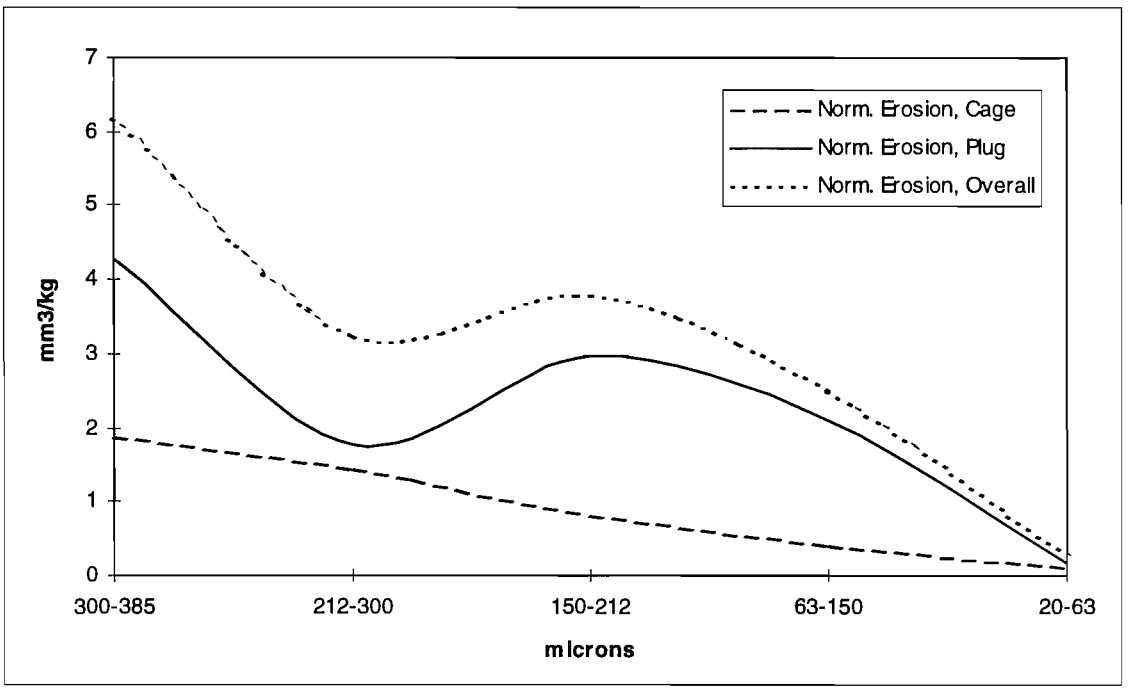

Figure 10-11 Normalised Erosion for the Stainless Steel CC30 Simulation

The normalised erosion presented an interesting picture, whereby the relative erosivity of each particle size was gauged. Figure 10-11 details the normalised erosion for the stainless steel CC30 simulation. The erosivity of the particles is seen to diminish with a reduced particle size for the cage. This profile was as expected, with the diminished erosivity being a function of squeeze film effects, which have already been discussed at length. However, the anomaly present for the plug, and hence the overall erosivity, is unusual and one which cannot be readily explained. This anomaly was also noted in the tungsten carbide simulation whereby the 212-300 μm size grouping was not inline with other particle sizes. One may hypothesize that such an anomaly was the result of an over active squeeze film

function, however if such was the case then one would expect the normalised erosion of the cage to express the same trending. However, an investigation of the average impact velocities and angles showed little variance between particle groups for that experienced for the cage or plug in terms of relatively magnitudes. As such one must conclude that this phenomenon was the result of the limited number of particle impacts upon the plug in comparison to the cage, which was statistically more sensible.

The projected erosion for each of the components is reported in Table 10-5, being 0.45, 273 and 909 mm^3 for the body, cage and plug. From the measured erosion for the plug and cage, the prediction errors were 8.4% and 6.1% respectively. Again such prediction accuracies were excellent, demonstrating the exceptional ability of the model to capture such complex erosional behaviours, even with the limiting assumption that the overall erosion was derived from only a one half simulation. As is expected given the accuracies of both erosion simulations, the predicted normalised erosion was inline with that found experimentally. Hence an interrogation of Table 10-4 and Table 10-5 in comparison with Table 9-11 summarises the various normalised erosion parameters. The breakdown of individual particle groupings is given in the Tables, however the salient points are presented through Table 10-6.

	Tungsten Carbide Prediction	Tungsten Carbide Experimental	Stainless Steel Prediction	Stainless Steel Experimental
Normalised Erosion - Plug	0.27	0.25	4.42	4.04
Normalised Erosion - Cage	0.21	0.16	1.33	1.24
Normalised Erosion - Sleeve	0.148	0.31	×	×
Normalised Erosion - Overall	0.631	0.565	5.75	5.28

Table 10-6 Comparison of Experimental and Predicted Normalised Erosions

The general accuracy was good, however one failing was the under-prediction of erosion to the sleeve of the tungsten carbide simulation. This had ramifications upon the stainless steel prediction, however in this instance it was not possible to highlight any prediction failings as the cage upon the stainless steel simulations was a one piece item. Given that the graphical erosion presentations of the Appendix O Figures detailed very similar erosional trends for both simulation cases, it was thus a just hypothesis that this under-prediction of the erosion at entry to the ports had occurred for the stainless steel case.

Finally the reader's attention is brought to the Erosion Intensity Index of Table 10-4 and Table 10-5. This references detailed the severity of the localised erosion, whereby the stainless steel simulation experienced much increased localised erosion than that of the tungsten carbide simulation.

10.4 Conclusions as to the Merit of the Numerical Technique Derived

The numerical techniques derived and applied within this and proceeding Chapters have proven to be most successful. These successes have demonstrated the ability of the CFD based erosion model to capture not only the overall erosion damage induced, but has also given trending and erosional pattern information, proven on a live test bed. This is an excellent accomplishment when consideration is given to the complexity of the problem investigated and the wider applicability of the model, which has been purposely in-built.

The trending information delivered by the model matched that provided by experimentation, including such complex phenomena as the reported flow biasing. These descriptions of the erosional patterns have proven reliable for the salient features, with some limitations found for the more subtle, underlying erosional trends presented through the experimentation. However, such subtle features were the result of complex interactions within the test chokes, proving difficult to be captured by the CFD erosion model due to the necessary numerical assumptions associated with any such model. These assumptions are wide spread, ranging through the turbulence closure model, the trajectory calculation and the actual erosion correlations employed to interpret particle impacts. Once considerations is given to the number of assumption necessary, the general performance and robustness of the model is proven excellent.

The structure of the erosion model was found to work well, with the empirical constants derived to describe the erosion process providing excellent results for both the tungsten carbide and the stainless steel cases. However, such a performance was reliant upon an accurate description of the particle impact events via the trajectory calculation, including such characterisations as the squeeze film function, the coefficient of restitution and turbulent dispersion term. For example, it was noted that due to a failing of the trajectory calculation (hang-up of particles upon the step within the ports) that an over-prediction occurred for the cage of the tungsten carbide case. Such empirical parameters were developed with the view of having general applicability, including differing carrier types. As such, the erosion model is heavily dependent upon good trajectory calculations, which in itself is reliant upon a good flow field correlation. The importance of accuracy at all stages of the modelling process cannot be sufficiently emphasised, which in part is reliant upon the competency of the user.

Further to the model's confident demonstration of its ability, additional findings in terms of particulate relationships have been noted by the validation exercise, allowing important learning to be presented. Here, such influences as the gravitational effect have been clearly shown, as have the contribution made by each particle grouping and ability of the model to transcend flow field effects into erosional effects and vice versa. This has proven itself to be an excellent investigative and design tool, enabling a much increased understanding of complex erosion synergies to be arrived at.

11. Concluding Comments and Recommendations Regarding Further Work

The conclusion philosophy utilised within this study has been to provide conclusions as to the individual elements of work at the end of each Chapter. The reader is referred to these concluding comments for greater detail, whilst the remarks here present the salient points.

11.1 Concluding Comments

A state-of-the-art computational fluid dynamics' erosion model has been developed for the analysis of erosional trends in complex geometries, such as chokes. The model utilises a three tier approach to providing an erosional solution, whereby the turbulent flow field is resolved and upon which a particle trajectory calculation is based, given consideration to the individual particle characteristics. The erosional prediction is then an interpretation of the individual particle impact events determined through the trajectory calculation. Such an approach provides an excellent insight into the erosional mechanisms, whereby such features as flow effects can be identified as the root cause of the erosion.

Large quantities of data can be processed by the *CFD* erosion model through the application of highly visual and informative surface plotting techniques that produce shaded contour plots of the choke internals. Such a visualisation approach allows rapid and accurate interpretation of the results, whereby the particle impact velocities, the particle impact angles, particle kinetic energy at impact and predicted erosion rates can be displayed as unique surface contour plots. The visualisation approach is extremely efficient in terms of data representation, such an efficiency allows large sample sizes to be considered, thus ensuring good statistical confidence in the results. Furthermore, the rapid interpretation times enable many subtle variations to be considered, promoting a tool which is excellent in terms of design optimisation of the choke or chosen geometric configuration.

In addition to the visualisation tools inbuilt to the code, a numerical interface is also provided which generates a range of supporting statistical data in the form of user files. Such files provide summarises of such particle impact data as, the average impact velocity, the average impact angle, the projected erosion rates, number of trajectory calculations made, and the number of impacts per particle. Furthermore each impact event is noted, providing such information as the impact co-ordinates, the individual impact velocity, including the velocity components, the individual impact angle, and the predicted volume loss per impact.

A unique naming scheme has been developed which allows individual components within the choke, or chosen geometry, to be identified. Once identified, the material characteristics of that component can be uniquely specified, including such details as the coefficient of restitution. The coefficient of restitution

has been incorporated to improve the accuracy of the particle trajectory calculation. Furthermore, the identification of individual components allows statistical analysis to be performed on these components. Here, the information described through the user files can then be presented upon an individual component basis, again providing an excellent method of results interpretation and design optimisation. To cater for the differing material types, a database of material constants is included within the code and summarised by Table 9-3.

The erosion model proved to be an excellent and robust vehicle for which erosional rates could be predicted for a number of differing operational regimes. The application of experimental techniques proved the validity of both the erosional equations and the overall erosional prediction technique. Further to the general comments of above, Chapter related conclusions can be summarised as follows.

1. From Chapter 1, the need and financial benefits obtainable from an improved understanding of the erosional mechanism within choke were presented. The aims of the project based upon these understandings were also established.

2. A wide and varied quantity of work is available in the current literature, where many variations to the theme of erosion modelling have been proposed. These proposals identified the principal mechanisms at work within the erosional process, developing relationships to describe these mechanisms. The findings of the literature was that erosion is a complex process and one which cannot be readily described through a purest approach. As such a number of empirical functions were presented and commented upon, with the author selecting those most suited to the application generated through this project. The development of a unique erosional relationship or function by the author was not deemed to be the ideal manner in which to progress this project, given the wealth of knowledge available in the literature.

3. The common design styles of current choke were identified in Chapter 3, and conclusions as to the relative performance of these choke styles in terms of erosion and general serviceability presented via Table 3-1. A number of observations are made including, the choke opening significantly influences the erosional intensity experienced, hence it is vital that the choke be correctly sized. Hard throttling of the flow to achieve the desired pressure drop results in rapid erosion and loss of flow control.

4. Building upon the finding of the literature review, Chapter 4 specified the erosion modelling approach utilised within the model, identifying the underlying mechanisms of erosion, being cutting and deformation erosion. The structure of the mechanisms was presented, along with the specifics of the rationale utilised in the development of these models. The author concluded as to the need to employ a dual equation approach, through the limitations of the individual equations. Furthermore,

the erosional equations were improved upon by the author to accommodate the needs generated by the application of a tungsten carbide target and the limited nature of the available materials characteristics for such a material.

5. Chapter 5 was concerned with developing an understanding of the working structure of the CFD package and in particular the structure and limitations of the turbulence closure models. The relative performance of the three main closure models was addressed, with the conclusion being that whilst the Differential Stress model was the most computationally expensive, the resolution of this model was "best in class" and that most suited to the application of supporting particle trajectory calculations. The particle trajectory calculation, and subsequent erosional prediction, was found to be sensitive to the turbulence structure predicted by the closure model, via the turbulent dispersion term. Whilst the structure of the dispersion term did not vary with closure model, the improved resolution of the localised turbulence provided by the Differential Stress model proved an important element in the erosional prediction.

6. The Lagrangian approach to the trajectory calculation was presented as that most applicable to the erosion prediction techniques. Whilst this approach limited the particulate loading, via the assumption that the momentum transfer was not bi-directional and that no particle-particle interactions occurred, it enabled the best trajectory and hence erosional resolution characteristics to be achieved. The failings of the trajectory calculation techniques within CFX-F3D were identified and modifications implemented to improve the near wall and wall interaction. The need for and the structure of the coefficient of restitution and squeeze film function were presented. Furthermore, a detailed summary of the oilfield sand characterisation was given, where conclusions were drawn as to the typical size, sharpness and loadings of produced solids.

7. Chapter 7 was involved with a summary of modification required to the basic code of CFX-F3D to enable quantitative erosion predictions to be made. The logic structure utilised to drive the erosion prediction was also presented. A number of problems were encountered throughout the development of the erosional routines, which have been commented upon in section 7.9, the main difficulties being associated with understanding the structure of the main CFX-F3D coding and the naming conventions utilised within the code. This required a close discourse with the software authors, AEA Technology.

8. In a demonstration of the versatility of the techniques developed, a reverse flow liquid droplet erosion example was presented in Chapter 8, along with a number of more conventional examples to investigate the sensitivity of the techniques utilised. The reverse flow case was most successful, enabling a limiting case to be identified for the operation of a choke in such a configuration, section

8.2.2. A sensitivity study completed upon a 90° bend enabled the relative merits of the turbulent dispersion and coefficient of restitution terms to be assessed. The strong conclusion to be drawn from this study was that it is essential that both terms be applied to the erosion prediction. With the terms applied a prediction error of -5.9 % was reported, however this increased to 39.2 % when such terms were neglected. Further to the numerical accuracies of the model, the ability of the model to capture erosional trends was reported.

A detailed investigation of the erosion within a needle and seat and cage type choke was completed. The needle and seat study focused upon the relationship of particle size upon the turbulent dispersion terms and the subsequent dependence of that term on the turbulence closure model. Whilst this study was in effect a sensitivity investigation of a similar nature to that of the 90° bend, it clearly summarised the particle size relationship in the live situation of a modelled choke. Unfortunately no experimental data was available to validate the findings, however the results were very encouraging.

The comparative cage type choke study probed the relative performance of differing cage type chokes, under a number of conditions and particle sizes. The conclusions to this study was that the comparative erosion rates between the designs was of a similar magnitude. However, the ability of the external sleeve design to remove its controlling surfaces from the high velocity jetting region, enables the service life of this design type to be extended over that of the plug and cage style. The figure quoted in terms of longevity was some 4.5 times, however the robustness of the external sleeve design was criticised and the recommendation made that for subsea developments - where interventions are financially prohibitive - the plug and cage design was the preferred option.

9. To assess the empirical constants within the erosion equations, a series of flat sample erosion tests were completed. The accuracy delivered by these quantification exercises was excellent, clearly vindicating the utilisation of a dual equation approach. A detailed discourse was then presented as to the full valve erosion testing undertaken at BP Sunbury on the high pressure flow loop. A total of eight choke combinations were tested, enabling an improved understanding of the erosional mechanism within chokes to be arrived at, and the provision of an excellent validation benchmark for the entire modelling process. A discussion of the erosive relationships between the eight tests was made in section 9.2.4.1.

10. Chapter 10 utilised two of the erosion tests presented through Chapter 9 and undertook a detailed erosion simulation to assess the performance of the model against real data. A number of effects are noted through the erosion testing which were transferred to the erosional prediction, including sand attrition effects and the influence of gravity upon the erosion process. The model constructed was extremely complex and represented the state-of-the-art in terms of erosion predictions. The

overall prediction error obtained for the simulations was 7.8 % for the tungsten carbide simulation and 7.9 % for the stainless steel investigation. Further to the excellent prediction accuracy, the location and intensity of the predicted erosion found good correlation with the experimental findings. Such a result was extremely encouraging and fully supports the applicability of a CFD based tool to such tasks as erosion predictions within complex geometries. For further comments as to the merits of the erosion model, review section 10.4.

11.2 Recommendations Regarding Further Work.

Due to the time constraints of a PhD research programme, the present worker was limited in the quantity of work that could be undertaken. Areas of further work by subsequent workers are identified, allowing a number of the underlying assumptions to be addressed.

The particle trajectory calculation was undertaken in a Lagrangian frame, this technique forces particle-particle interactions to be ignored for simplicity. The assumption made was that the suspension was sufficiently dilute to avoid direct particle-particle interactions; at the wall and mid-flow. This assumption can be shown to be valid for the sand concentrations commonly experienced in oil field applications; below 0.1 % by volume. However, if suspension concentrations were to be increased, then such interactions would be influential. An important extension of the present work would be the inclusion of particle-particle interaction, at both the wall and mid-stream. A somewhat more simplistic approach, which does not directly consider particle-particle interactions, would be as follows. The particle volume fraction within any one cell is known, including those adjacent to the walling. As such, a weighting to the predicted erosion could be applied as a function of this particle volume fraction, allowing the concentration effects at the wall to be captured.

The need for such a consideration of the particle volume fraction was demonstrated in the CC30 simulations, where dead zoning in the port steps of the flowcage resulted in an excessive erosion prediction in this area. Here, no consideration was given to the volume fraction, implying that repeated impact events were recorded and the subsequent over prediction. An investigation of the particle volume fraction found a physically impossible value of >1 being reported for the step area of the CC30.

Furthermore, transient particulate loading would be an important consideration. The production of solids from a well is known to be transient, with slugs of solids being produced as the conditions within the well change. These transient slugs of sand would interact with one another at the walling and interrupt the erosion effect, such a transient interrupt effect would need to be captured. An additional consideration of fluctuating particulate loading would be the validity of the momentum coupling and the necessity to include a bi-direction consideration between the continuous and particle

phase. Such a requirement would introduce the need for an iterative solution scheme and the complication of treating this.

The erosion model computes an eroded volume, given such data as impact velocity and material type, where the location of that impact is known. The next iteration of this cycle would be to couple this information to generate a flow domain or geometry which was intelligent. It would up-date itself to reflect the erosion predicted, i.e. it would generate its own erosion scars. However, such a process would be very complicated. The grid generated in the pre-processing is very complex, requiring many constraints to ensure its consistency. The production of an intelligent link to reflect erosion in such complex grids is an extremely complex process, requiring an iterative approach to be adapted. After a pre-set time period or eroded volume, the processor would be stopped and the erosion data supplied to the pre-processor for grid generation. Upon production of an up-dated grid, the flow field must once again be solved, particle trajectory calculations made, then erosion rates predicted once more on the merits of the trajectory calculations. Such a process would be very time consuming and computationally very expensive.

An alternative method of representing the erosional damage and trending the surface data would be 3 dimension surface modelling. Given the improvement in graphical tools, the erosional data could be manipulated within such a tool to present the erosion scarring in real terms. This would greatly increase the perception of the erosional damage, giving real depths and effected areas, as opposed to the somewhat limited shading convention which is currently employed.

The erosion model utilised in the code is the best presently available in the literature. The author was restricted to a literature based model due to the time constraints of the programme. The model has been modified to best suit the needs of the operator. However, as it is a generic model it contains a number of weaknesses. Subsequent work would benefit from modifications to the present or the development of a new model that was better tailored to the specific requires presented by the study. See discussion of section 2.3.2.

In addition to the enhancement of the present erosion modelling strategy, addition wear phenomena such as flashing flows could be easily incorporated in the present modelling structure. Liquid droplet erosion has been briefly investigated by the author, finding that this wear phenomena can be easily accommodated within the present computational structure. Furthermore, given that the fluid properties, shear rates at the wall and temperatures are known, the CFD erosion model developed would be an excellent vehicle to investigate the erosion-corrosion synergy within oilfield components. The corrosion effects are currently neglected by the model, however facility is available to incorporate such considerations.

Improvements in multiphase modelling are becoming evident. The question of solid particle erosion driven by multiphase flows is one of extreme complicity but also interest. This subject area would require much investigation, and the investigator should not enter into it lightly. Here consideration must be given to the transport characteristics of the three phases produced from the reservoir; oil, gas and water. Furthermore, the partitioning of the particulate phase into such a multiphase mixture is of great interest. Further to the erosional effects generated by a multiphase mixture, the presence of water would have significant implications in terms of the erosion-corrosion synergy and the degradation of any corrosion inhibitor at the wall by sand impact.

The particulate phase is currently considered to be none deformable, in terms of both the erosion equations and the trajectory calculation. However, it was found that attrition of the particulate phase, in terms of both size and sharpness, occurs with impact events. The characterisation and incorporation of such an effect would be an important consideration if a series of components were to be considered simultaneously, or high velocity impacts were common, i.e. gas carrier.

Whilst the merits of the modified coefficient of restitution and squeeze film function were clearly demonstrated, the theory behind such terms is somewhat weak currently. The overall accuracy of the trajectory calculation, and hence the erosion prediction, would benefit from additional workings in this area. Furthermore, relatively little attention was applied to the turbulence closure models and their significance on the erosion prediction process. Additional work should be undertaken on the use of such closure models in the arduous prediction application presented by a control choke.

Finally, whilst a number of examples are provided whereby the investigative and optimisation abilities of the CFD erosion model are presented, the full ability of the model has yet to be explored and value, in terms of improved knowledge, to both choke manufactures and operators could be provided by further use and application.

12. References

Ref. 1 - ABB. Kent Introl Ltd.; '*Technical Sizing and Selection Manual*'; 1993.

Ref. 2 - Abbott M.B, Basco D.R; '*Computational Fluid Dynamics - An Introduction for Engineers*'; Longman Scientific & Technical, Harlow, England; 1989.

Ref. 3 - Asakura K, Asari T, Nakajima I; '*Coefficient of restitution and kinetic friction of particles colliding against wall in water*'; Hokkaido University, Faculty of Engineering; Slurry Handling and Pipeline Transport - Hydrotransport 12; bHr Group; 1993; pp 785-797.

Ref. 4 - Bahadur S; '*The Structure of Erosive Wear Models*'; Tribological Modelling for Mechanical Designers; ASTM; 1991.

Ref. 5 - Bahadur S, Badruddin R; '*Erodent Particle Characterisation and the Effect of Particle Size and Shape on Erosion*'; Wear of Materials; ASME; 1989; pp 143-153.

Ref. 6 - Bahadur S, Ambrosini L; '*Erosion of AISI 4140 Steel*'; Wear; Vol 117; 1987; pp 37-48.

Ref. 7 - Bechmann G, Gotzmann J; '*Analytical Model of the Blast Wear Intensity of Metals Based on a General Arrangement for Abrasive Wear*'; Wear; Vol. 73; 1981; pp 325-353.

Ref. 8 - Benchaita M.T, Griffith P, Rabinowicz E; *'Erosion of a metallic plate by solid particles entrained in a liquid jet.';* Journal of Engineering for Industry; Vol. 105; 1983; pp 215-222.

Ref. 9 - Bitter J.G.A; *'A study of the Erosion Phenomena, Parts 1 and 2'*; Wear; Vol. 6; 1963; pp 5-21, 169-190.

Ref. 10 - Boart International Hardmetal Division; '*Data Sheets for Tungsten Carbide Grades*'.

Ref. 11 - Boart International Hardmetal Division; '*Properties and Applications of Hardmetal*'.

Ref. 12 - Bolio E.J; *'Dilute turbulent gas-solid flow with particle interactions and turbulence modulation.';* PhD Thesis; Carnegie Mellon University; Pennsylvania; U.S.A; 1994.

Ref. 13 - Bourgoyne A.T; '*Experimental Study of Erosion in Diverter Systems Due to Sand Production.*'; SPE/IADC Drilling Conference; pp 807-816; 1989.

Ref. 14 - Bradshaw P (Ed); *'Topics in Applied Physics, Turbulence'*; Springer-Verlag; 1978.

Ref. 15 - Bradshaw P, Cebeci T, Whitelaw J.H; *'Engineering Calculation Methods for Turbulent Flow'*; Academic Press, London; 1981.

Ref. 16 - Bridwell H.C, Ward C.E, Rowley D.S; '*Erosion of Various Materials by Liquid-Entrained Abrasives*'; AMSE-65-WA/PET 2.

Ref. 17 - Burnett A.J, Pittman A.N, Bradley M.S.A; *'Observations on, and the Modelling of, Erosive Wear of a long Radius Pneumatic Conveyor Bend'*; World Tribology Congress; Institute of Mechanical Engineers; pp 308; 1997.

Ref. 18 - Carey W.W; *'Settling of spheres in Newtonian and non-Newtonian fluids'*; PhD Thesis; Syracuse University; U.S.A; 1970.

Ref. 19 - '*CFX User Guide*'; Computational Fluid Dynamics Services; Harwell Laboratory, U.K, 1994.

Ref. 20 - Cheremisinoff N.P (Ed); '*Encyclopaedia of Fluid Mechanics, Volume 6, Complex Flow Phenomena and Modelling*'; Gulf Publishing Company; 1987.

Ref. 21 - Clark H McI, Burmeister L.C; '*The influence of the squeeze film on particle impact velocities in erosion*'; International Journal of Impact Engineering; Vol. 12; No 3; 1992; pp 415-426.

Ref. 22 - Clark H McI; '*A comparison of particle impact in gas-solid and liquid-solid erosion.*'; Wear; Vol. 186; No 2; 1995; pp 465-472.

Ref. 23 - Crowe C. T, Sharma M. P, Stock D. E; '*The Particle-Source-in Cell (PSI-CELL) Model for Gas Droplet Flows*'; Transactions of the ASME, Journal of Fluids Engineering; 1977; pp 325-332.

Ref. 24 - Douglas J. F, Gasiorek J. M, Swaffield J.A; '*Fluid Mechanics*'; Longman Scientific & Technical; 1986.

Ref. 25 - Finnie I; '*Erosion of Surfaces by Solid Particles*'; Wear; Vol. 3; 1960; pp 87-103.

Ref. 26 - Finnie I; '*The Mechanism of Erosion of Ductile Metals*'; 3rd US National Congress of Applied Mechanics; 1958.

Ref. 27 - Finnie I, Stevick G.R, Ridgely J.R; '*The Influence of Impingement Angle on the Erosion of Ductile Metals by Angular Abrasive Particles*'; Wear; Vol. 152; 1992; pp 91-98.

Ref. 28 - Fitzpatrick M.J; '*Design Evaluation of Subsea Production Choke Valves*'; Internal BP Development Publication; 1987; ETC.86.ER.179; Unpublished.

Ref. 29 - Fitzpatrick M.J; '*Retrievable Subsea Production Choke Valve, Forward Strategy to 1997*'; BP Exploration, Technology Development Division, Engineering and Technical Report; 1988; ETC.88.ER.070; Unpublished.

Ref. 30 - Fitzpatrick M.J; '*Final Report on Design Study and Test Programme for a Choke Valve and Actuator for the DISPS Project*'; BP Petroleum Development (UK) Ltd, Riser Systems Group; 1989; BPE.89.ER.108; Unpublished.

Ref. 31 - Forder A.F; '*Erosion of oilfield control valves by turbulent particulate suspensions - Development of an erosion model.*'; University of Southampton, Department of Mechanical Engineering, U.K; ME/95/13; Aug 1995.

Ref. 32 - Forder A.F; '*The behaviour of Individual Solid Particles Suspended in a Confined Flow of Turbulent Fluid*'; Department of Mechanical Engineering; University of Southampton; Report No: ME/95/15; Oct. 95.

Ref. 33 - Frisch U, Keller J.B, Papanicolaou G, Pironneau O (Ed); '*Lecture Notes in Physics, Macroscopic Modelling of Turbulent Flows*'; Springer-Verlag; 1984.

Ref. 34 - Frost W, Bitte J; '*Statistical Concepts in Turbulence, Handbook of Turbulence, Volume* 1'; Plenum Press, New York; 1977.

Ref. 35 - Grant G, Tabakoff W; '*Erosion Prediction in Turbomachinery Resulting from Environmental Solid Particles*'; Journal of Aircraft; Vol. 12; No. 5; 1975; pp 471-478.

Ref. 36 - Hamzah R, Stephenson D.J, Strutt J.E; '*Erosion of Materials used in Petroleum Production*'; Wear; Vol. 186-187; 1995; pp 493-396.

Ref. 37 - Hashish M; '*An Improved Model of Erosion by Solid Particles*'; Proc. 7th Int. Conf. on Erosion by Liquid and Solid Impact; 1988; Paper 66.

Ref. 38 - Haugen K, Kvernvold O, Ronold A, Sandberg R; '*Sand Erosion of Wear Resistant Materials: Erosion in Choke Valves*'; Wear; Vol. 186-187; 1995; pp 179-188.

Ref. 39 - Head W.J, Lineback L.D, Manning C.R; '*Modification and Extension of a Model for Predicting the Erosion of Ductile Materials*'; Wear; Vol. 23; 1973; pp 291-198.

Ref. 40 - Head W.J, Harr M.E; '*The Development of a Model to Predict the Erosion of Materials by Natural Contaminants*'; Wear; Vol. 15; 1970; pp 1-46.

Ref. 41 - Hearing J.R; '*Free Turbulent Shear Flows*'; Conference Proceedings; NASA SP-321; 1973.

Ref. 42 - Hinze J.O; '*Turbulence, 2nd Edition*'; McGraw-Hill Book Company, New York; 1975.

Ref. 43 - Hotley H; '*Uber den Abnutzungsvorgang in Blasversatzrohren und die Frage der Bekampfung des Verschliesses*'; Geologie und Mijnbouw; Vol. 1; 1946. (Translation)

Ref. 44 - Hutchings I.M; '*A Model for the Erosion of Metals by Spherical Particles at Normal Incidence*'; Wear; Vol. 70; 1981; pp 269-281.

Ref. 45 - Hutchings I.M; '*Tribology, Friction and Wear of Engineering Materials*'; Arnold, Hodder Headline Group, 1995.

Ref. 46 - Hutchison J.W (Ed.); '*ISA Handbook of Control Valves, 2nd Edition*'; Instrument Society of America; 1976.

Ref. 47 - Jackson L.D.A; '*Slurry Abrasion*' CIM Trans.; Vol. 70; 1967; pp 219-224.

Ref. 48 - Jennings W.H, Head W.J, Manning C.R; '*A Mechanistic Model for the Prediction of Ductile Erosion*'; Wear; Vol. 40; 1976; pp 93-112.

Ref. 49 - Kleis I; '*Probleme der Bestimmung des Strahlverschleisses bei Metallen*'; Wear; Vol. 13; 1969; pp 199-215. (Translation)

Ref. 50 - Kovasznay L.S.G; '*Turbulent Shear Flow*'; Presented at Convegno Sulla Teoria Della Turbulenza; Rome; 1970.

Ref. 51 - Kozierv S.P; '*Analogy between Erosion Damage and Pitting of Machine Component Surfaces*'; Characterisation and Determination of Erosion Resistance; ASTM STP 474; 1970; pp 409-421.

Ref. 52 - Launder B. E, Spalding D. B; '*Mathematical Models of Turbulence*'; Academic Press; 1972.

Ref. 53 - Lesieur M; '*Turbulence in Fluids*'; Kluiver Academic Publishers; 1990.

Ref. 54 - Lomax H; '*Some Prospects for the Future of Computational Fluid Dynamics*'; AIAA J; 1982.

Ref. 55 - Lun C.K.K, Savage S.B; '*The effect of an impact velocity dependent coefficient of restitution on stresses developed by sheared granular* material'; Acta Machanica 63; 1986 pp 15-44.

Ref. 56 - Lynn R.S, Wong K.K, Clark H McI; *'On the particle size effect in slurry erosion.';* Journal of Wear; Vol. 149; 1991; pp 55-71.

Ref. 57 - Lyons J.L; *'Lyons' Valve Designer's Handbook'*; Van Nostrand Reinhold Company; 1982.

Ref. 58 - McLaughlin M; *'Experimental study of particle wall collisions relating to flow of solid particles in a fluid'*; PhD Thesis; California Institute of Technology; U.S.A; 1968.

Ref. 59 - McLaury B.S; MPhil Thesis; *'A Model to Predict Solid Particle Erosion in Oilfield Geometries.'* University of Tulsa; 1993.

Ref. 60 - Miller A.E, Coyle J; *'Erosion by Aqueous Slurries'*; Dept. Engineering and Material Science; University of Notre Dame; 1972.

Ref. 61 - Moore A.J, Wood R.J.K; *'The Erosive Wear Behaviour of Pipeline Materials in Slurry Flow Streams'*; BP Technical Report; Unpublished.

Ref. 62 - Munday A.J, Farrar R.A; *'An Engineering Data Book'*; University of Southampton; 1979.

Ref. 63 - Naim M, Bahadur S; *'Effect of Microstructure and Mechanical Properties on the Erosion of 18 Ni (250) Maraging Steel'*; Wear; Vol. 112; 1986; pp 217-234.

Ref. 64 - Naim M, Bahadur S, *'The Significance of the Erosion Parameter and the Mechanisms of Erosion in Single-Particle impacts'*; Wear; Vol. 94; 1984; pp 219-232.

Ref. 65 - Neilson J.H, Gilchrist A; *'Erosion by a Stream of Solid Particles'*; Wear; Vol. 11; 1968; pp 123-143.

Ref. 66 - Nesic S, Postlethwaite J; *'Relationship Between the Structure of Disturbed Flow and Erosion-Corrosion'*; Corrosion; Vol. 46; No. 11; 1990; pp 874-880.

Ref. 67 - Nokleberg L, Sontvedt T; *'Erosion in Choke Valves - Oil and Gas Industry Applications'*; Wear; Vol. 186-187; 1995; pp 401-412.

Ref. 68 - Percy R.J; *'Guidelines for the Selection of Choke Valves'*; BP Engineering, Risers & Subsea Equipment Group; 1990; BPE.90.ER.151; Unpublished.

Ref. 69 - Percy R.J; *'The Operational Performance of BP choke Valves'*; BP Engineering, Risers and Subsea Equipment Group; 1990; BPE.90.ER152; Unpublished.

Ref. 70 - Peters J; *'Reliable Hydrodynamic Energy Dissipation in Subsea Choke Valves'*; Progress in Subsea Engineering; BHRA; 1989; pp 99-113.

Ref. 71 - Pourahmadi F, Humphrey J.A.C; *'Modelling Solid-Fluid Turbulent Flows with Application to Predicting Erosive Wear'*; PCH PhysicoChemical Hydrodynamics; Vol. 4; 1983; pp 191-219.

Ref. 72 - *'Production Choke Technical Review'*; Masterflo Valve Inc.

Ref. 73 - Raask E; *'Tube Erosion by Ash Impaction'*; Wear; Vol. 13; 1969; pp 301-315.

Ref. 74 - Rochester M.C, Brunton J.H; *'Influences of Physical Properties of the Liquid on the Erosion of Solids'*; Erosion, Wear and Interfaces with Corrosion; ASTM STP 567; 1973; pp 128-147.

Ref. 75 - Roco M.C; *'Liquid solid two-phase flow.';* CSIRO Seminar Notes; Melbourne; 1992.

Ref. 76 - Sato S, Shimizu A, Yokomine T; *'Numerical Prediction of Erosion for Suspension Flow Duct'*; Wear; Vol. 186-187; 1995; pp 203-209.

Ref. 77 - Shames I. H; '*Mechanics of Fluids*'; McGraw-Hill Inc; 1992.

Ref. 78 - Sheldon G.L; '*Similarities and Differences in the Erosion Behaviour of Materials*'; Trans. ASME; J. Basic Engineering; Series D 92; No. 3; 1970; pp 619-626.

Ref. 79 - Sheldon G.L, Kanhere A; '*An Investigation of Impingement Erosion using Single Particles*'; Wear; Vol. 21; 1972; pp 195-209.

Ref. 80 - Shewmon P.G, Sundarajan G; '*A New Model for the Erosion of Metals at Normal Incidence*'; Wear; Vol. 84; 1983; pp 237-258.

Ref. 81 - Shirazi S.A, McLaury B.S, Shadley J.R, Rybicki E.F; *'Generalisation of the API RP14E guideline for erosive service.';* Journal of Pressure Vessel Technology - Transaction of ASME; 1995.

Ref. 82 - Siebel E, Brockstedt H.C; '*Verschleissminderung*'; Maschinenbau; Vol. 20; 1941. Translation.

Ref. 83 - Smeltzer C.E, Gulden M.E, Compton W.A; '*Mechanisms of Metal Removal by Impacting Dust Particles*'; Trans. ASME; J. Basic Engineering; 1970; pp 639-652.

Ref. 84 - Speziale C.G; '*On Non-linear k-l and k-Epsilon Models of Turbulence*'; Journal of Fluid Mechanics; Vol 178; pp 459-475; 1987.

Ref. 85 - Sundararajan G, Shewmon P.G; '*A New Model for the Erosion of Metals at Normal Incidence*'; Wear; Vol. 84; 1983; pp 237-258.

Ref. 86 - Tabor D; '*Hardness of Solids';* Endeavour, Vol. 13, pp 49, 1954.

Ref. 87 - Tennekes H, Lumley J.L*; 'A First Course in Turbulence*'; MIT Press, Cambridge; 1972.

Ref. 88 - Tilly G.P, Sage W; '*The Interaction of Particle and Material behaviour in Erosion Processes*'; Wear; Vol. 16; 1970; pp 447-465.

Ref. 89 - Tilly G.P; *'Erosion caused by Airborne Particles'*; Wear; Vol. 14; 1969; pp 63-79.

Ref. 90 - Tilly G.P; '*A Two Stage Mechanism of Ductile Erosion*'; Wear; Vol. 23; 1973; pp 87-96.

Ref. 91 - Tritton D.J; '*Physical Fluid Dynamics, 2nd Edition*'; Oxford Science Publications; 1988.

Ref. 92 - Uuemois H, Kleis I; '*A Critical Analysis of Erosion Problems which have been little studied*'; Wear; Vol. 31; 1975; pp 359-371.

Ref. 93 - Welliner K, Uetz H; '*Gleit, Spul-Und Strahlverschleiss-Prufung*'; Wear; Vol. 1; 1958; pp 225-31. (Translation)

Ref. 94 - Wellinger K, Brockstedt H.C; '*Ermittling des Verschleiss-Widerstandes van Werkstoffen fur Blasversatzrohre*'; Stahl und Eisen; Vol. 62; 1942. (Translation)

Ref. 95 - Wood R.J.K; '*Material Selection for Reducing Erosive Damage to Valves';* Erosion and Corrosion Research Consultancy Service, Department of Mechanical Engineering, University of Southampton; Unpublished.